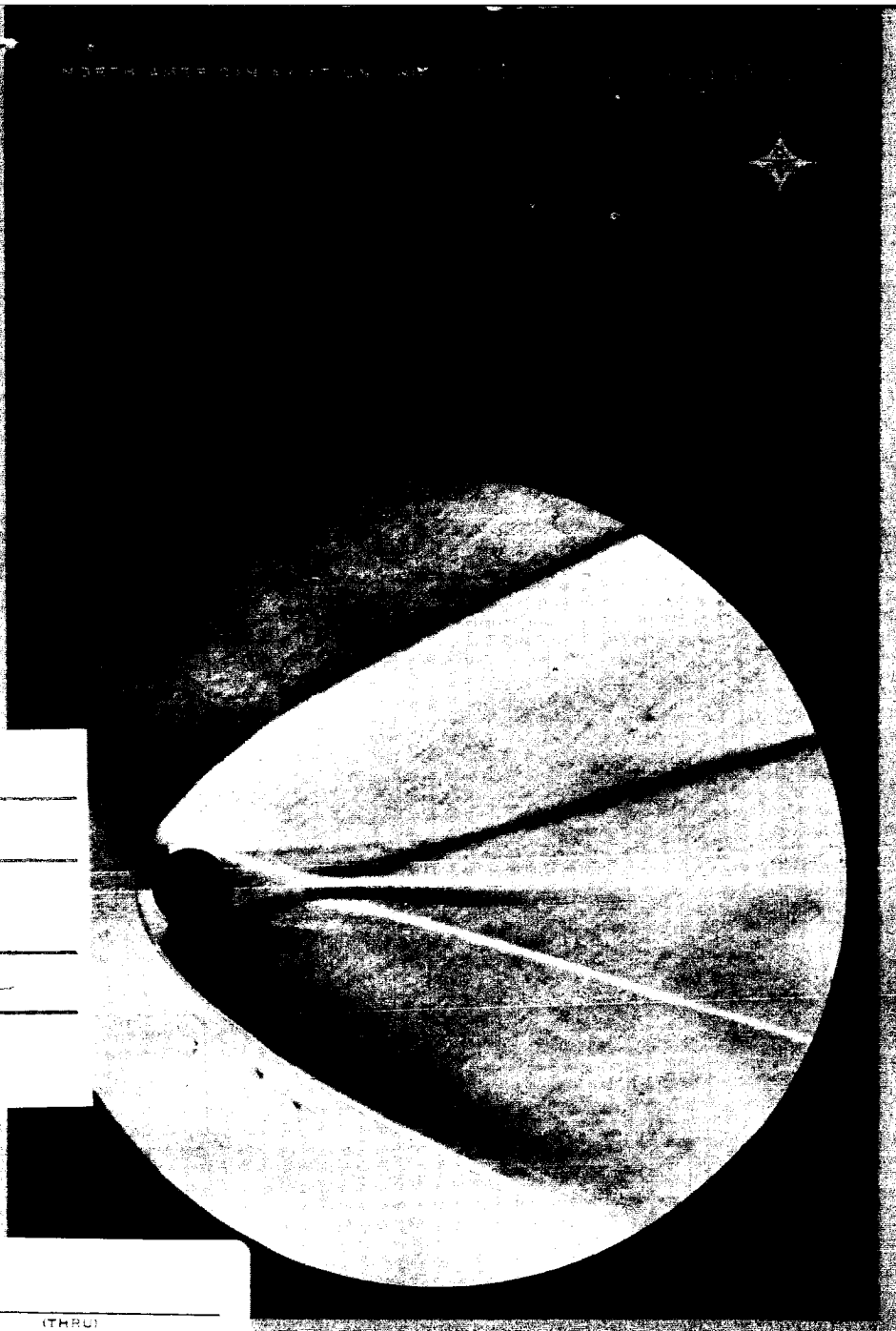

FLIGHT SCIENCES DEPARTMENT

Final Report — Flow Field Prediction and Analysis Study for Project RAM B-3

W. H. Ball

Prepared for
Langley Research Center
National Aeronautics and Space Administration
Langley Station, Virginia

Copy No. 90

SID 65-1113

FINAL REPORT

FLOW FIELD PREDICTION AND ANALYSIS

STUDY FOR PROJECT RAM B3

(Contract No. NAS1-4743)

20 August 1965

Prepared by

Flight Sciences Department

W. H. Ball
Project Engineer

H. G. Webb, Jr.
Gasdynamics Supervisor
Aero-Thermodynamics

F. J. Lyon
Project Manager
Flight Sciences Department

NORTH AMERICAN AVIATION, INC.
SPACE and INFORMATION SYSTEMS DIVISION

FOREWORD

This document comprises the final report on Project RAM B3 flow field prediction work accomplished between March and August 1965 by the Space and Information Systems Division (S&ID) of North American Aviation, Inc. (NAA), for the NASA Langley Research Center under Contract NAS1-4743, Flow Field Prediction and Analysis Study for Project RAM. This work was conducted by the NAA/S&ID Flight Sciences Department under the direction of Mr. F. J. Lyon, Program Manager and Mr. H. G. Webb, Jr., Gasdynamics Supervisor, with Mr. W. H. Ball serving as the study Project Engineer. The following individuals contributed significantly to this study in the areas indicated: Dr. S. A. Waiter, boundary layer calculations; Mr. R. L. Norcross, boundary layer calculations, transonic flow field calculations, and data preparation; Messrs. S. Hersh and C. E. Hildebrand, nonequilibrium chemistry calculations; and Mrs. M. F. DeWolf, inviscid-viscous merger profile determination and data preparation.

Mr. W. L. Grantham was the NASA Technical Monitor responsible for this study.

SUMMARY

This report presents the results of a theoretical analysis conducted to predict the flow field properties in the shock layer surrounding the RAM B3 vehicle shape for fourteen different flight conditions. These flight conditions varied along an ascent trajectory from an altitude of 124,775 ft at a velocity of 9,221 ft per second to an altitude of 247,373 ft at a velocity of 17,649 ft per second. A maximum velocity of 18,154 ft per second was achieved. The vehicle shape is a spherically blunted, nine-degree semi-apex angle cone.

Special emphasis was attached in this study to the determination of the flow field properties which are essential in the prediction of radio signal attenuation effects. The properties of most significance in the definition of these effects are the free electron concentration, concentrations of neutral and ionic species, temperature, and pressure. The final results of the analysis take into account the effects of finite chemical reaction rates on local properties by means of a nonequilibrium reacting gas streamtube analysis.

The complete inviscid and viscous regions of the flow field were computed assuming chemical equilibrium using three digital computer programs. The first program computed the boundary layer characteristics using locally similar solutions coupled to the momentum integral equation. The second program was used to compute the transonic flow field properties, utilizing a direct method blunt body procedure. The results from this calculation provided the starting line data for a real gas method-of-characteristics computation of the supersonic inviscid flow field. In these calculations, displacement thickness effects from the initial boundary layer growth calculation were included. Following the calculation of the supersonic inviscid flow field properties, a refined boundary layer growth calculation was made to provide improved property distribution data through the viscous region.

Nonequilibrium effects in the merged inviscid and viscous flow regions were computed by application of a one-dimensional reacting gas program along streamlines using appropriate matching parameters. In the inviscid flow field the matching parameter used in the nonequilibrium analysis was pressure, while in the viscous region three matching parameters were used: pressure, velocity, and streamtube area.

Complete flow field properties were computed along eight streamlines for each case, and the property distribution profiles are presented along nine normals to the body surface spaced from the stagnation point to the aft end of the body. The results of the analysis show significant departures from chemical equilibrium conditions along the RAM B3 flight trajectory at both high altitudes and low flight velocities.

CONTENTS

	Page
SUMMARY	v
LIST OF ILLUSTRATIONS AND TABLES	ix
INTRODUCTION	1
DISCUSSION OF METHODS	3
GENERAL	3
APPROXIMATE BODY PROPERTY CALCULATION	7
PRELIMINARY BOUNDARY LAYER GROWTH	7
BLUNT BODY FLOW FIELD	11
SUPERSONIC INVISCID FLOW FIELD	17
REFINED BOUNDARY LAYER GROWTH	20
STREAMLINE DEFINITION	20
DETERMINATION OF MATCHING PARAMETERS	27
NONEQUILIBRIUM ANALYSIS	32
RESULTS	43
CONCLUSIONS AND RECOMMENDATIONS	187
NOMENCLATURE	189
REFERENCES	193

ILLUSTRATIONS

Figure		Page
1	Steps in Flow Field Analysis	4
2	Geometry and Coordinate Systems for RAM B3 Vehicle	5
3	RAM B3 Geometrical Relations	6
4	RAM B3 Trajectory Points	9
5	Method of Estimating Preliminary Body Pressure Distribution	10
6	Displacement Thickness Model	12
7	Definition of Transonic Flow Field Geometry	13
8	Streamline Pattern	15
9	Shock Shape Calculation	16
10	Typical CRT Output of the Transonic Flow Field (Case 5)	18
11	Enlarged View of the Transonic Flow Field Showing the Computed Starting Line (Case 5)	19
12	Distribution of Flow Field Properties Along the Starting Characteristic for Case 5	21
13	Typical Characteristics Network and Streamline Pattern (Case 10)	22
14	Final Equilibrium Boundary Layer Edge Properties for Case 9	23
15	Final Equilibrium Boundary Layer Edge Properties for Case 9	24
16	Boundary Layer Growth Over the RAM B3 Surface for Case 9	25
17	Streamline Location in Boundary Layer	26
18	Typical Velocity and Pressure Distribution in the Stagnation Region of a Blunt Body	28
19	Comparison of Velocity and Pressure Matched Results for the Stagnation Streamline (Case 7)	29
20	Pressure Matching Parameter for Case 14	30
21	Thermodynamic Properties Behind an Oblique Shock Wave for Frozen Free-Stream Chemistry (Case 7)	31
22	Example of Merged Viscous-Inviscid Regions (Case 3, Normal 5)	33
23	Velocity Matching Parameter for Case 14	34
24	Area Matching Parameter for Case 14	35
25a-i	Flow Field Properties - Case 1	47-55
26a-i	Flow Field Properties - Case 2	57-65
27a-i	Flow Field Properties - Case 3	67-75
28a-i	Flow Field Properties - Case 4	77-85
29a-i	Flow Field Properties - Case 5	87-95
30a-i	Flow Field Properties - Case 6	97-105

Figure		Page
31a-i	Flow Field Properties - Case 7	107-115
32a-i	Flow Field Properties - Case 8	117-125
33a-i	Flow Field Properties - Case 9	127-135
34a-i	Flow Field Properties - Case 10	137-145
35a-i	Flow Field Properties - Case 11	147-155
36a-i	Flow Field Properties - Case 12	157-165
37a-i	Flow Field Properties - Case 13	167-175
38a-i	Flow Field Properties - Case 14	177-185
39	Variation of Peak Electron Density Along RAM B3 Flight Trajectory	186

TABLES

Table		Page
1	RAM B3 Flight Conditions	8
2	Chemical Reactions and Rate Constants	40
3	Analytic Expressions for Equilibrium Constants $K_p(j)$ vs Temperature	41

INTRODUCTION

The problem of radio-frequency attenuation caused by the interaction of the electromagnetic wave with the plasma sheath during entry into the earth's atmosphere has become the subject of considerable interest in recent years. The importance of the problem has been emphasized by the loss of communications during Mercury and Gemini flights. During these flights, the loss of radio contact lasted for only a few minutes; but for future manned space flights such as Apollo, the loss of communications will exist for longer periods, during which the space vehicle could travel thousands of miles. The National Aeronautics and Space Administration (NASA) has established a program known as RAM (Radio Attenuation Measurement) at the Langley Research Center to study the factors which contribute to this blackout problem. As a part of this program, reentry flight tests have been conducted to obtain experimental data under realistic flight conditions. The RAM B3 vehicle was used during such a flight test to obtain plasma parameter measurements for use in evaluating theoretical methods for defining reentry plasma characteristics.

The work documented in this report represents the results of a study in which theoretical concepts and engineering techniques are applied to the calculation of the flow field properties around the RAM B3 vehicle for a series of fourteen flight conditions. These flight conditions represent a series of points along the ascent trajectory followed by the vehicle during the flight test. The flight velocities vary from 9,221 ft/sec to 18,154 ft/sec and altitude extremes from 124,775 ft to 247,373 ft. A comparison of the theoretically predicted results documented in this report with the flight data will allow an evaluation of the adequacy of the analytical methods employed.

Special importance is attached to the determination of the distribution of free electrons and neutral and ionic species in the flow field. The free electron concentration is an important factor in defining the plasma frequency at which a significant part of the wave electric energy can be transformed into electron kinetic energy and thus alter the wave characteristics. The concentrations of neutral and ionic species are used in the calculation of another important plasma property, the electron collision frequency. Since electron interactions may be binary with neutral species or ions, or with several particles concurrently, all significant concentrations of ions and neutral species, as well as electrons, are calculated in this study.

The following sections of this report present and describe the aerothermochemical flow field methods employed in this study and the numerical results obtained.

DISCUSSION OF METHODS

GENERAL

The first part of the analysis concerns the chemical equilibrium flow field surrounding the body. This includes computing the properties of the subsonic, transonic, and supersonic flow regimes, in both inviscid and viscous regions, which are necessary for the final computation of the non-equilibrium flow field.

The calculation of the equilibrium flow field involves the following series of steps. A preliminary calculation of the boundary layer displacement thickness is made, based upon estimated body flow properties. The analysis utilizes similar boundary layer solutions coupled to the momentum integral equation. The boundary layer displacement thickness, added to the geometrical shape of the body, gives an effective body shape which is then used for the inviscid flow field calculations. The transonic flow field, computed by a direct method, gives sufficient flow field detail to define a starting characteristic, which is used as input data for the method-of-characteristics solution of the supersonic flow field.

These calculations provide improved aerodynamic properties at the wall of the body for use in a refined analysis of the boundary layer. The refined boundary layer analysis provides viscous region property distribution data which are used to determine streamline locations in the merged viscous-inviscid region.

The nonequilibrium chemistry calculations are then performed along predetermined streamlines in the inviscid region, using a matching parameter assumed to be insensitive to finite reaction rate effects. The results from these calculations provide nonequilibrium inviscid properties which are merged with the previously calculated equilibrium boundary layer properties to obtain flow field property distribution profiles at various locations along the surface. These profiles and the streamline locations are used to determine the three matching parameters utilized in the boundary layer version of the nonequilibrium chemistry program. Calculation of nonequilibrium chemistry effects along streamlines in the boundary layer completes the sequence of steps required to obtain the final data. A diagram illustrating the sequence of steps used in the analysis is shown in Figure 1. The details of each step of the analysis will be described in the following sections of this report.

The RAM B3 vehicle is a spherically blunted, nine-degree semi-apex angle cone. The geometry of the vehicle, the coordinate systems used in the analysis, and the locations of the normals along which property distributions are presented in later sections of this report are shown in Figure 2. The relationships between the body coordinates, Z and R, the local surface inclination angle θ_w, and the distance parameter S/S_{max} are shown in Figure 3.

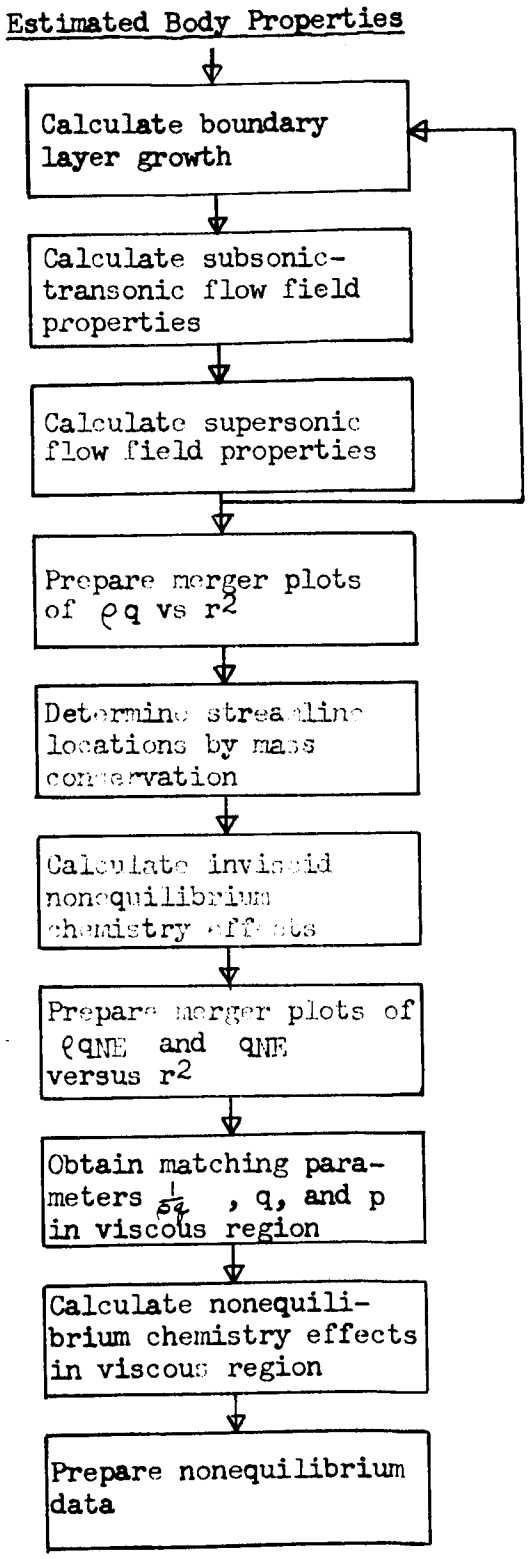

Figure 1. Steps in Flow Field Analysis

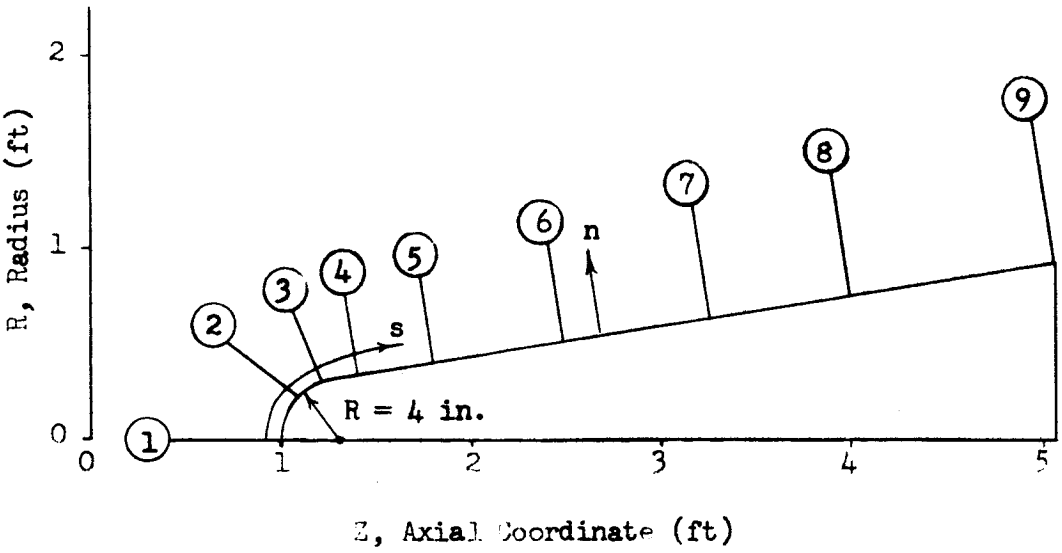

Normal Number	Dimensionless Axial Coordinate from Stagnation Point $\bar{X}/D$	Axial Coordinate Z, ft
1	0.0	1.000
2	.14750	1.098
3	.32600	1.217
4	.60000	1.400
5	1.20000	1.800
6	2.25000	2.500
7	3.40000	3.267
8	4.50000	4.000
9	6.10000	5.064

Note: The axial coordinate from the stagnation point, $\bar{X}$, is equal to (Z-1).

Figure 2. Geometry and Coordinate System for RAM B3 Vehicle

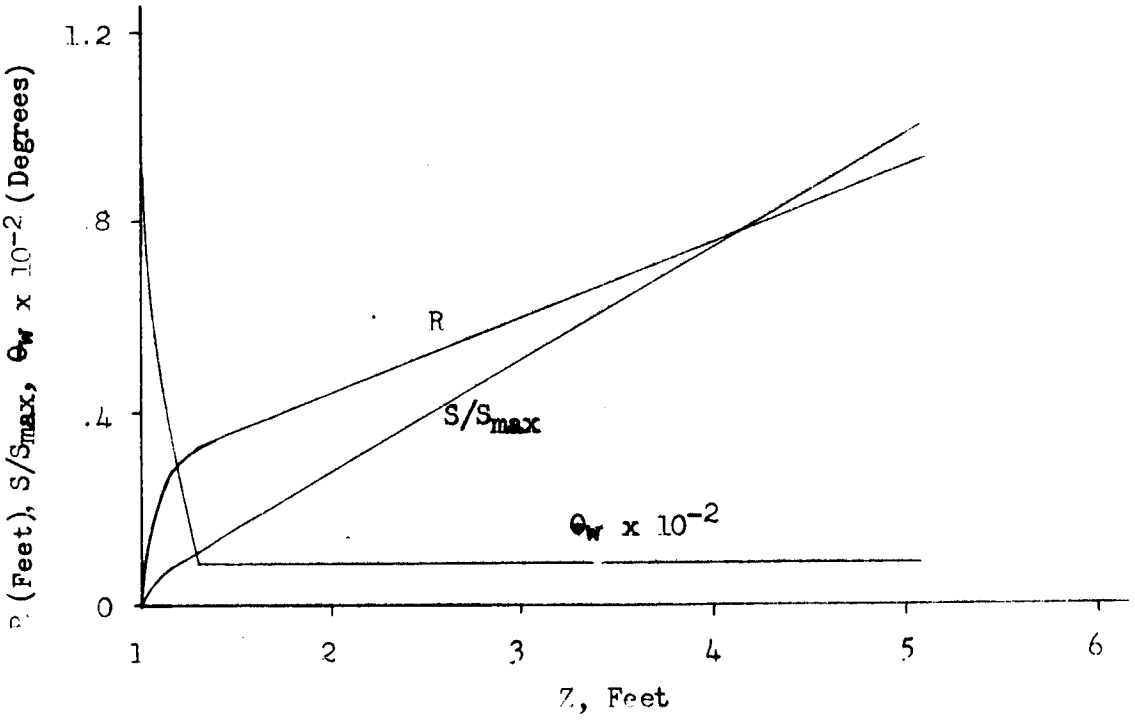

Figure 3. RAM B3 Geometrical Relations

The analysis is based on a flight attitude of zero degrees angle-of-attack. The flight conditions used in the analysis are shown in Table 1, and the plotted variation of velocity with altitude is shown in Figure 4.

APPROXIMATE BODY PROPERTY CALCULATION

A preliminary estimate of aerodynamic properties along the body is required to start the boundary layer calculations. Assuming thermodynamic equilibrium, the state of the gas is defined if entropy and pressure are known. Entropy is computed from the solution of a normal shock at free-stream conditions, and standard aerodynamic methods are used to predict body pressure distribution. On the spherical portion of the body, modified Newtonian-matched Prandtl-Meyer theory is used to predict the pressure distribution. The pressure distribution far back on the conical portion of the body is assumed to approach the modified Newtonian cone value. Between the last Prandtl-Meyer point and the cone pressure, the rate of pressure decay is predicted by blast wave theory. Figure 5 illustrates the method of predicting pressure distribution over the body surface.

PRELIMINARY BOUNDARY LAYER GROWTH

The objective of the preliminary analysis is the calculation of a boundary layer displacement thickness which, when added to the geometrical body, gives an aerodynamically effective body shape which is used for inviscid flow field calculations.

The methods used most frequently to analyze boundary layers are similarity solutions and integral methods. The similarity method expresses the fact that under certain conditions boundary layer profiles at all points on a body are nondimensionally similar, and property distributions through the boundary layer may be described in terms of a single parameter. The results of this method have been verified experimentally (e.g., by measuring local skin friction or heat transfer). The similarity solution gives a complete description of all properties in the boundary layer.

Integral methods of boundary layer analysis are also used frequently in problems involving boundary layer growth or separation. These methods utilize the simplification in the analysis which can be made by assuming the form of the property distribution across the boundary layer. By satisfying appropriate boundary conditions at the wall and outer edge of the boundary layer, the complexity of the partial differential boundary layer equations can be reduced. By integrating the momentum equation across the boundary layer, the momentum integral equation describes the longitudinal growth of the momentum thickness, a gross or integrated parameter. Use of the assumed profiles with the appropriate boundary conditions allows the solution of a particular problem. This solution satisfies the conservation equations on a gross or integrated basis across the boundary layer, rather than satisfying exactly the original partial differential equations at all points. The integral technique furnishes a valuable tool for cases in which no exact solution is available. In the RAM B3 analysis, some features of both the similarity and the integral techniques were used. The profiles, rather than being assumed, are obtained

Table 1. RAM B3 Flight Conditions

Case Number	Time of Flight (sec)	Velocity (ft/sec)	Altitude (ft)	Ambient Pressure (lb/sq ft)	Ambient Temperature (°K)	Ambient Density (slugs/cu ft)
1	96.17	9,221	124,775	8.2788	255.1	1.0544×10^{-5}
2	104.67	10,707	135,539	5.4002	264.8	6.6244×10^{-6}
3	111.6	12,657	144,458	3.8331	272.8	4.5616×10^{-6}
4	116.67	14,631	151,179	2.9495	278.4	3.4308×10^{-6}
5	120.17	16,388	156,222	2.4779	282.6	2.8603×10^{-6}
6	122.17	17,535	159,276	2.1924	282.6	2.3463×10^{-6}
7	125.07	18,154	163,868	1.8747	282.6	2.1467×10^{-6}
8	133.0	18,028	175,996	1.2079	282.0	1.3990×10^{-6}
9	147.	17,888	194,892	0.58964	256.3	7.4122×10^{-7}
10	166.	17,782	215,600	0.24728	228.5	3.4833×10^{-7}
11	177.	17,740	225,400	0.15803	215.3	2.3605×10^{-7}
12	185.	17,718	231,400	0.11683	207.3	1.8192×10^{-7}
13	202.	17,683	240,800	0.072283	194.6	1.1996×10^{-7}
14	235.	17,649	247,373	0.051819	185.8	8.9610×10^{-8}

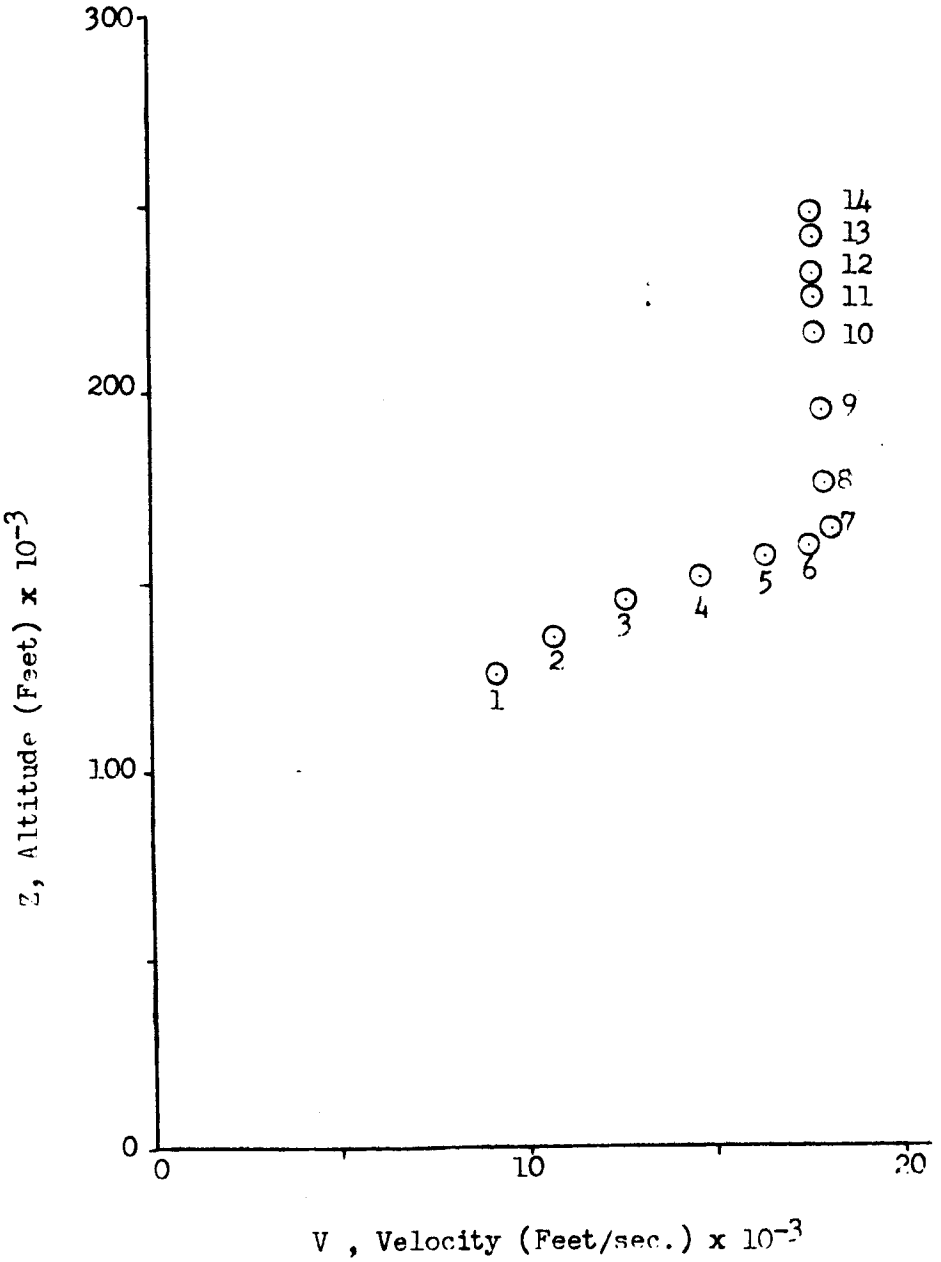

Figure 4. RAM B3 Trajectory Points

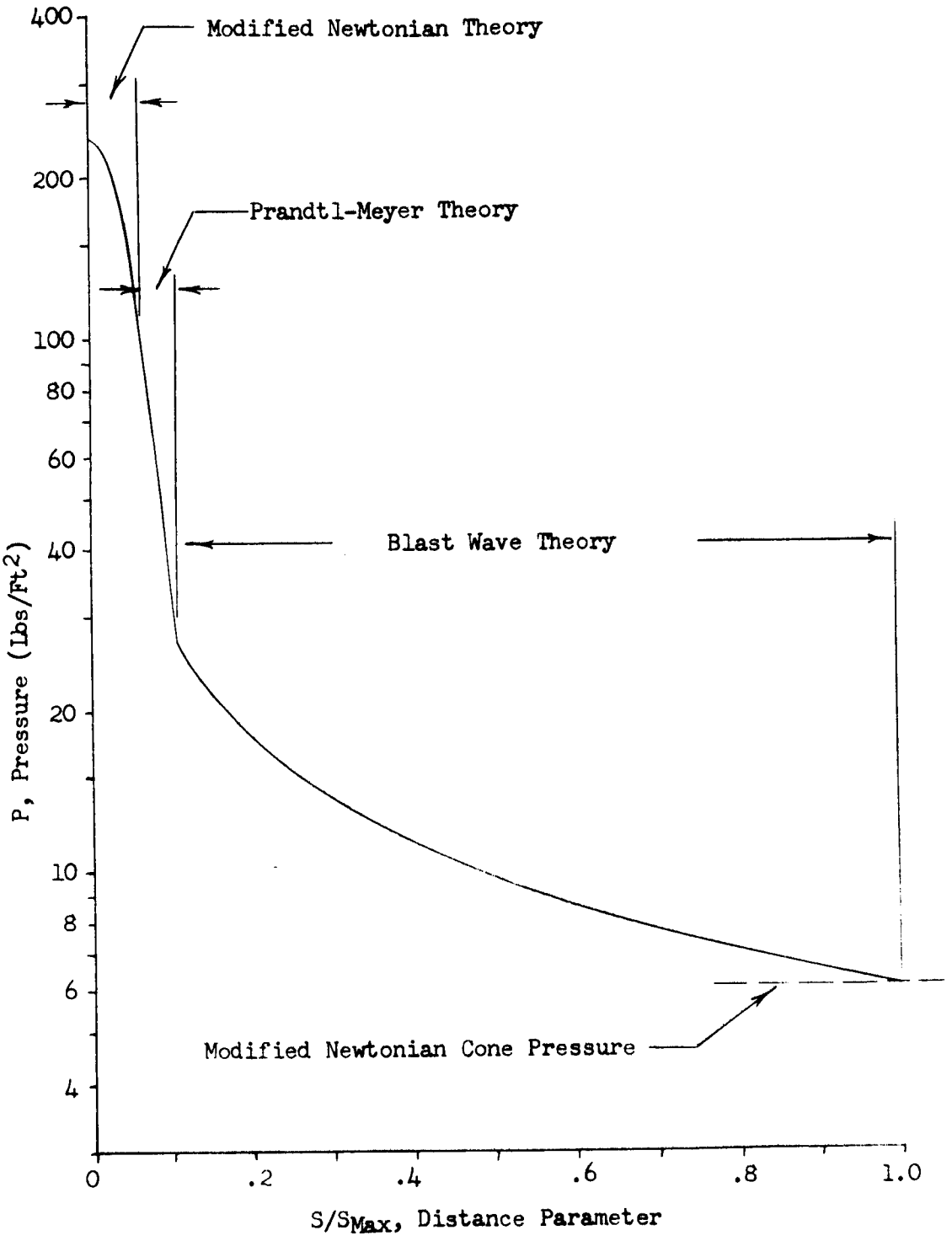

Figure 5. Method of Estimating Preliminary Body Pressure Distribution

from the locally similar solution, while the boundary layer momentum thickness growth is computed with the momentum integral equation.

The similarity solutions are used with local edge properties and their gradients to calculate the nondimensional distribution of properties across the boundary layer at selected points on the body. The properties are nondimensionalized with respect to the property values at the outer edge of the boundary layer. The actual thickness results from the integration of the momentum integral equation. An IBM computer program is used to perform the calculation of the boundary layer growth over the body surface. The theoretical methods used in the calculation procedure are fully documented in Reference 1.

The displacement thickness resulting from the preliminary boundary layer growth calculation is used to define the effective body shape. From the results of the RAM B3 preliminary boundary layer growth calculations, it is concluded that the displacement thickness on the spherical portion of the body is a negligible fraction of the nose radius. The computed displacement thickness on the spherical portion of the body varies from .00017 ft to .001 ft for the range of flight conditions considered but is essentially constant over the surface for any one flight condition. Therefore, the effect of displacement thickness on the calculation of the stagnation region inviscid flow field properties can be neglected; and a simplified model of the displacement thickness growth is used which results in negligible error in body property distributions. A diagram illustrating the displacement thicknesss growth model used in the study is presented in Figure 6. This model uses a negligible displacement thickness correction over the forward portion of the spherical nose up to the sonic point and a linear growth rate from that point to the rear of the body. This model fits the actual growth of the displacement thickness at all points with an error less than one per cent of the body radius and is adequate for taking into consideration the small displacement effect of the boundary layer.

BLUNT BODY FLOW FIELD

The method used in computing the transonic flow field is based on the concept of mass flow conservation (Reference 2). This method is related to other direct methods in the sense that the free-stream conditions and body shape are known; and the flow field, shock wave shape, and location are obtained as a solution. The three equations of conservation are solved as a function of the streamtube cross section; and, as a result, the streamlines are direct solutions of the problem. A high level of accuracy is required in the input data, as in most other methods of solving the transonic flow field, to avoid instabilities in the numerical solution. The method requires, in addition to the flight conditions and the body shape, a preliminary estimate of the body pressure and shock shape. This method is iterative, so the better these initial approximations, the fewer the iterations required.

The solution near the stagnation point cannot be determined accurately by this calculation method, since the calculated pressure gradient depends on the streamline curvature and becomes unusable near the stagnation point where the flow radius of curvature becomes infinite. The method used to obtain the stagnation line flow properties is discussed in the section on Matching Parameters.

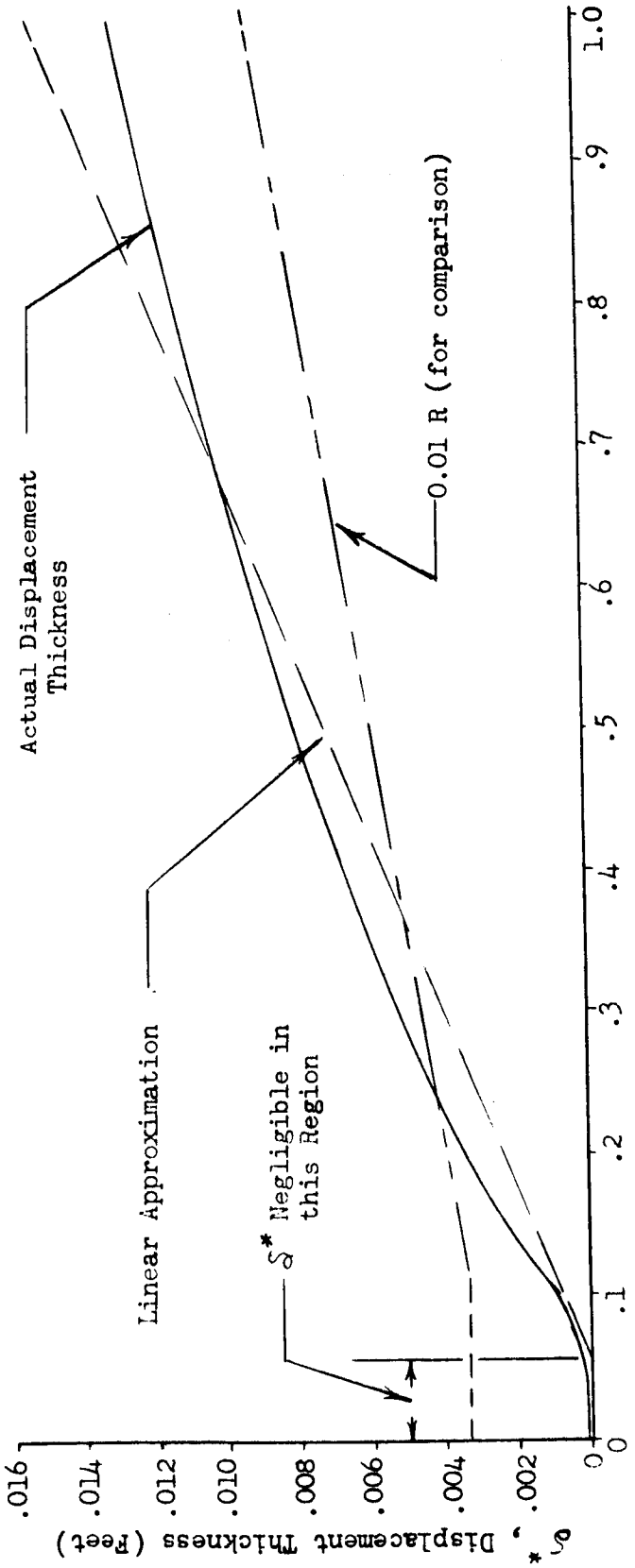

Figure 6. Displacement Thickness Model

Theoretical Development

The equations of conservation, when applied to the flow field shown in Figure 7, are used in the following forms:

Continuity Equation

The usual form of the equation of continuity

$$\vec{\nabla} \cdot (\rho \cdot \vec{q}) = 0 \tag{1}$$

is expressed along a streamtube and gives, for the 2-Dimensional case,

$$\rho_\infty q_\infty (r_1 - r_2) = \rho_{I,J} q_{I,J} \cdot \Delta n \tag{2}$$

and, for the axisymmetrical case,

$$\pi \rho_\infty q_\infty (r_1^2 - r_2^2) = \rho_{I,J} q_{I,J} 2\pi \left(\frac{r_3 + r_4}{2}\right) \Delta n \tag{3}$$

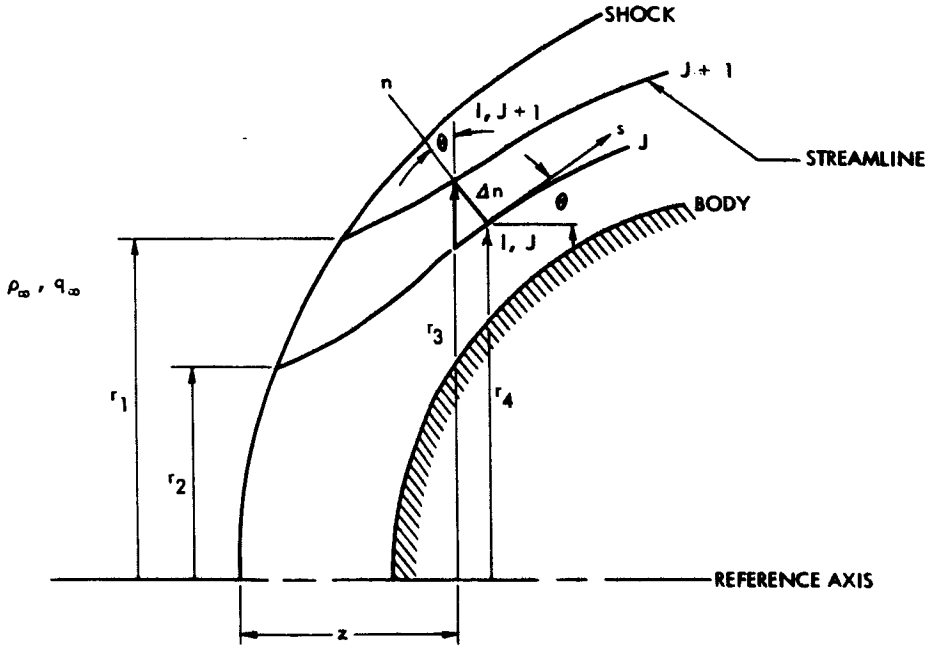

Figure 7. Definition of Transonic Flow Field Geometry

Momentum Equation

The equation of momentum

$$\frac{d\vec{q}}{dt} = -\frac{1}{\rho}\,\vec{grad}\ p \tag{4}$$

is applied along a normal to the streamlines as

$$\frac{dp}{dn} = \rho_{I,J}\,\frac{q^2_{I,J}}{R_{c\,I,J}} \tag{5}$$

Energy Equation

Along a streamline, the energy equation is simply written

$$\frac{dS}{dt} = 0 \tag{6}$$

and, as a consequence,

$$h + \frac{q^2}{2} = H_0 \tag{7}$$

It can be seen that the three conservation equations now have assumed a very simple form under these conditions.

The general procedure for the calculation proceeds step by step, starting from the body where geometric and aerodynamic parameters are known or estimated with the highest accuracy available. From this starting condition, other streamlines are constructed. The Hugoniot relationships are used across the assumed shock shape for a set of ordinates r_n, and the value of entropy S for each chosen streamline is computed. The conservation equations of mass and momentum are solved for S = constant to compute the streamline network. The details of the process are as follows:

a. Let $M_{I,O}$ be a point on the body, as shown in Figure 8, where entropy and radius of curvature are known, from Hugoniot relationships and exact body coordinates. With the hypothesis of thermodynamic equilibrium, the other aerodynamic characteristics, such as ρ and q, are defined by available data on thermodynamic properties of air and the energy equation. The term $\Delta p/\Delta n$ of the momentum equation (5) then can be computed along the body.

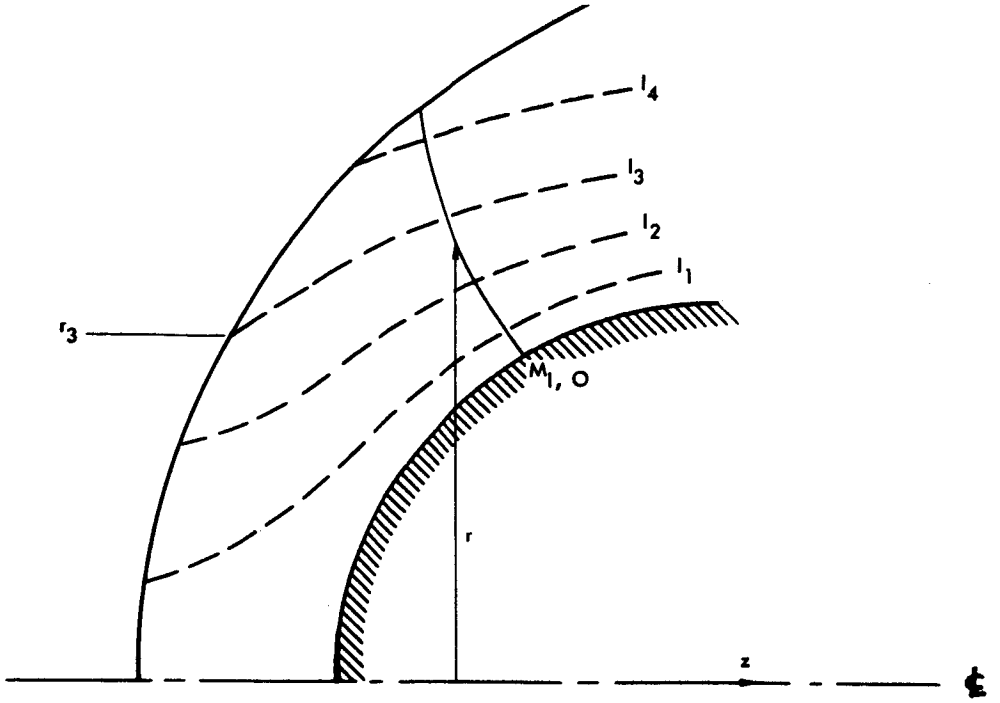

Figure 8. Streamline Pattern

b. The continuity equations (2) or (3) are used now to compute Δn at each point of the second streamline. From Figure 7 it can be seen that, for the case of an axisymmetrical body, $r_3 = r_4 + \Delta n \cos \theta_w$.

Two versions of the computer program have been developed to compute the aerodynamic characteristics on the second streamline, S_1 . The first version, which was used for the RAM Phase II calculations (Reference 3) assumes as a first step that the $\rho_{I,1}$ and $q_{I,1}$ on the second streamline are the same as those on the body at the I point. From Equations (2) and (3), Δn can then be calculated; and its introduction in the momentum equation gives p_1 . Pressure and entropy define a new state; and, with the assumption of thermodynamic equilibrium, the other parameters required-- $\rho_{I,1}$ and $q_{I,1}$ for instance--are obtained easily. The second version uses mean values of the aerodynamic characteristics on the upper and lower streamlines $\bar{\rho}_{I,1}$, $\bar{q}_{I,1}$, $\bar{R}_{cI,1}$ to refine the first approximation of Δn . This refined value of Δn is then introduced in the momentum equation, from which a new p_1 is computed; and, associated with the still-unchanged entropy S_1 , the final values of $\rho_{I,1}$, $q_{I,1}$, $h_{I,1}$, and $T_{I,1}$ are obtained.

This second method is very accurate; and because of the simplicity of the RAM B3 configuration, it was selected for use in the present computations.

c. The determination of subsequent streamlines follows the procedures outlined above where properties on the lower streamline resulted from the integration across the previous streamtube.

d. A new shock shape is defined, when the complete flow field has been computed, by intersections of the streamlines calculated through the conservation equation with their homologues in front of the shock. This case occurs when $y_j = r_j$, as shown in Figure 9.

e. The Hugoniot relationships are used to compute the pressure across the newly obtained shock wave and to compare it with the pressure on the streamline at the same ordinate. If satisfactory agreement is obtained, iterations to the shock shape and body pressure distribution are not required. Since the RAM B3 configuration is composed of a spherically blunted cone, adequate data were obtained from Reference 4 to predict the initial shock shape and body pressure distribution within the accuracy required to eliminate the necessity for iterations.

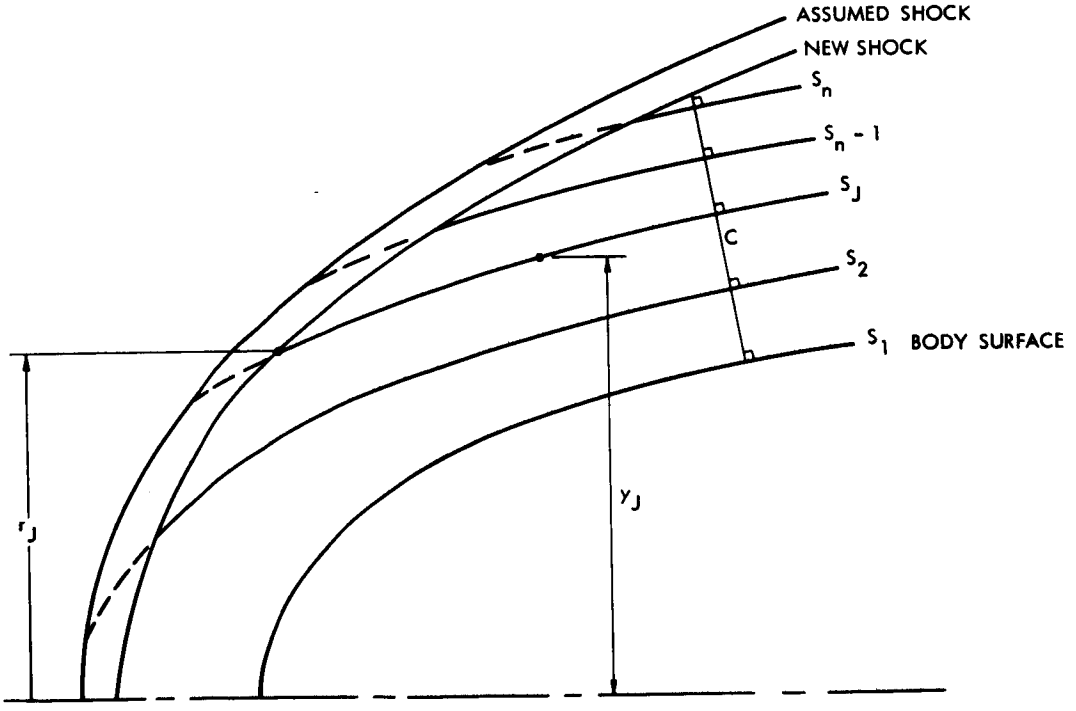

Figure 9. Shock Shape Calculation

A subsonic-transonic IBM 7090/7094 computer program is used to determine the transonic flow field properties and locate the shock relative to the RAM B3 body shape. The program uses the basic approach outlined in the last section, starting at the body and working outward from one streamline to the next along normals. A detailed description of the program is contained in Reference 2. A typical CRT output showing streamline and shock locations in the transonic flow field computed by the program is shown in Figure 10. A typical CRT output showing the computed starting line properties required as input to the method of characteristics program is presented in Figure 11.

SUPERSONIC INVISCID FLOW FIELD

The equilibrium, supersonic inviscid flow field computations were accomplished by means of a digital computer program utilizing the well-known method of characteristics. This method entails solving a system of first-order, hyperbolic partial differential flow equations using the simplifications made possible by recognition and use of characteristic equations. Once the characteristic equations are available, finite difference techniques can be applied; and the flow field problem is easily adapted to solution by means of high-speed computers. Such a program was used to determine the supersonic flow fields for the RAM B3 cases.

The basic theoretical development for the method of characteristics is found in most elementary texts on gasdynamics, such as Reference 5. After transforming the three basic flow conservation relationships (mass, momentum, and energy) from intrinsic coordinate form into ordinary differential equations along characteristic lines, the following equation is obtained:

$$dp \pm \frac{\rho q^2}{\sqrt{M^2-1}}\, d\theta + \frac{j\rho q^2 \sin\theta}{M^2-1}\,\frac{ds}{r} = 0 \qquad (8)$$

The positive sign applies to a left-running characteristic line and the negative sign to a right-running characteristic line. Since the characteristics are Mach lines, their directions with respect to the streamline are given by the Mach angle. In Equation (8), the symbol "j" is used to adapt the expression to either two-dimensional $(j = 0)$ or axisymmetric $(j = 1)$ flow. In addition to the characteristic relationships along Mach lines, there is another characteristic relationship defined along the streamline itself. This is the streamline energy relationship. Assuming the flow to be inviscid and adiabatic, this energy relationship implies a constant entropy along streamlines. These flow conditions also make available the relationship between the flow velocity and thermodynamic state of the gas given by

$$H_o = h + \tfrac{1}{2} q^2 = \text{CONSTANT} \qquad (9)$$

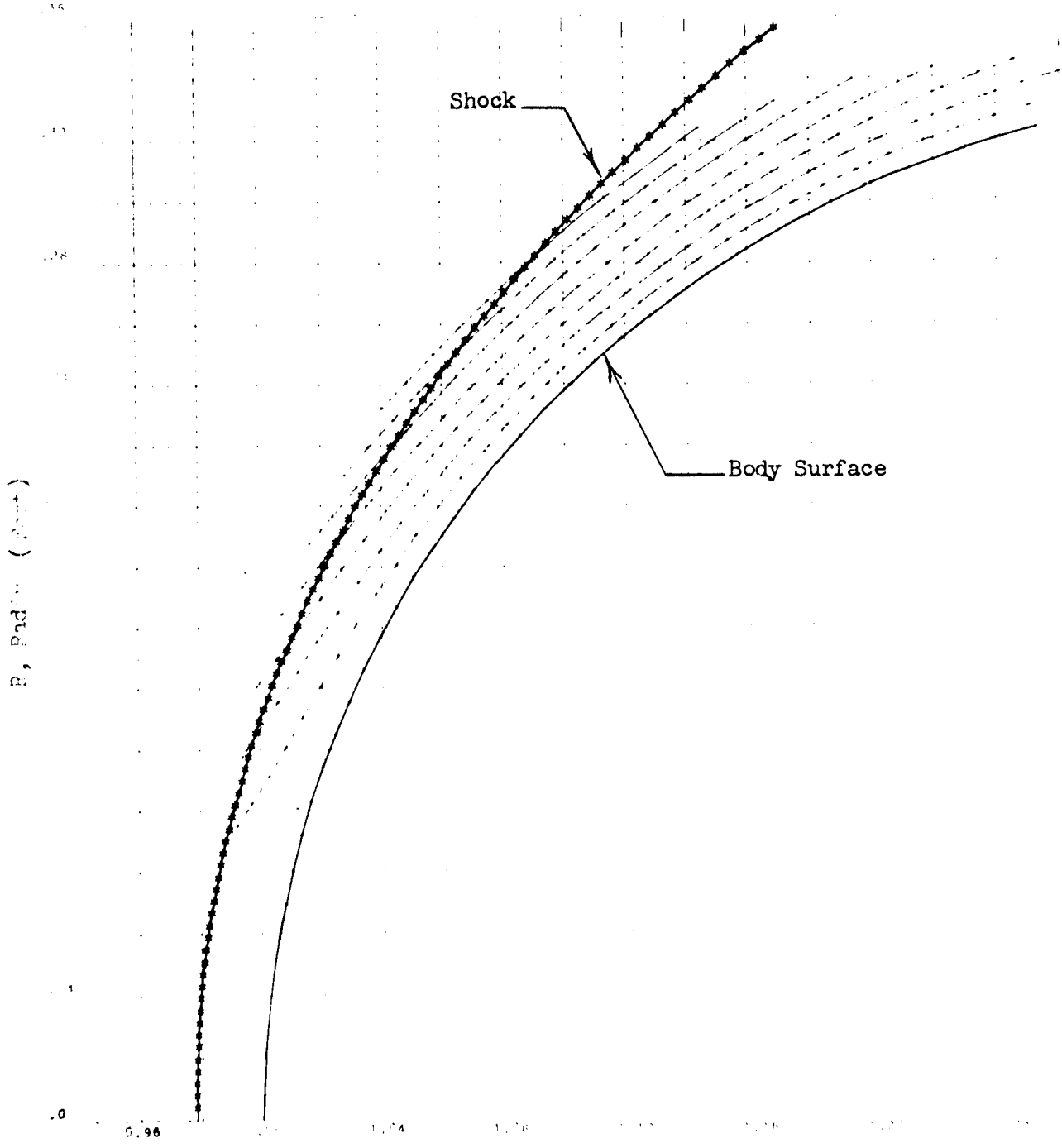

Figure 10. Typical CRT Output of the Transonic Flow Field (Case 5)

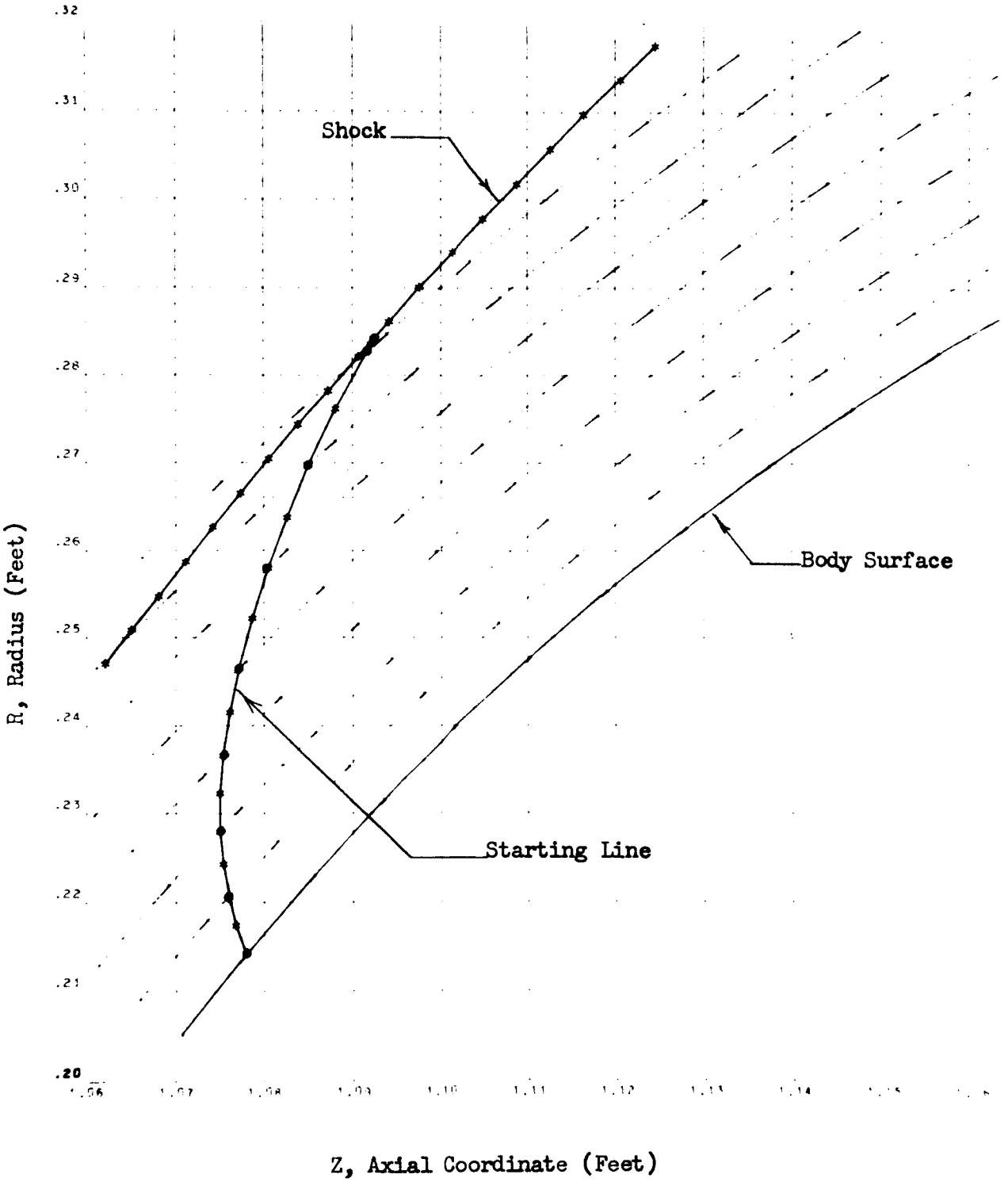

Figure 11. Enlarged View of the Transonic Flow Field Showing the Computed Starting Line (Case 5)

Specification of the thermodynamic state of the gas is required to obtain a characteristic solution, in addition to the flow property relationships discussed in the previous section. These thermodynamic properties are represented by equations taken from Reference 6, empirically fitted to the thermodynamic data, and are discussed in greater detail in the section on Thermodynamic Properties and Chemical Kinetics.

The characteristics computer program, described in Reference 7, is designed to solve the supersonic flow field over convex, two-dimensional or axisymmetric body shapes in a real gas, chemical equilibrium air media. Since the speed of sound is needed to compute Mach number, it is convenient to introduce the effective specific heat-ratio data into the program. These data, obtained from Reference 8, are entered in tabulated form as functions of temperature and pressure.

Starting line properties, as stated earlier, are obtained from a direct method transonic solution. Typical distributions of properties along the starting line are shown in Figure 12. The body shape downstream of the sonic point is altered to include a preliminary estimate of the boundary layer displacement thickness. This alteration to the basic body shape defines the body coordinates supplied as input to the characteristic program. The streamline pattern determined by the transonic solution is continued downstream by the characteristics program. In addition to supplying the streamline pattern, the characteristic program determines the shock shape and the flow properties throughout the flow field. These flow properties on the body are used to refine the preliminary boundary layer calculations, as will be described in the next section. The method-of-characteristics solution produces complete flow field details downstream of the starting line, both on a characteristic network and along streamlines. A typical example of the characteristic network and streamlines obtained from this program is shown in Figure 13.

REFINED BOUNDARY LAYER GROWTH

Following the computation of the supersonic inviscid flow field properties, a second computation of the boundary layer growth is made, using the edge properties from the method-of-characteristics calculations as input data to the boundary layer program. This computation provides the property distribution data through the boundary layer which are used later in merging the viscous and inviscid flow fields. Examples of the edge properties resulting from the method of characteristics and transonic solutions are shown in Figures 14 and 15. The boundary layer growth resulting from the calculations is shown in Figure 16. The boundary layer thicknesses resulting from the refined calculations were only slightly greater than those from the preliminary calculations, the difference being too small to warrant further iterations on either boundary layer or inviscid flow field calculations.

STREAMLINE DEFINITION

This section describes the methods used to define the streamlines required for the one-dimensional nonequilibrium chemistry analysis.

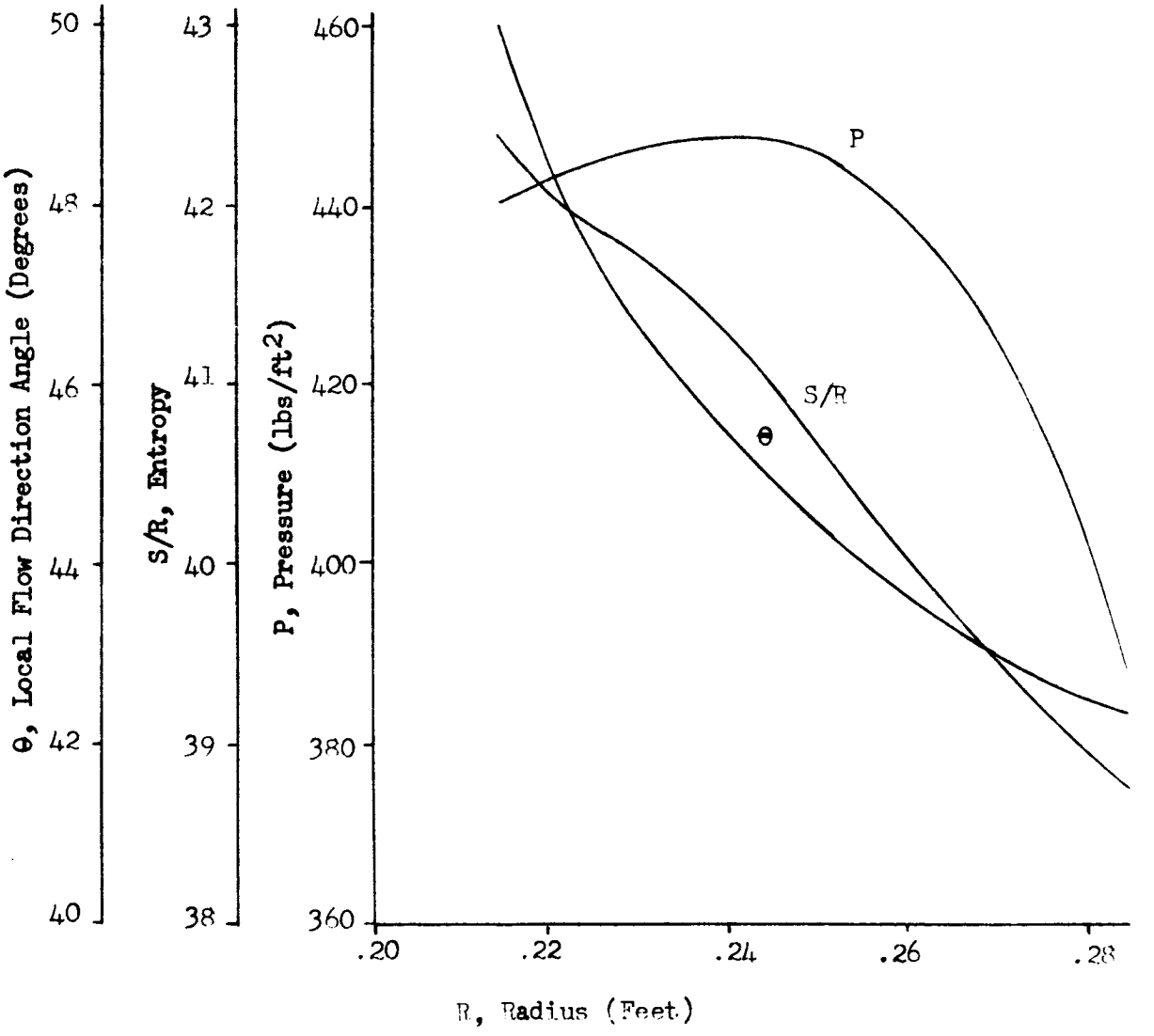

Figure 12. Distribution of Flow Field Properties Along the Starting Characteristic for Case 5

Note: Many computed characteristics and streamlines have been omitted for the sake of clarity.

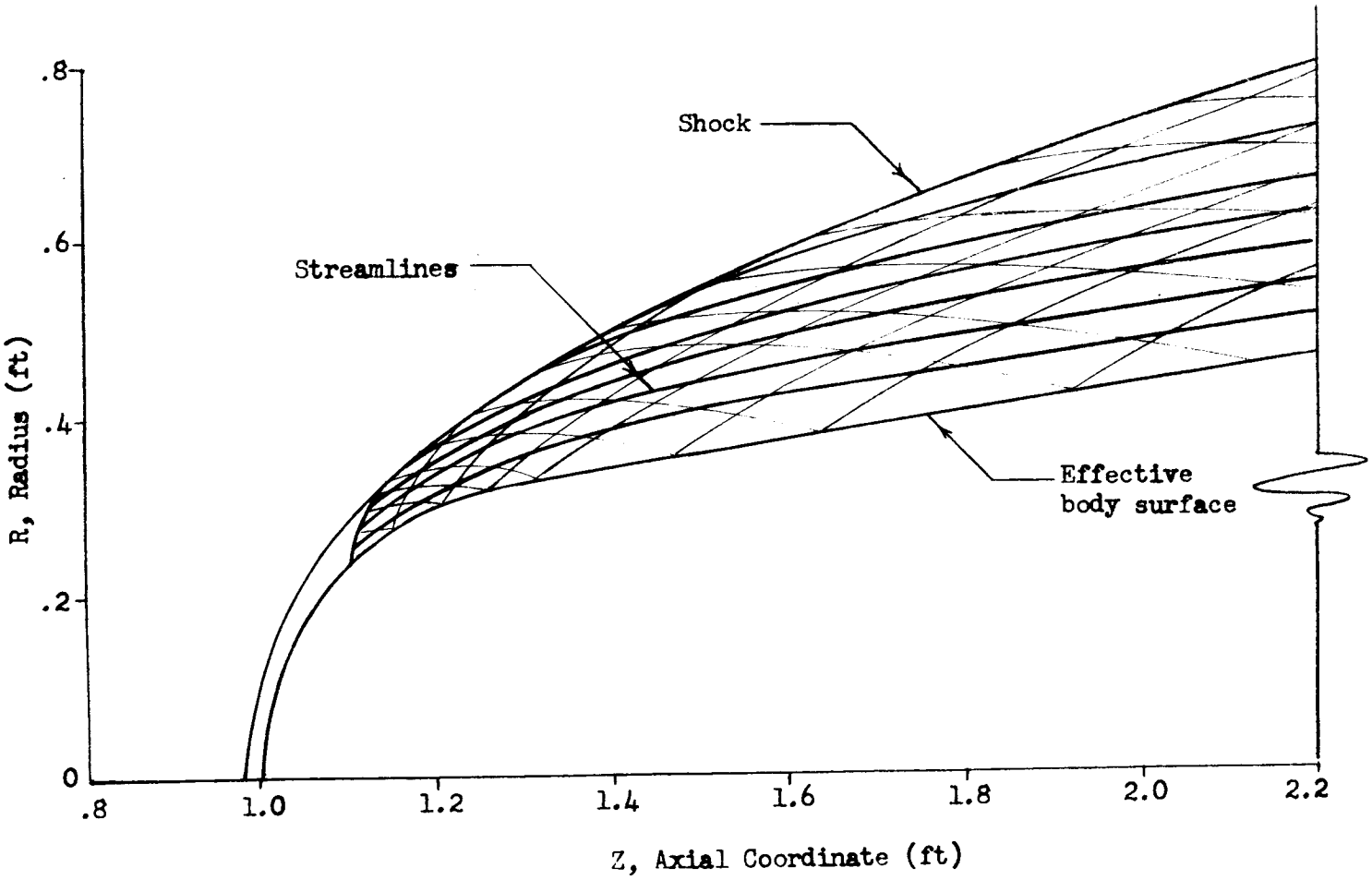

Figure 13. Typical Characteristics Network and Streamline Pattern (Case 10)

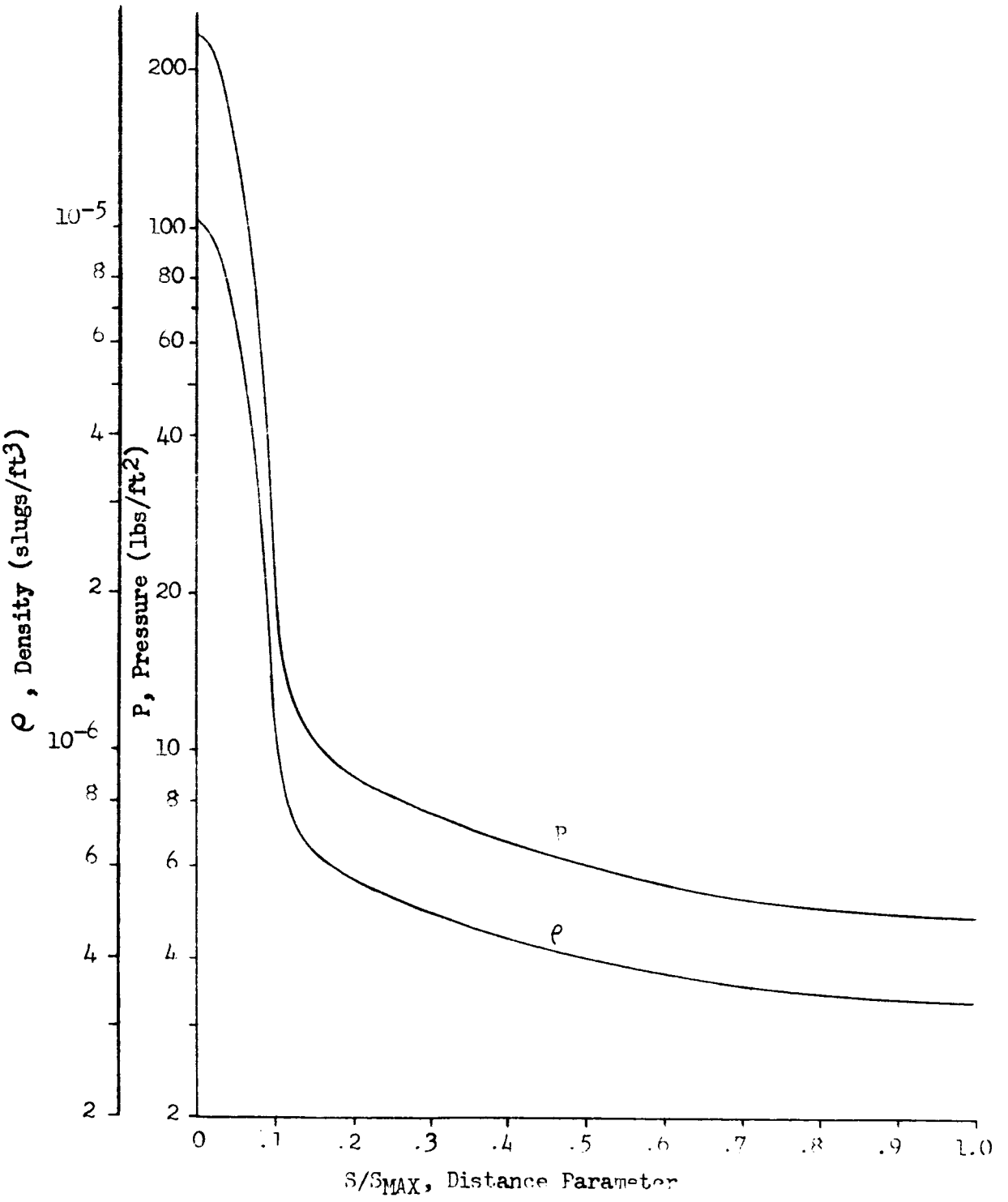

Figure 14. Final Equilibrium Boundary Layer Edge Properties for Case 9

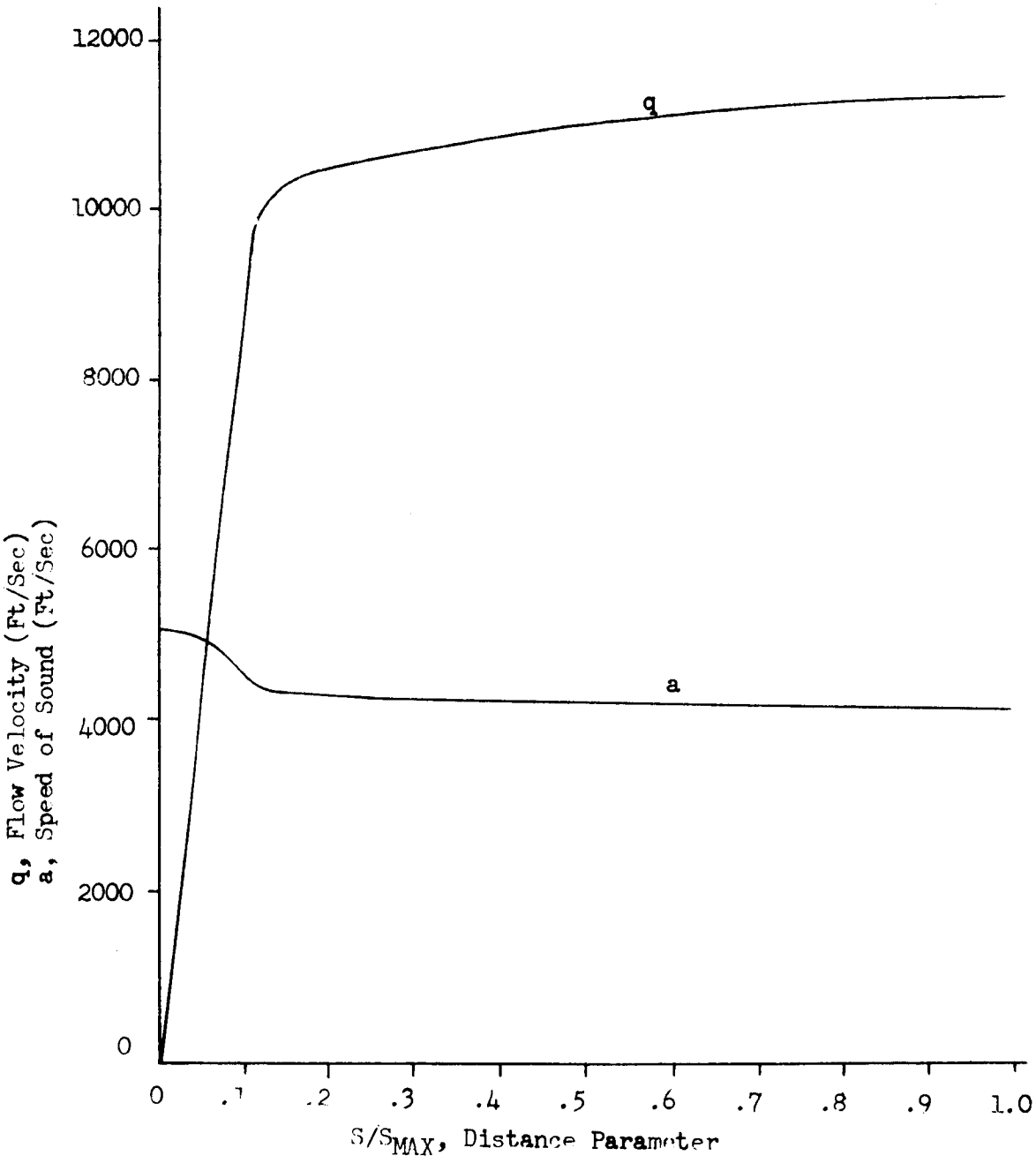

Figure 15. Final Equilibrium Boundary Layer Edge Properties for Case 9

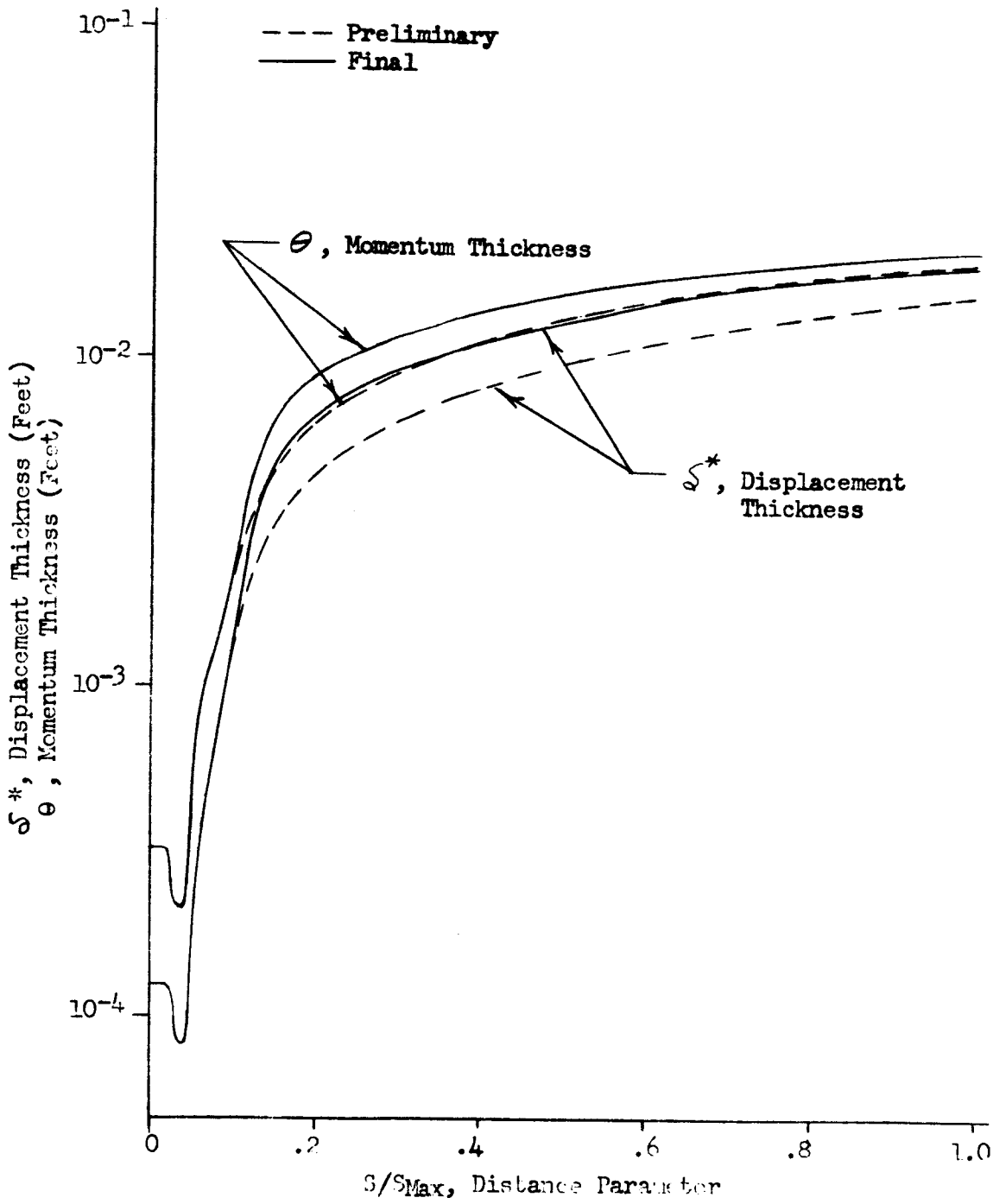

Figure 16. Boundary Layer Growth over the RAM B3 Surface for Case 9

In the inviscid flow field (i.e., outside the boundary layer height where $u/u_e = 0.99$), the streamlines resulting from the blunt body and characteristics solutions are available. The streamline pattern used to compute non-equilibrium effects was assumed to be adequately represented by the equilibrium flow streamline pattern. It is necessary only to relocate the streamlines that enter the boundary layer by satisfying mass flow conservation, and to find new intermediate boundary layer streamlines to provide closer spacing in regions of high property gradients.

The distribution of the product ρ_q is plotted versus r^2 for each normal location. The ρ_q product obtained from the final equilibrium boundary layer results is faired into the inviscid flow field values near the outer edge of the boundary layer. Mass flow passing through the annulus between a body point and a point on the normal erected at the body point (Figure 17) is found by solving the equation

$$\rho_1 q_1 = \frac{\pi}{\cos\theta} \int_{(r_1)^2}^{(r_2)^2} \rho q \, d(r^2) \qquad (10)$$

Since the boundary layer streamlines are close to the body, it is assumed that the local streamline inclination angle (θ) is equal to the local body surface inclination angle (θ_w) on the same normal.

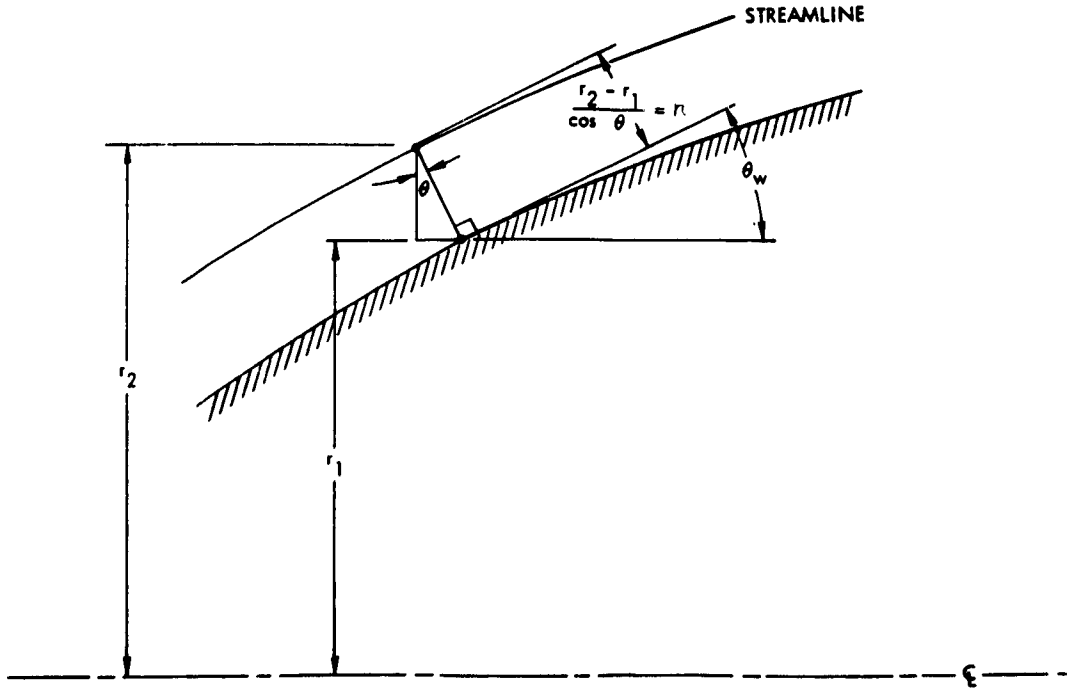

Figure 17. Streamline Location in Boundary Layer

The normal distance to each streamline is found by satisfying mass flow conservation between the surface and the streamline. The amount of mass flow contained within the annulus between the streamline and the body surface is determined by computing the mass flow entering the bow shock at the point where the streamline crosses the shock.

DETERMINATION OF MATCHING PARAMETERS

The use of pressure as an invariant matching parameter in inviscid analyses of nonequilibrium flow fields is an accepted approach (References 9 and 10). The streamline geometry and shock location are also assumed to be identical to the equilibrium flow field results. The matching parameter was changed on the stagnation streamline from pressure to velocity for reasons discussed in the following paragraph.

The transonic flow field calculation program provides no information on the flow field properties along the stagnation streamline because of the limitations of the calculation technique employed, which is based on the Gravalos method (Reference 11). Therefore, engineering estimates of the flow field properties were made after reviewing the behavior of typical stagnation streamline property distributions computed with an inverse method blunt body program (Reference 4). In the transonic and supersonic inviscid regions, the matching parameter used in the nonequilibrium chemistry analysis is pressure. On the stagnation streamline, however, pressure is nearly constant from the shock to the body surface; and when it is used as a matching parameter in the nonequilibrium chemical analysis, a small error in the pressure distribution near the stagnation point results in the computed velocity becoming zero at a point in the flow field ahead of the stagnation point, making it impossible to obtain a valid solution without extensive iterations on the pressure distribution. On the other hand, the data obtained using the program described in Reference 4 indicates that the velocity distribution along the stagnation streamline can be easily and accurately approximated with a linear distribution with negligible error in the computed pressure distribution. The linear velocity distribution is used in the present analysis to obtain a predicted velocity for use as a matching parameter. Figure 18 shows typical non-dimensionalized pressure and velocity distributions along the stagnation streamline of a sphere. Figure 19 shows a comparison of the results from using the pressure and velocity matched versions of the nonequilibrium program.

The pressure distribution obtained from the equilibrium flow computation is shown for typical streamlines in the flow field from Case 14 in Figure 20. Oblique shock calculations were performed for all cases, to find flow properties immediately behind the shock wave, assuming no change from the equilibrium solution in the shock wave angle. Thermodynamic properties required for these calculations were obtained from Reference 12, and assume equilibrium thermodynamics with fully excited translation, rotation, vibration, and electronic states. The chemical composition of the air was assumed constant at free-stream values (i.e., frozen chemical composition). Typical results of this calculation are shown in Figure 21. The pressure obtained from these plots

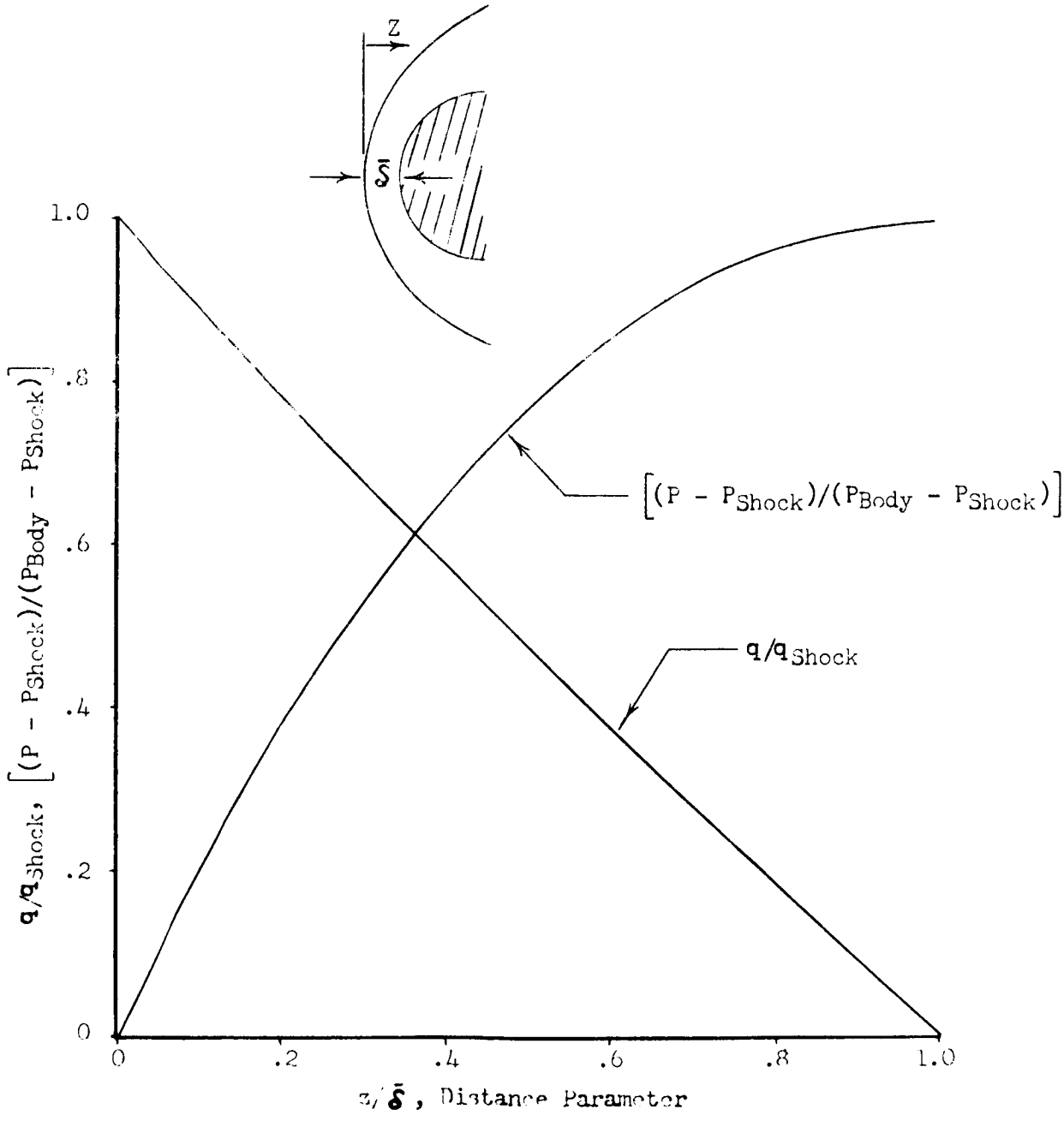

Figure 13. Typical Velocity and Pressure Distributions in the Stagnation Region of a Blunt Body

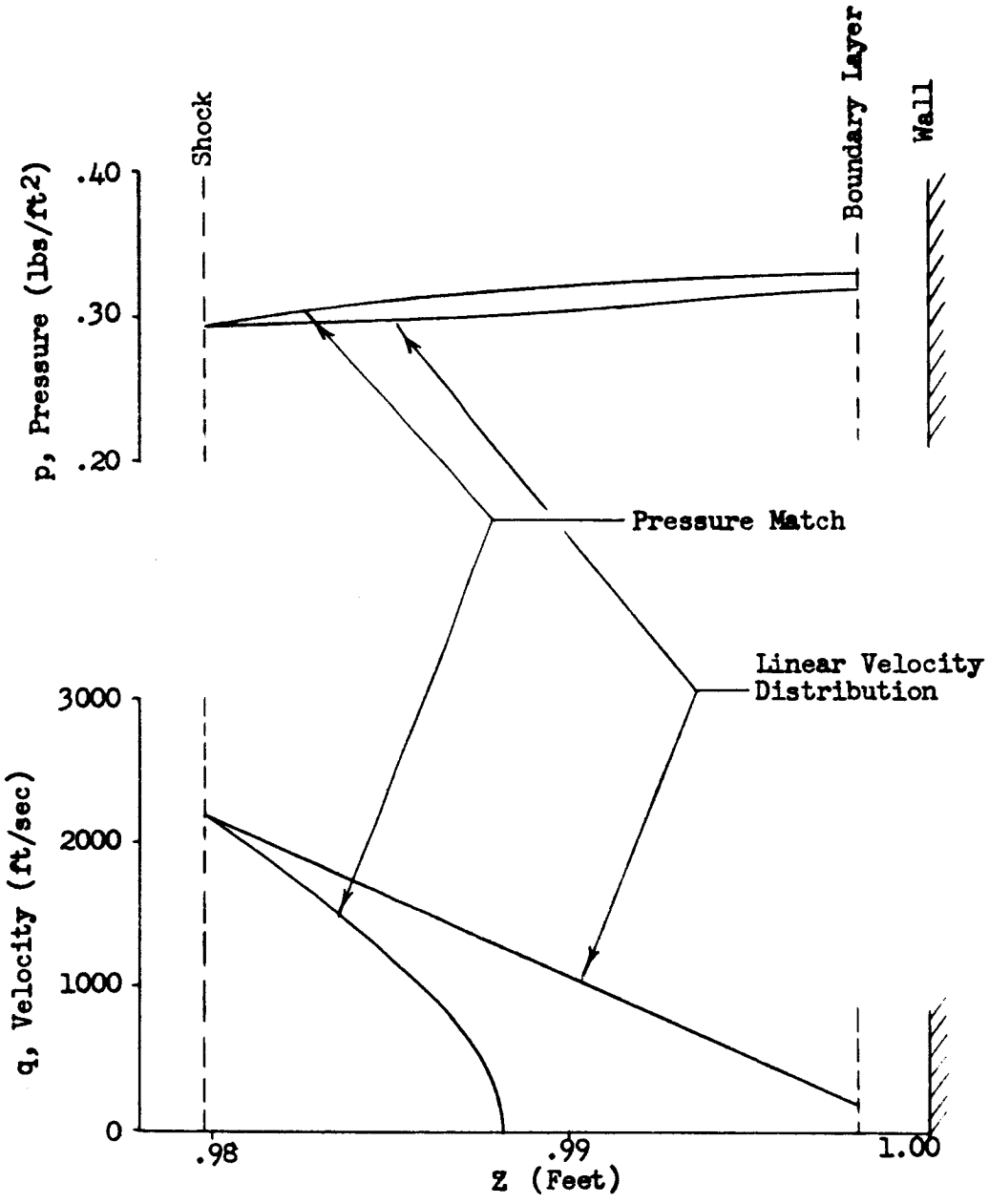

Figure 19. Comparison of Velocity and Pressure Matched Results for the Stagnation Streamline (Case 7)

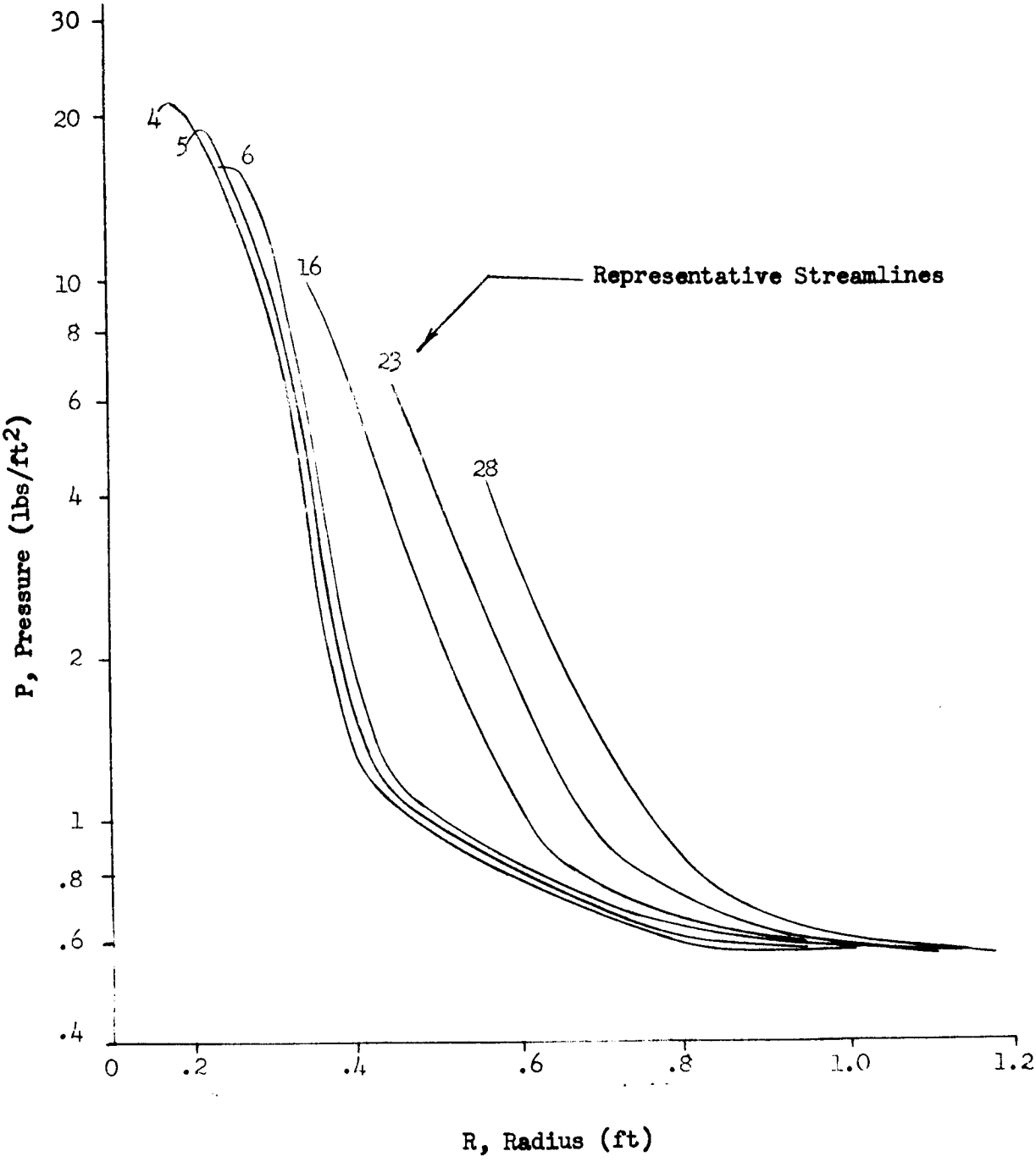

Figure 20. Pressure Matching Parameter for Case 14

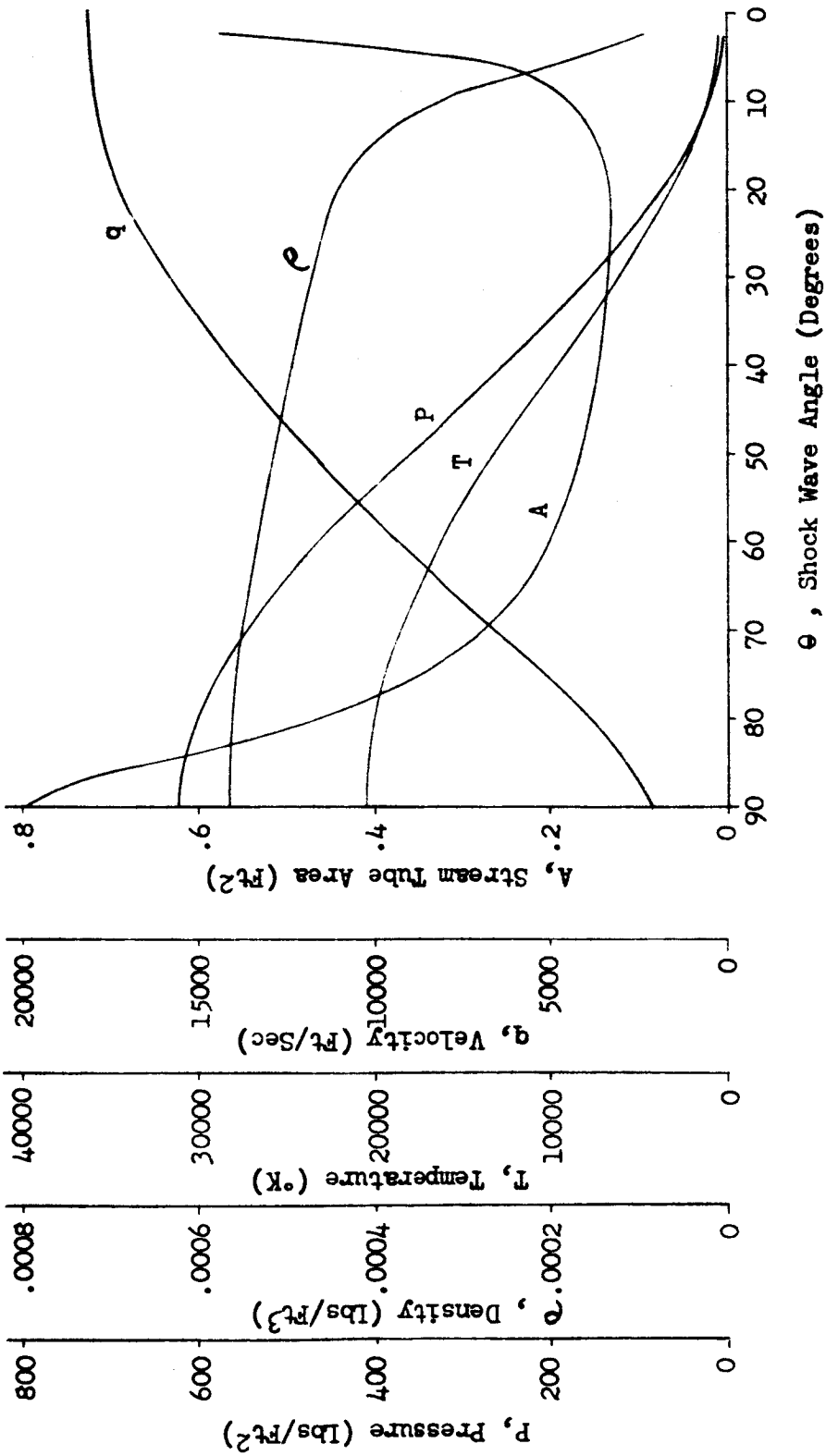

Figure 21. Thermodynamic Properties behind an Oblique Shock Wave for Frozen Free-Stream Chemistry (Case 7)

is used as an initial condition for the pressure behind the shock on the streamlines. A fairing to the equilibrium pressure distribution curve is selected to account for the chemical relaxation distance expected, although the percentage change in pressure is relatively small. Other values of initial conditions for the nonequilibrium streamtube analysis also are obtained from the results of these computations.

It is appropriate to discuss at this point how the values of the matching parameters in the boundary layer are found. Pressures are obtained directly from the inviscid flow field results. The one-dimensional energy and momentum equations used in the pressure-matching version of the nonequilibrium reacting gas computer program are valid only in inviscid flow, since viscous stresses and heat conduction invalidate such an approach in the boundary layer, and necessitate replacing the energy and momentum equations by known distributions of two additional matching parameters (velocity and streamtube area). The boundary layer nonequilibrium analysis thus is reduced to the calculation of chemical reactions along streamlines, while satisfying continuity and the equation of state. It is necessary to plot nonequilibrium property distribution along normals, using the inviscid nonequilibrium results, to find the two remaining matching parameters--velocity and streamtube area. The ρq product is necessary, since the matching parameter streamtube area is found from the definition

$$A \equiv \frac{1}{\rho q} \tag{11}$$

A typical plot of these property distributions is shown in Figure 22. The equilibrium boundary layer distribution of these properties is used as a guide in judiciously fairing the nonequilibrium q and ρq curves to the wall. The final faired curves are then used to define values of the matching parameters q and $1/\rho q$ on the previously located boundary layer streamlines. The final distributions of q and $1/\rho q$ along several streamlines for Case 14 are shown in Figures 23 and 24. A smooth variation or merger of properties at the outer edge of the boundary layer is achieved for the nonequilibrium results by the fairing procedure. This procedure is consistent with the equilibrium boundary layer analysis in regions of near equilibrium flow, and a reasonable boundary layer distribution is obtained in nonequilibrium or frozen regions.

NONEQUILIBRIUM ANALYSIS

The analysis of flow fields with nonequilibrium chemistry involves coupling chemical rate equations for the formation and destruction of chemical species with the fluid dynamic equations describing the flowing media. The media in this analysis is air, and the fluid dynamic equations are the conservation equations for one-dimensional flow. The coupling is achieved through modifications to the energy and state equations, causing them to reflect the contributive effects of each specie considered in the chemical model. The complexity of this coupling is largely a matter of the sophistication used in defining the chemical model. The details of this method

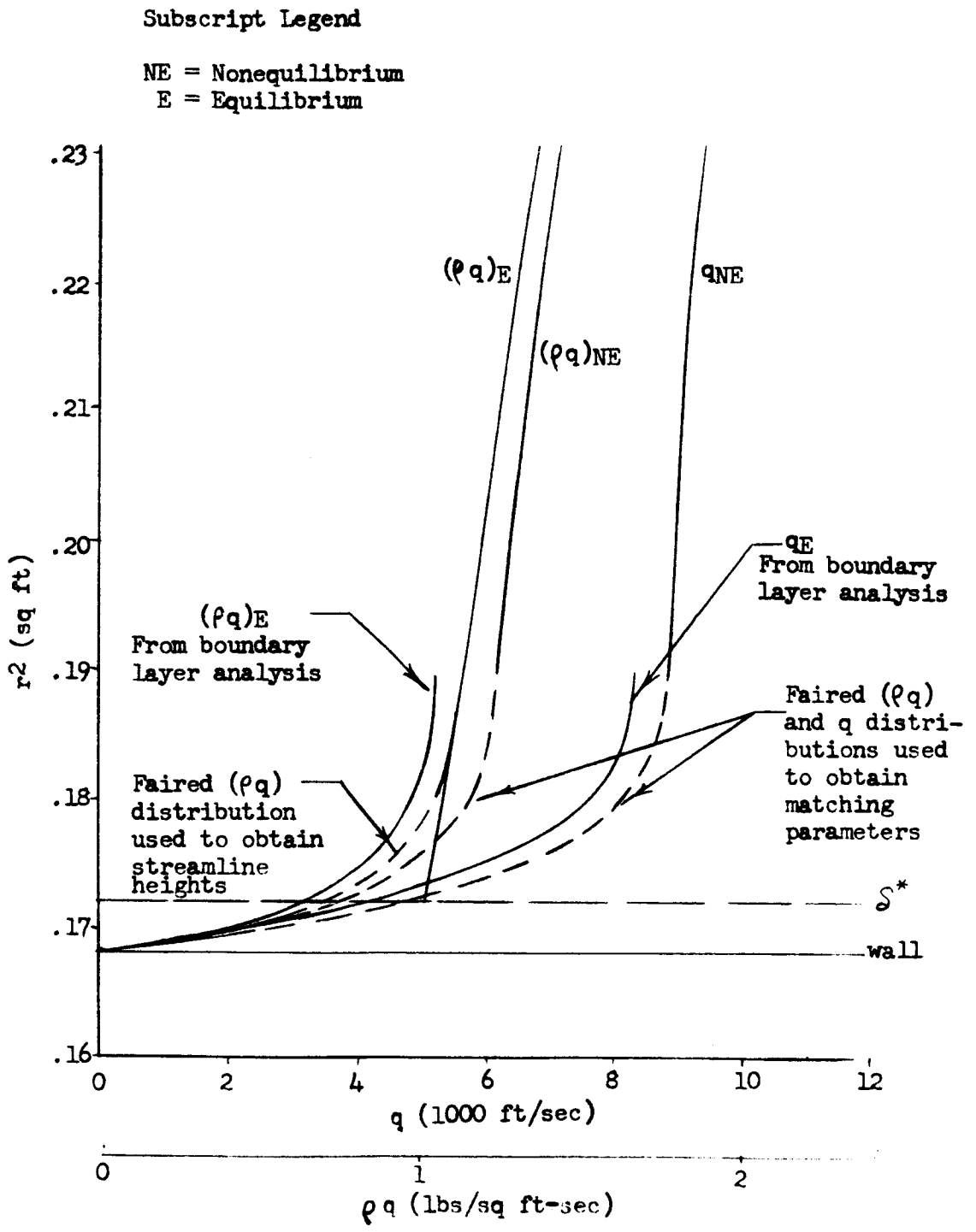

Figure 22. Example of Merged Viscous-Inviscid Regions (Case 3, Normal 5)

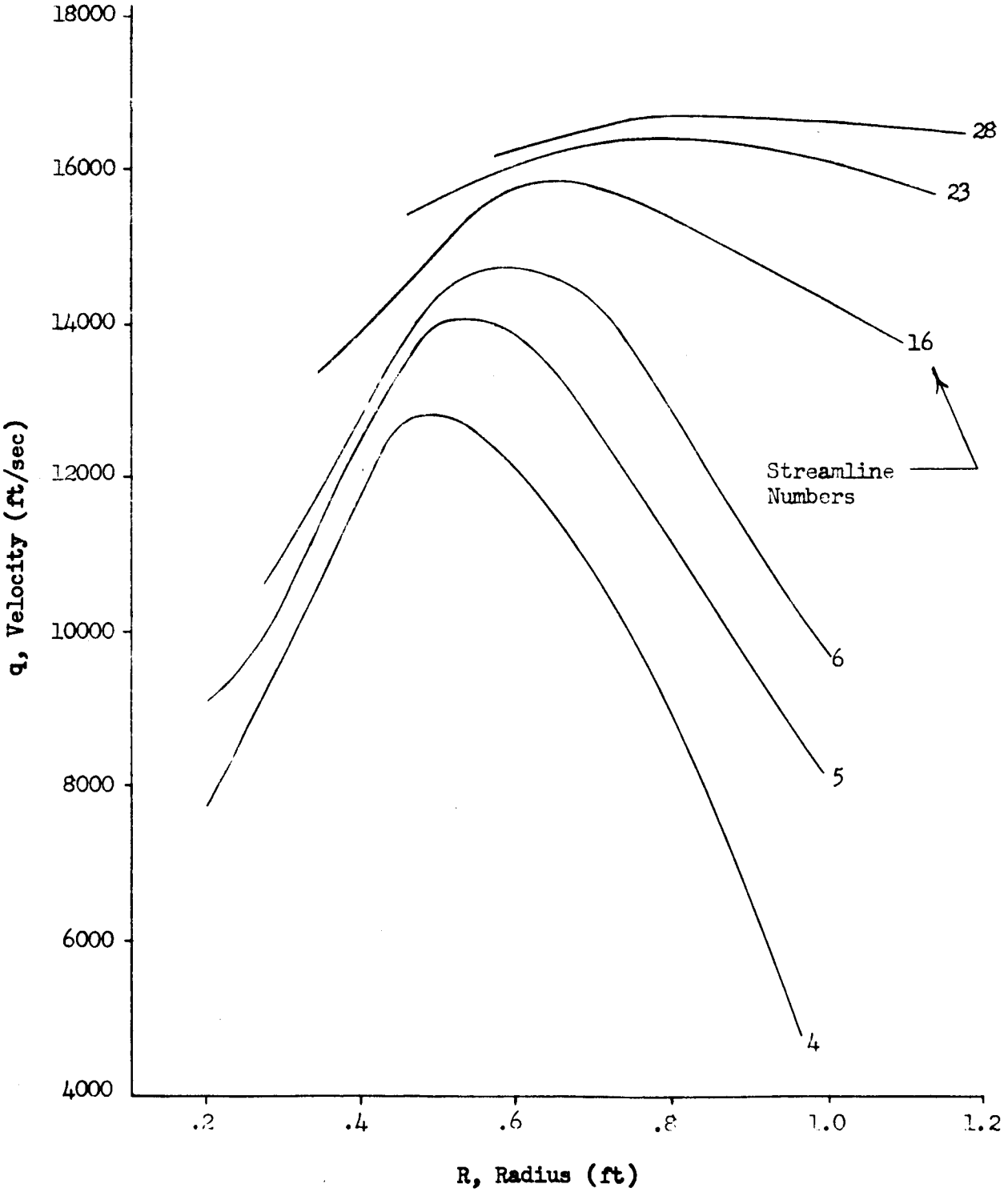

Figure 23. Velocity Matching Parameter for Case 14

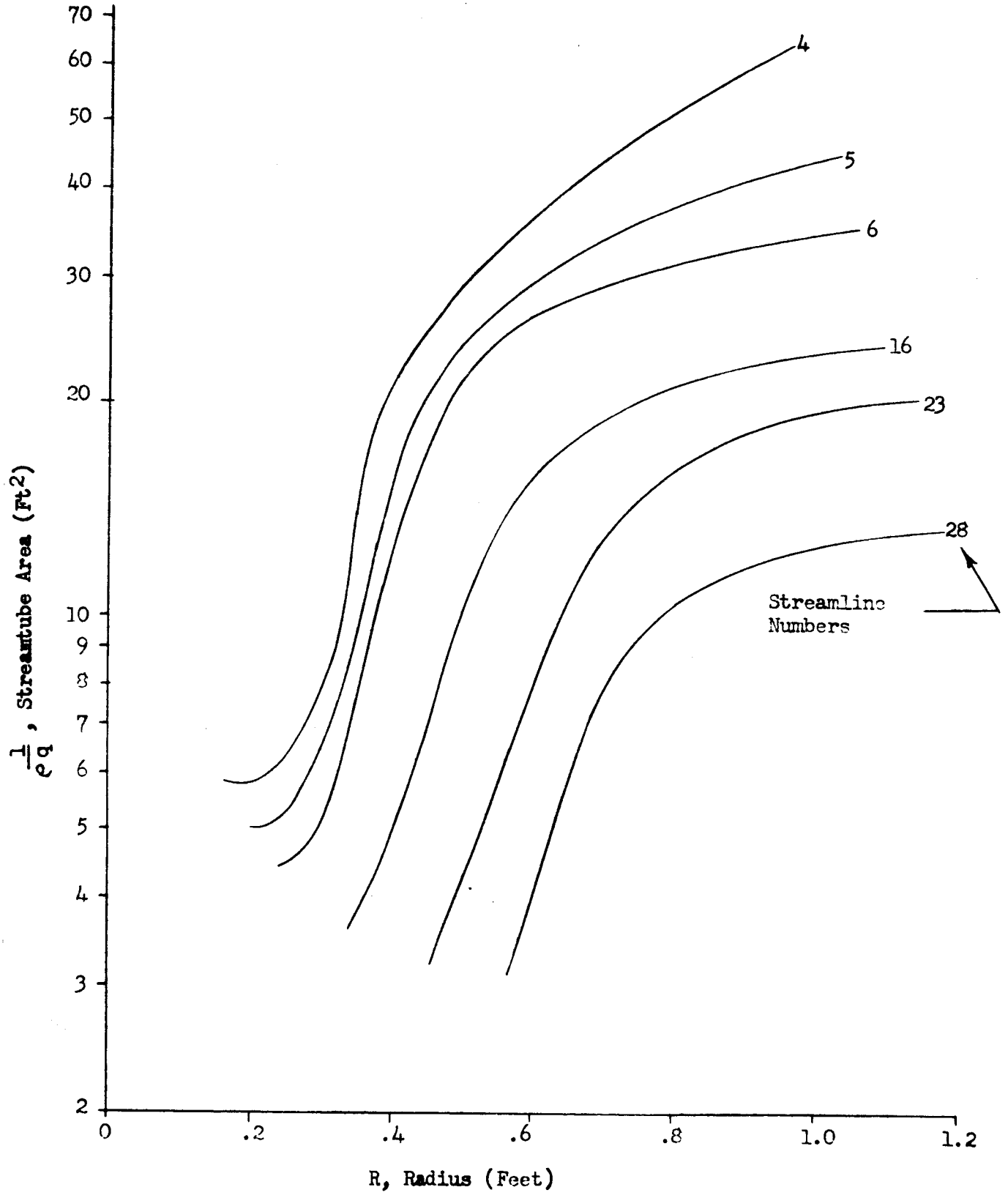

Figure 24. Area Matching Parameter for Case 14.

are described in the following paragraphs.

Basic Equations

Nonequilibrium flows may be described by a set of fluid flow equations: the one-dimensional flow equations for mass, momentum, and energy conservation; thermodynamic relationships in the form of the state equation and definition of enthalpy; and a set of chemical rate expressions. Basing the analysis on inviscid, one-dimensional flow along streamlines, the conservation equations assume the following form:

$$\frac{d\rho}{\rho} + \frac{dq}{q} + \frac{dA}{A} = 0 \tag{12}$$

$$\frac{dp}{ds} = -\frac{\rho q}{g}\frac{dq}{ds} \tag{13}$$

$$h + \frac{q^2}{2gJ} = H_0 \tag{14}$$

The thermodynamic equations, represented by the equation of state and the definition for enthalpy, must include the contributive effects of each chemical specie. Equations (15) and (16) illustrate this point.

$$p = \rho R T \sum_{i=1}^{N1} n_i \tag{15}$$

$$h = \sum_{i=1}^{N1} n_i w_i h_i \tag{16}$$

Finally, the chemical rate for the i'th specie is obtained from the following expression:

$$\frac{dn_i}{ds} = \frac{1}{\rho q}\sum_{k=1}^{N2}\left(\beta_{i,k} - \alpha_{i,k}\right)\left[K_{f_k}\prod_{j=1}^{N1}\left(\rho n_j\right)^{\alpha_{j,k}} - K_{b_k}\prod_{j=1}^{N1}\left(\rho n_j\right)^{\beta_{j,k}}\right] \tag{17}$$

The subscript j applies to the particular species participating in the k particular reactions. This equation is derived from basic kinetic theory (References 13 and 14) and summarizes the effective influence of a particular specie in the chemical reactions comprising the chemical model. The forward and reverse reaction rate constants, K_{f_k} and K_{b_k}, in the chemical analysis are related to one another through the chemical equilibrium constant by the following relationship:

$$K_{EQ_k} = \frac{K_{f_k}}{K_{b_k}} \tag{18}$$

These are the basic equations to be solved in a nonequilibrium flow analysis, and it is a simple matter to combine them into a form that will follow a prescribed streamline path. Equations for the change in temperature with distance using pressure and velocity as matching parameters are presented below:

Pressure Match

$$\frac{dT}{ds} = \frac{\frac{1}{J\rho}\frac{dp}{ds} - \sum_{i=1}^{N1} \omega_i h_i \frac{dn_i}{ds}}{\sum_{i=1}^{N1} C_{p_i} n_i} \tag{19a}$$

Velocity Match

$$\frac{dT}{ds} = \frac{-\left(\frac{q}{gJ}\frac{dq}{ds} + \sum_{i=1}^{N1} \omega_i h_i \frac{dn_i}{ds}\right)}{\sum_{i=1}^{N1} C_{p_i} n_i} \tag{19b}$$

The detailed derivations of these coupling equations are presented in Reference 15. The remaining nonequilibrium discussion will be confined to pressure match, since the inviscid portion of the nonequilibrium flow field for RAM B3 is based on that solution. In addition to the coupling equation (19a), chemical rate equations and the momentum equation must be solved for each integrated interval along the streamline path.

The first step in the nonequilibrium solution is the evaluation of the chemical rate for each specie. This depends only on known conditions at the beginning of the integration interval. These rates, along with the local slope of the matching parameter curve (dp/ds), are sufficient to evaluate

the coupling equation for dT/ds . The quantity dq/ds is obtained from the momentum equation and the argument dp/ds . These three differential equations, after evaluation, are integrated over an interval of streamline path to give temperature, velocity, and the chemical composition at some new downstream point. The value of pressure at this new point is determined from the matching parameter curve. Density and streamtube area are obtained from the equation of state and the mass conservation equation, respectively. This completes the calculation of a new downstream point, and the procedure is repeated for each of the subsequent downstream points.

A special version of the calculation procedure is used to study nonequilibrium chemistry effects in the boundary layer. This version simultaneously matches pressure, velocity, and streamtube area along streamlines. In using all three of these properties as matching parameters, it is no longer necessary to integrate the coupled flow equation and the momentum equation, but only the chemical rate equations. The procedure followed in the boundary layer version consists of evaluating the chemical rate equations at a known point and then integrating to find the chemistry at the new downstream point. The pressure, velocity, and streamtube area at the new point are obtained from tabulated values of the matching parameter distribution. Density at the new point is determined from the mass conservation equation and used in the state equation to determine temperature. The cycle is then repeated for each new integration interval.

Nonequilibrium Reacting Gas Program

The IBM 7090/7094 nonequilibrium computer program is described in detail in Reference 15. It requires a complete knowledge of all of the fluid and chemical properties at a starting point. This point generally is chosen immediately downstream of the shock, assuming no dissociation of the free-stream air but complete relaxation of the translational, rotational, vibrational, and electronic modes of excitation. Coordinates of the streamline path and a description of the matching parameter along this path must be specified as program input information, in addition to starting point properties. The differential equations are integrated with a fourth-order Runge-Kutta scheme modified for a Gill-type correction (Reference 16).

The program has a built-in provision for altering integration step size. Step size must be small in regions where the flow is near equilibrium, since there is a tendency for the integration of the chemical rate equations to become unstable. This is due to the extreme sensitivity of the rates to slight changes in the local chemical composition. Conversely, if the program is operating in a region of the flow field where the rates are insensitive to changes in chemical composition (as in the case of frozen chemistry flow), integration step size is increased to minimize program running time.

The results of this computer program compare very well with theoretical results obtained by Vincenti (References 17 and 18) for nozzle flow in a spark-heated facility.

Thermodynamic Properties and Chemical Kinetics

The thermodynamic properties, enthalpy and specific heat at constant pressure, are determined from statistical mechanics and results of experimental spectroscopy, and are entered into the program in tabulated form as a function of temperature. These properties are obtained from the high temperature air properties program described in Reference 12. The basic assumptions and method for solving the partition functions are discussed thoroughly in References 3 and 12.

The chemical model used in the nonequilibrium reacting gas computer program (Reference 16) is depicted in Table 2 and consists of eleven reactions involving the following twelve chemical species:

$$N_2,\ N,\ O_2,\ O,\ NO,\ NO^+,\ e^-,\ N_2^+,\ O_2^+,\ N^+,\ O^+,\ \text{and}\ A$$

In the computer program, the nitrogen dissociation reaction is listed as two separate reactions; since two forms of the rate constant expression are needed, depending on the third body participating in the reaction. Catalytic efficiencies are presented in Table 2 for Reactions 1 through 3. The specie argon (A) is used as a reference point for assigning values of catalytic efficiency to each of the species in the chemical model. For example, in Reaction 1 of Table 2, the species A, N, N^+, NO, and NO^+ all possess catalytic efficiencies of one; whereas the species N_2 and N_2^+ have catalytic efficiencies of two, etc. Reactions 1 through 3 actually represent a series of reactions, since the symbol M can represent any of the catalytic species listed in the table exclusive of electrons. The catalytic efficiencies allow this series of reactions to be grouped into a single reaction, since they differ only in the sense that the rate constants are simple multiples of one another. The basic reaction rate data used in the program are obtained from References 19 and 20.

Equilibrium constants for the reactions listed in Table 2 are obtained from the difference in the free energies of products and reactants. The theoretical considerations for determining equilibrium constants over the desired temperature range are presented in Reference 3. Data for the equilibrium constants employed in the nonequilibrium program also are determined from the air properties program (Reference 12) and are entered into the nonequilibrium program as tabulated data. It is difficult to obtain closely spaced data for temperatures below 9000°R and still employ a linear interpolation on temperature to determine intermediate values. This problem is solved by using analytic expressions for the equilibrium constants below 9000°R. These relationships are presented in Table 3.

It is necessary to use the equilibrium constant to determine the opposing rate constant, since Table 2 only presents either the forward or reverse rate constants. The opposing rate constant is obtained from the equilibrium relationship presented in Equation (18).

Table 2. Chemical Reactions and Rate Constants

No.	Reaction	Catalyst, M	Rate Constant Expression
1	$O_2 + M + 5.1\ ev \rightleftharpoons O + O + M$ $(D_K = 211,644)$	A, N, N^+, NO, NO^+ N_2, N_2^+ O_2, O_2^+ O, O^+	$K_{f_1} = 2.98 \times 10^9\ T^{1/2}\ (JD_K/RT)^{3/2}\ EXP(-JD_K/RT)$ $K_{f_1} = 2\ K_{f_{1(A)}}$ $K_{f_1} = 9\ K_{f_{1(A)}}$ $K_{f_1} = 25\ K_{f_{1(A)}}$
2a	$N_2 + M + 9.8\ ev \rightleftharpoons N + N + M$ $(D_K = 406,690)$	A, O, O^+, O_2, O_2^+, NO, NO^+ N_2, N_2^+	$K_{f_{2a}} = 2.207 \times 10^{10}\ T^{1/2} (JD_K/RT)\ EXP(-JD_K/RT)$ $K_{f_{2a}} = 3.47\ K_{f_{2a(A)}}$
2b	$N_2 + M + 9.8\ ev \rightleftharpoons N + N + M$ $(D_K = 406,690)$	N, N^+	$K_{f_{2b}} = 3.82 \times 10^{10}\ T^{1/2}\ (JD_K/RT)^2\ EXP(-JD_K/RT)$
3	$NO + M + 6.5\ ev \rightleftharpoons N + O + M$ $(D_K = 269,744)$	A, O_2, O_2^+, N_2, N_2^+ NO, NO^+, O, O^+, N, N^+	$K_{f_3} = 8.35 \times 10^8\ T^{1/2}\ (JD_K/RT)^2\ EXP(-JD_K/RT)$ $K_{f_3} = 20\ K_{f_{3(A)}}$
4	$N_2 + O + 3.3\ ev \rightleftharpoons NO + N$		$K_{f_4} = 1.120 \times 10^{12}\ EXP\ (-J \times 1.359 \times 10^5/RT)$
5	$NO + O + 1.4\ ev \rightleftharpoons O_2 + N$		$K_{f_5} = 2.842 \times 10^7\ T\ EXP\ (-J \times 7.038 \times 10^4/RT)$
6	$N_2 + O_2\ 1.9\ ev \rightleftharpoons NO + NO$		$K_{f_6} = 6.32 \times 10^{23}\ T^{-5/2}\ EXP\ (-J \times 2.31 \times 10^5/RT)$
7	$N + O \pm 2.8\ ev \rightleftharpoons NO^+ + e^-$		$K_{f_7} = 7.63 \times 10^7\ T^{1/2}\ EXP\ (-J \times 1.139 \times 10^5/RT)$
8	$N + N + 5.8\ ev \rightleftharpoons N_2^+ + e^-$		$K_{b_8} = 3.72 \times 10^{20}\ T^{-3/2}$
9	$O + O + 6.9\ ev \rightleftharpoons O_2^+ + e^-$		$K_{b_9} = 7.45 \times 10^{19}\ T^{-3/2}$
10	$O_2^+ + O + 1.6\ ev \rightleftharpoons O_2 + O^+$		$K_{b_{10}} = 9.349 \times 10^9\ T^{1/2}$
11	$N_2 + N^+ + 1.0\ ev \rightleftharpoons N + N_2^+$		$K_{b_{11}} = 9.349 \times 10^9\ T^{1/2}$

1. All units are in the English system. The units of D_K are BTU/LbMole and the units of K_f and K_b are Ft^3/LbMole-Sec.
2. The forward and backward rate constant expressions were taken from References 19 and 20
3. The 'A' in parentheses refers to Argon.

Table 3. Analytic Expressions for Equilibrium Constants
$K_p(j)$ vs Temperature

Reaction Number	$K_p(j)$	E_o^o Heat of Reaction at O^oK	
		Calories Per Mole	Electron Volts
1	$9.16 \times 10^{6} \exp \left[-\Delta E_o^o/RT\right]$	117,580.5	5.1
2	$1.72 \times 10^{2}\, T^{5/4} \exp \left[-\Delta E_o^o/RT\right]$	225,939	9.8
3	$1.28 \times 10^{2}\, T^{1.1} \exp \left[-\Delta E_o^o/RT\right]$	149,857.5	6.5
4	$5.42 \exp \left[-\Delta E_o^o/RT\right]$	76,081.5	3.3
5	$8.2 \times 10^{-2}\, T^{0.124} \exp \left[-\Delta E_o^o/RT\right]$	32,274.2	1.4
6	$1.71 \times 10^{1} \exp \left[-\Delta E_o^o/RT\right]$	43,800.7	1.9
7	$4.20 \times 10^{-11}\, T^{7/4} \exp \left[-\Delta E_o^o/RT\right]$	64,554	2.8
8	$3.00 \times 10^{-10}\, T^{5/3} \exp \left[-\Delta E_o^o/RT\right]$	133,719	5.8
9	$2.56 \times 10^{-12}\, T^{2.1} \exp \left[-\Delta E_o^o/RT\right]$	159,079.5	6.9
10	$1.12 \times 10^{-1}\, T^{0.177} \exp \left[-\Delta E_o^o/RT\right]$	36,888	1.6
11	$8.09 \times 10^{-4}\, T^{0.863} \exp \left[-\Delta E_o^o/RT\right]$	23,053	1

$R = 1.9872$ Calories deg^{-1} $mole^{-1}$

Application to RAM B3

The streamlines located entirely within the inviscid flow field are obtained in a single run of the nonequilibrium program; whereas, those entering the boundary layer are obtained in two steps. The inviscid portion of the streamline is determined by the pressure-matching version up to the point where the streamline enters the boundary layer; at this point, new initial conditions are defined; and the remainder of the flow field is evaluated with the boundary layer version of the program.

RESULTS

The final nonequilibrium results are displayed in two plots for each normal location for each case. The first plot shows the variation of electron density, temperature, pressure, and streamline locations as a function of distance outward along the normal from the body surface. The second type of plot shows the variation of chemical species concentration along normals.

The variations of electron density, pressure, temperature, and chemical species concentration have been faired between computed points to provide smooth property variations. Streamline locations are indicated by short lines at the top of the first plot for each normal. The neutral species are plotted as mole fraction (X_i) versus normal distance, and the ions are plotted as the log of the mole fraction versus normal distance, since they are present in very small quantities. In the data plots, all ion concentrations greater than 10^{-6} mole fraction are considered to be of significance. This value generally occurs near the same point where the electron density decreases to 10^6 particles/cc and was selected as a reasonable minimum value for data presentation.

For all cases, computations were made along at least eight streamlines through the flow field; however, fewer streamlines appear on the forward body normals since some streamlines cross the shock downstream of the intersection of the normal and the shock. Data are presented along nine normals originating at the body locations shown in Figure 2 (repeated here for convenience).

The shock layer thickness is clearly indicated on each normal plot by a dashed line. The data curves originate at the body and continue completely through the viscous and inviscid regions of the shock layer, terminating at the shock. For all cases, it is assumed that the wall is at a temperature of 700°K and that the local wall flow velocity is zero, consistent with the assumptions of classical boundary layer theory. Under these conditions, the wall is always at a condition of chemical equilibrium, no dissociation or ionization is present, and the chemical composition corresponds to that of undissociated equilibrium air at the local pressure and temperature. At the shock, the air is initially undissociated and at a temperature corresponding to that of a mixture of gases of the same composition as free stream. The enthalpy and density levels at the shock are compatible with an iterative solution of the real gas shock equations. These conditions at the wall and shock were used to establish the end points of the data plots. Between the body and shock, the local properties are dependent on the fluid dynamic conditions and the time history of the chemical reactions which occur along each streamline.

The data plots are presented by case number and normal number. The complete data for each case (nine consecutive normals) are presented in ascending sequence, beginning with Normal 1 of Case 1 and terminating with

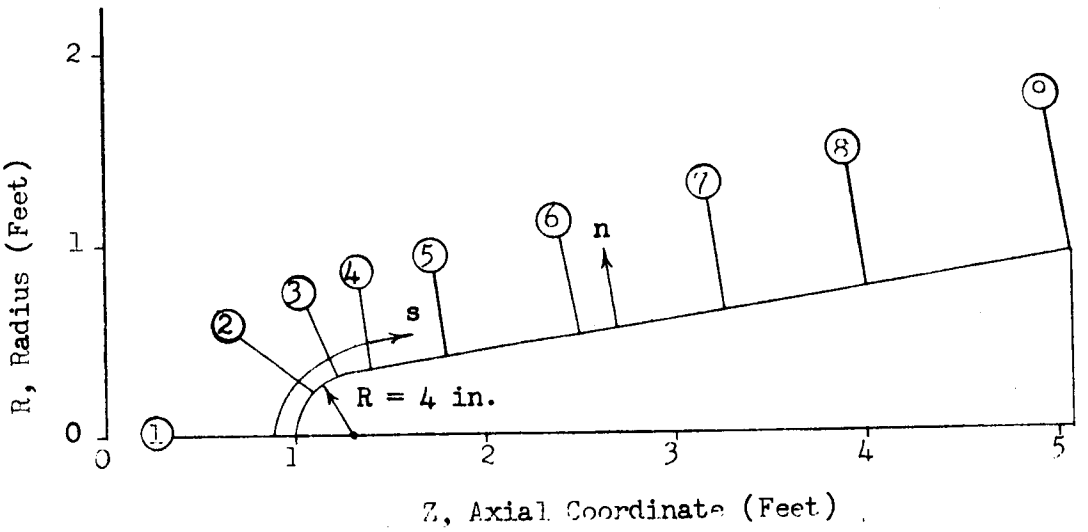

Normal Number	Dimensionless Axial Coordinate from Stagnation Point $\bar{X}/D$	Axial Coordinate Z, ft
1	0.0	1.000
2	.14750	1.098
3	.32600	1.217
4	.60000	1.400
5	1.20000	1.800
6	2.25000	2.500
7	3.40000	3.267
8	4.50000	4.000
9	6.10000	5.064

Note: The axial coordinate from the stagnation point, $\bar{X}$, is equal to (Z-1).

Figure 2. Geometry and Coordinate System for RAM B3 Vehicle

Normal 9 of Case 14. These data are presented in Figures 25a through 38i. A complete list of the flight conditions for each case is presented in Table 1.

The data show several interesting features. Case 1, which is at the lowest velocity and altitude of the flight conditions analyzed, shows very little dissociation or ionization. As velocity is increased along the trajectory from Case 1 to Case 7, reaction rates increase greatly due to their exponential dependence on temperature, which increases rapidly as velocity is increased along the lower portion of the trajectory. Reaction rates are also affected by pressure; however, the pressure does not change greatly from Case 1 to Case 7 because the altitude increases as velocity increases, resulting in the Case 7 pressures being only slightly lower than those of Case 1. On the other hand, the temperature increases by roughly a factor of two along the same portion of the trajectory. For Cases 1 through 7, the viscous layer is relatively thin; and high gradients in thermodynamic and chemical properties are present near the surface. For Cases 8 through 14, however, velocity is nearly constant; and altitude is greatly increased, resulting in a much thicker viscous region, and consequently, lower property gradients near the surface.

The finite reaction rates result in local electron concentrations which can be either greater or less than the corresponding local equilibrium values, depending on the chemical history of the streamtube. This is noticeable in the present study, due to the wide variation in reaction rates created by the analysis of several flight conditions along a trajectory which encompasses a wide range of altitudes and velocities. A comparison was made of the computed nonequilibrium peak electron densities with the inviscid stagnation point peak electron densities obtained from Reference 21. This comparison is presented in Figure 39. The peak electron density for Normal 1, which is the stagnation streamline, agrees well with the equilibrium value except at the two extreme ends of the trajectory. At the low velocity and high altitude ends of the trajectory, the dissociation and ionization reactions proceed so slowly that insufficient time is available for the electron concentration to build up to the equilibrium value before the boundary layer is reached.

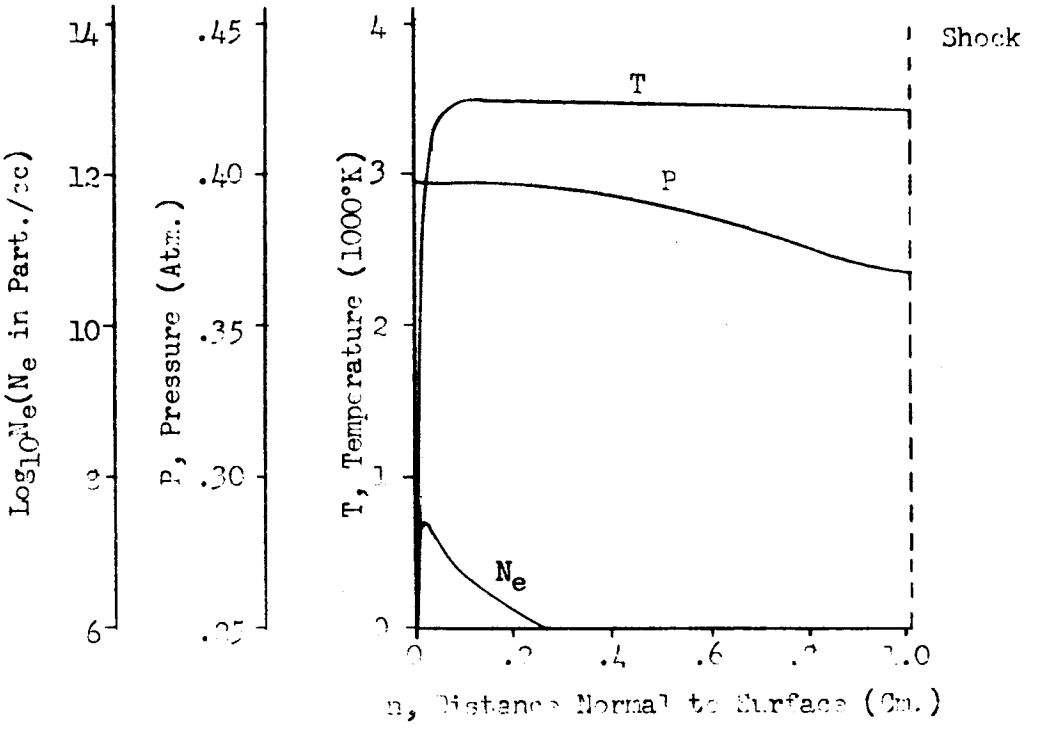

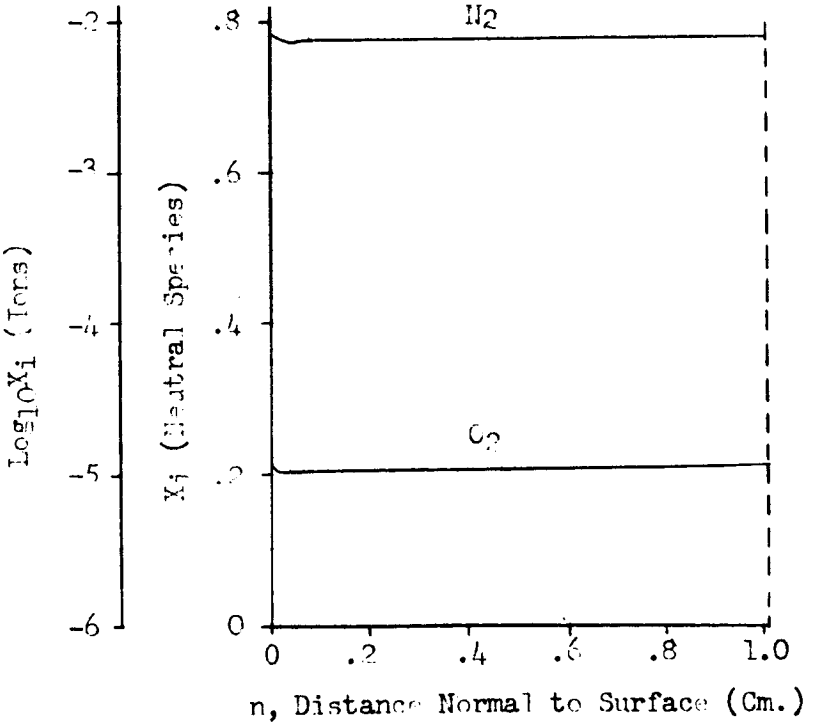

Figure 25a. Flow Field Properties - Case 1, Normal 1

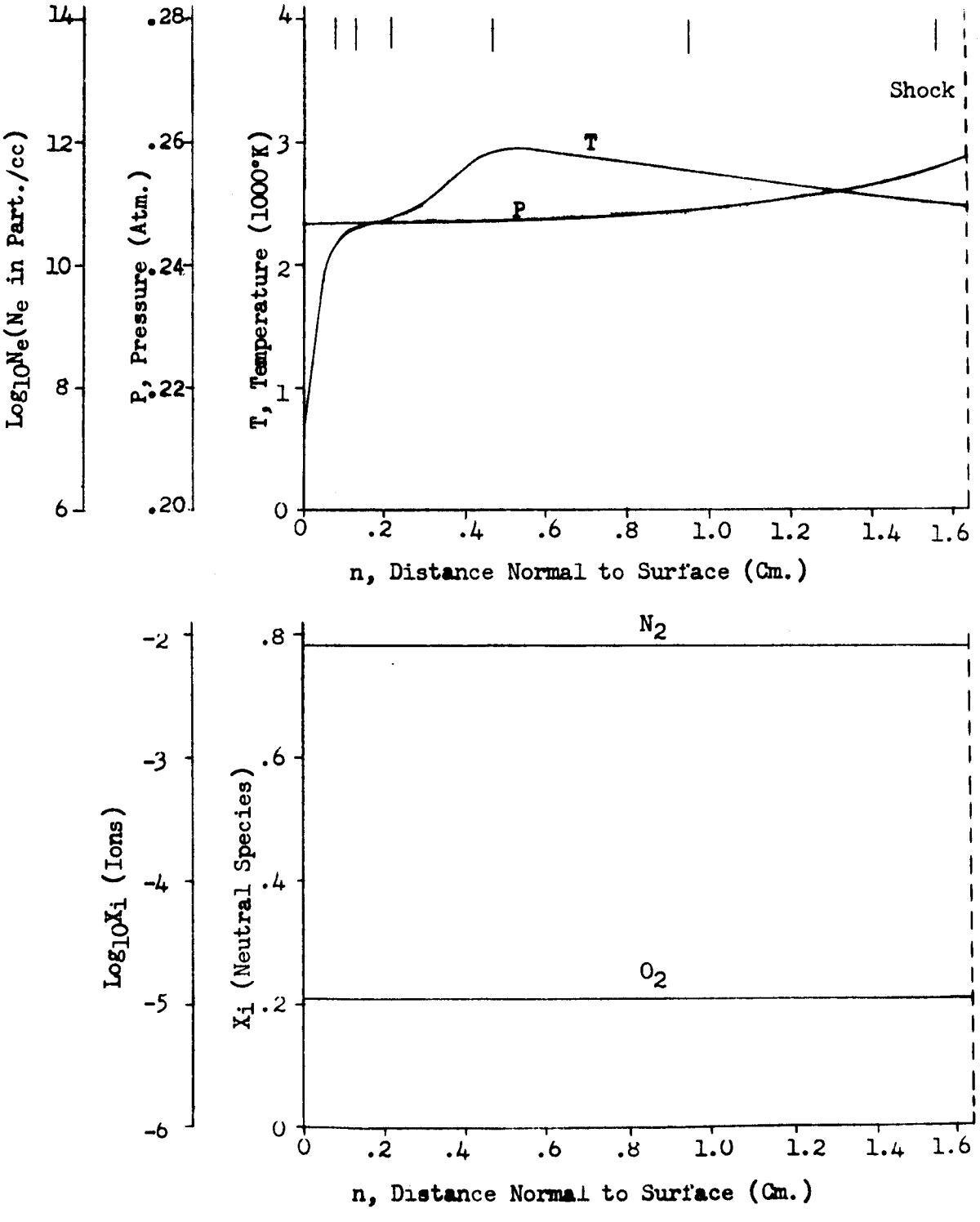

Figure 25b. Flow Field Properties - Case 1, Normal 2

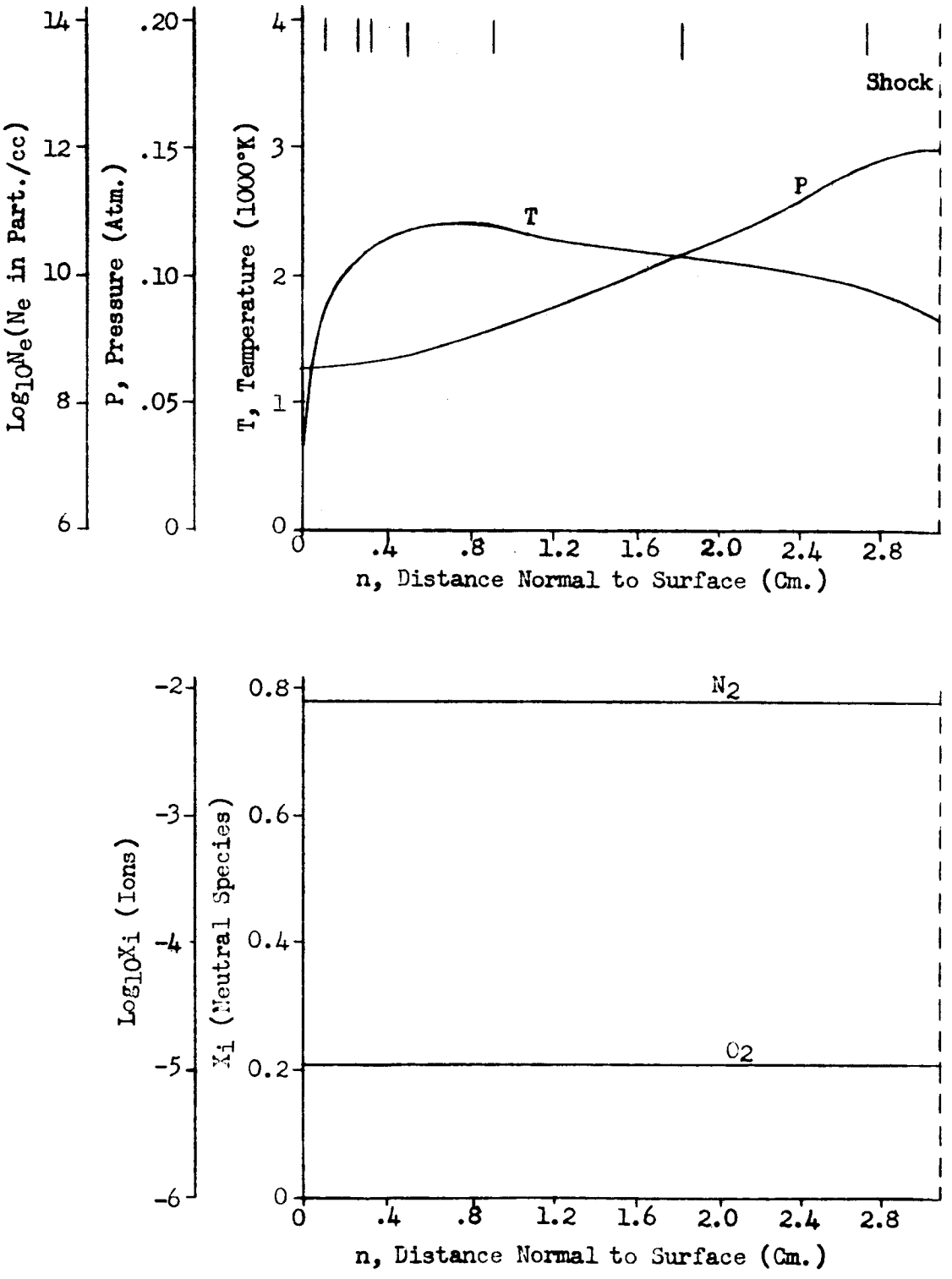

Figure 25c. Flow Field Properties - Case 1, Normal 3

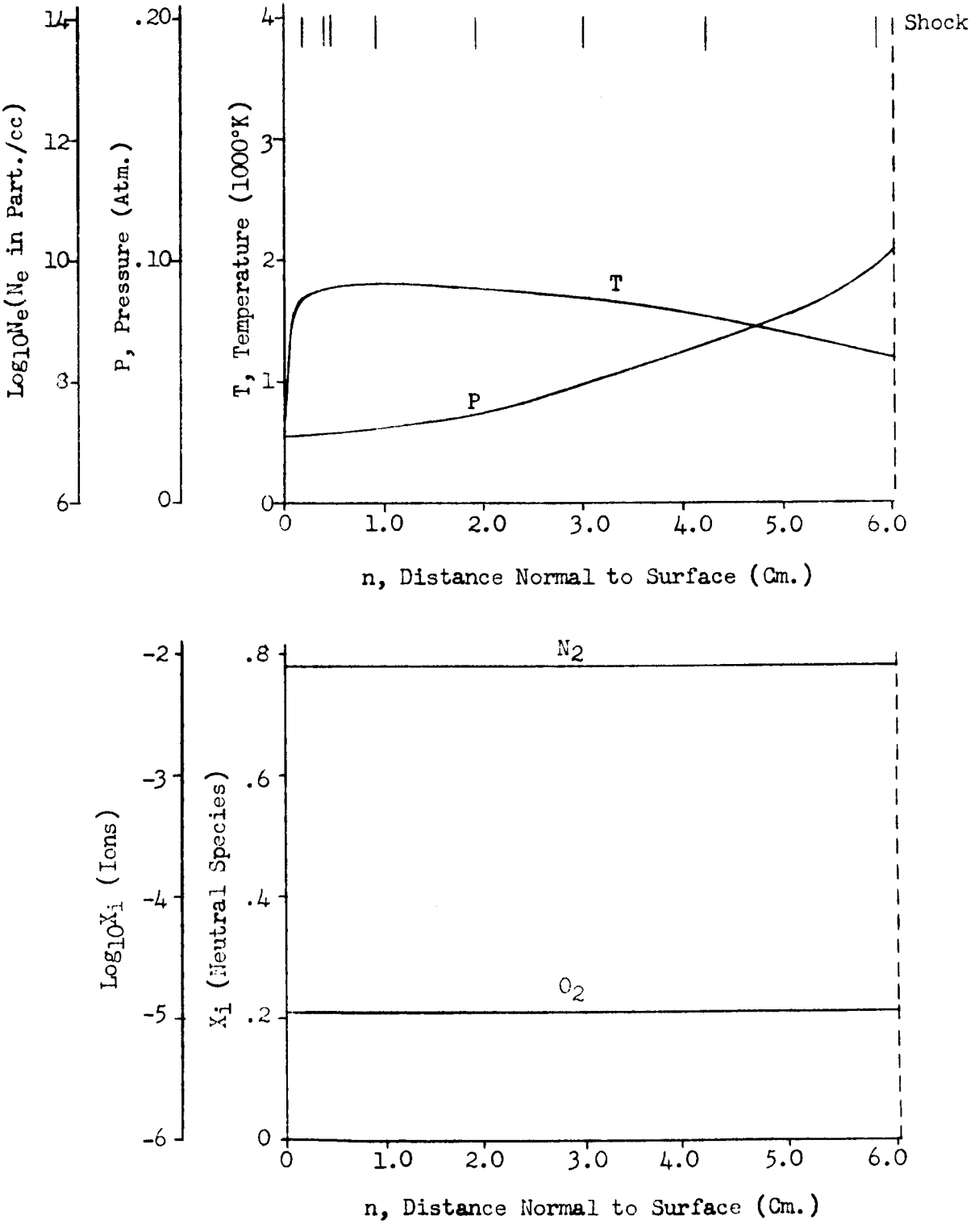

Figure 25d. Flow Field Properties - Case 1, Normal 4

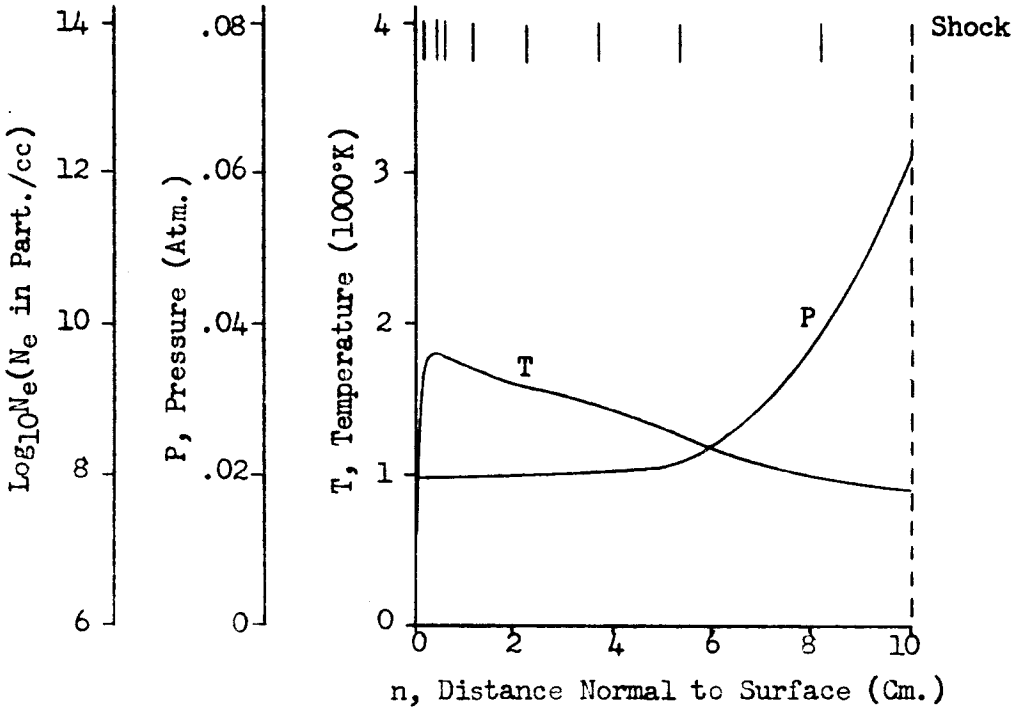

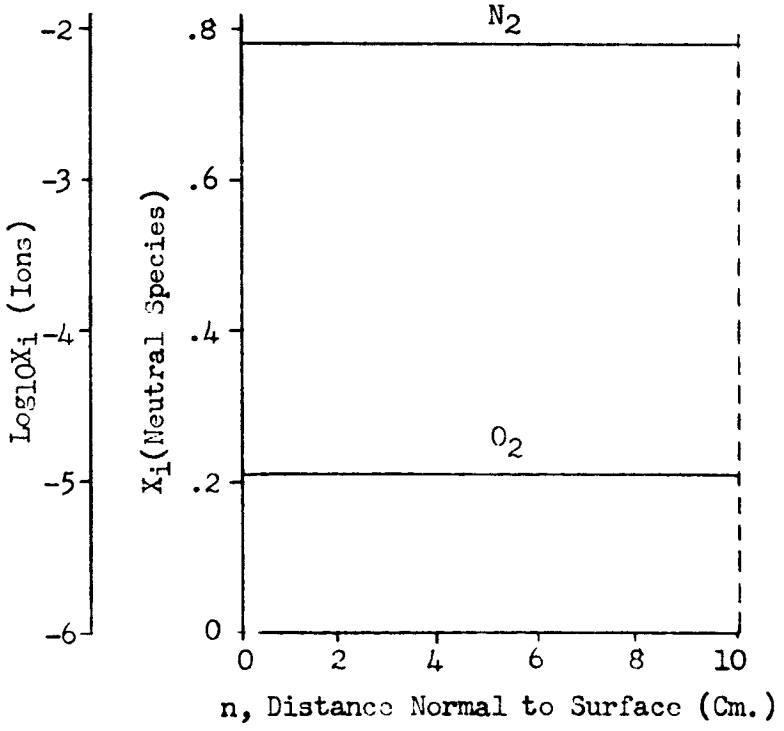

Figure 25e. Flow Field Properties - Case 1, Normal 5

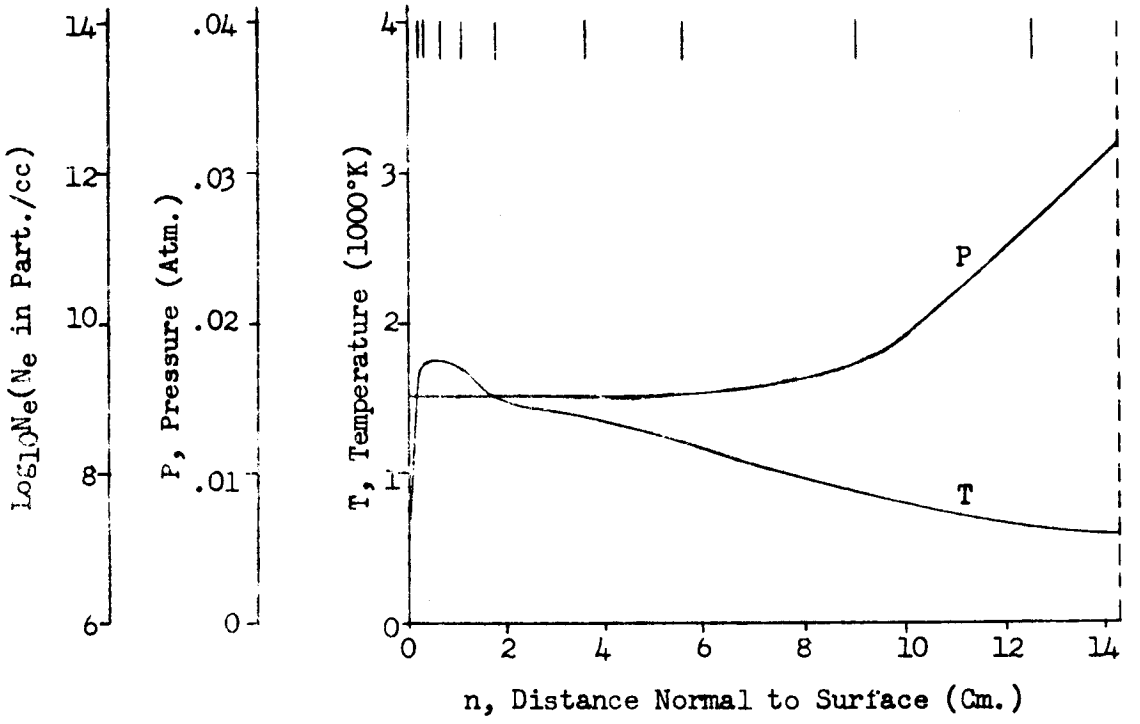

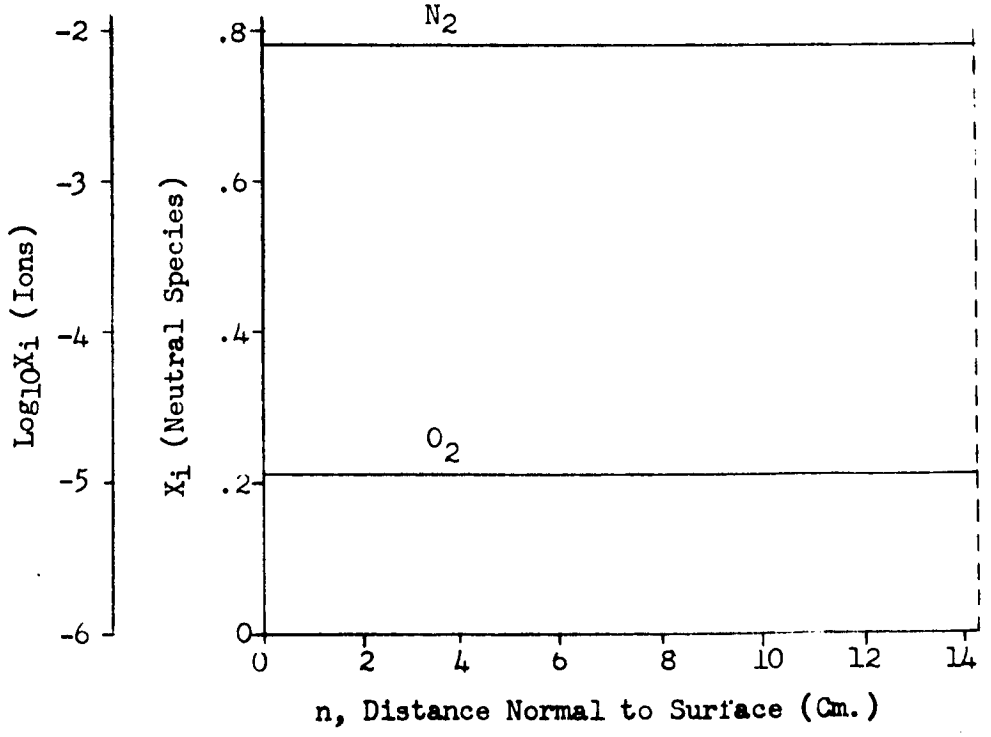

Figure 25f. Flow Field Properties - Case 1, Normal 6

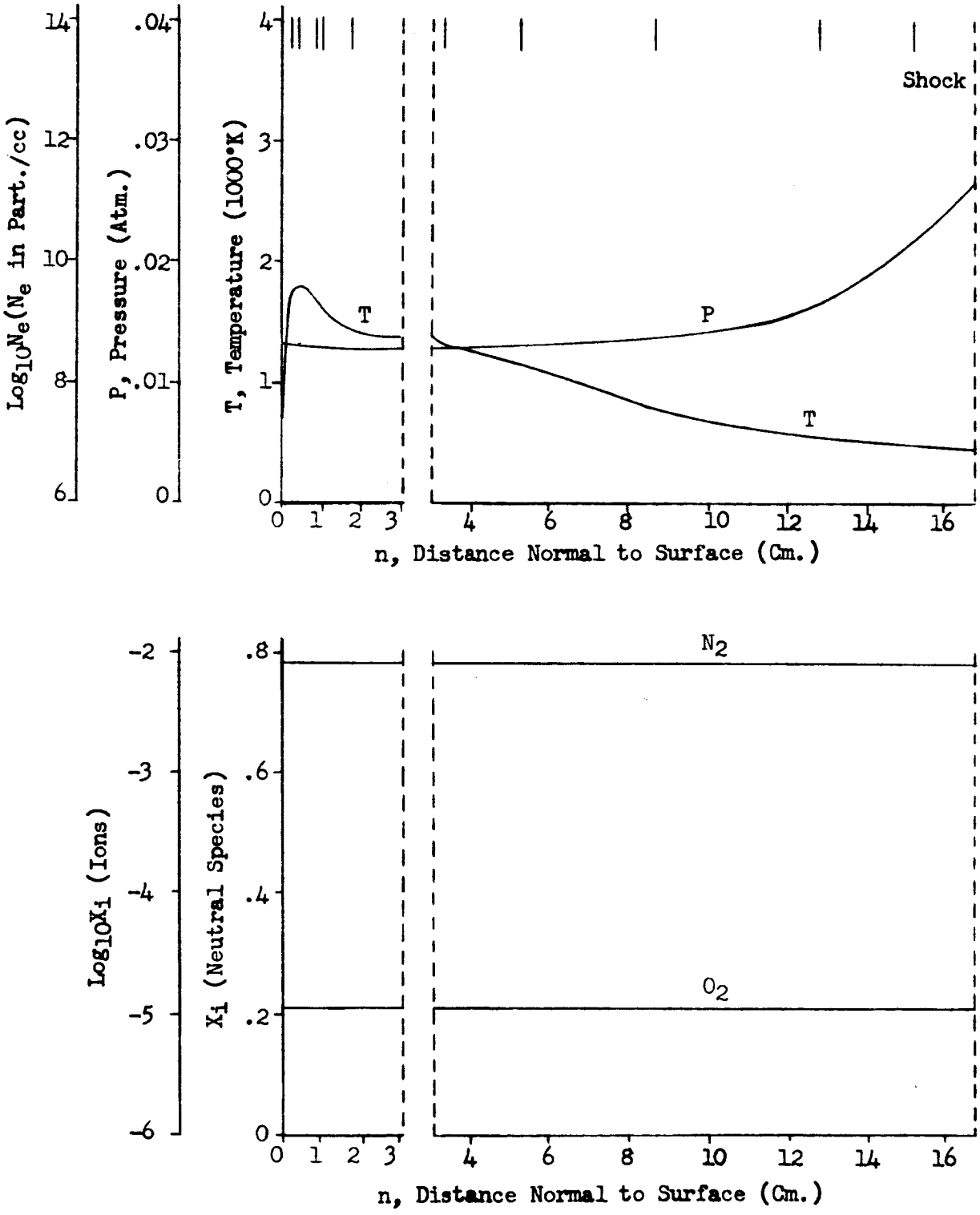

Figure 25g. Flow Field Properties - Case 1, Normal 7

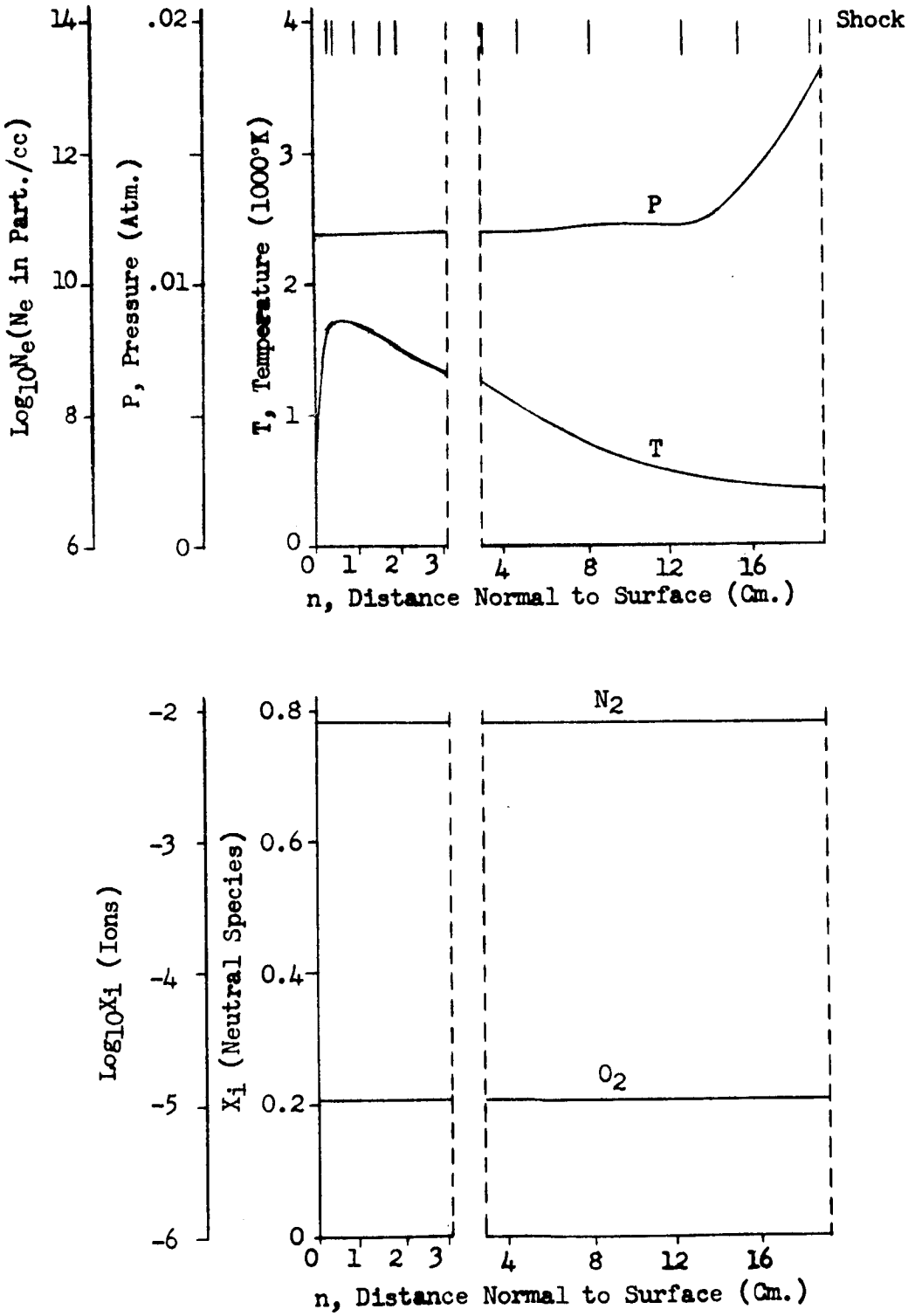

Figure 25h. Flow Field Properties - Case 1, Normal 8

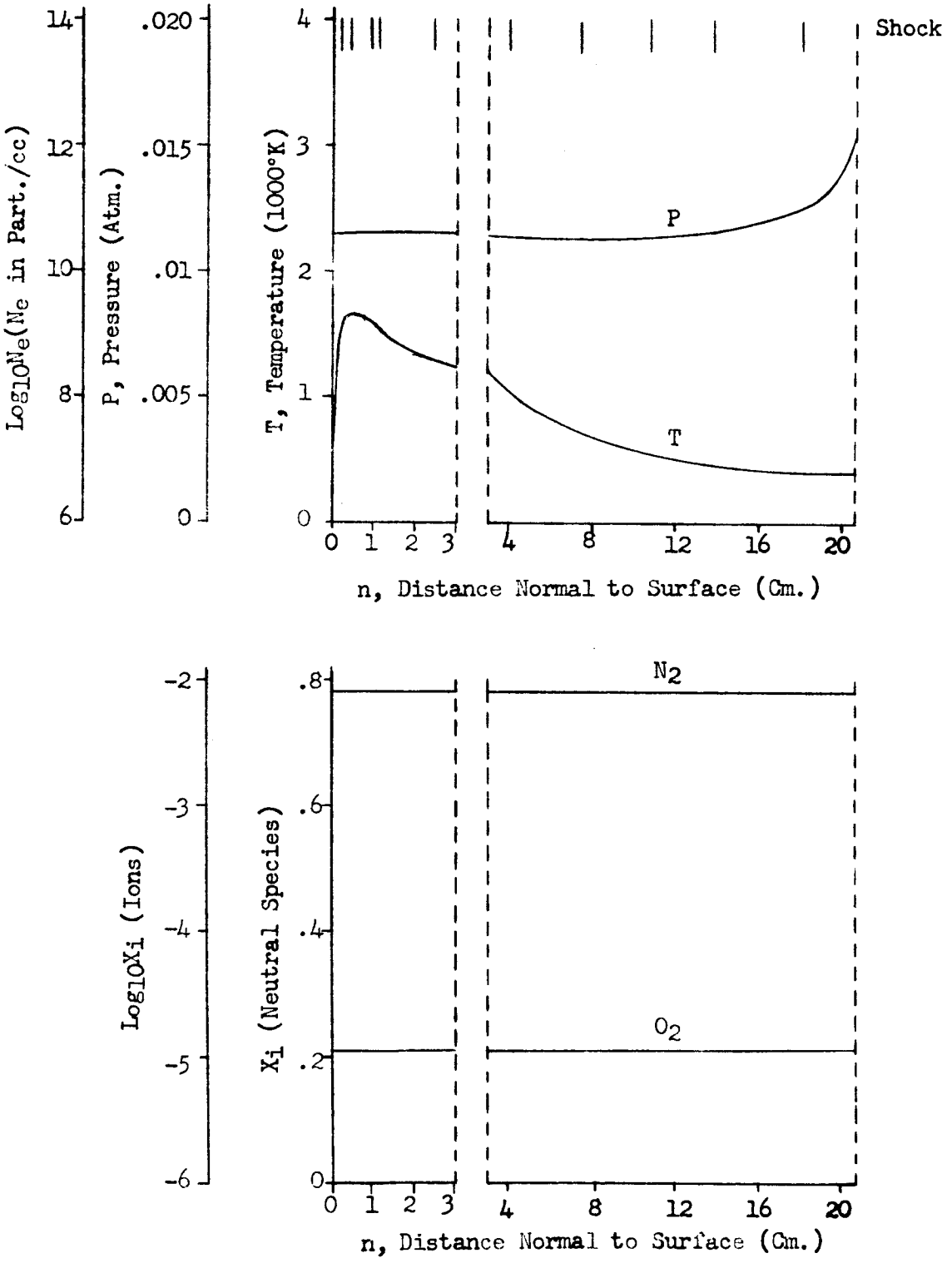

Figure 25i. Flow Field Properties - Case 1, Normal 9

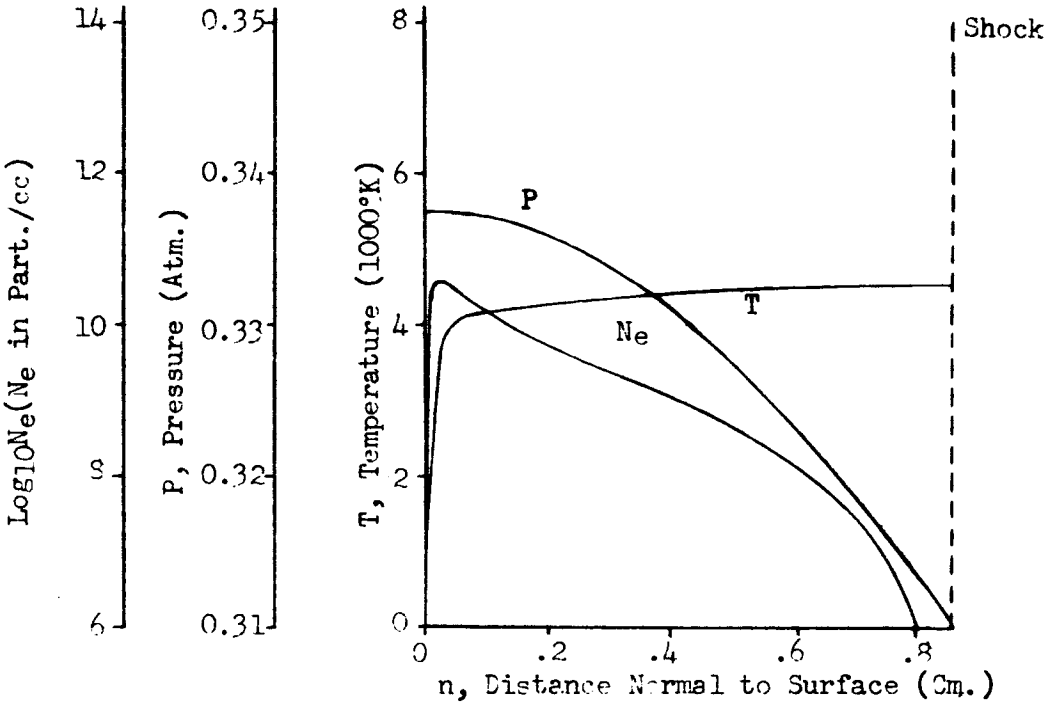

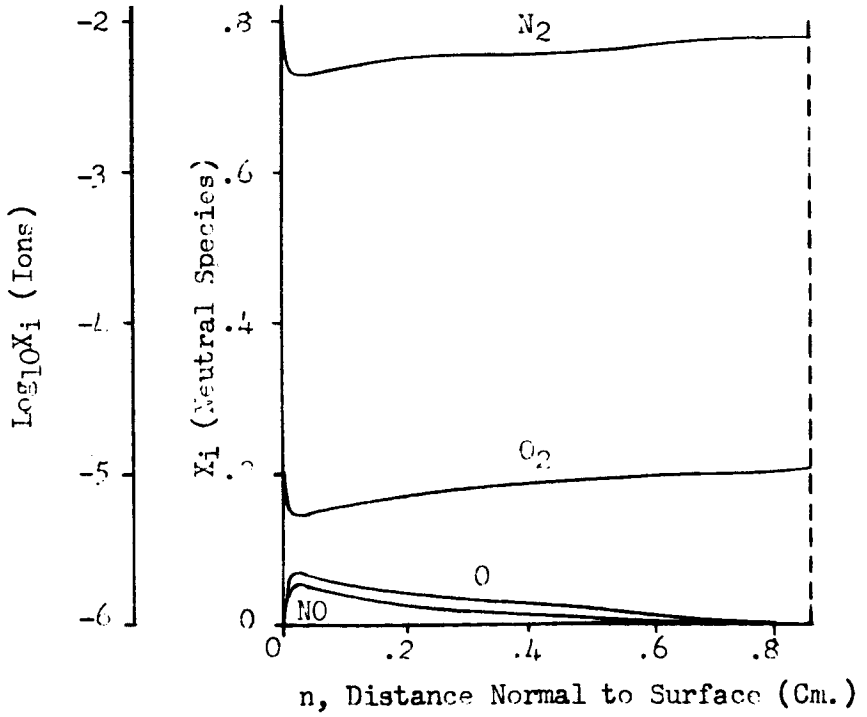

Figure 26a. Flow Field Properties - Case 2, Normal 1

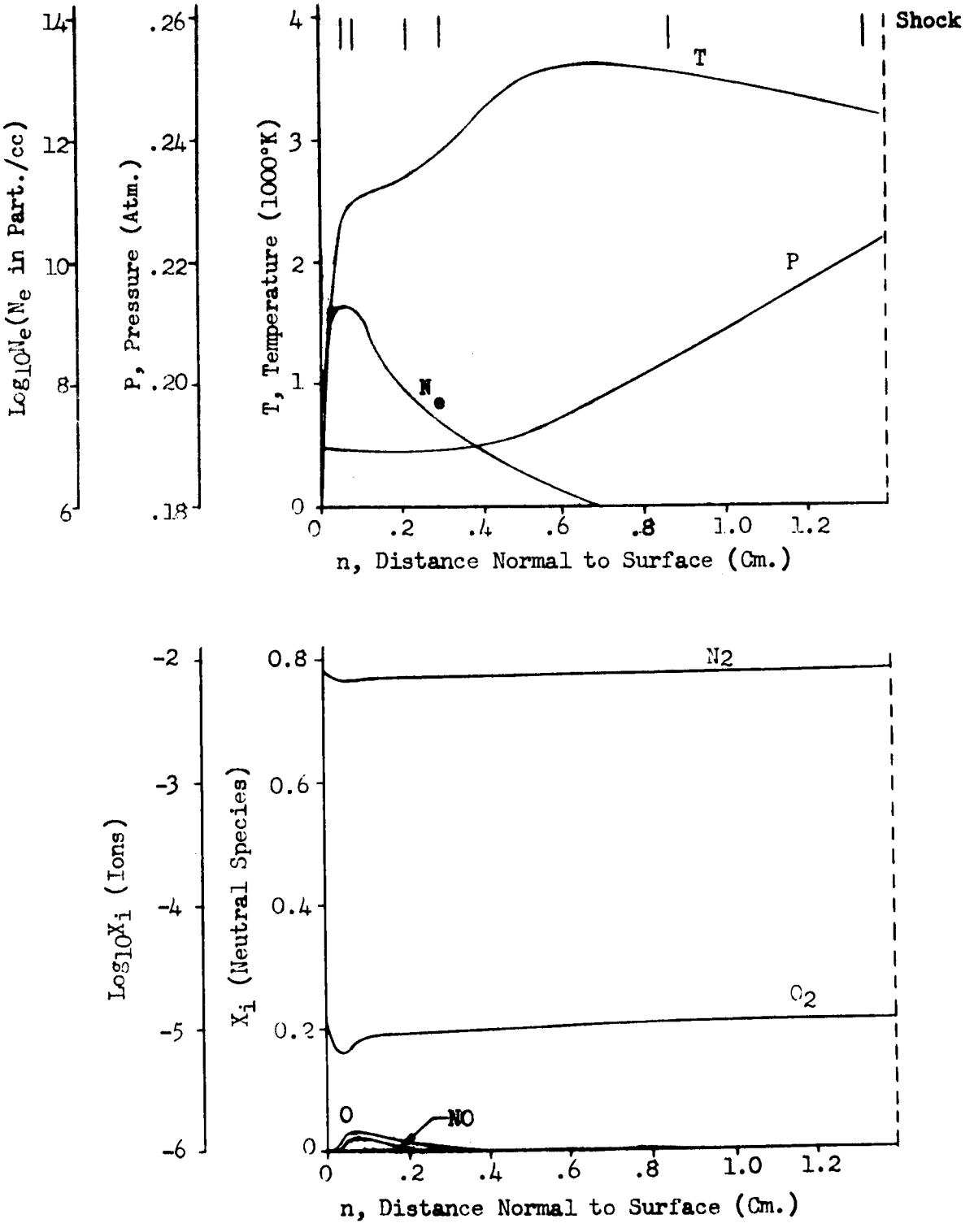

Figure 26b. Flow Field Properties - Case 2, Normal 2

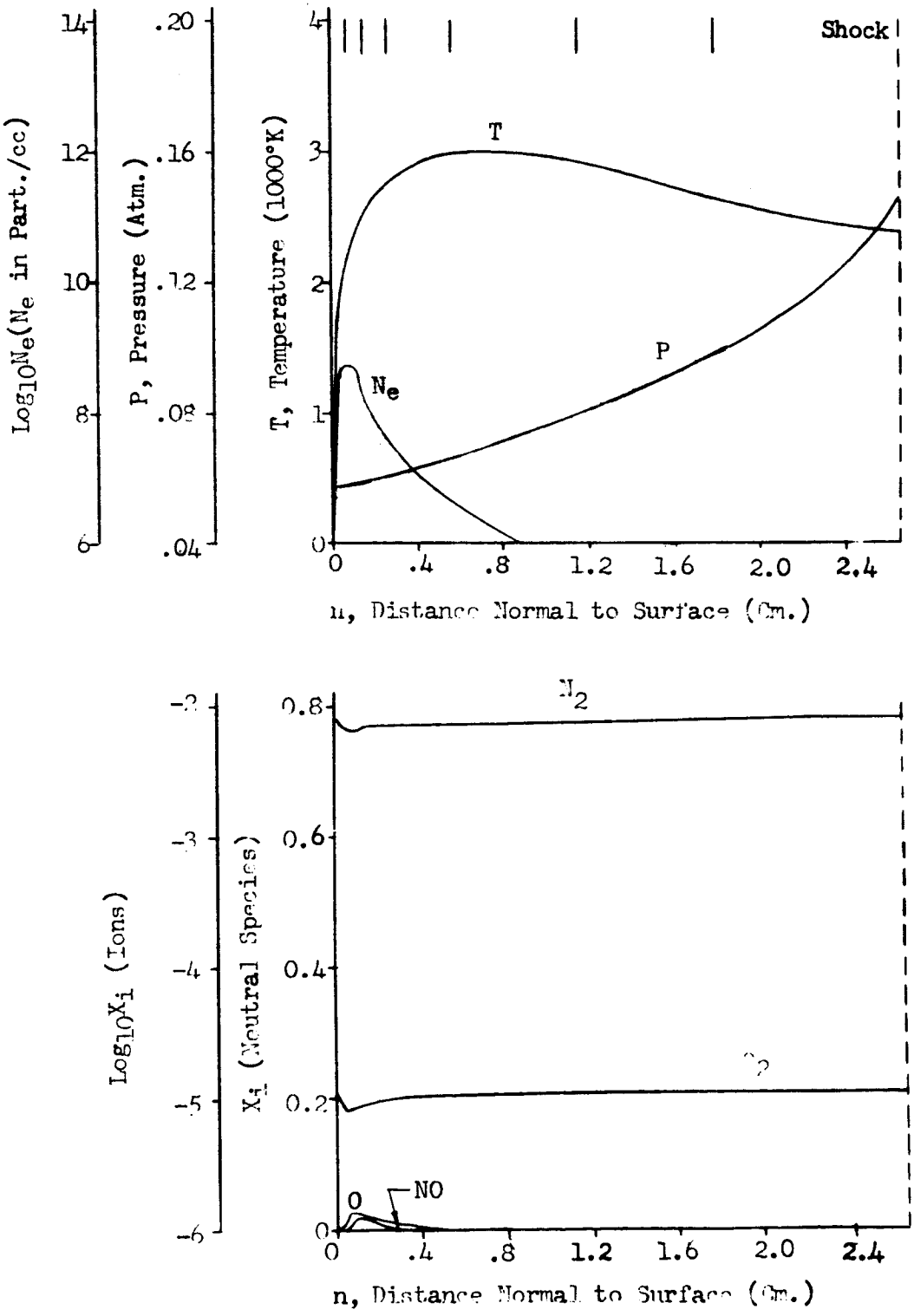

Figure 26c. Flow Field Properties - Case 2, Normal 3

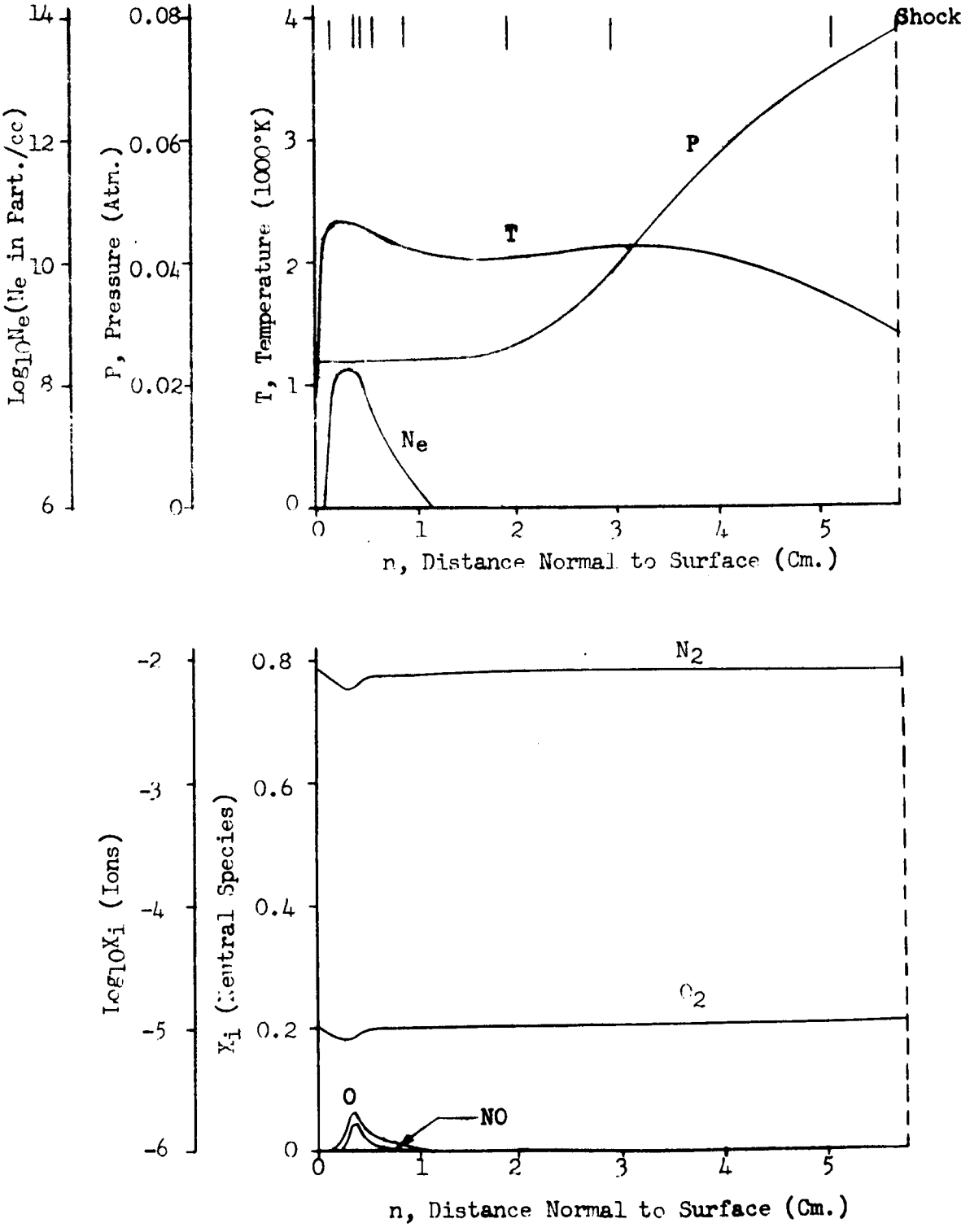

Figure 26d. Flow Field Properties - Case 2, Normal 4

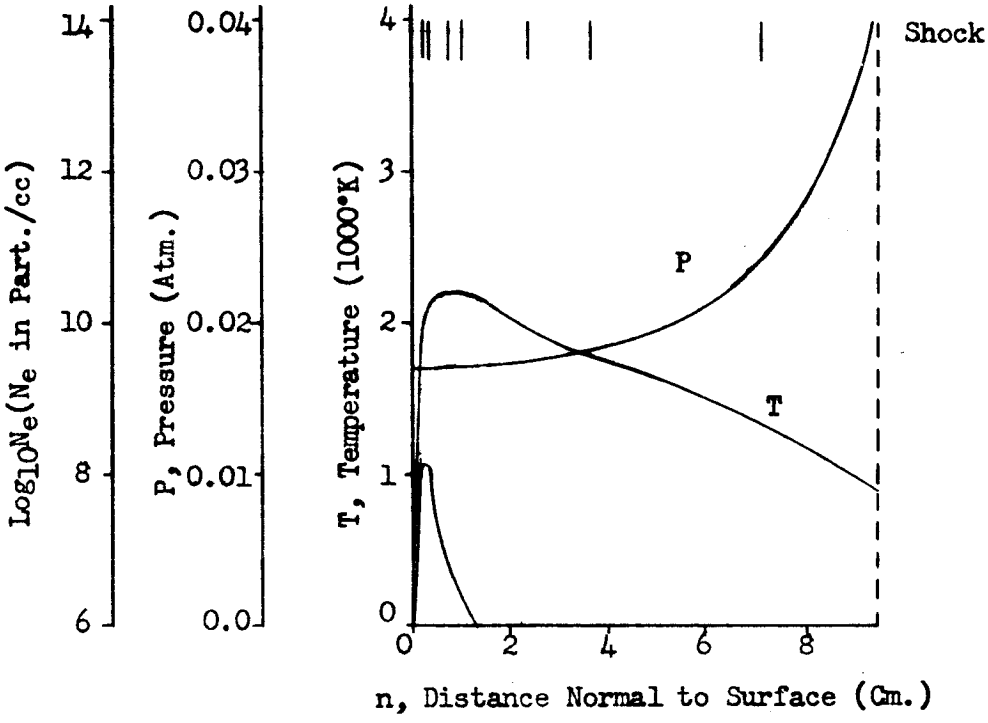

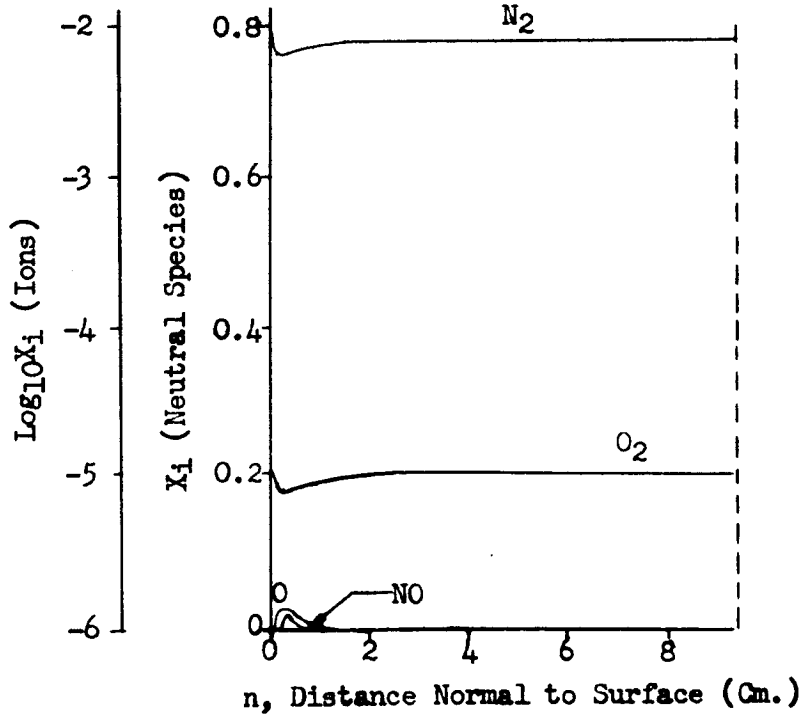

Figure 26e. Flow Field Properties - Case 2, Normal 5

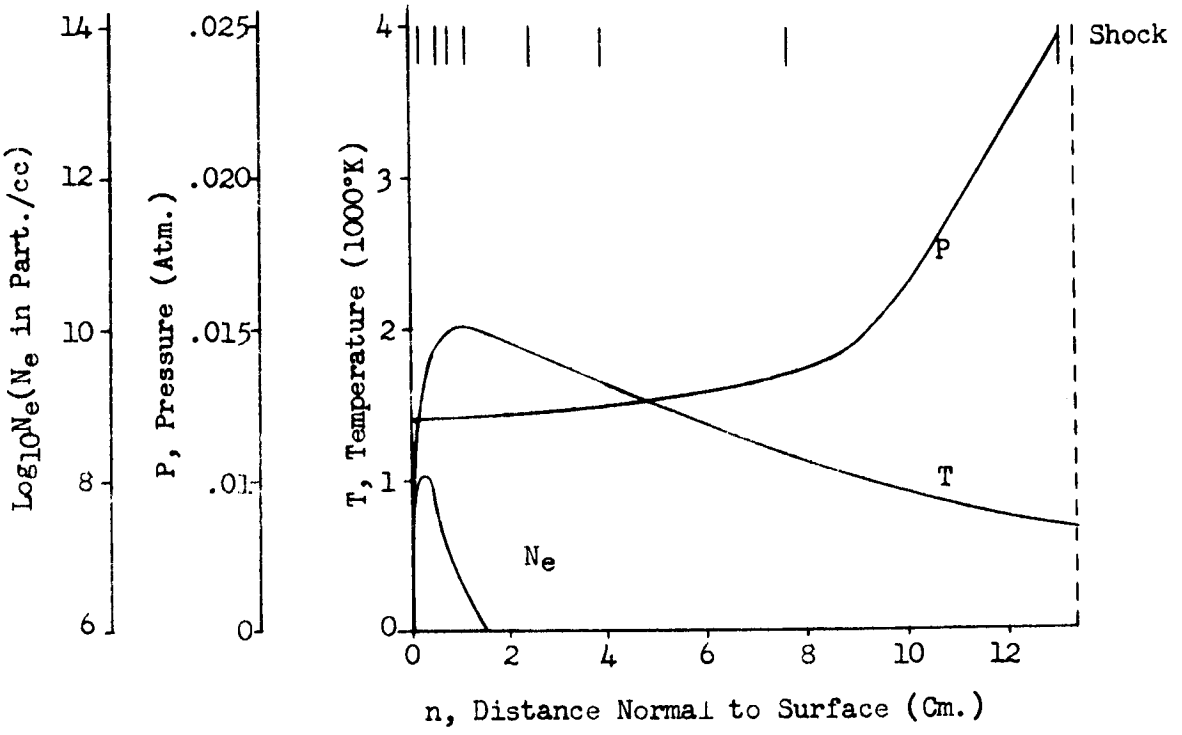

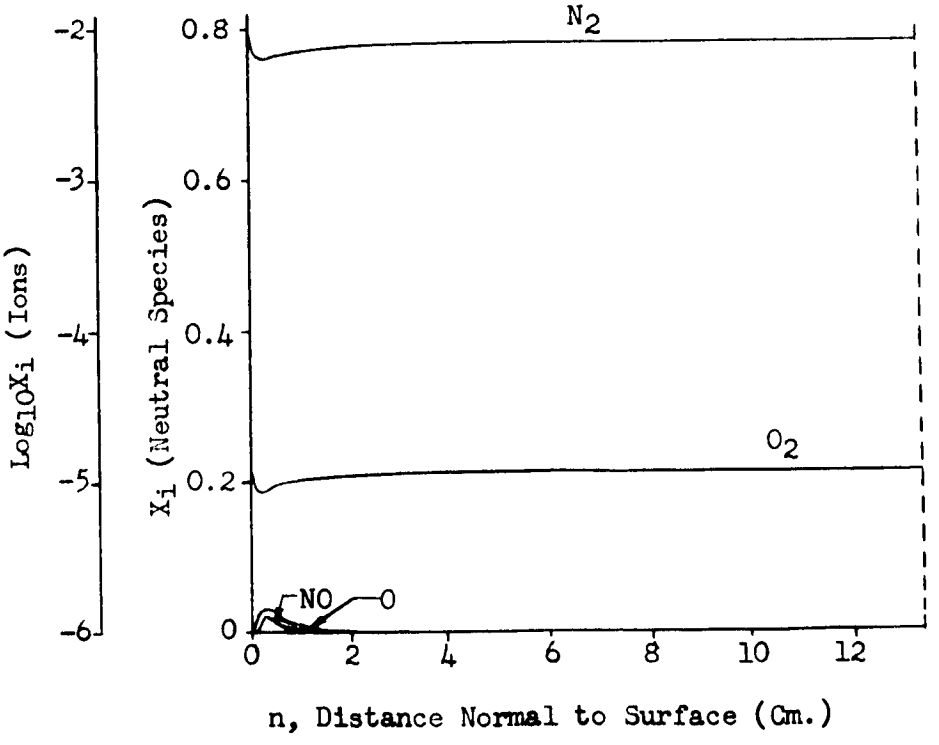

Figure 26f. Flow Field Properties - Case 2, Normal 6

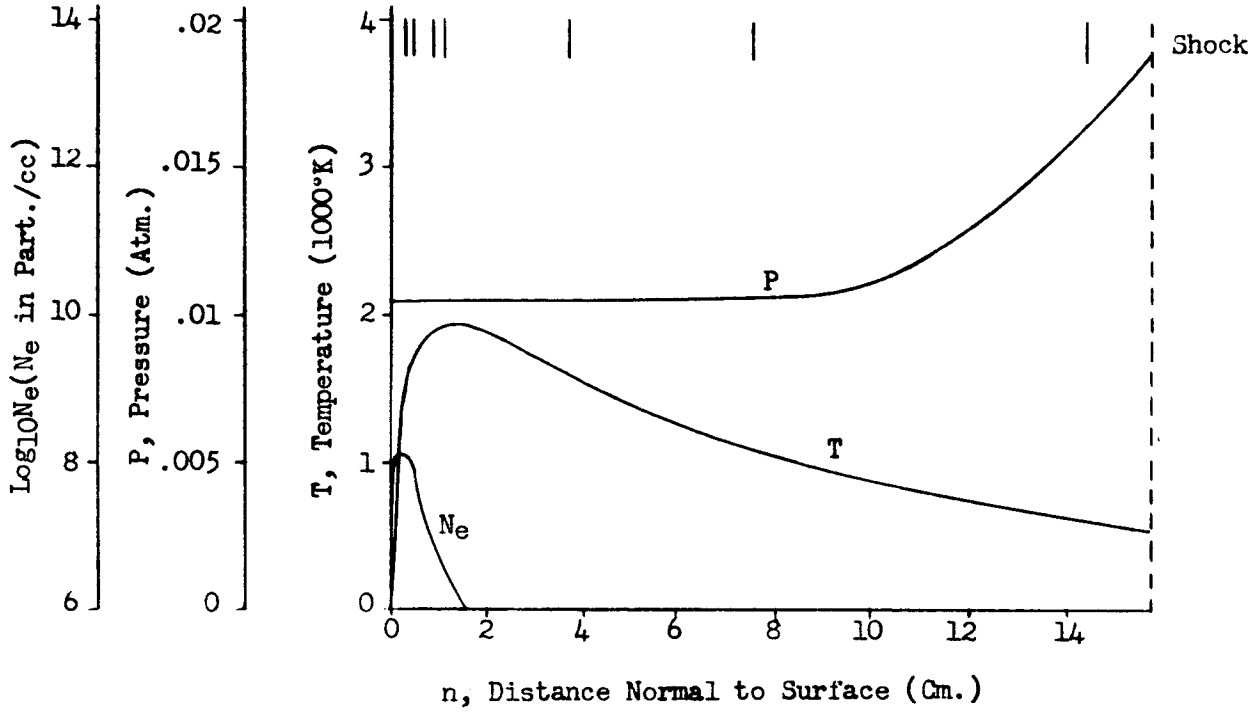

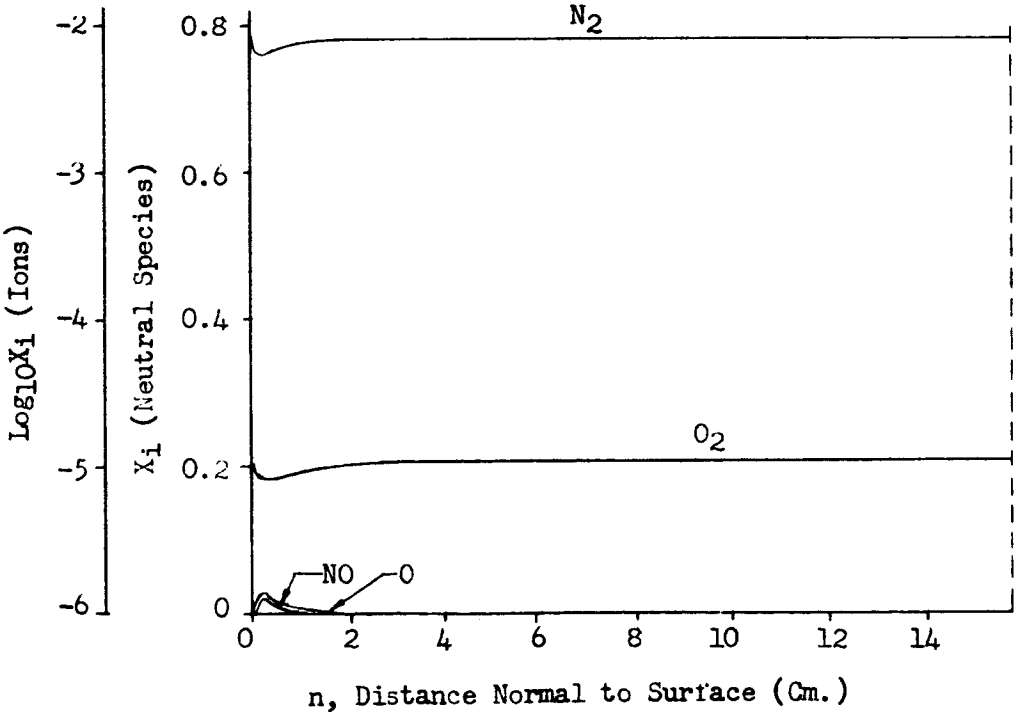

Figure 26g. Flow Field Properties - Case 2, Normal 7

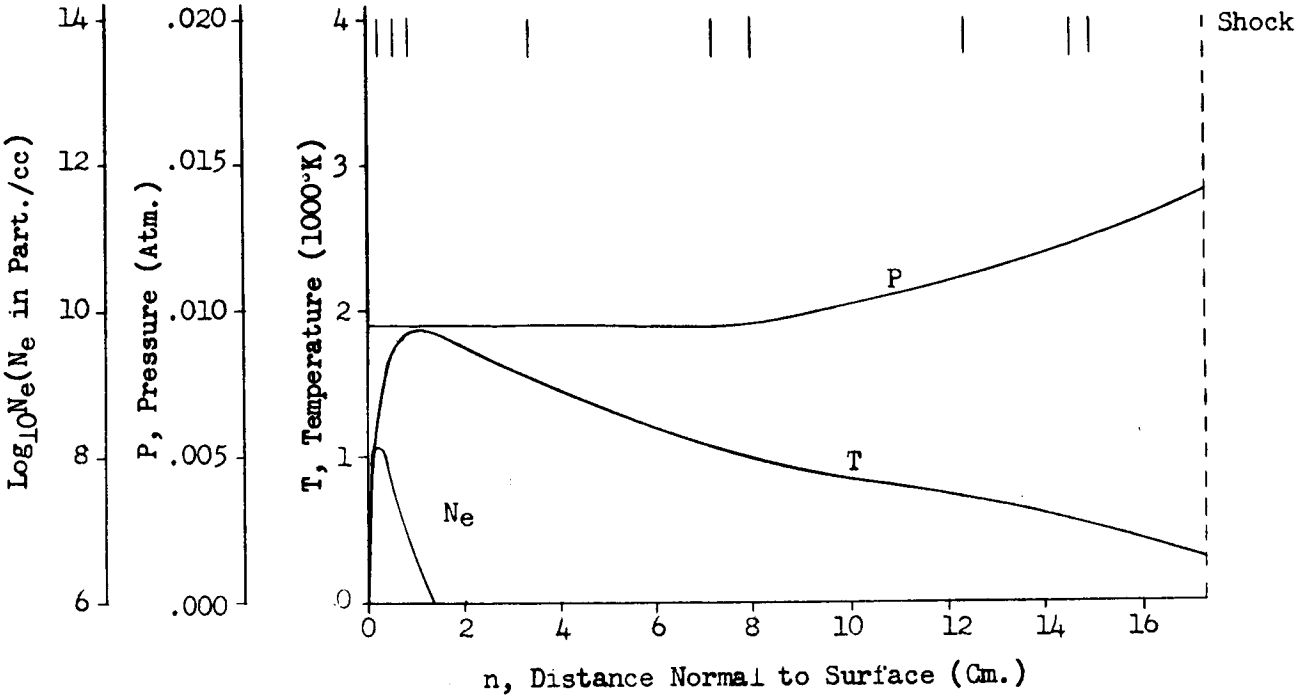

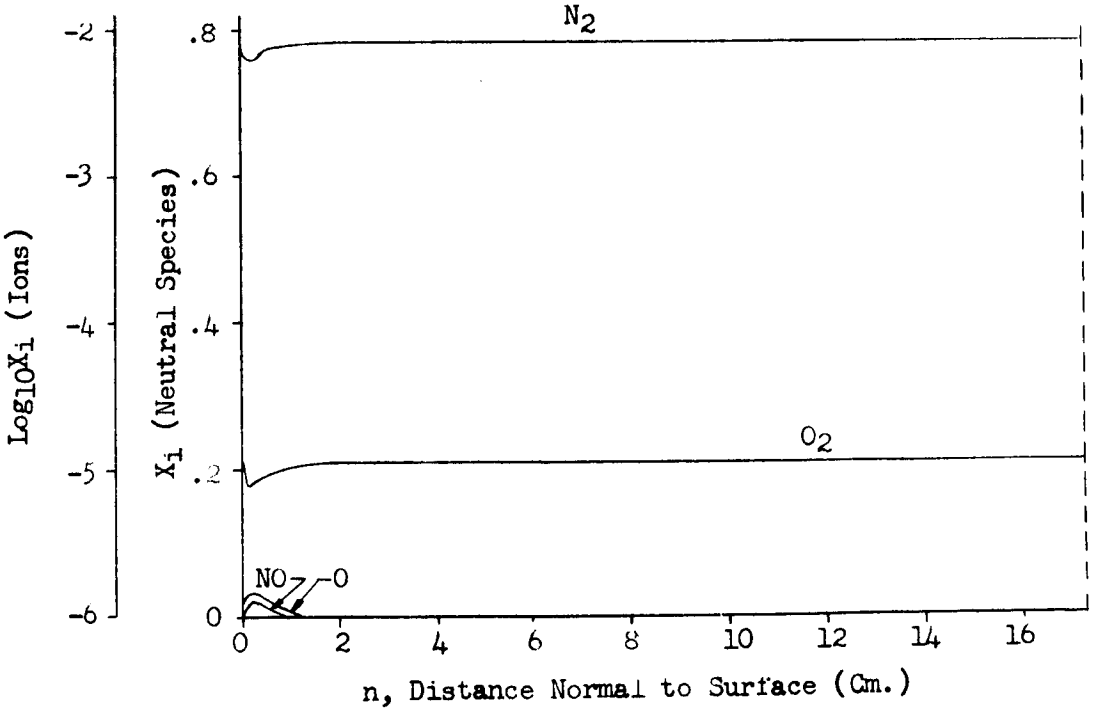

Figure 26h. Flow Field Properties - Case 2, Normal 8

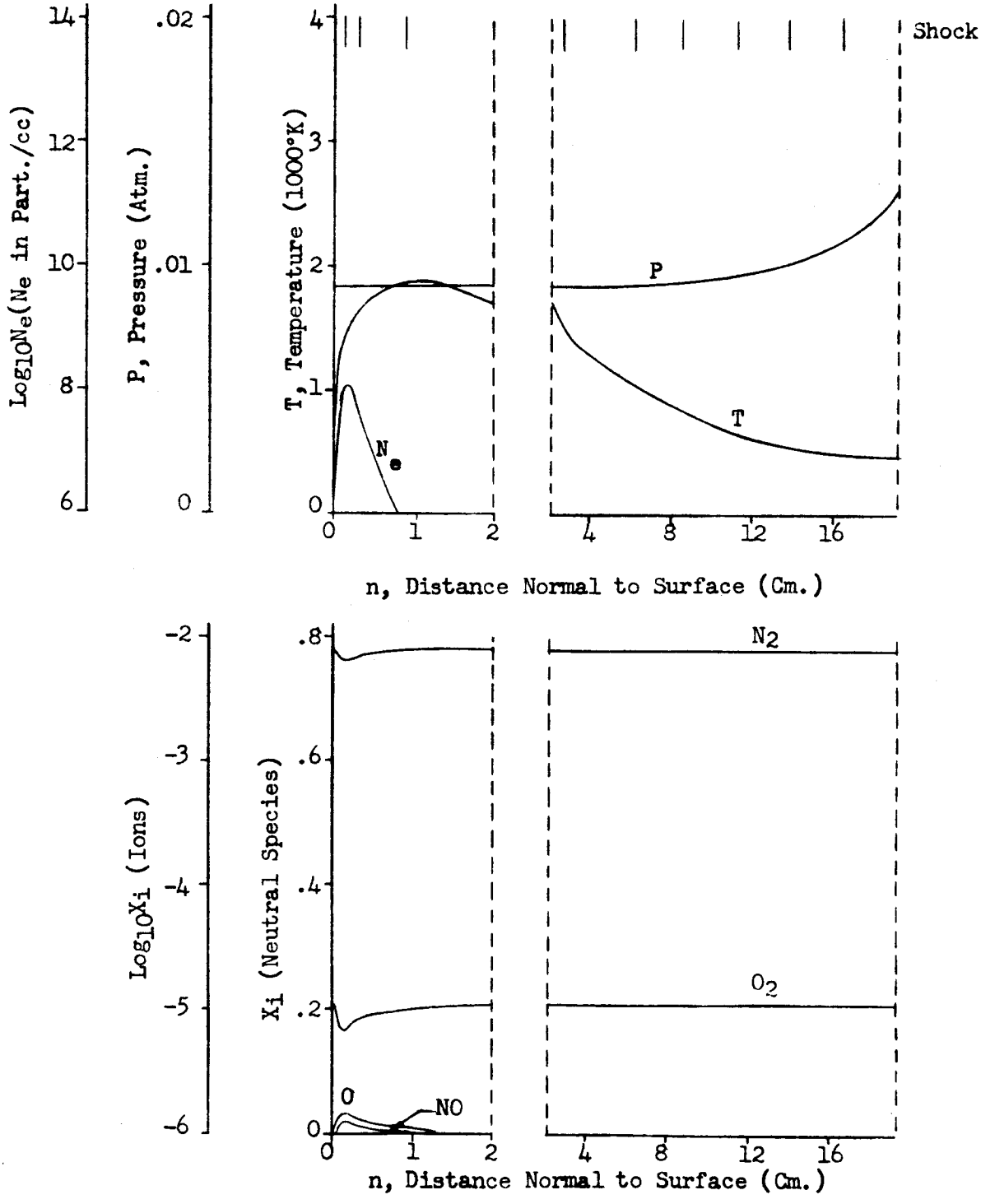

Figure 26i. Flow Field Properties - Case 2, Normal 9

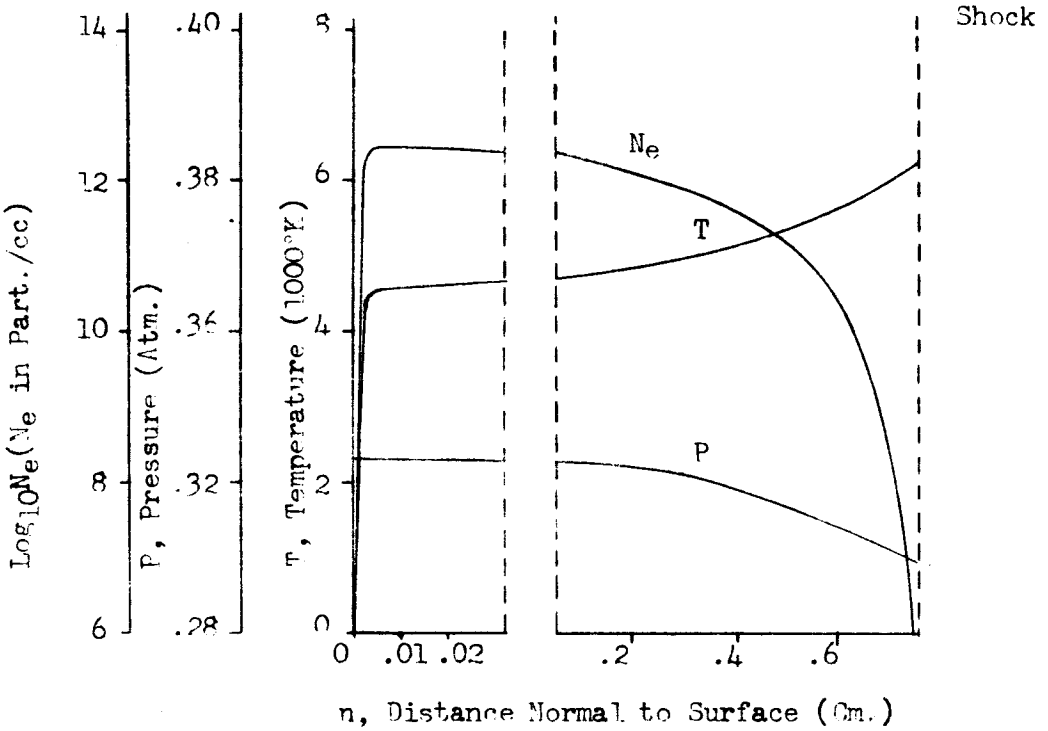

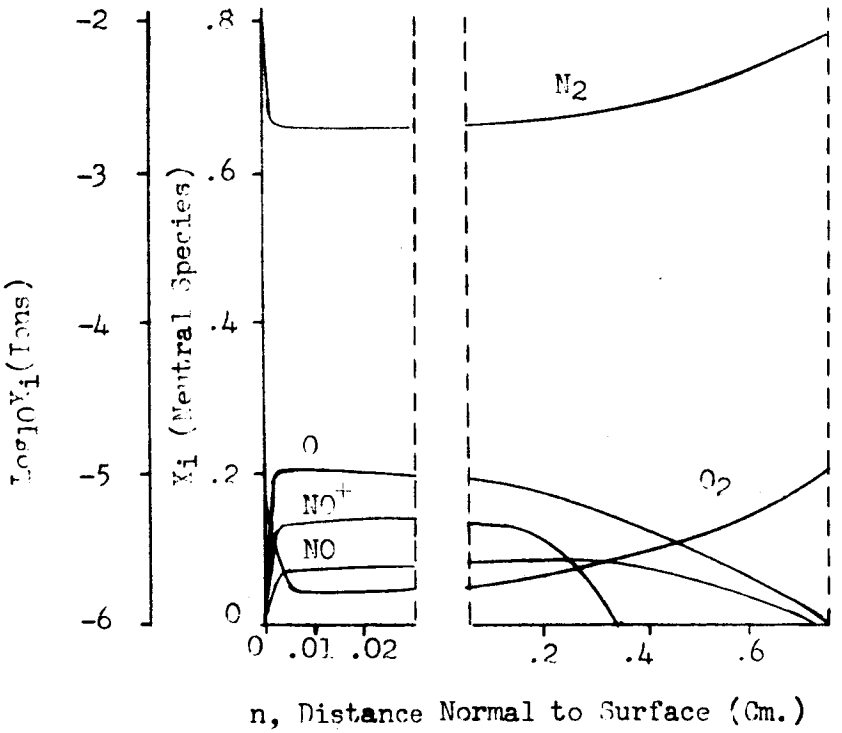

Figure 27a. Flow Field Properties - Case 3, Normal 1

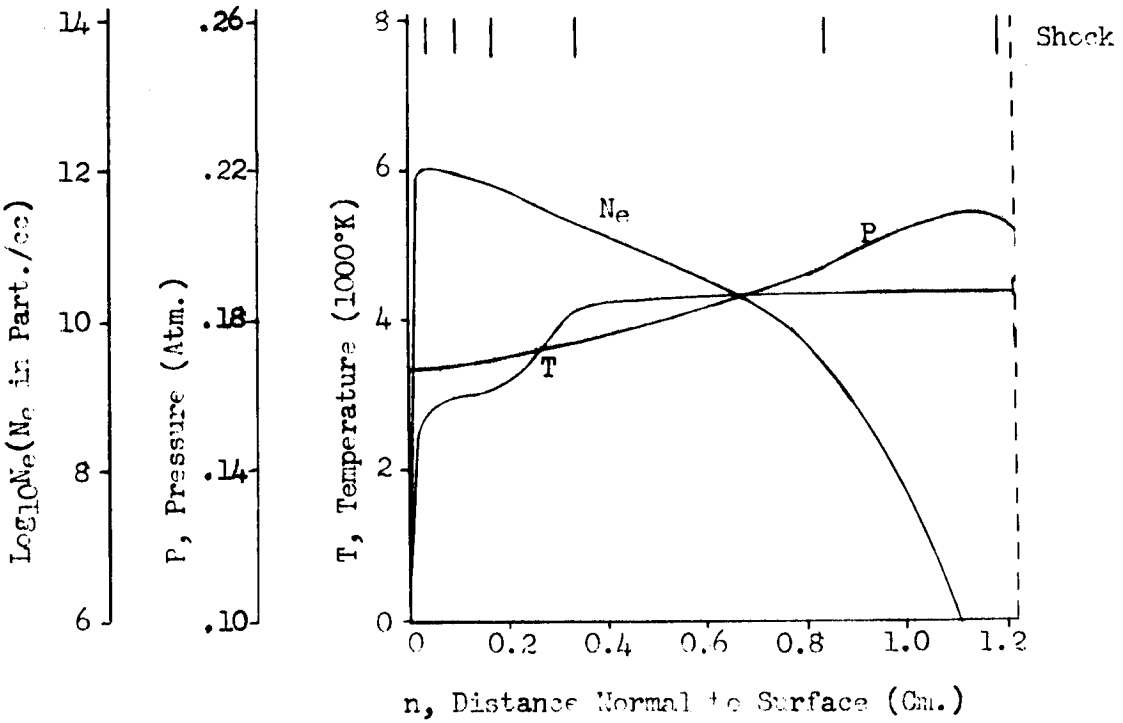

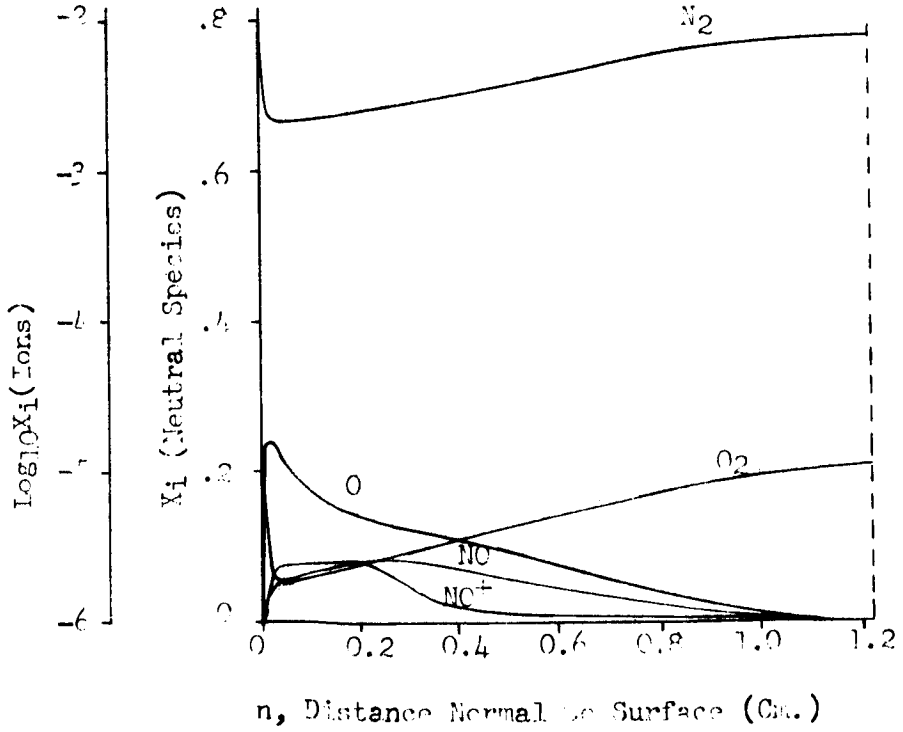

Figure 27b. Flow Field Properties - Case 3, Normal 2

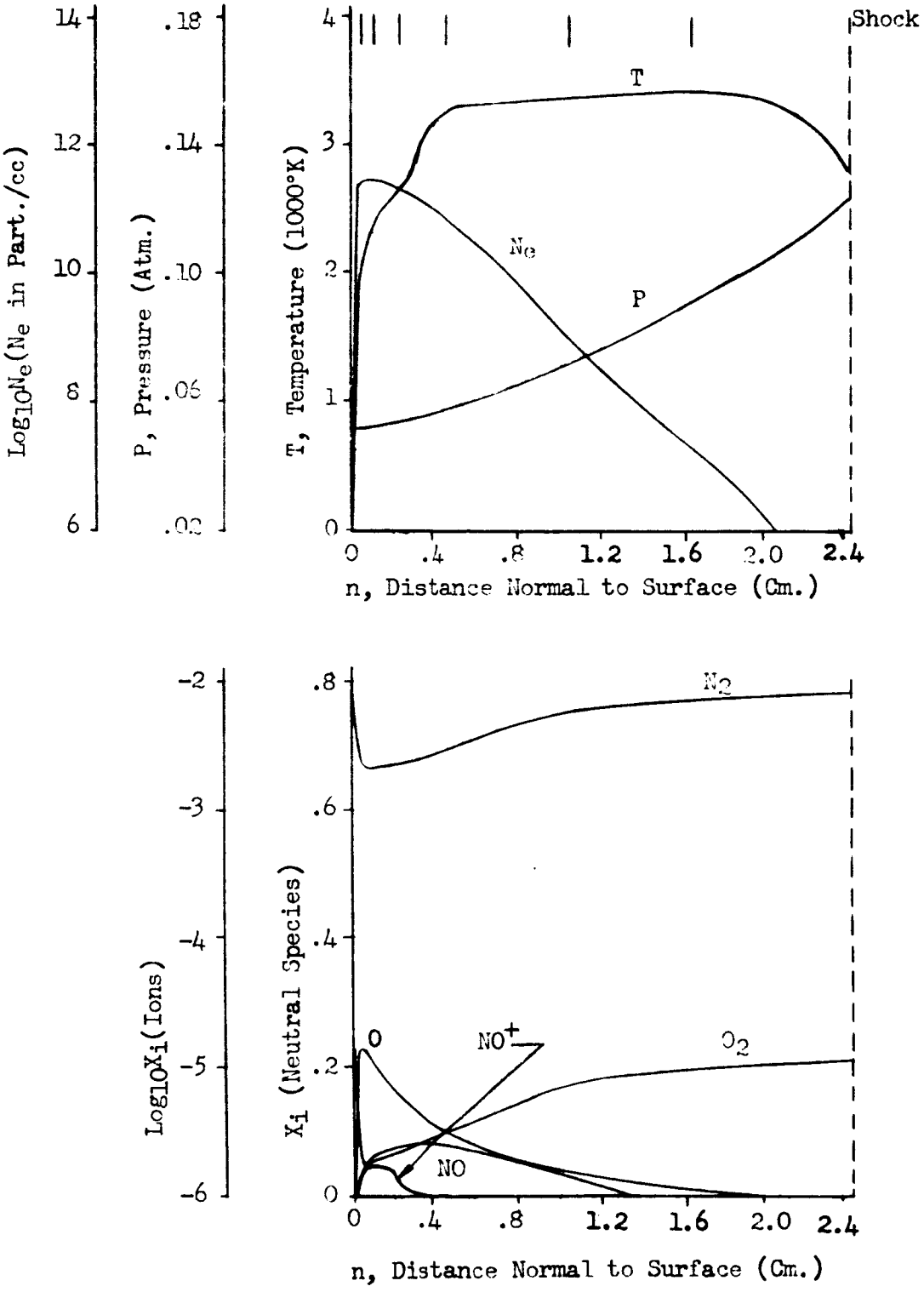

Figure 27c. Flow Field Properties - Case 3, Normal 3

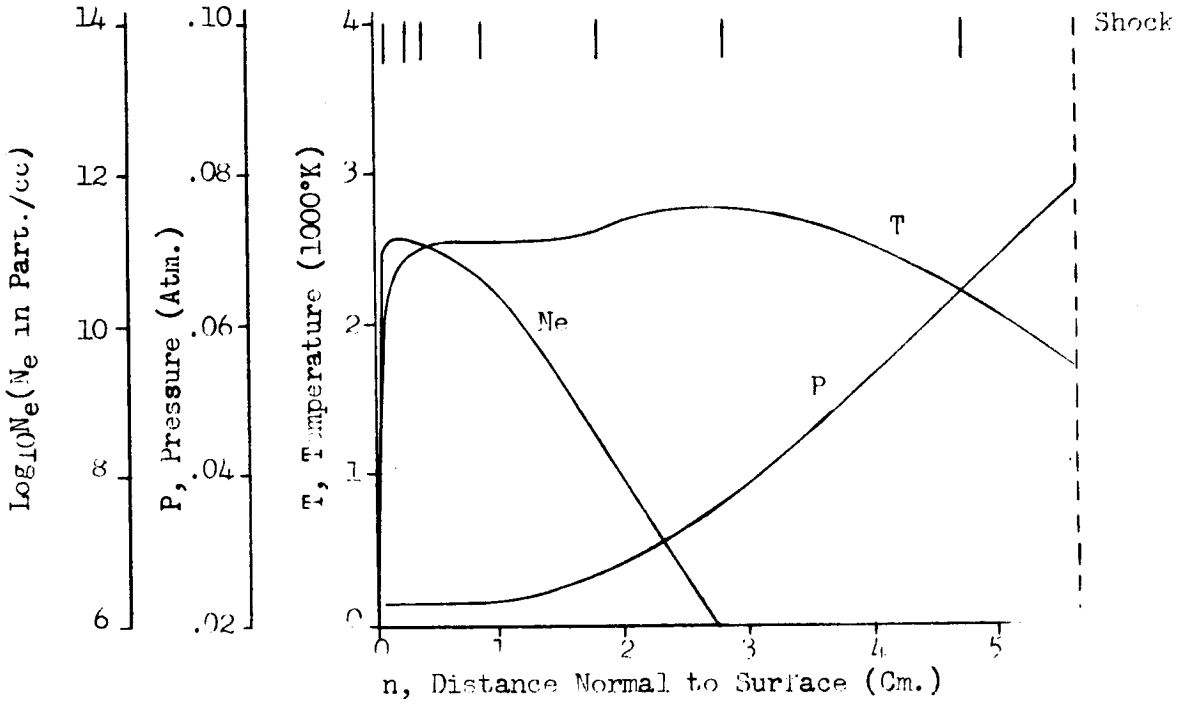

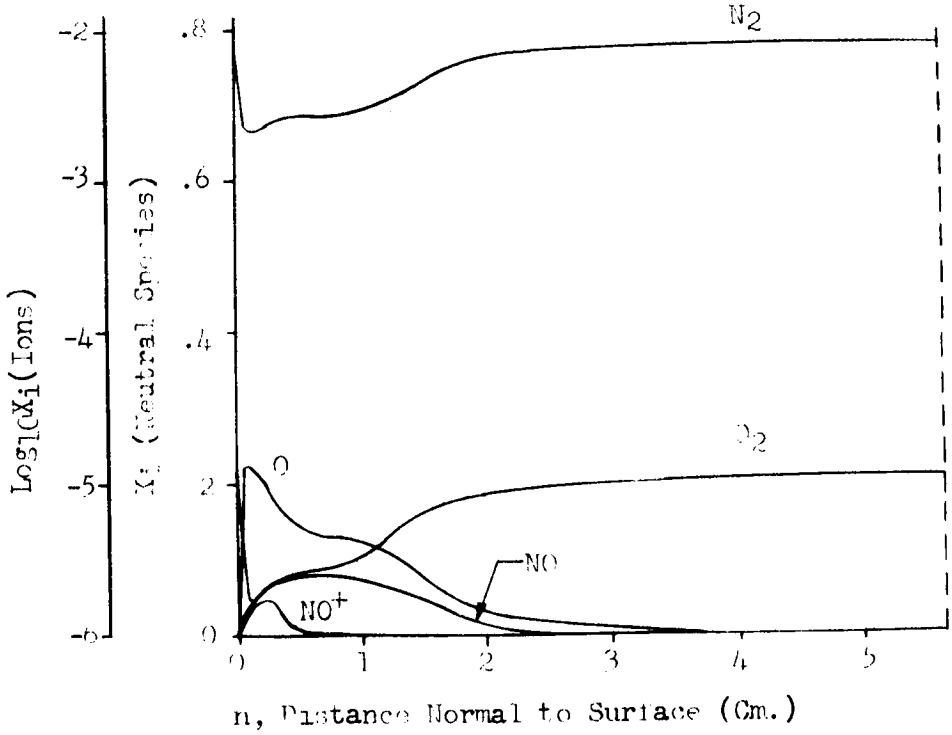

Figure 27d. Flow Field Properties - Case 3, Normal 4

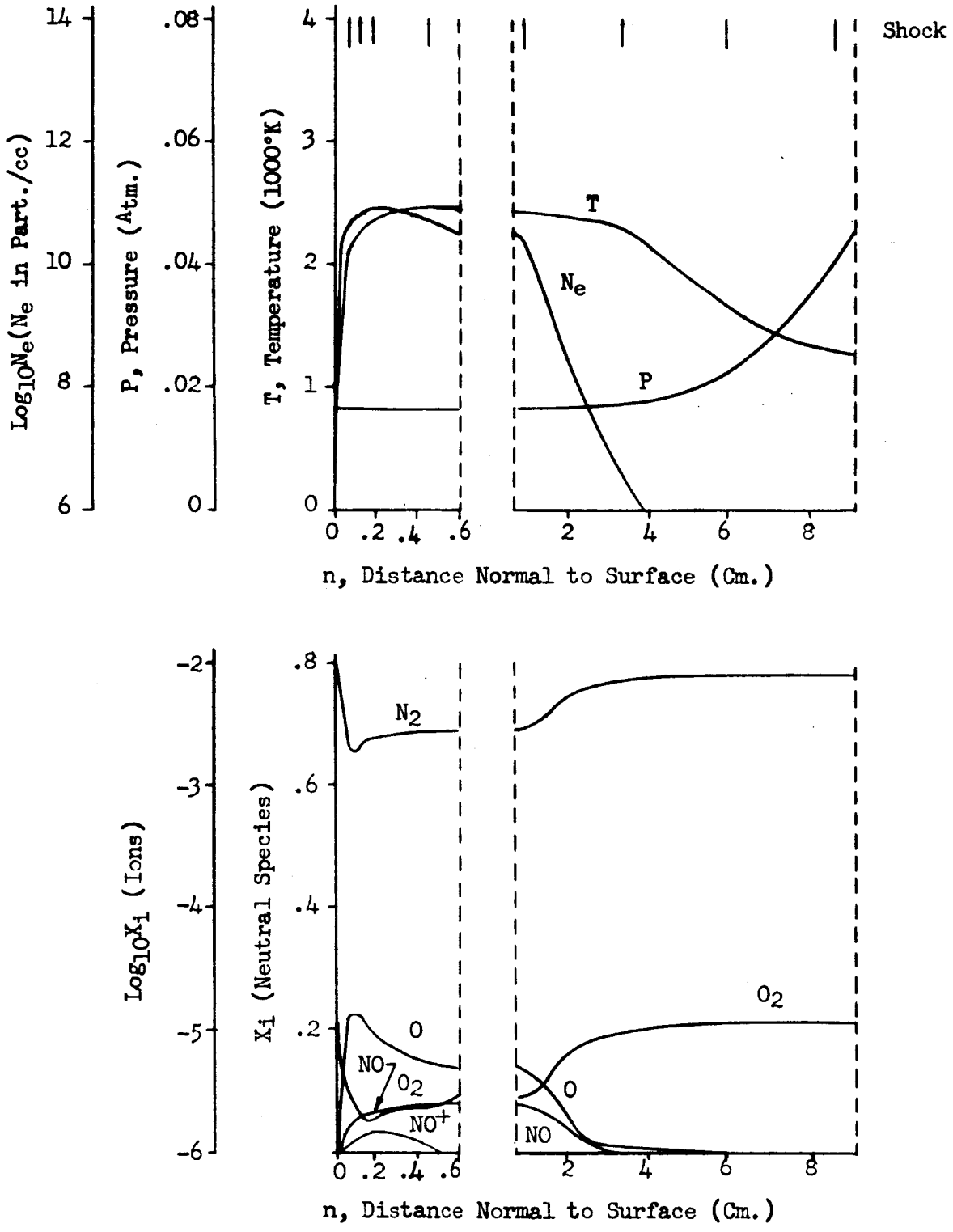

Figure 27e. Flow Field Properties - Case 3, Normal 5

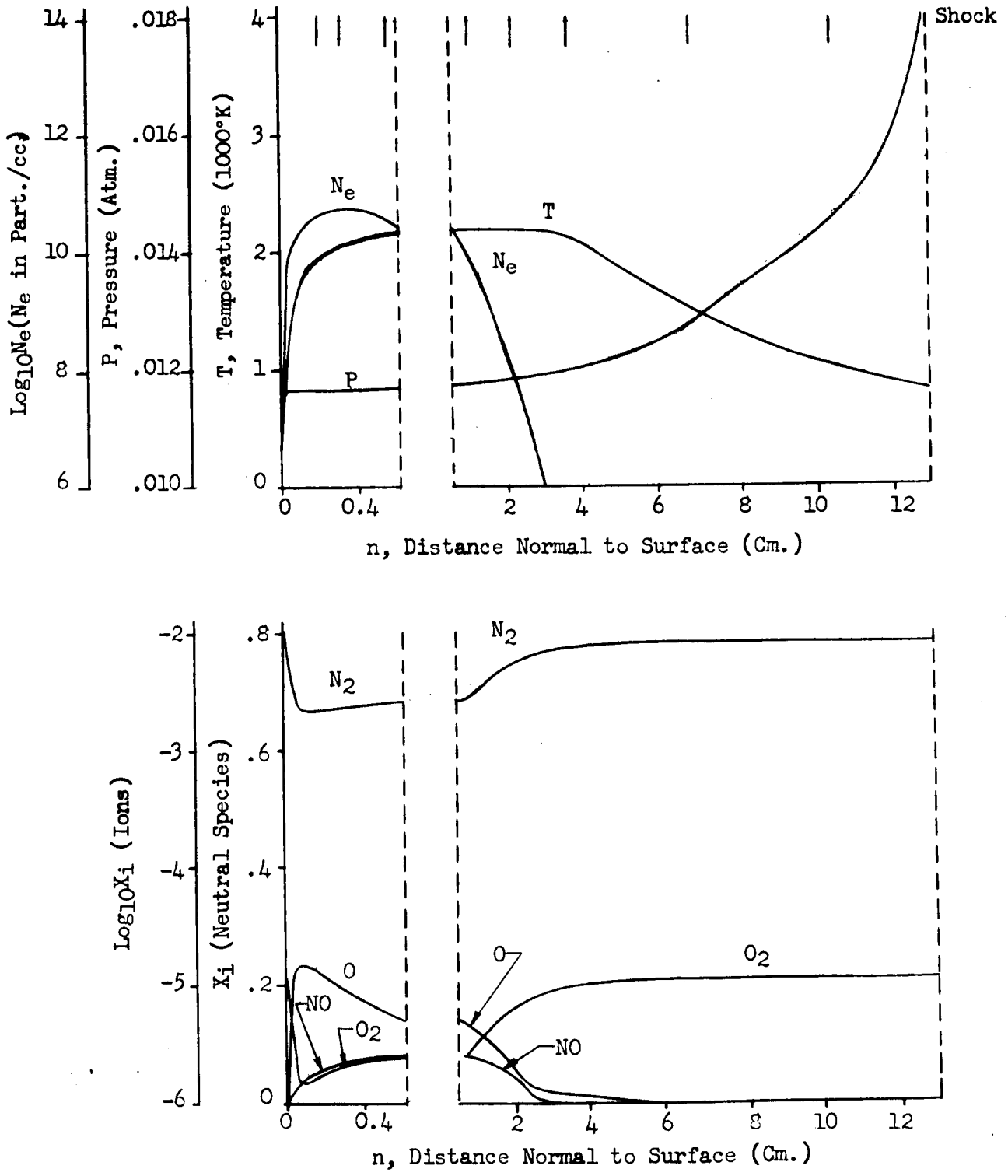

Figure 27f. Flow Field Properties - Case 3, Normal 6

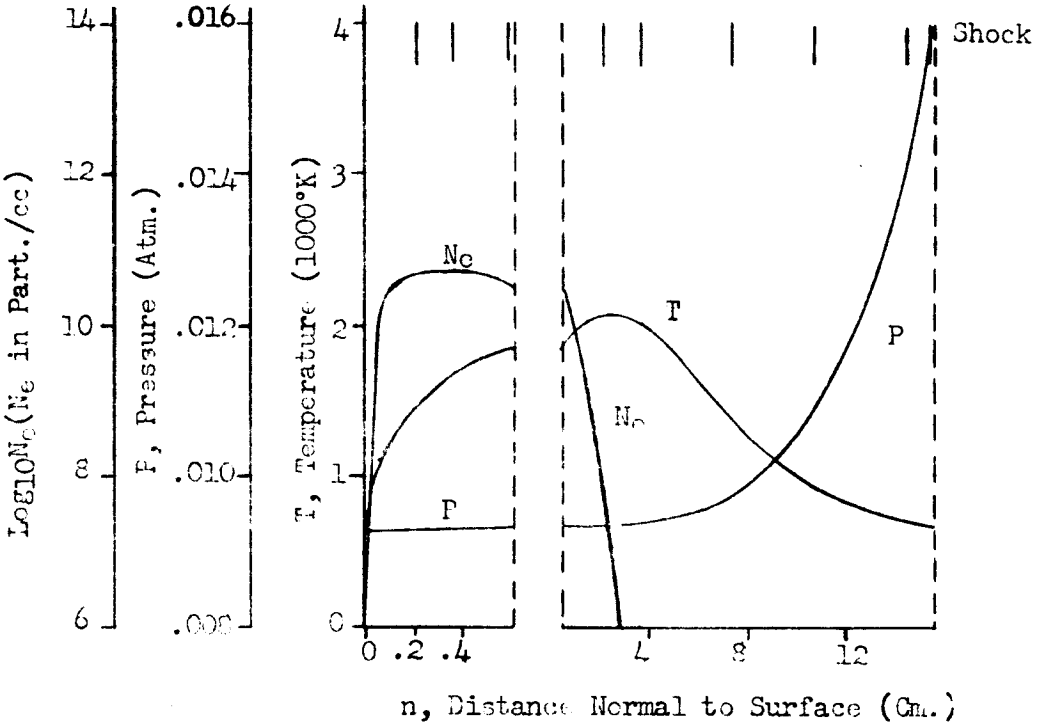

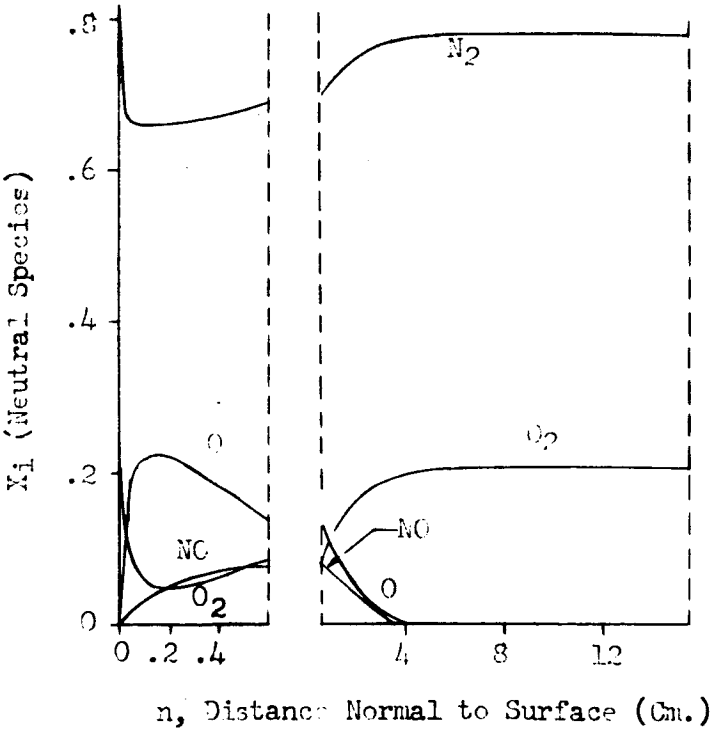

Figure 27g. Flow Field Properties - Case 3, Normal 7

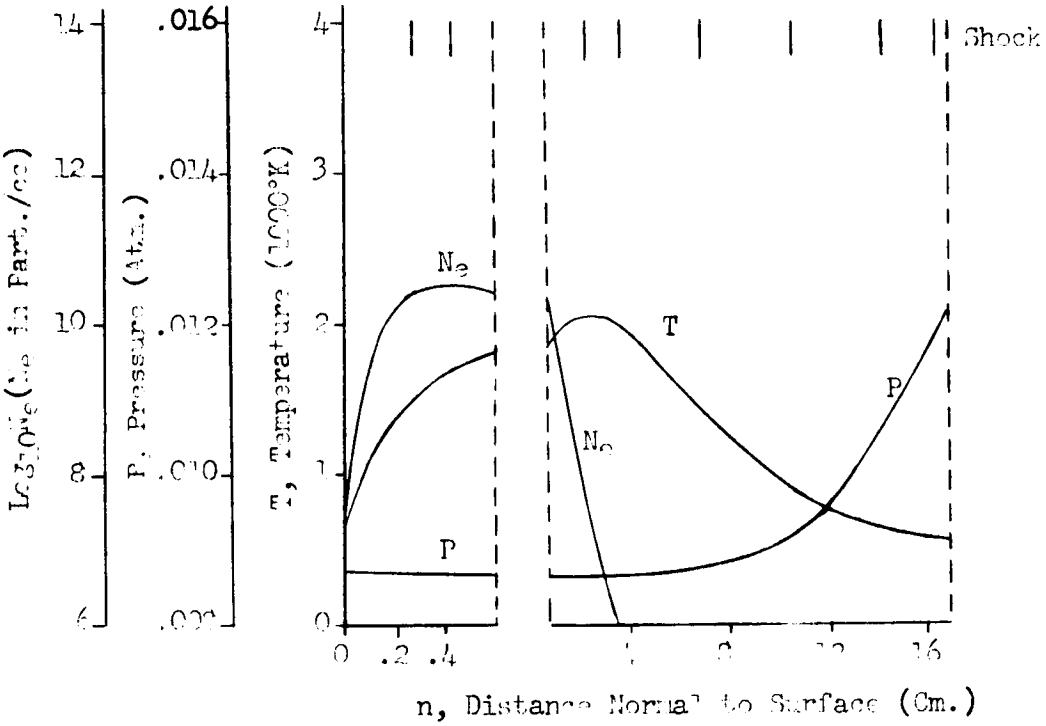

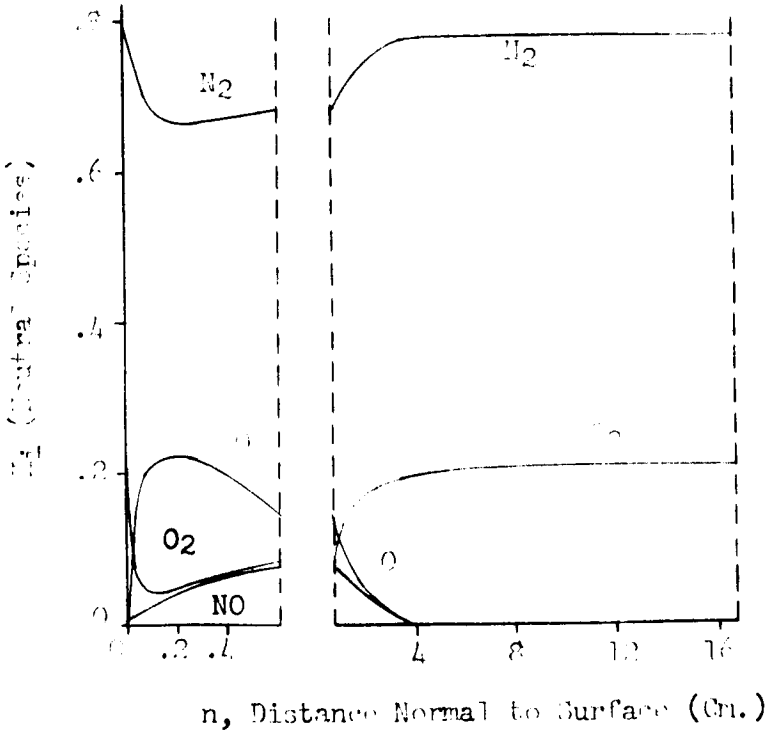

Figure 27h. Flow Field Properties - Case 3, Normal 8

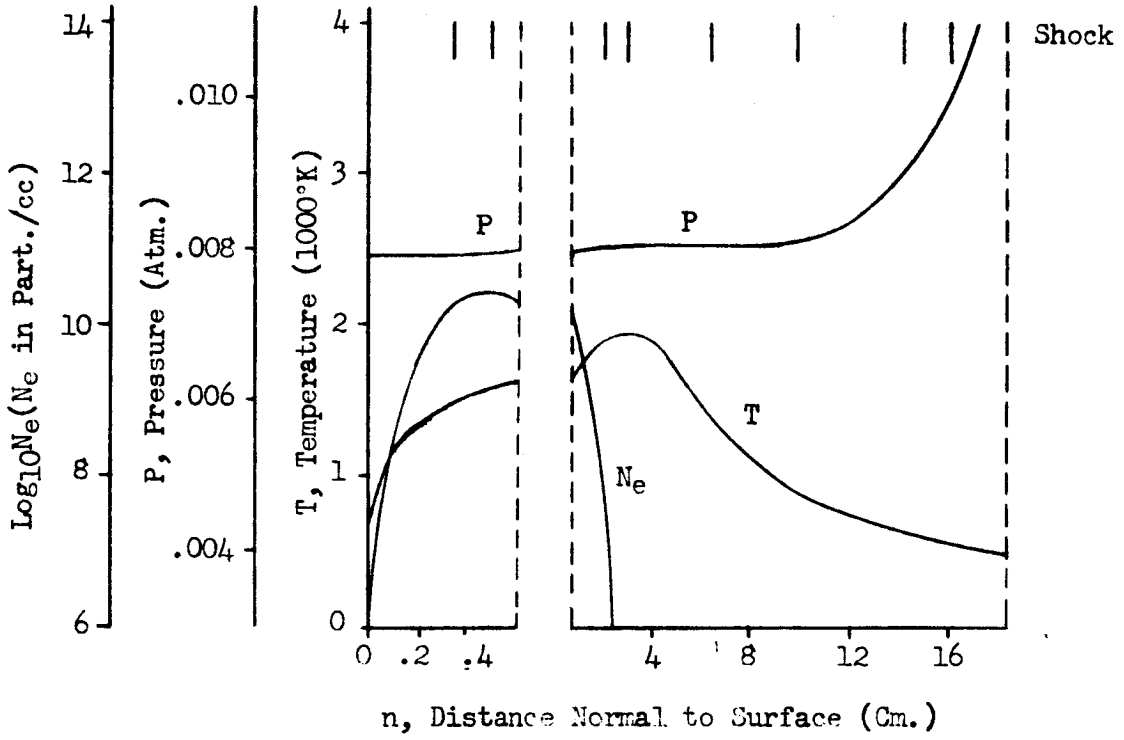

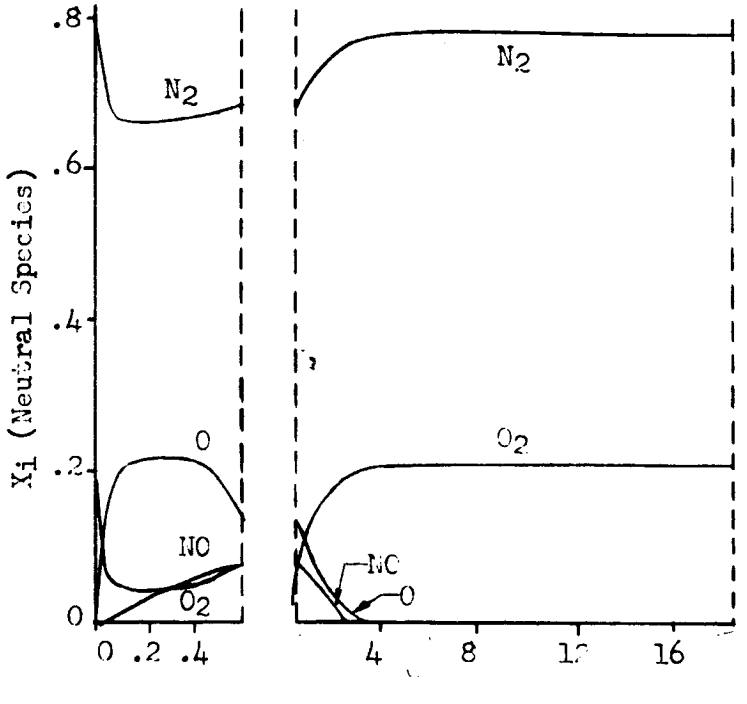

Figure 27i. Flow Field Properties - Case 3, Normal 9

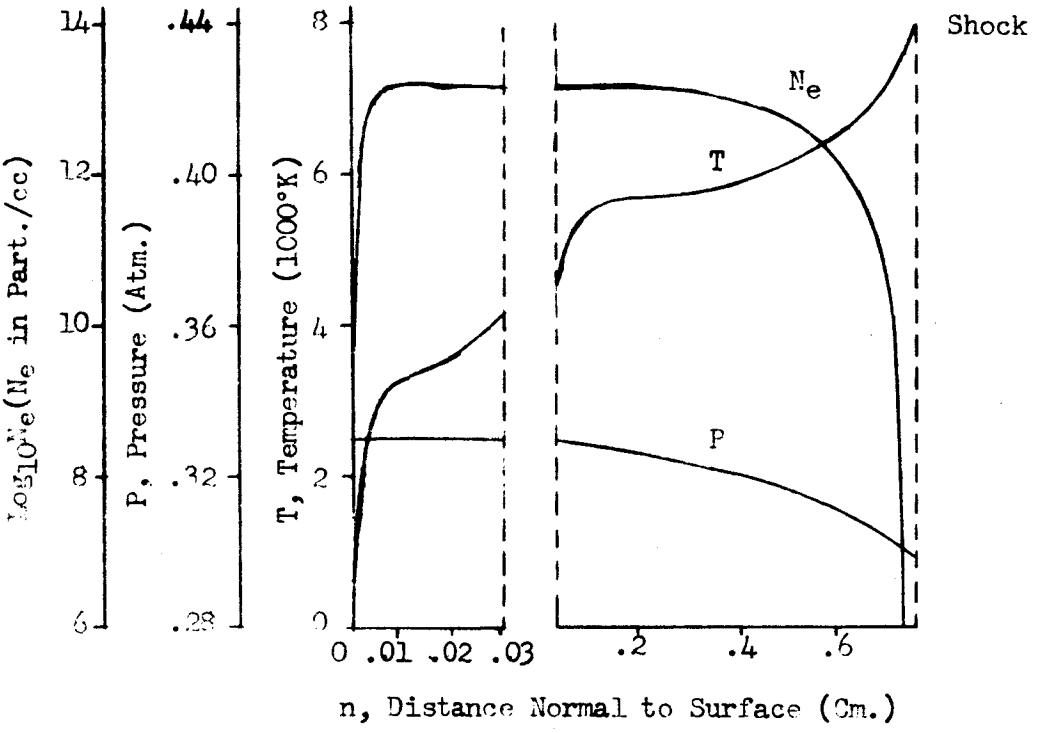

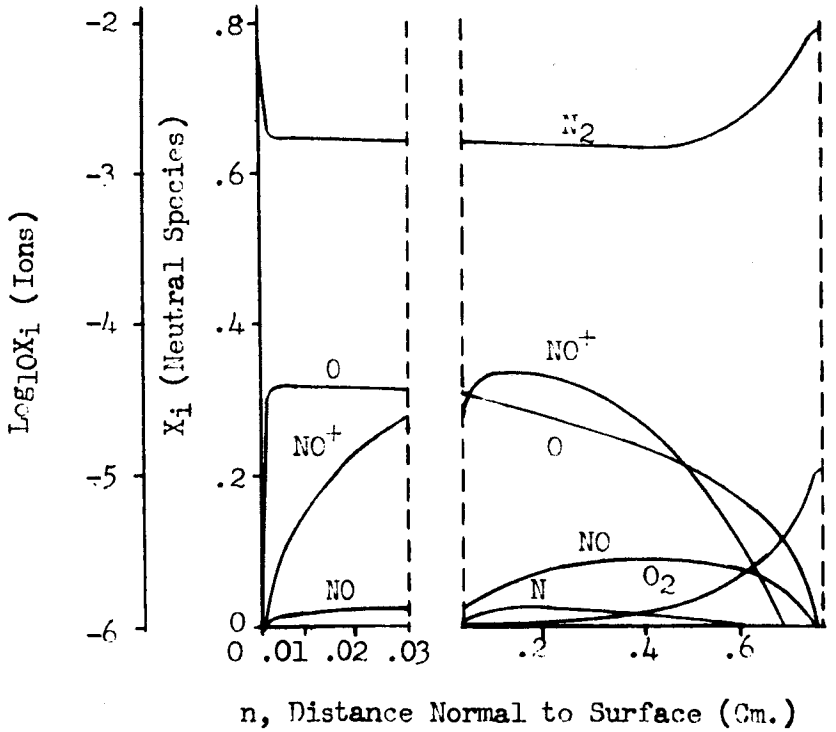

Figure 28a. Flow Field Properties - Case 4, Normal 1

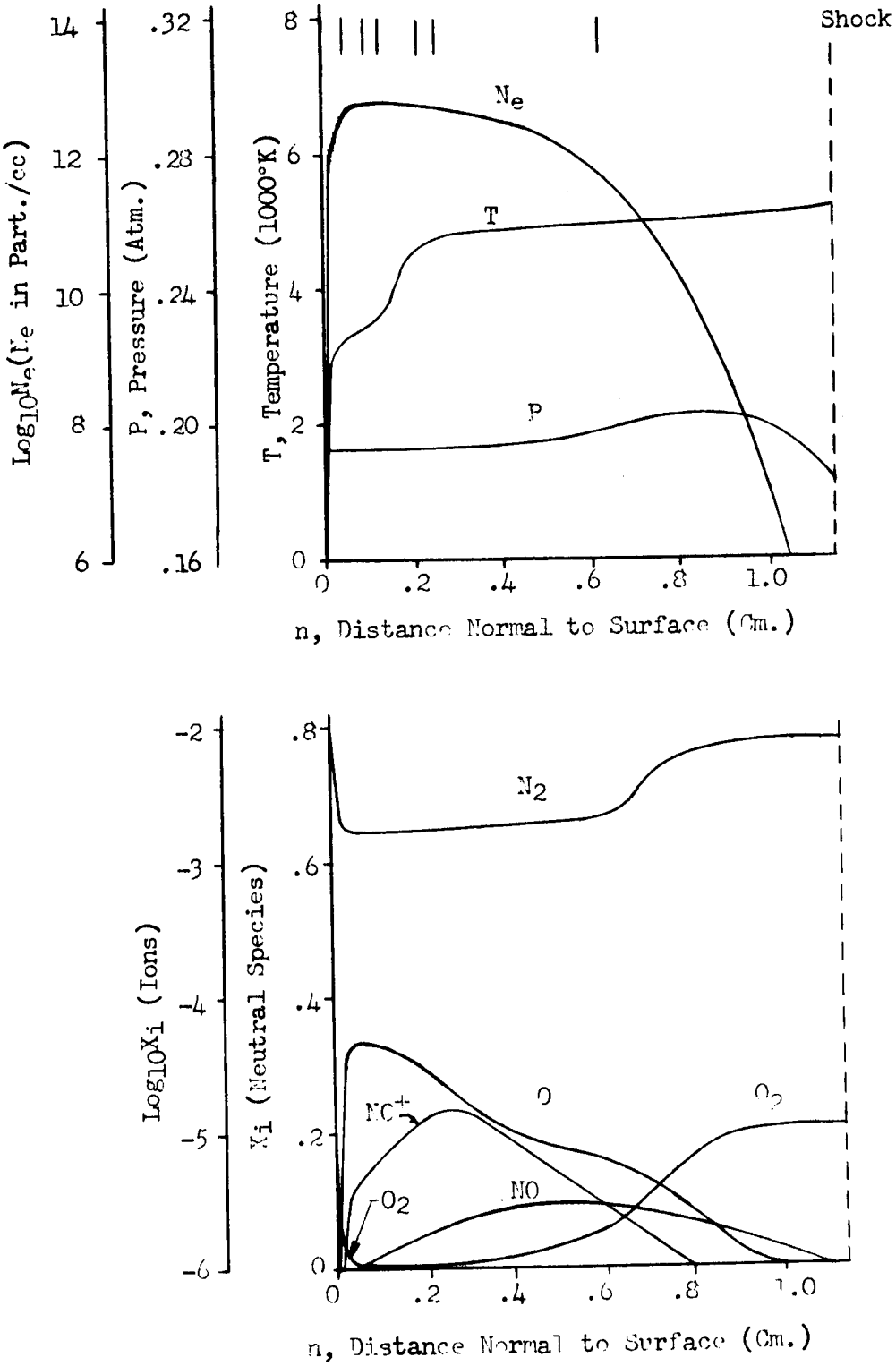

Figure 28b. Flow Field Properties - Case 4, Normal 2

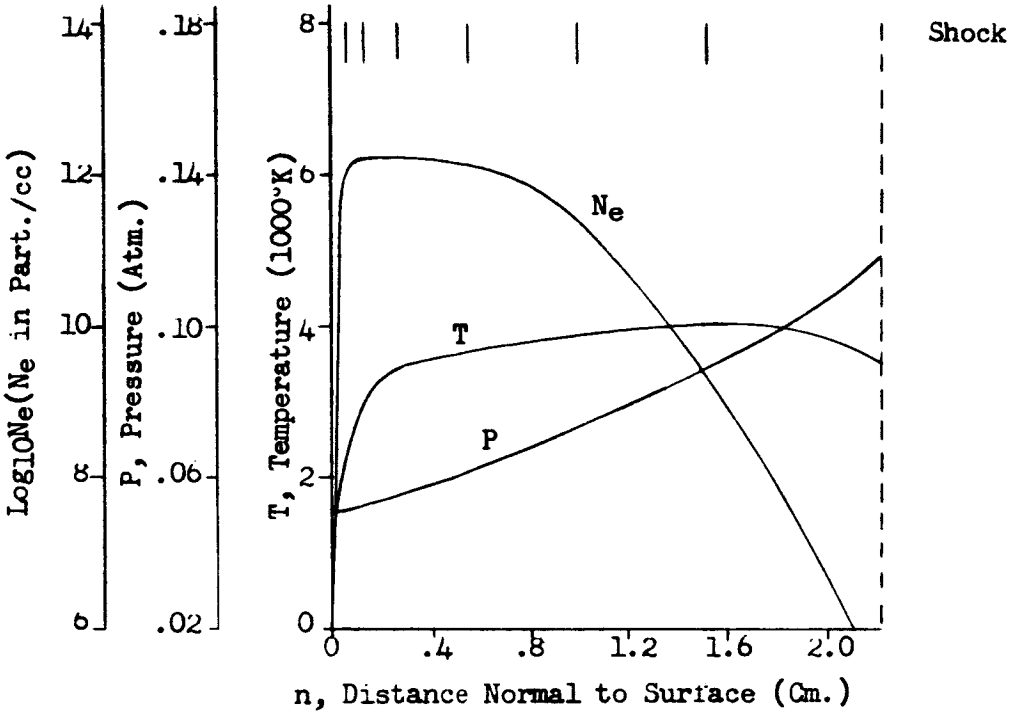

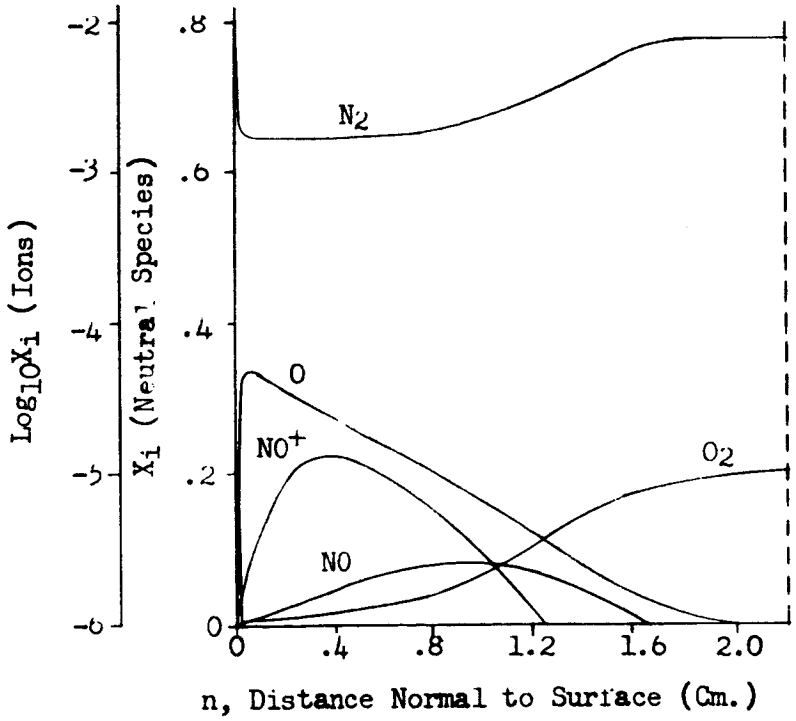

Figure 28c. Flow Field Properties - Case 4, Normal 3

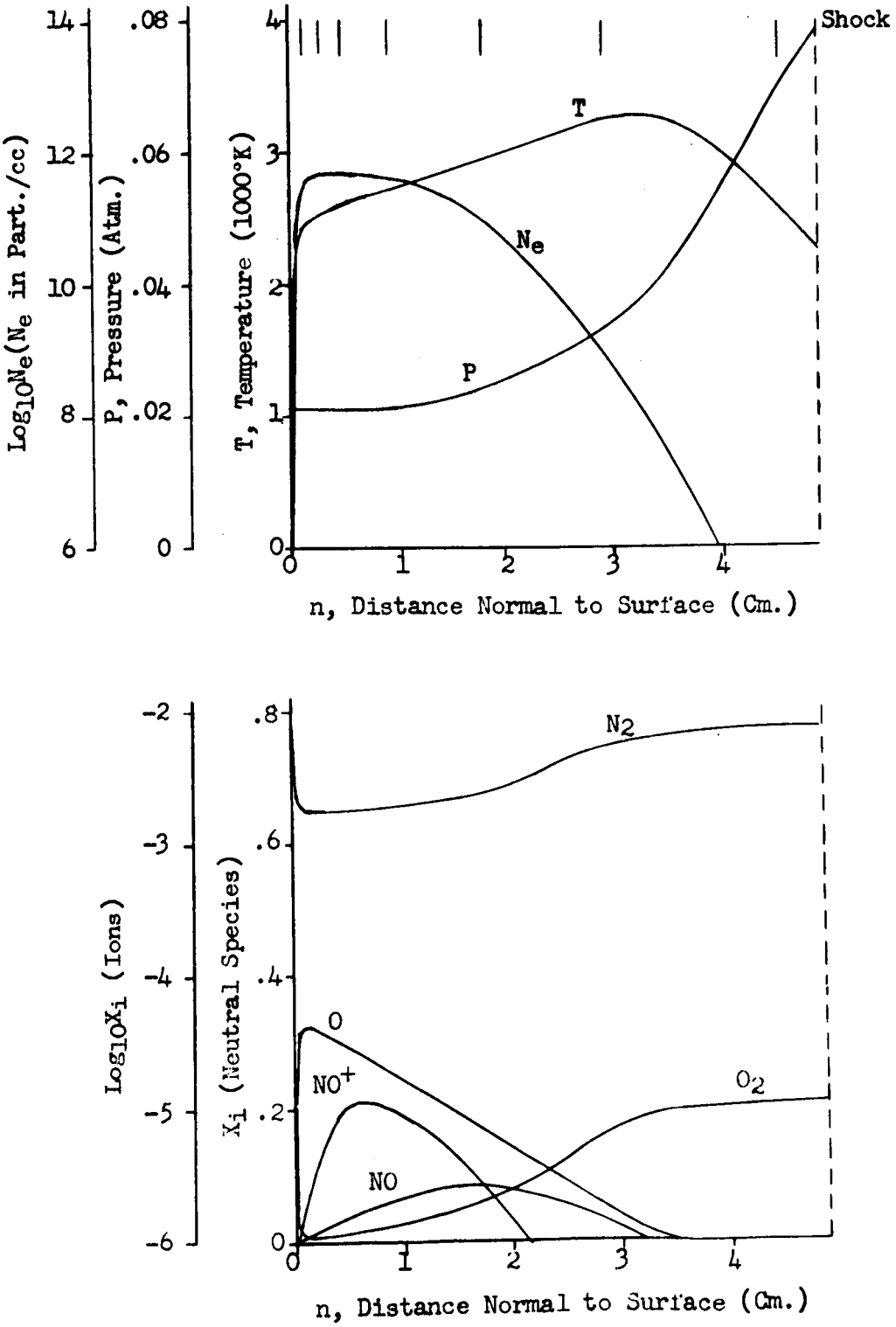

Figure 28d. Flow Field Properties - Case 4, Normal 4

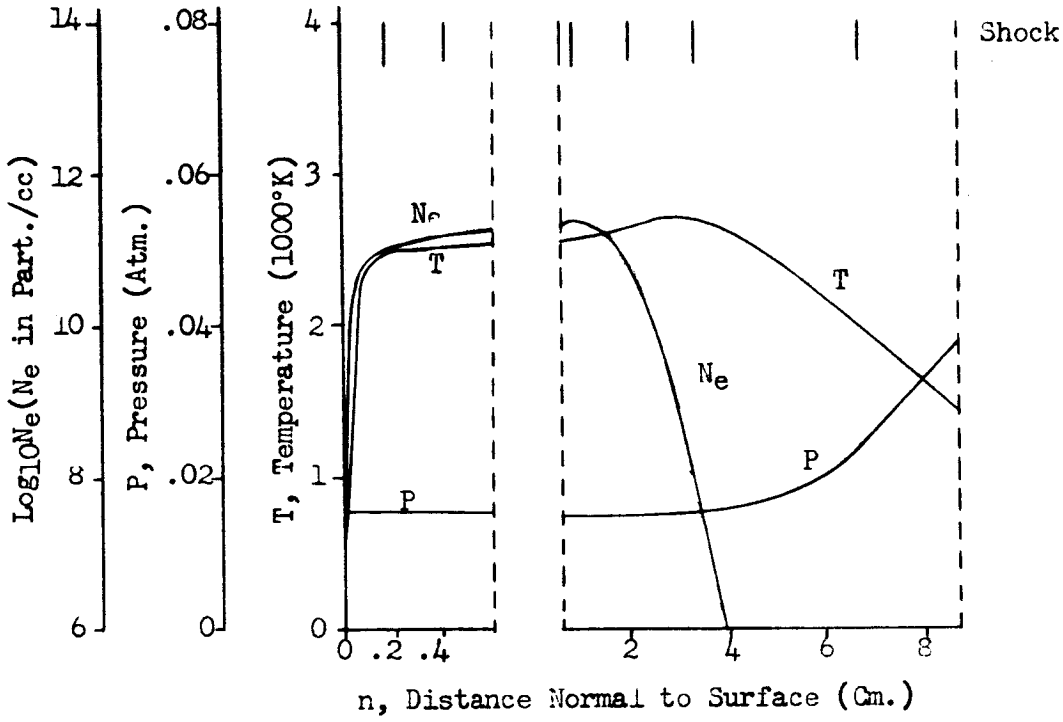

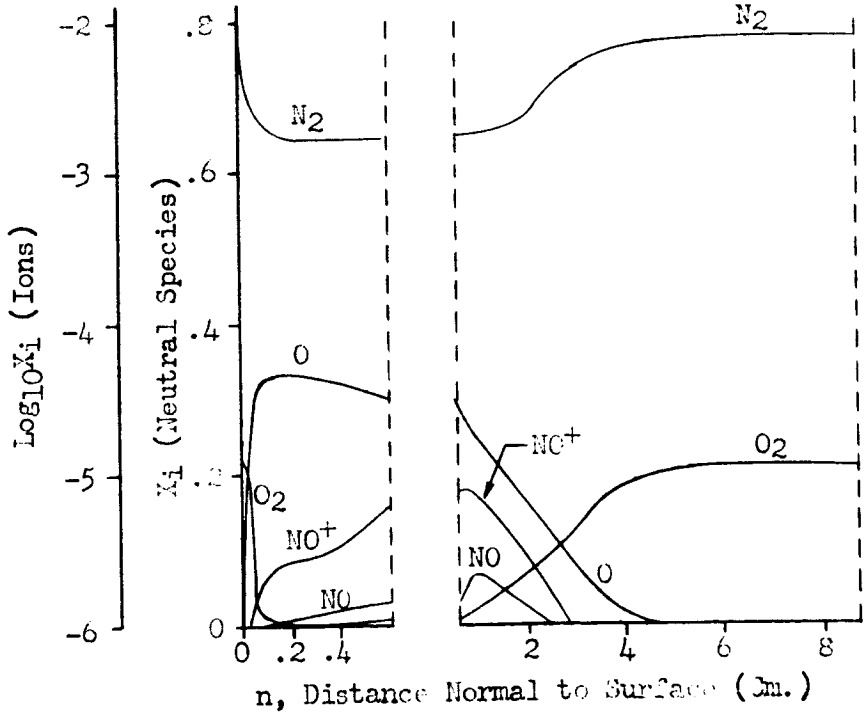

Figure 28e. Flow Field Properties - Case 4, Normal 5

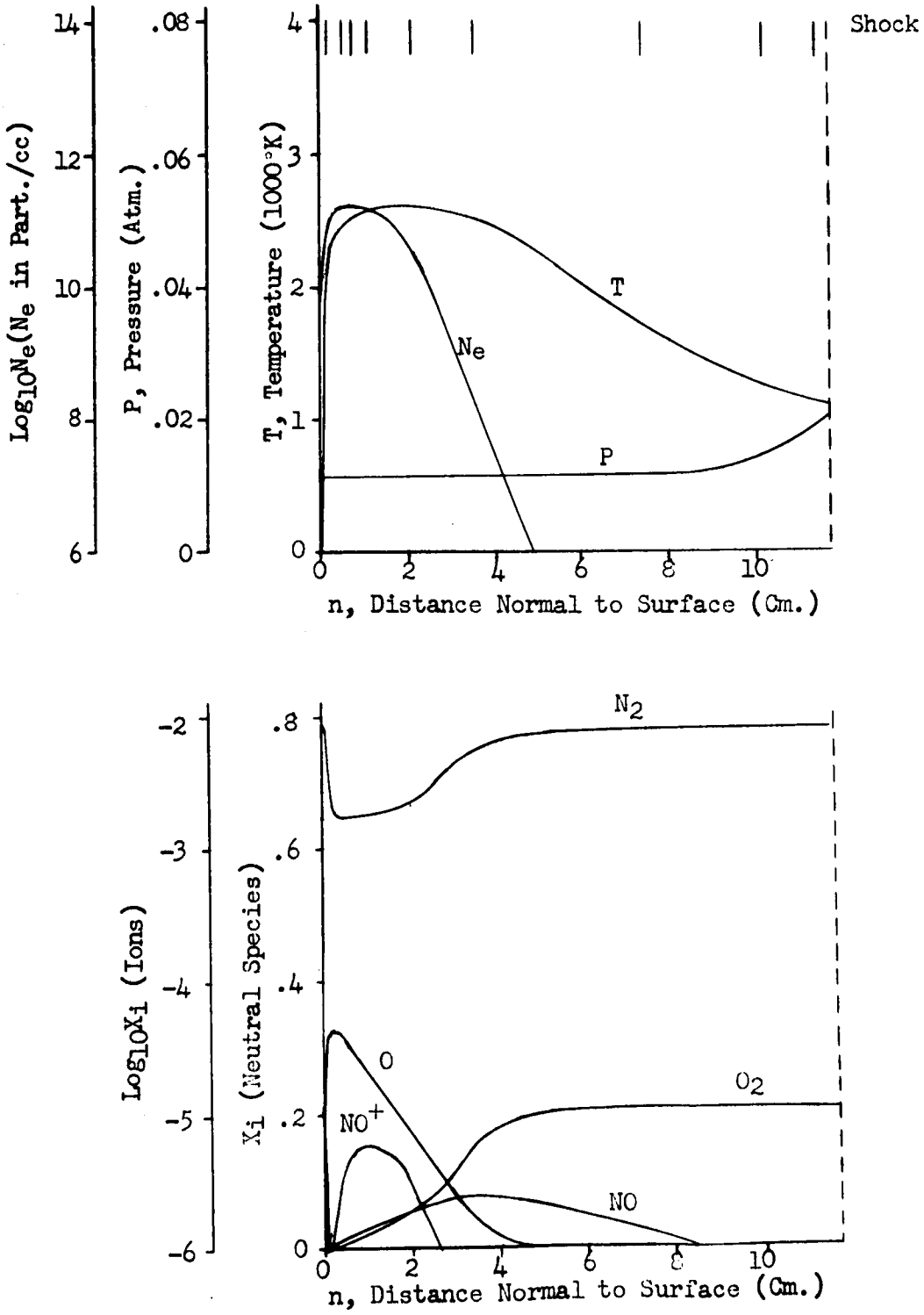

Figure 28f. Flow Field Properties - Case 4, Normal 6

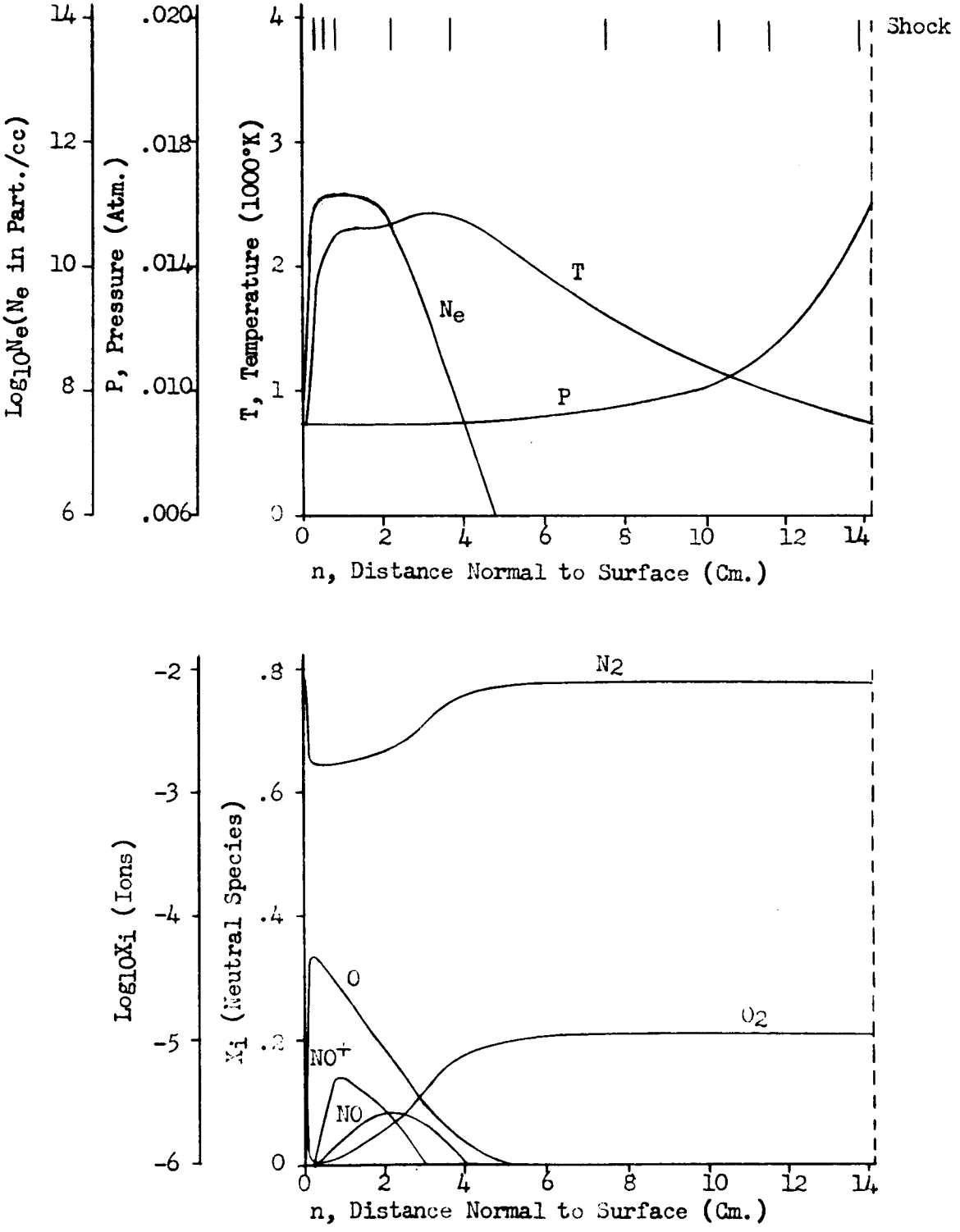

Figure 28g. Flow Field Properties - Case 4, Normal 7

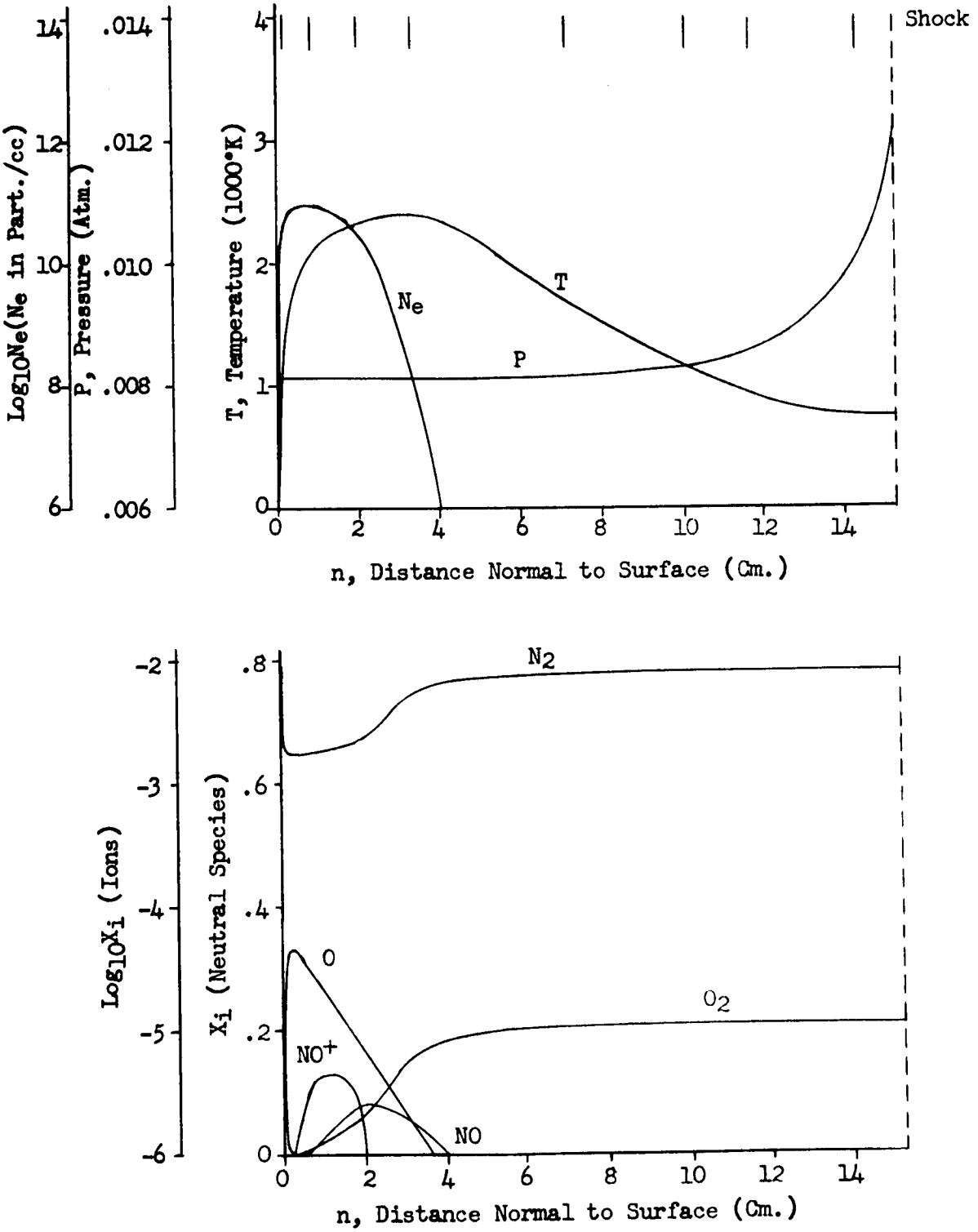

Figure 28h. Flow Field Properties - Case 4, Normal 8

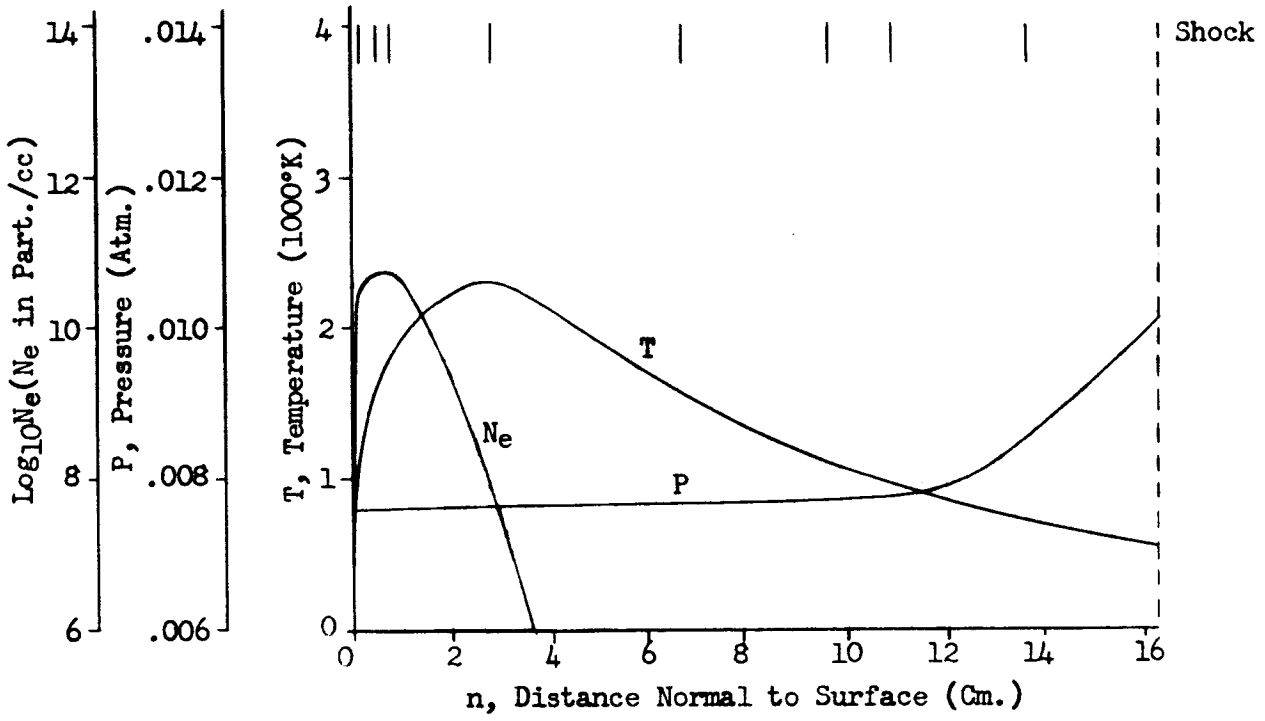

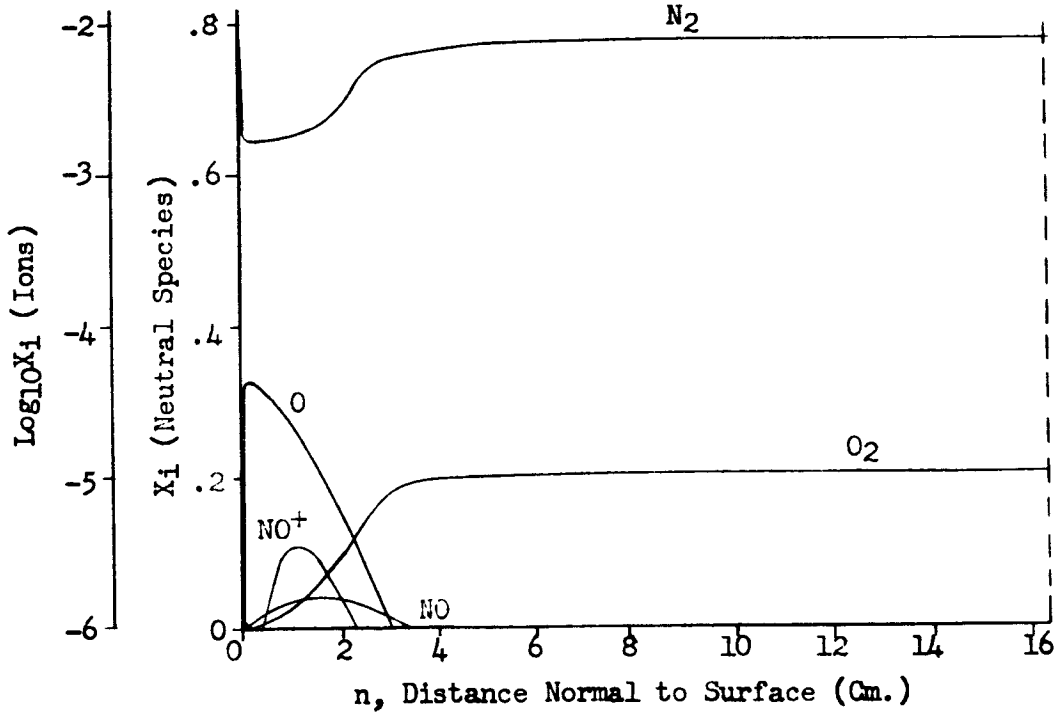

Figure 28i. Flow Field Properties - Case 4, Normal 9

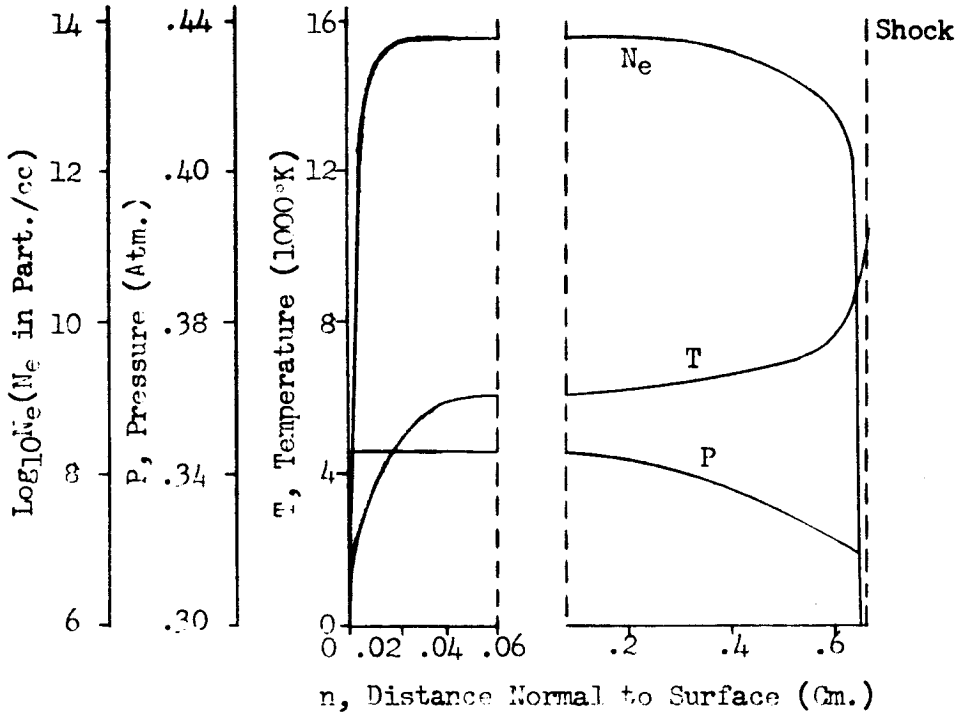

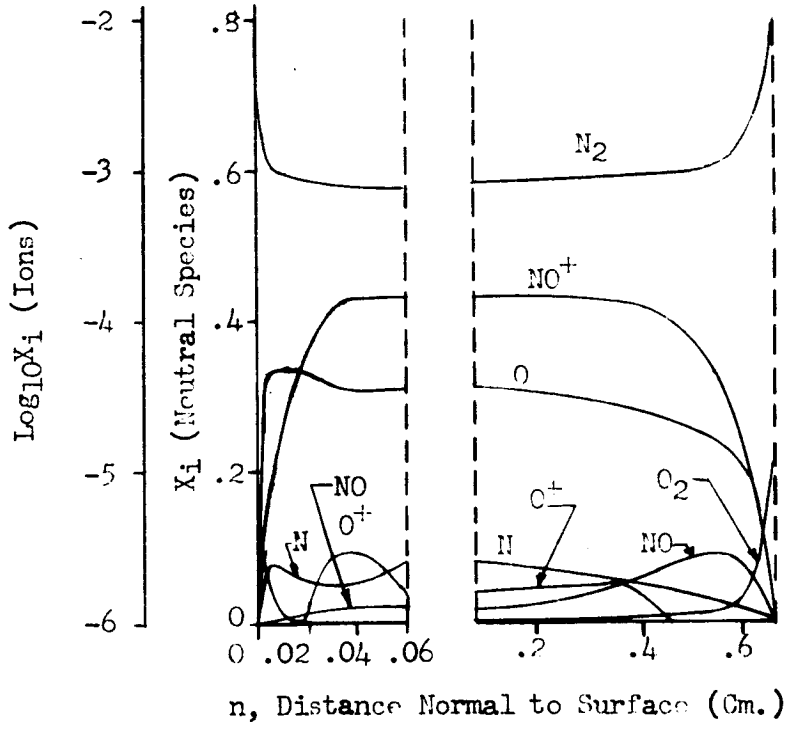

Figure 29a. Flow Field Properties - Case 5, Normal 1

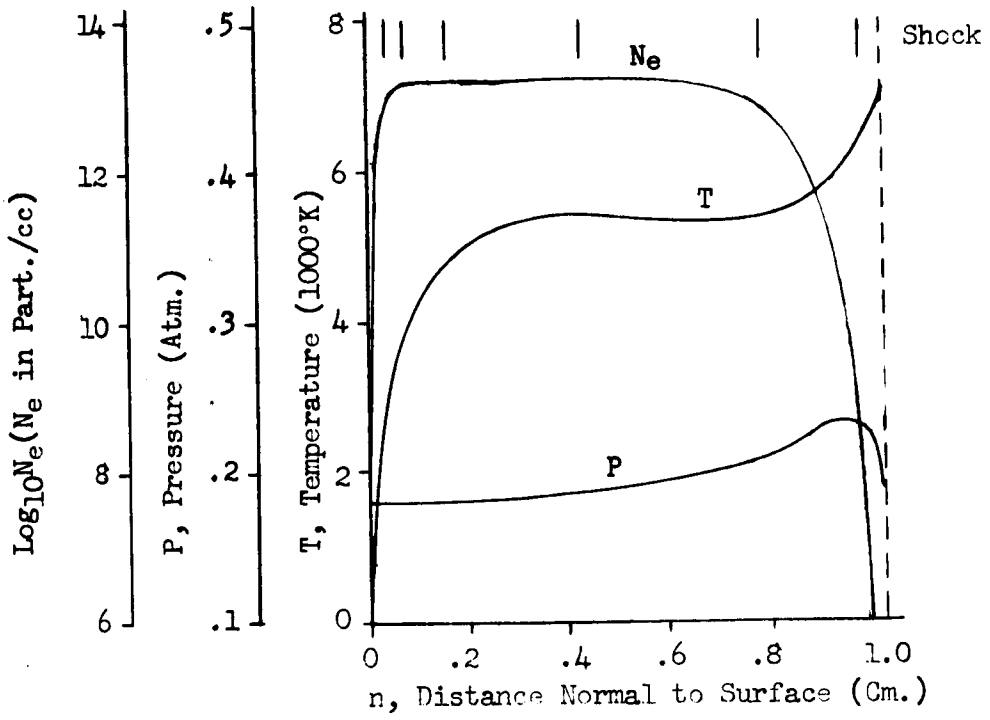

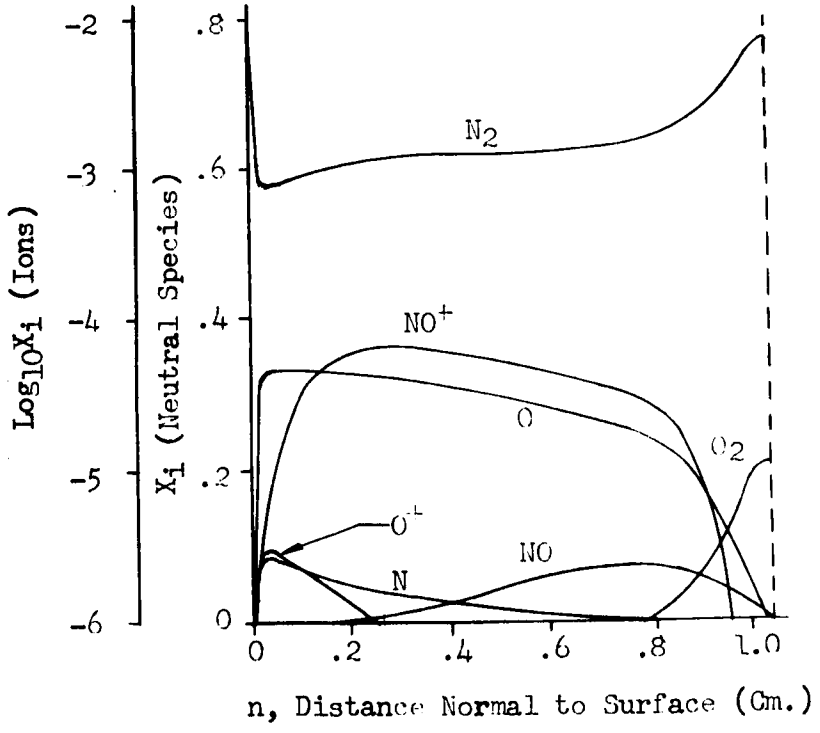

Figure 29b. Flow Field Properties - Case 5, Normal 2

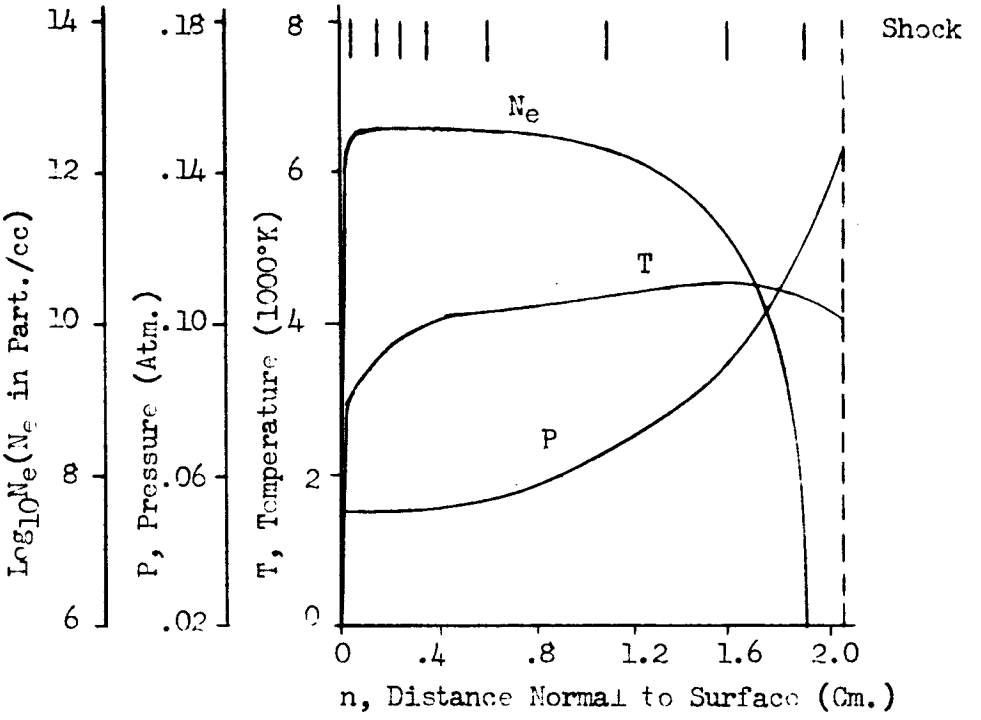

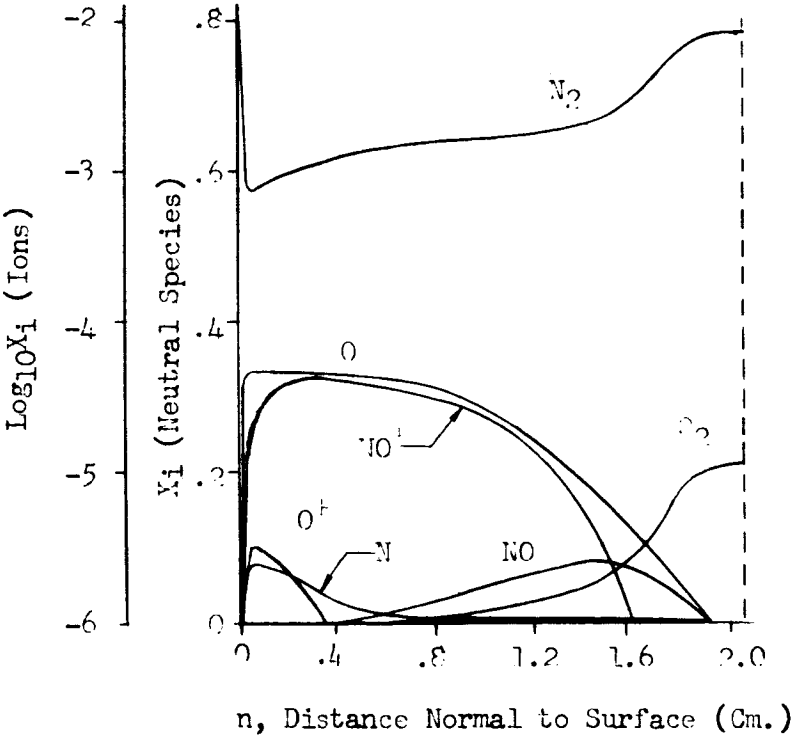

Figure 29c. Flow Field Properties - Case 5, Normal 3

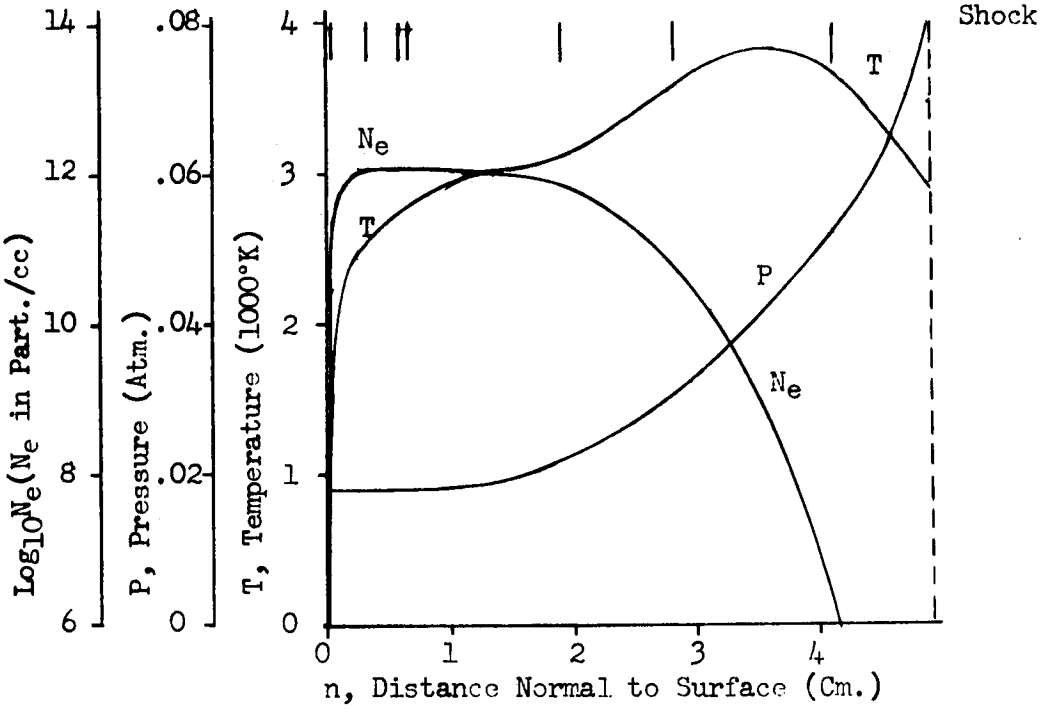

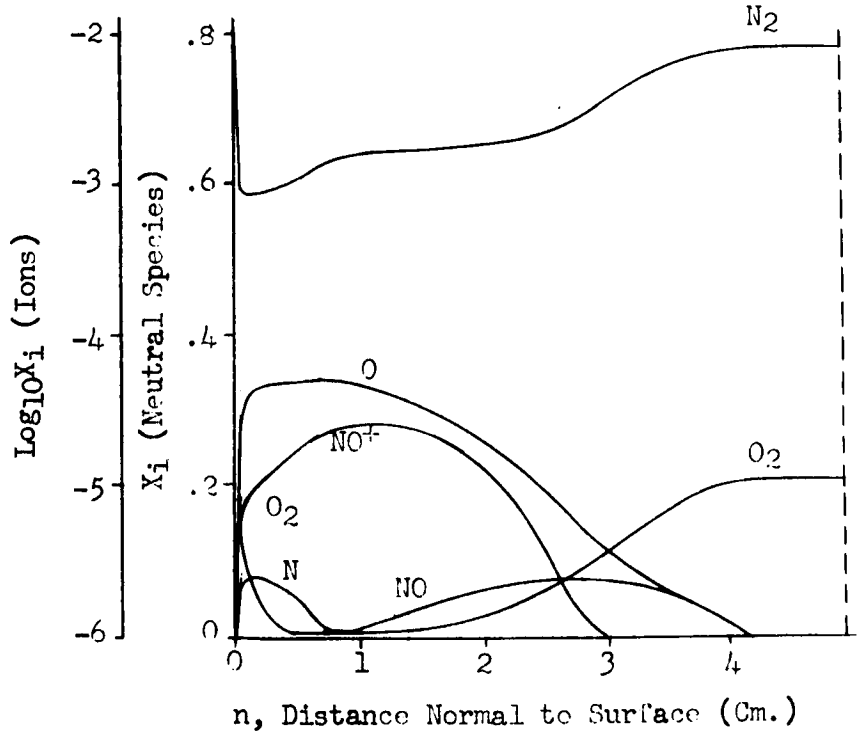

Figure 29d. Flow Field Properties - Case 5, Normal 4

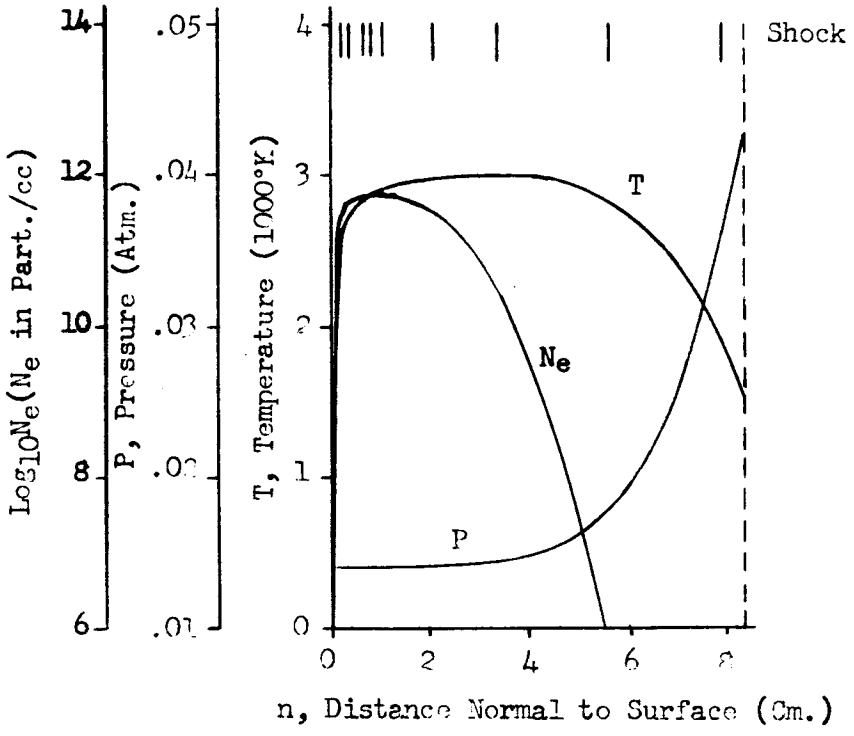

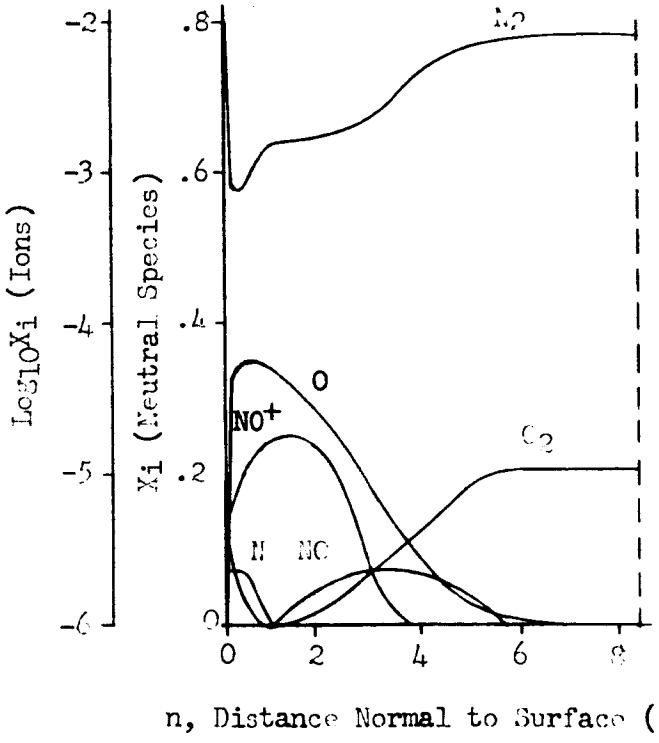

Figure 29e. Flow Field Properties - Case 5, Normal 5

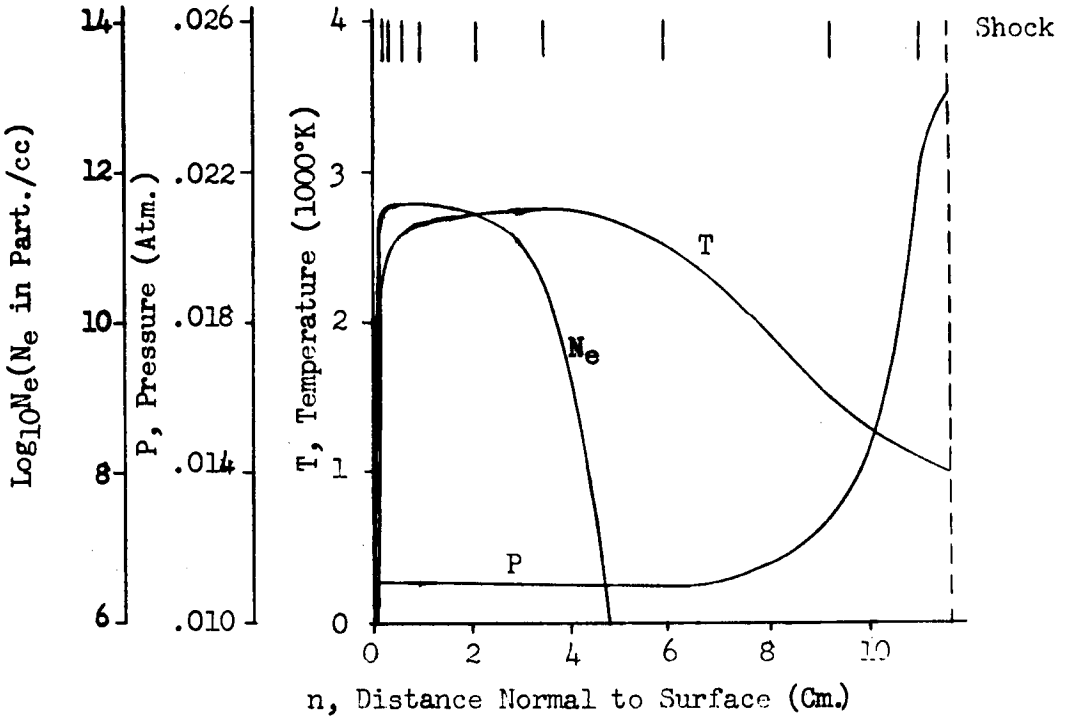

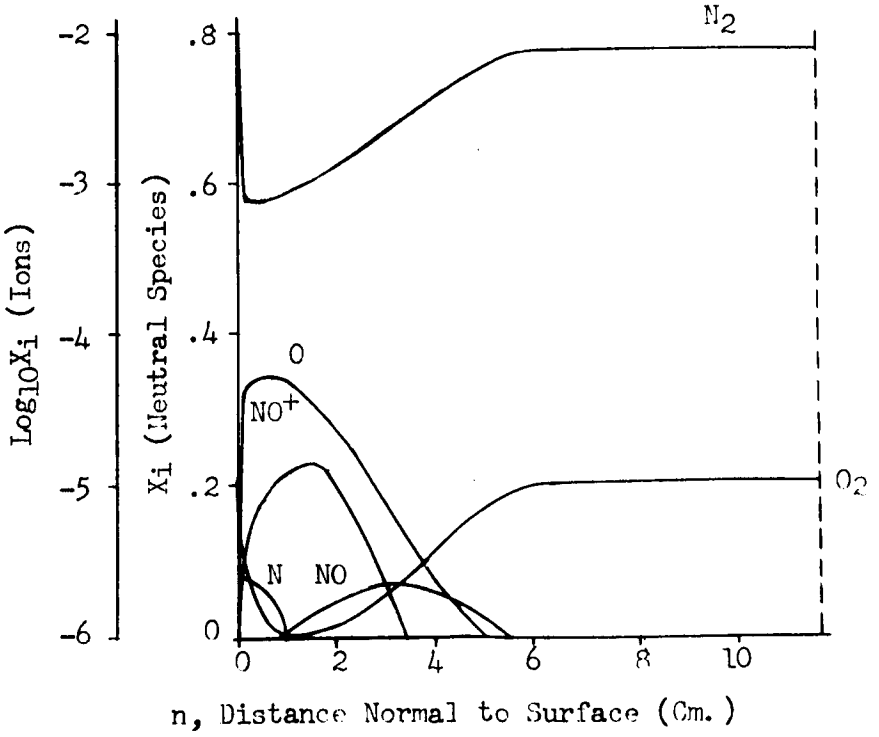

Figure 29f. Flow Field Properties - Case 5, Normal 6

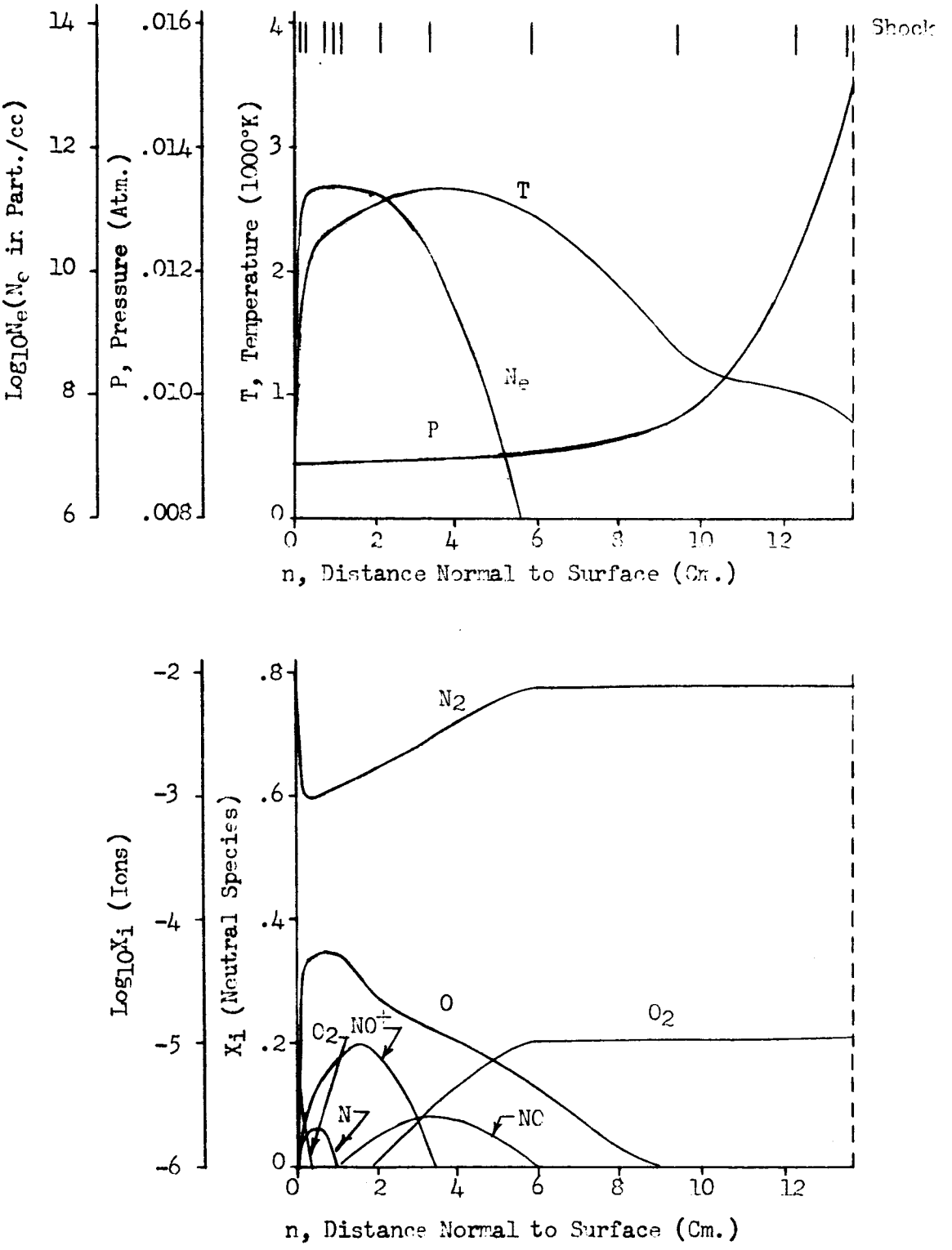

Figure 29g. Flow Field Properties - Case 5, Normal 7

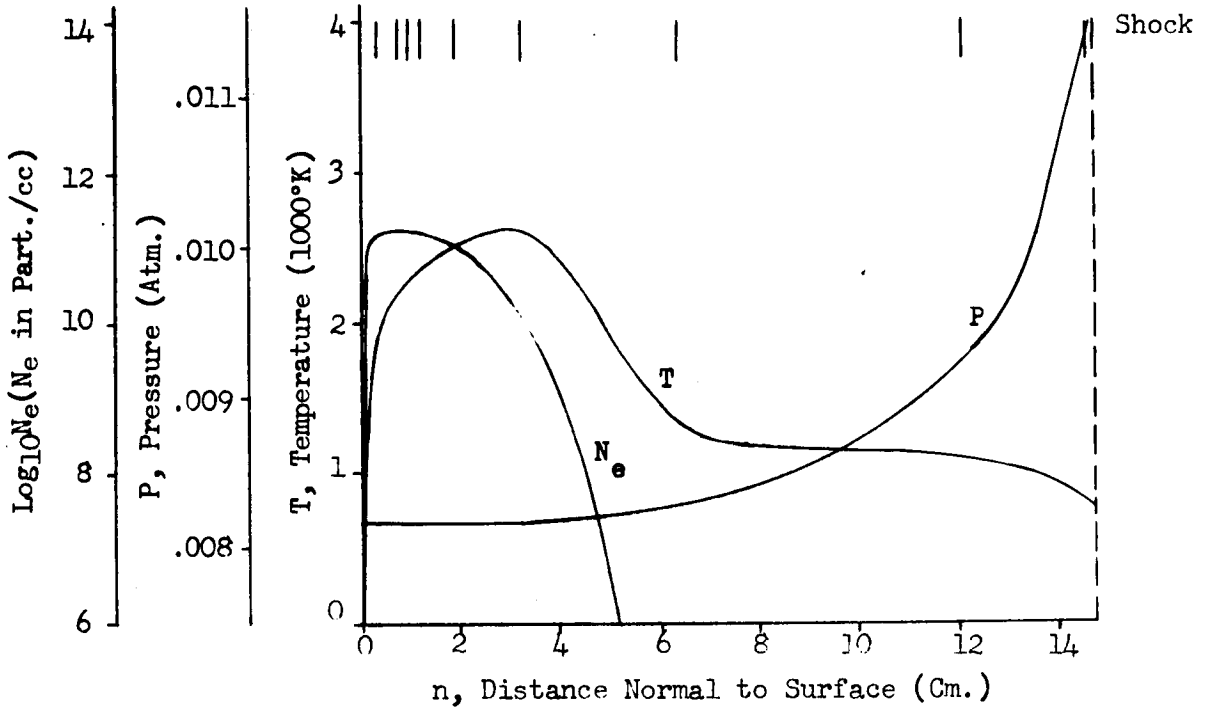

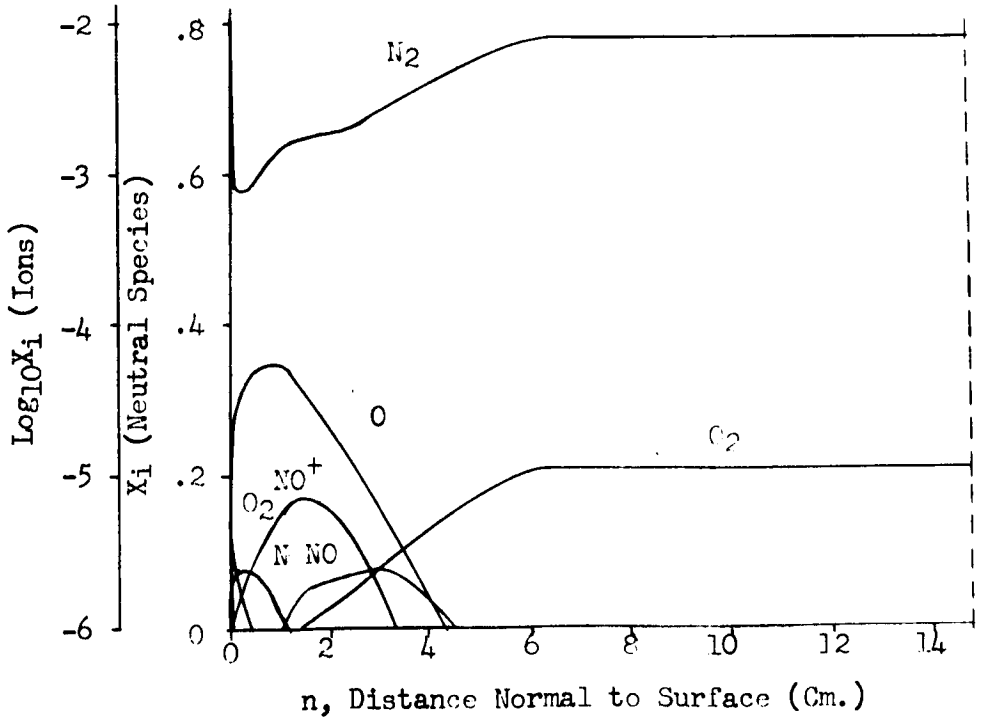

Figure 29h. Flow Field Properties - Case 5, Normal 8

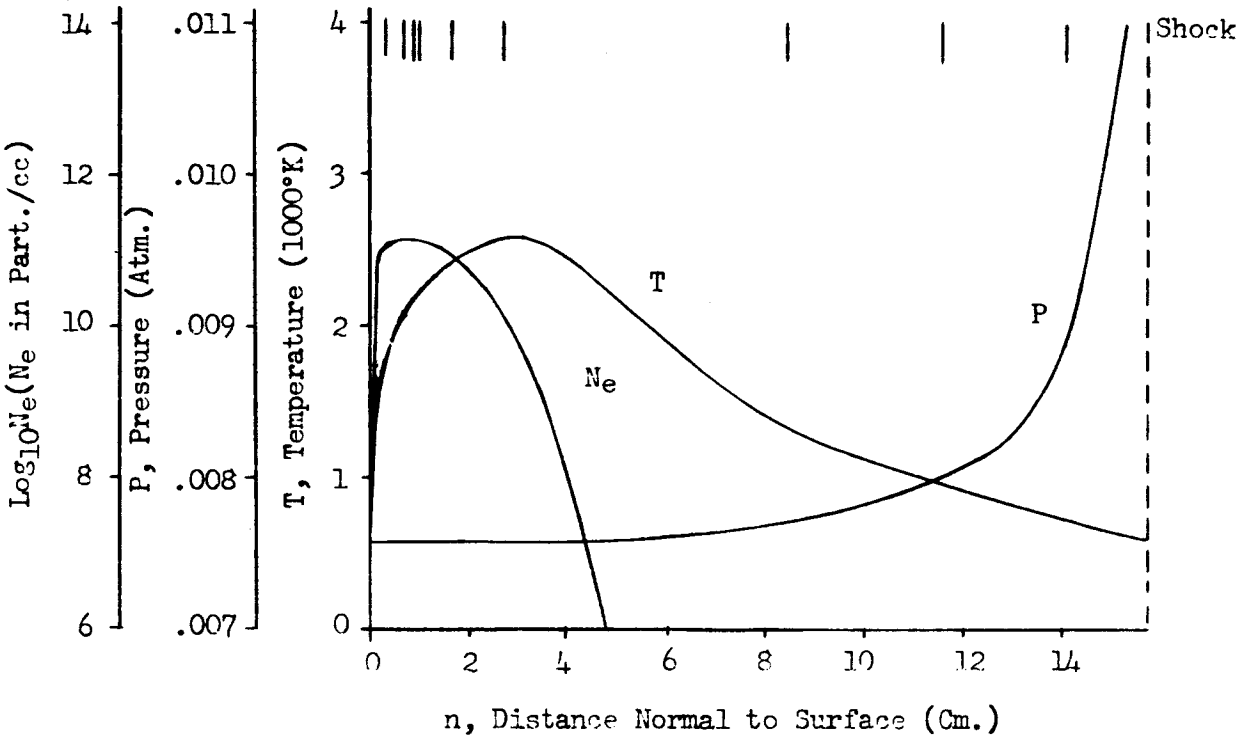

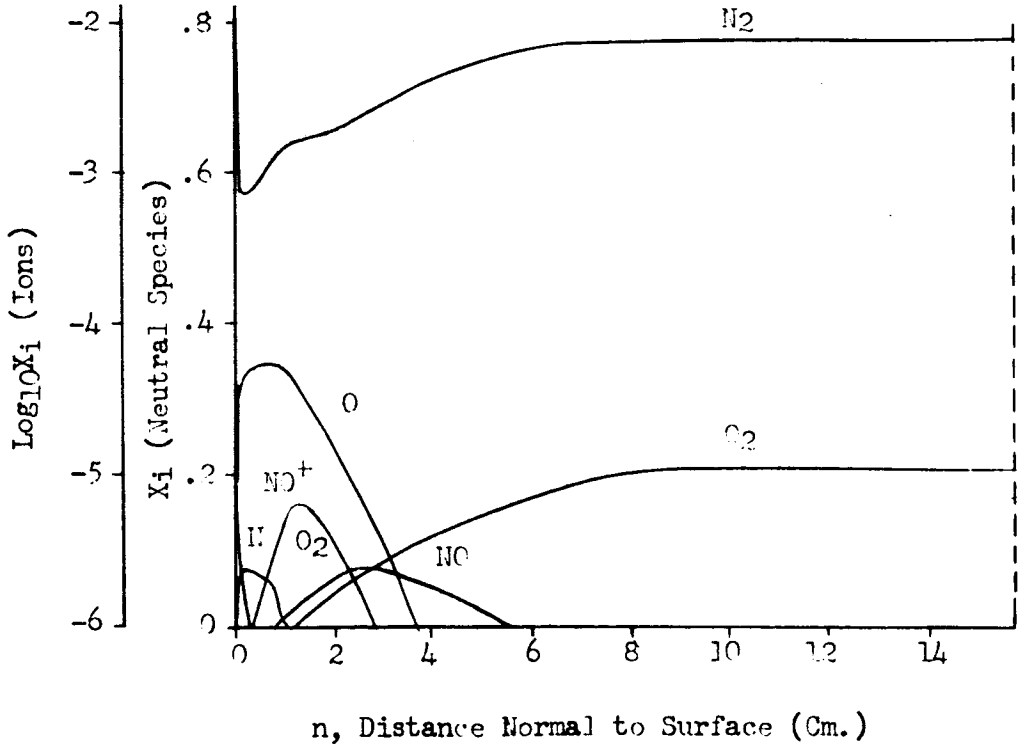

Figure 29i. Flow Field Properties - Case 5, Normal 9

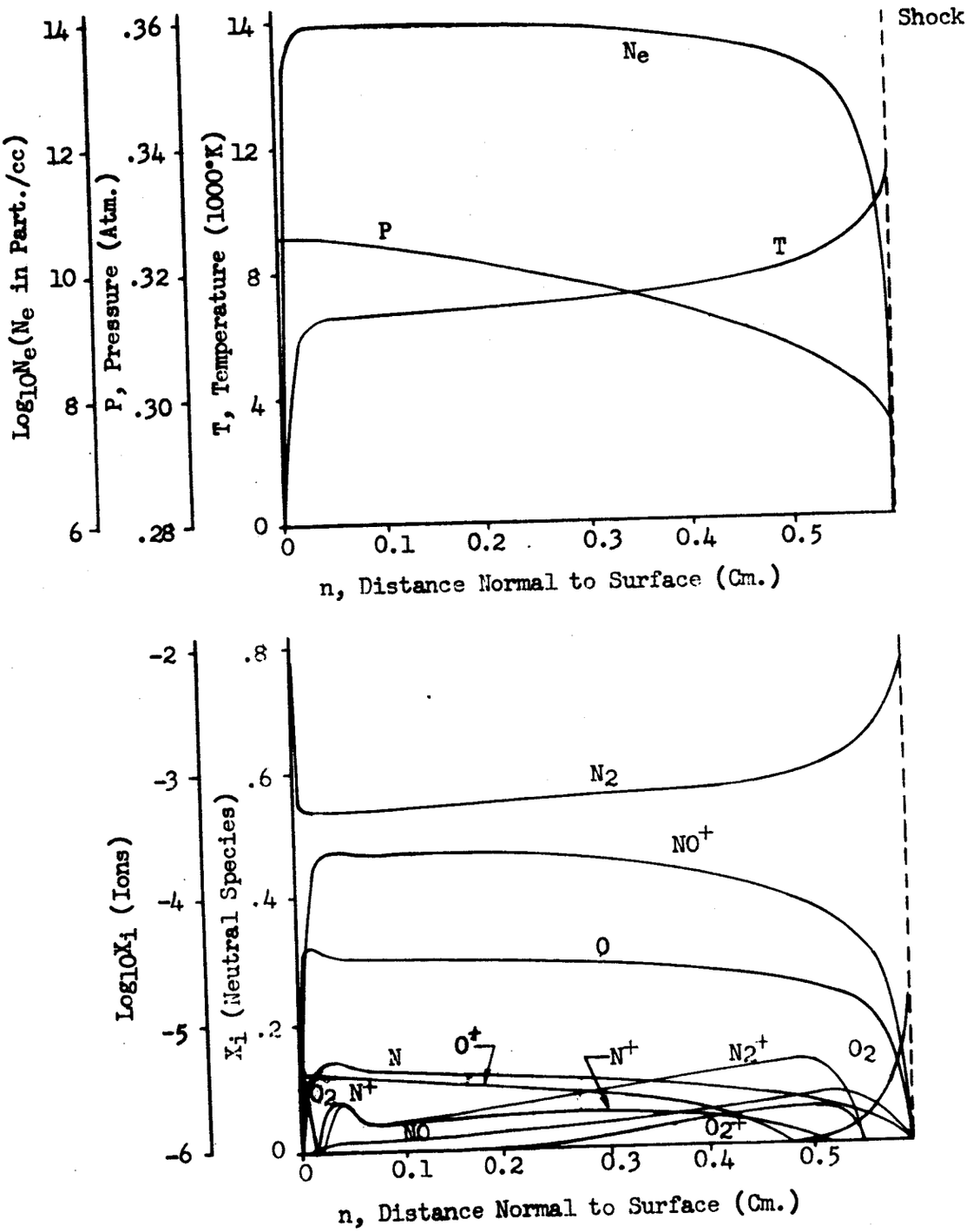

Figure 30a. Flow Field Properties - Case 6, Normal 1

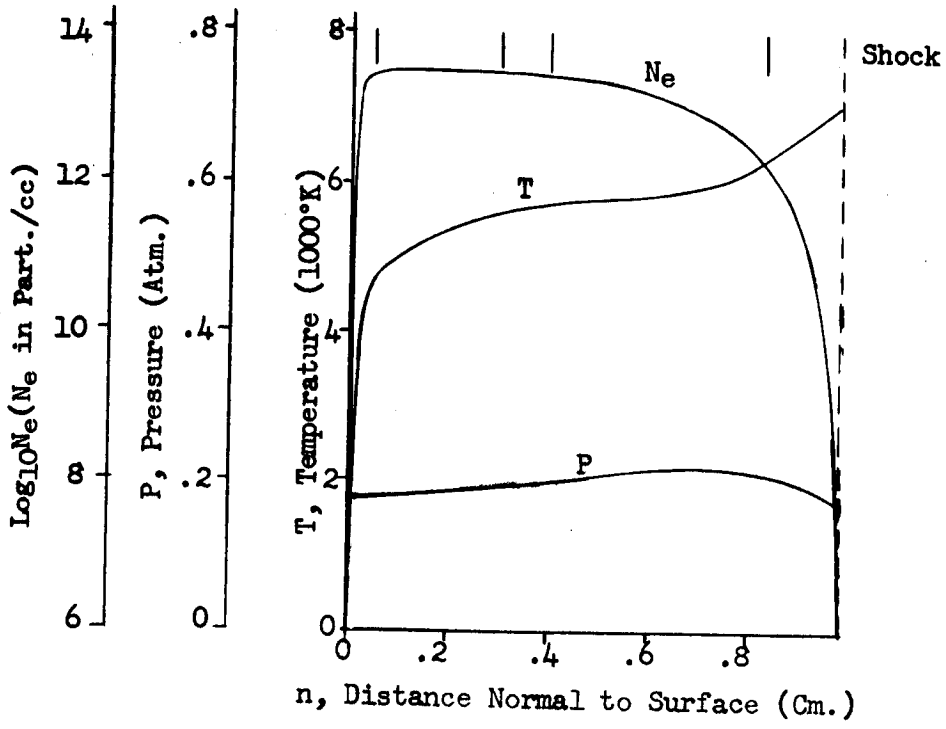

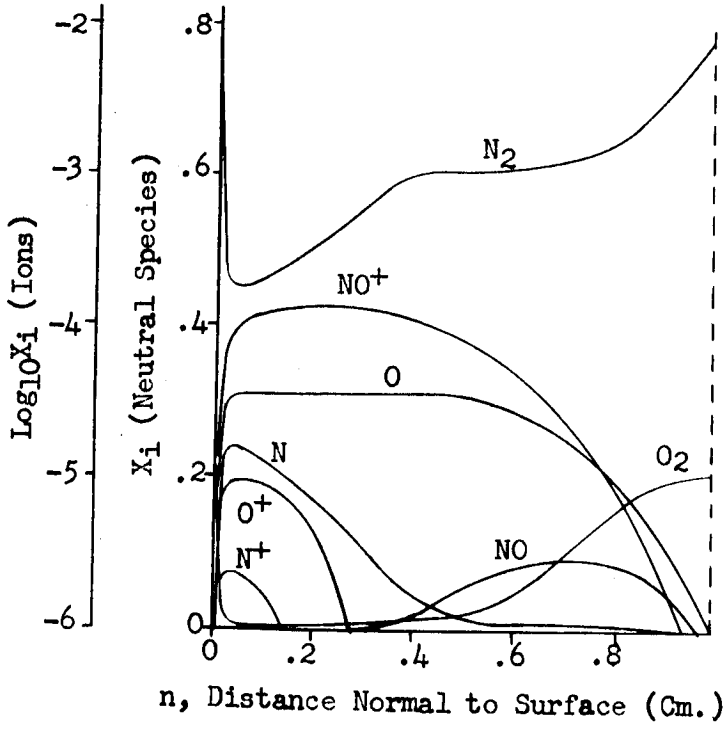

Figure 30b. Flow Field Properties - Case 6, Normal 2

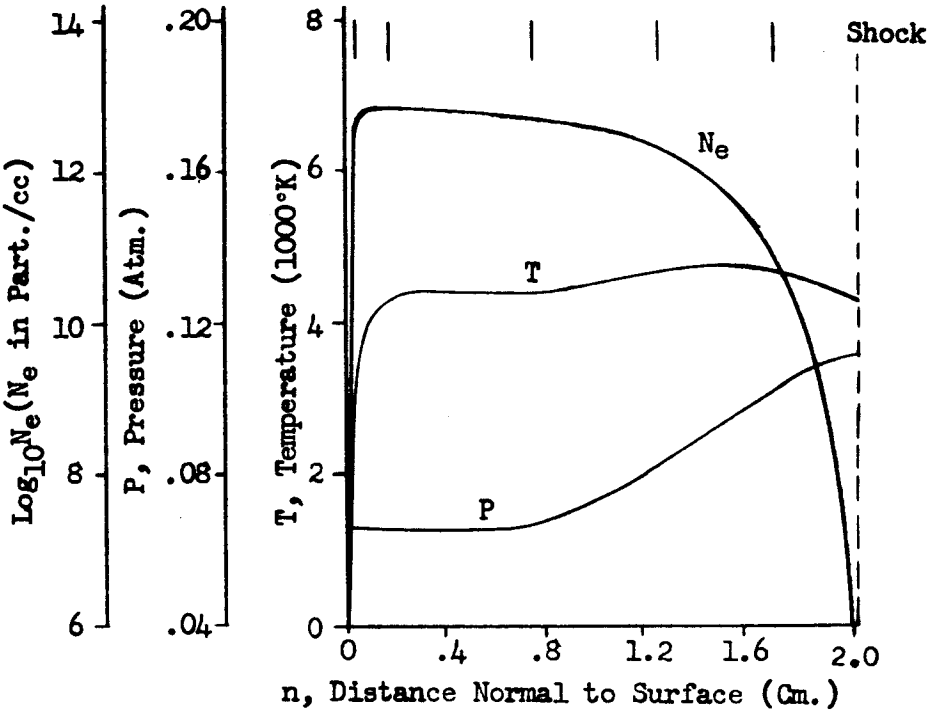

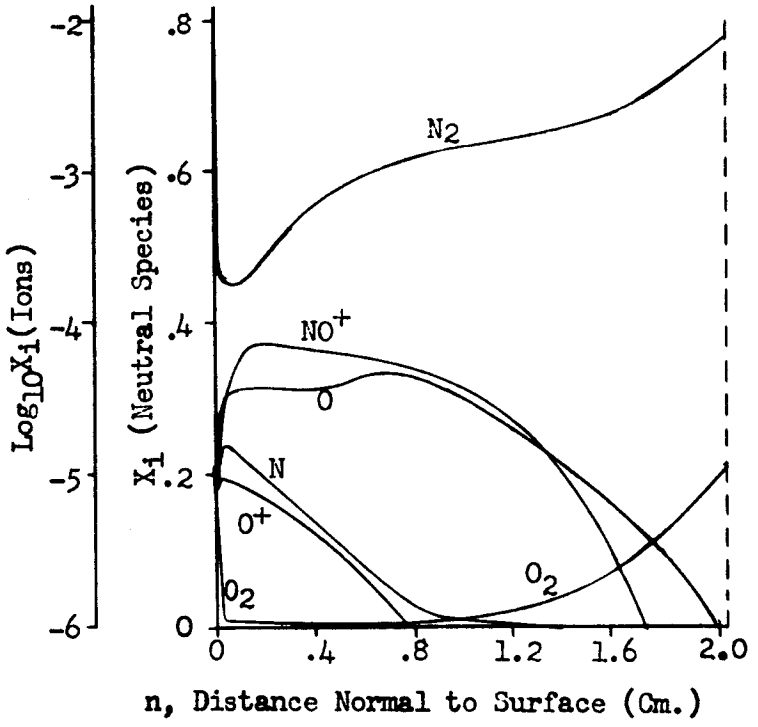

Figure 30c. Flow Field Properties - Case 6, Normal 3

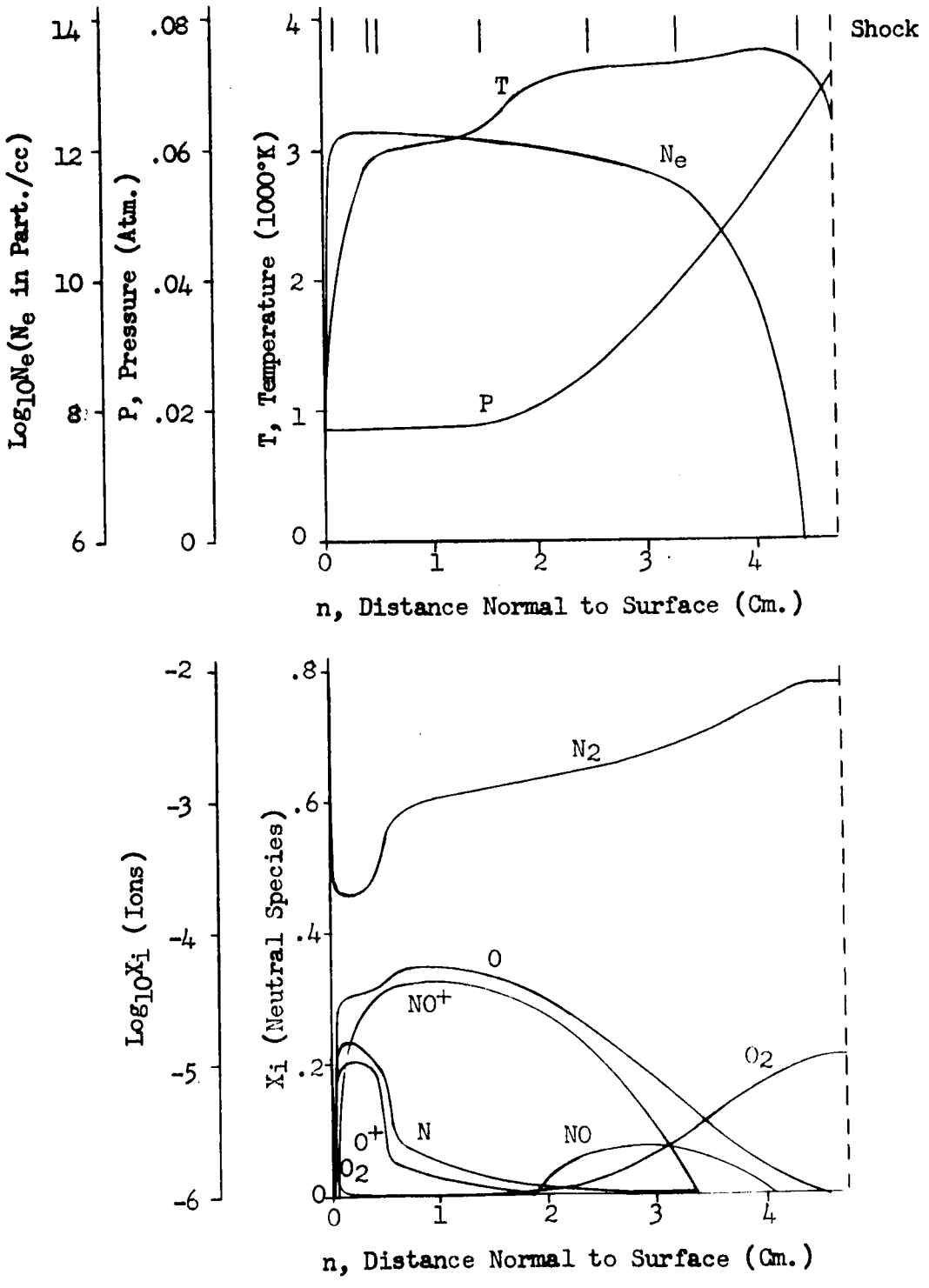

Figure 30d. Flow Field Properties - Case 6, Normal 4

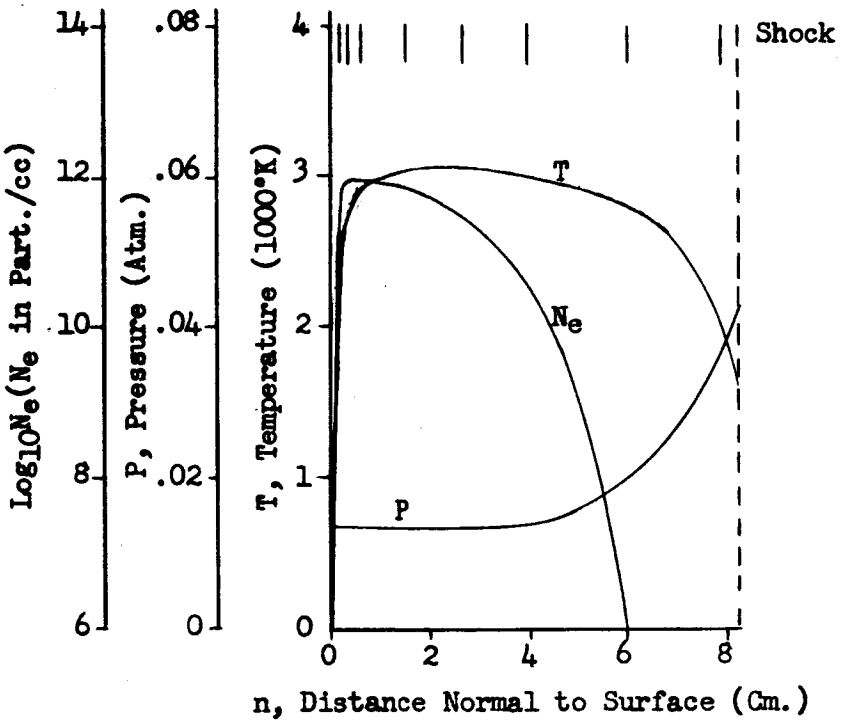

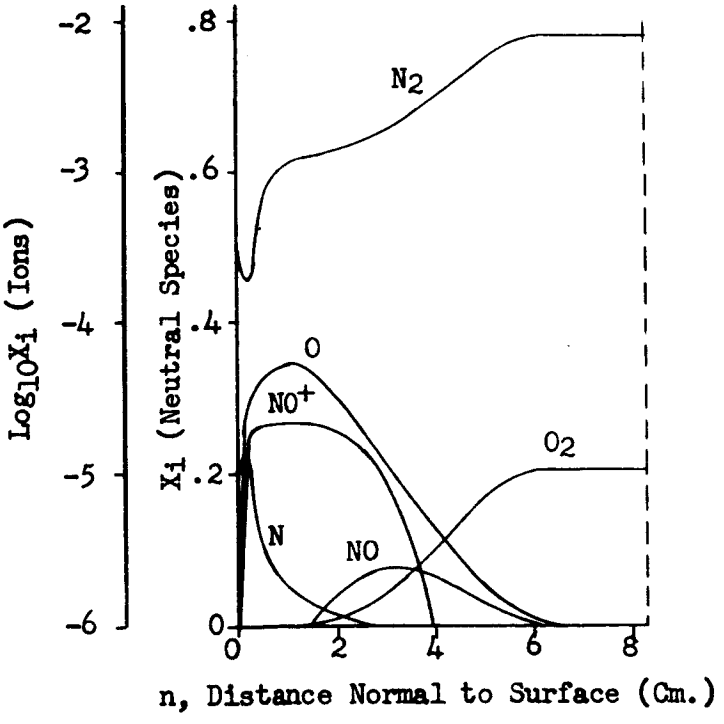

Figure 30e. Flow Field Properties - Case 6, Normal 5

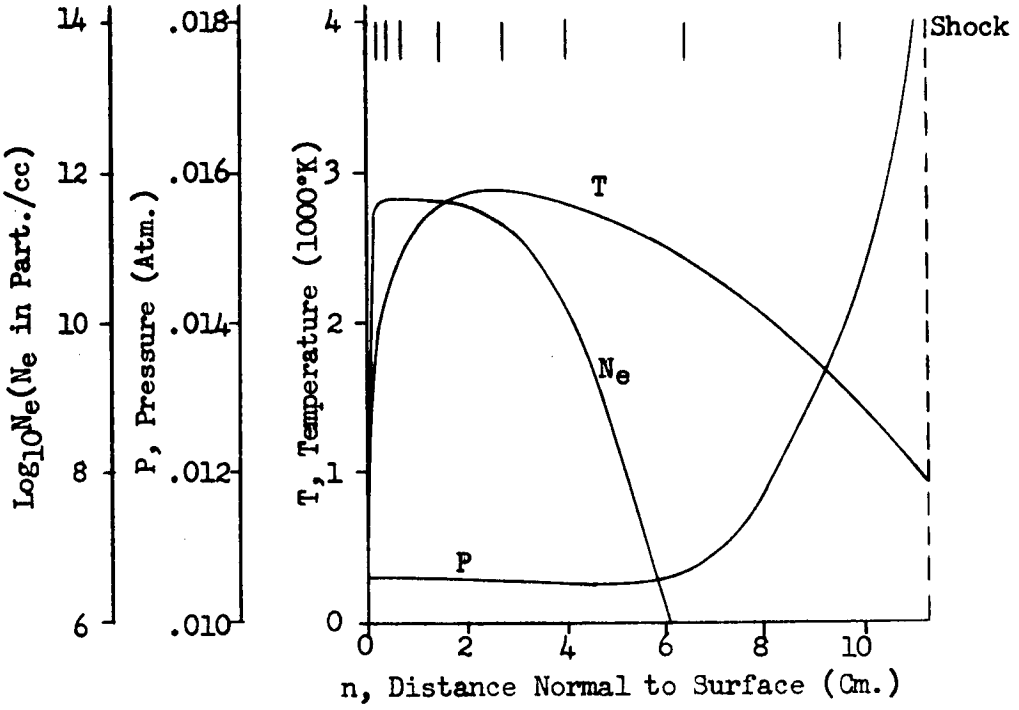

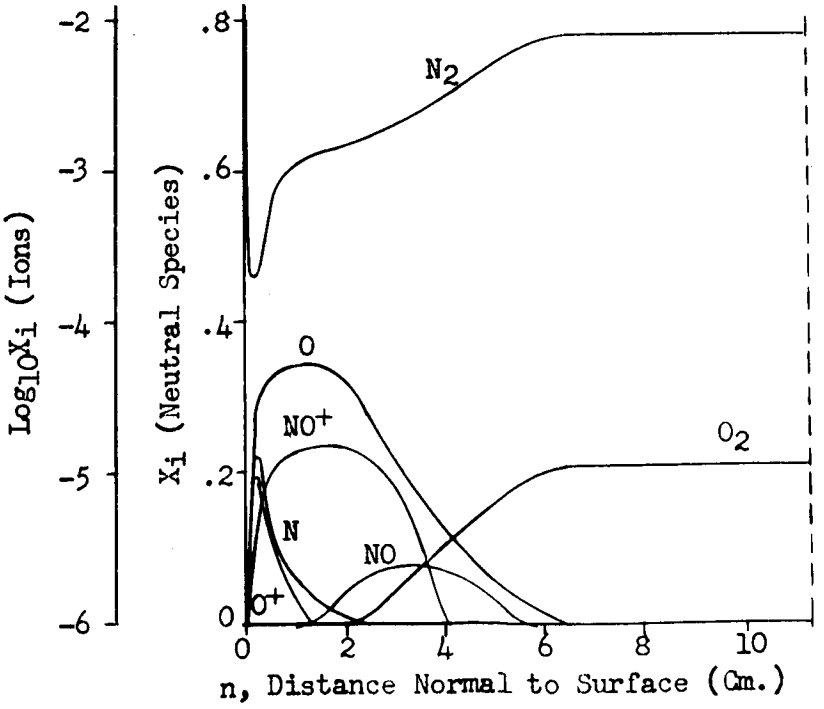

Figure 30f. Flow Field Properties - Case 6, Normal 6

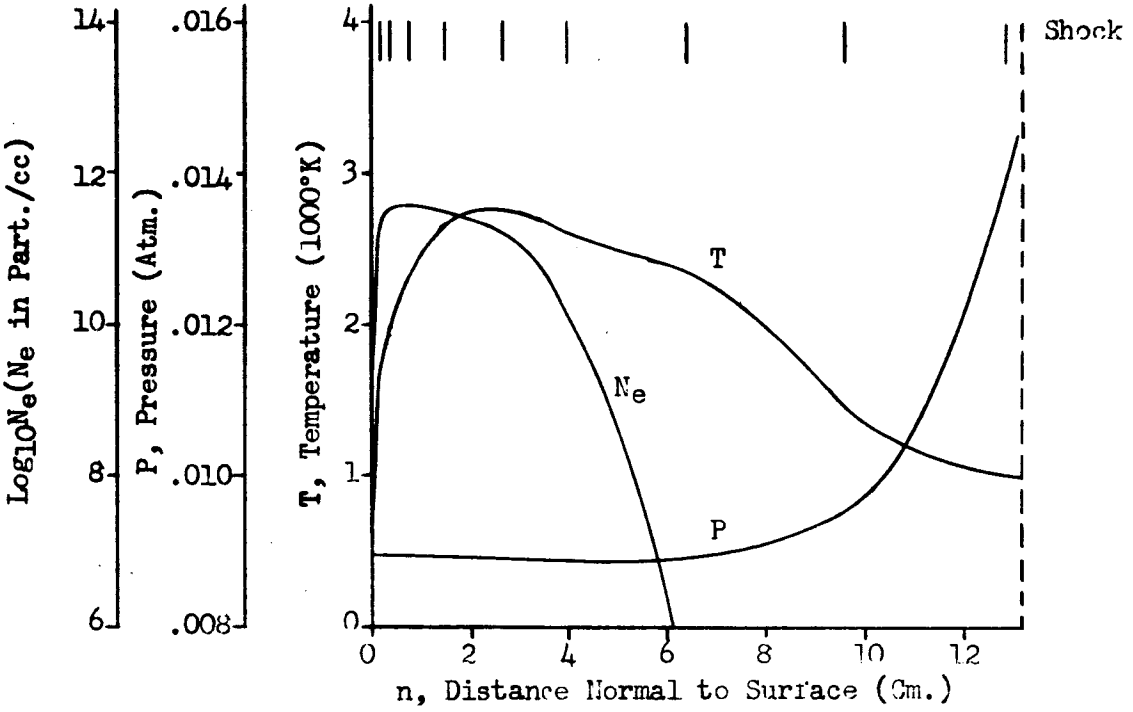

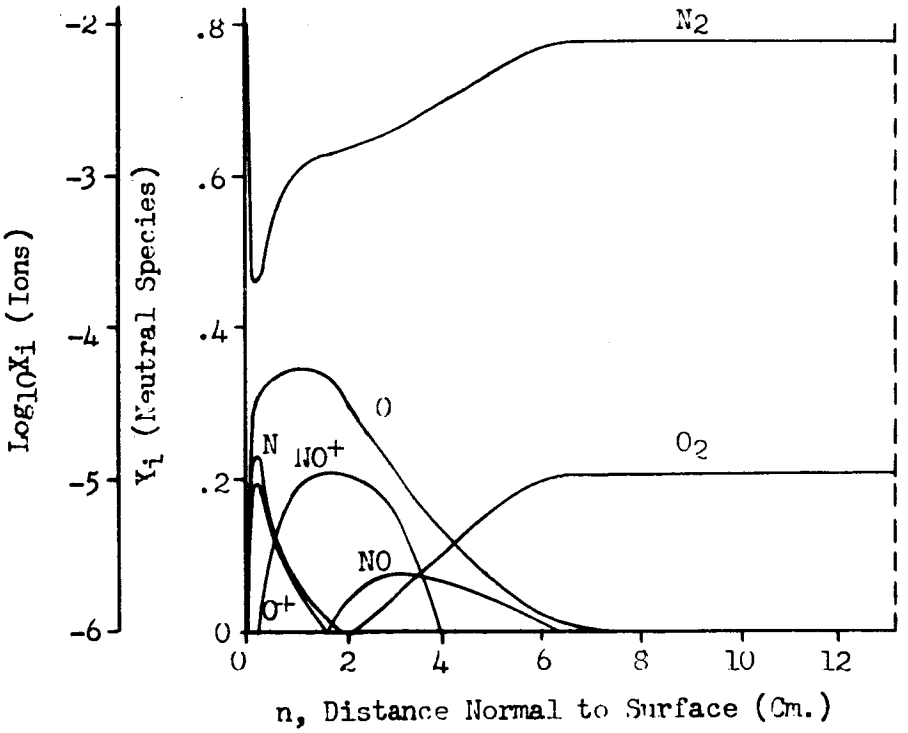

Figure 30g. Flow Field Properties - Case 6, Normal 7

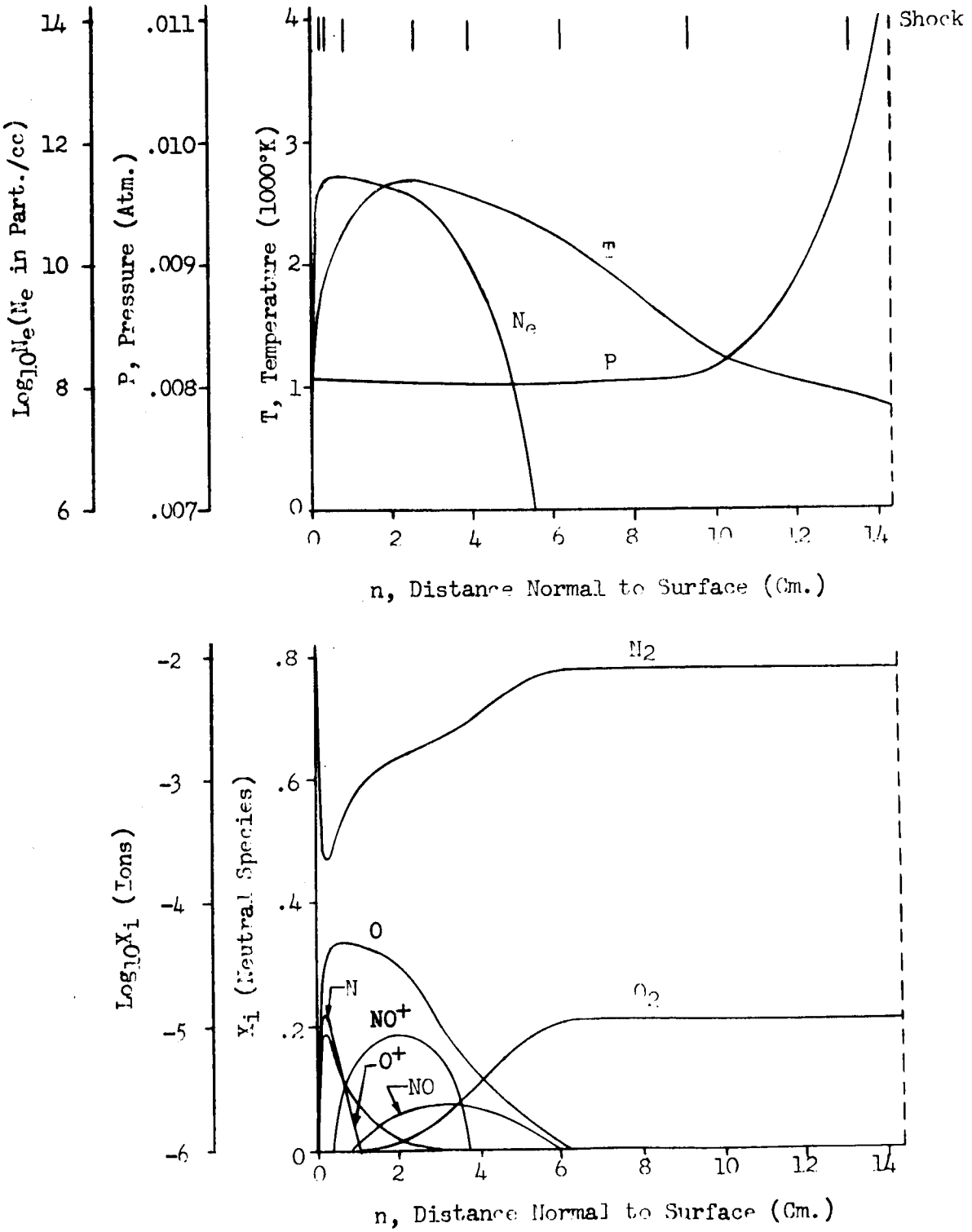

Figure 30h. Flow Field Properties - Case 6, Normal 8

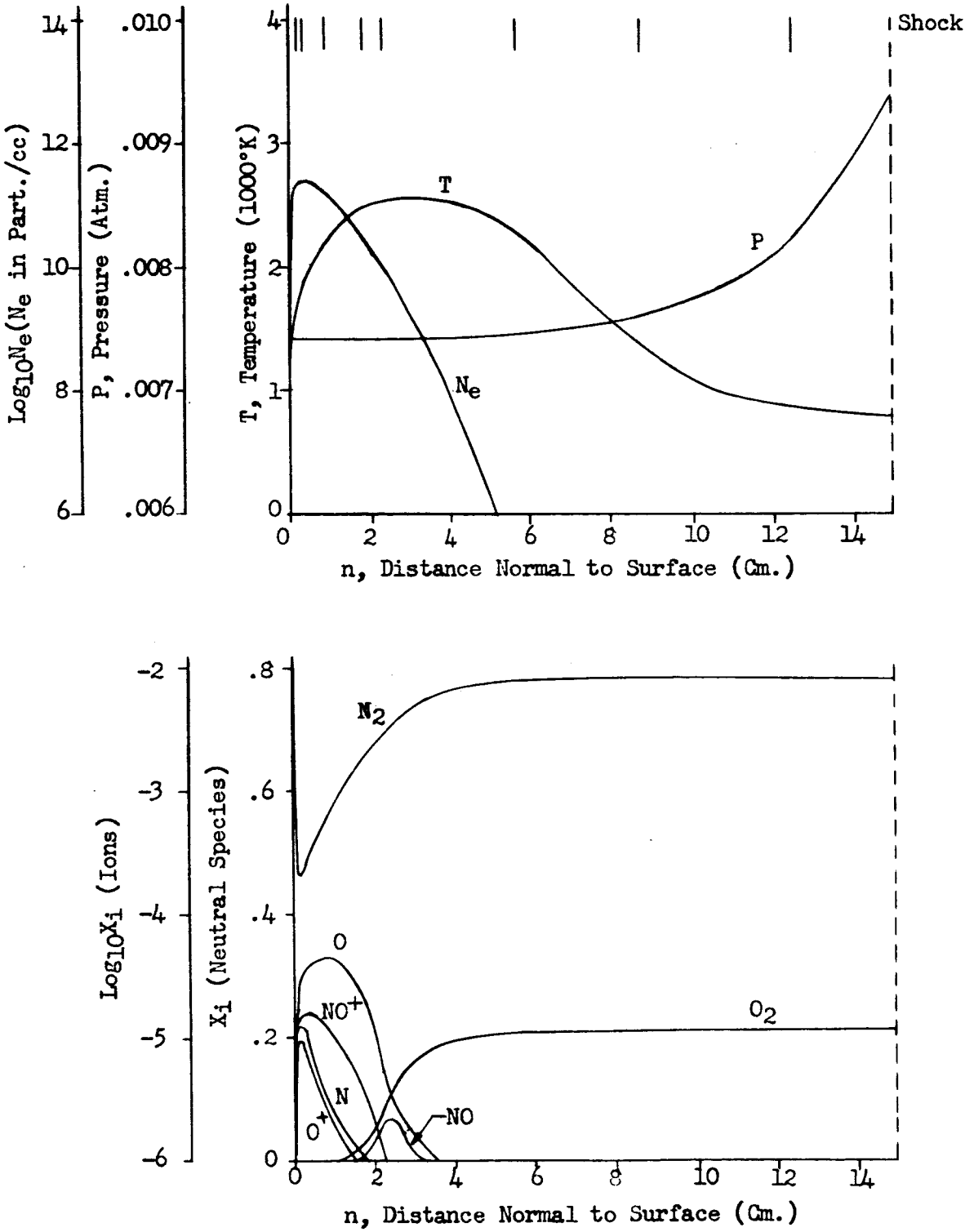

Figure 30i. Flow Field Properties - Case 6, Normal 9

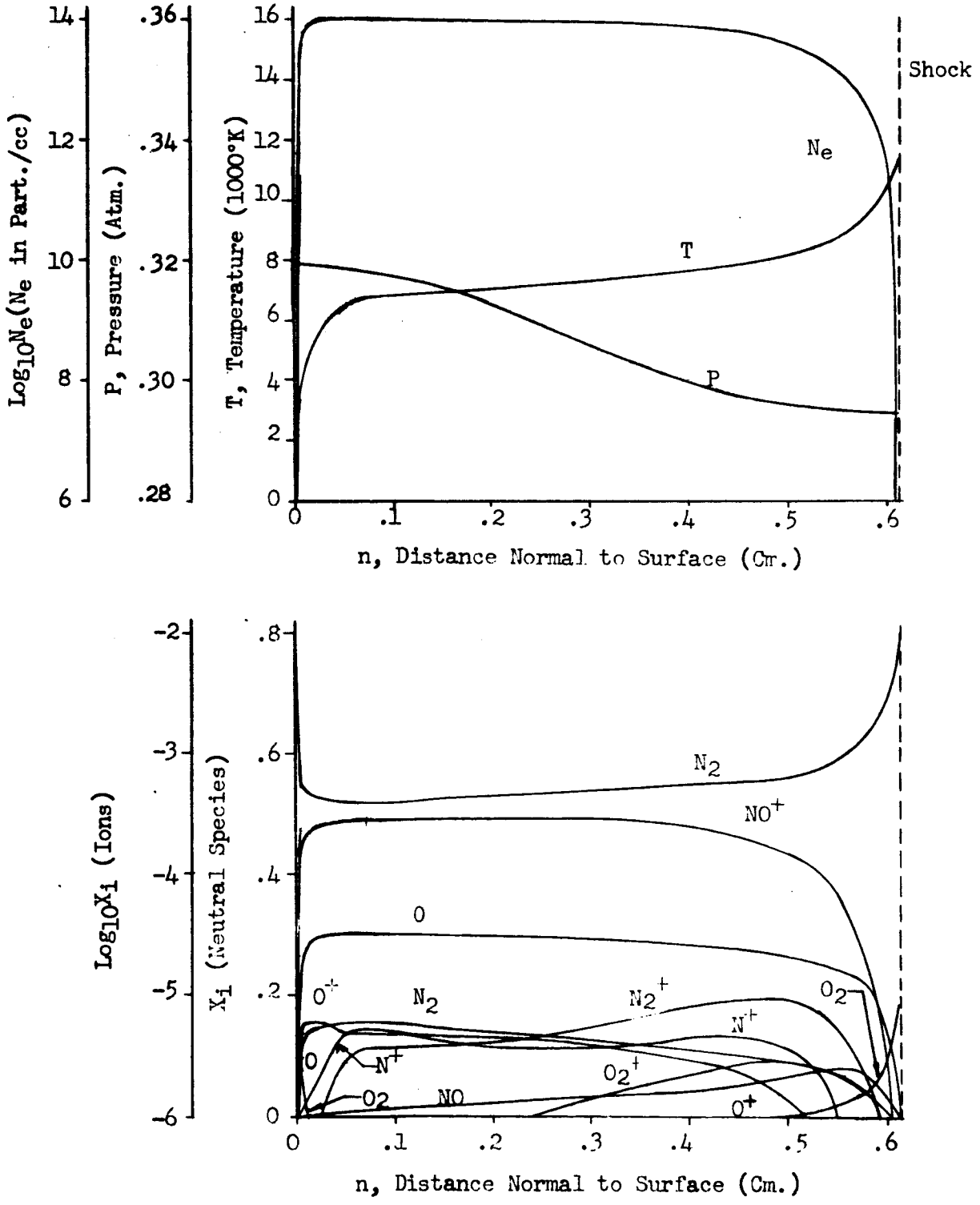

Figure 31a. Flow Field Properties - Case 7, Normal 1

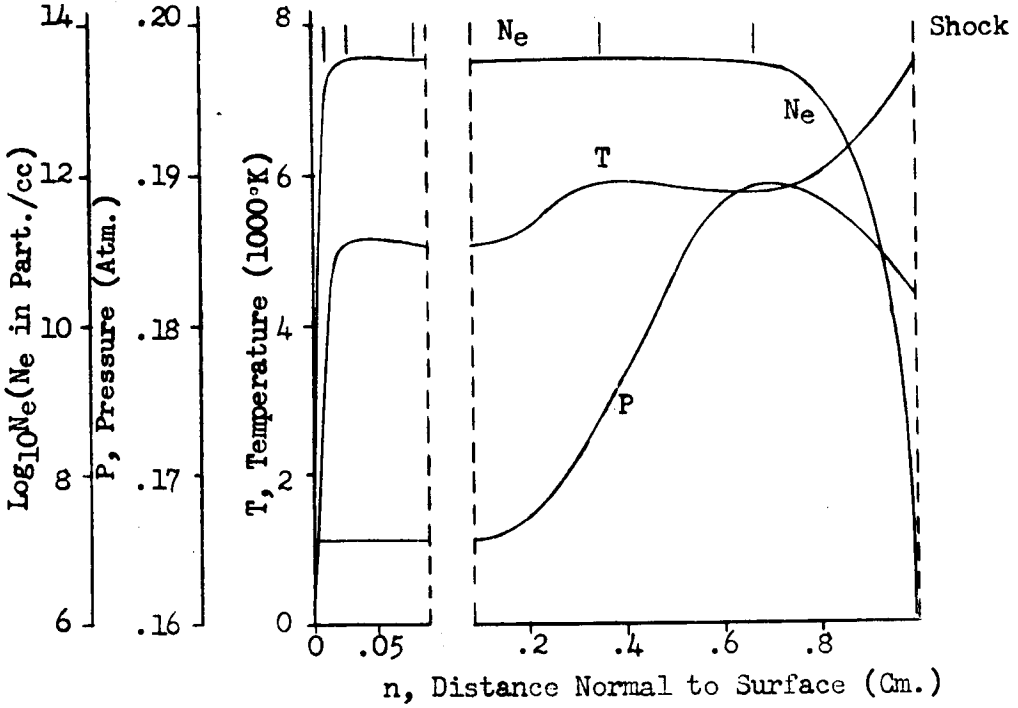

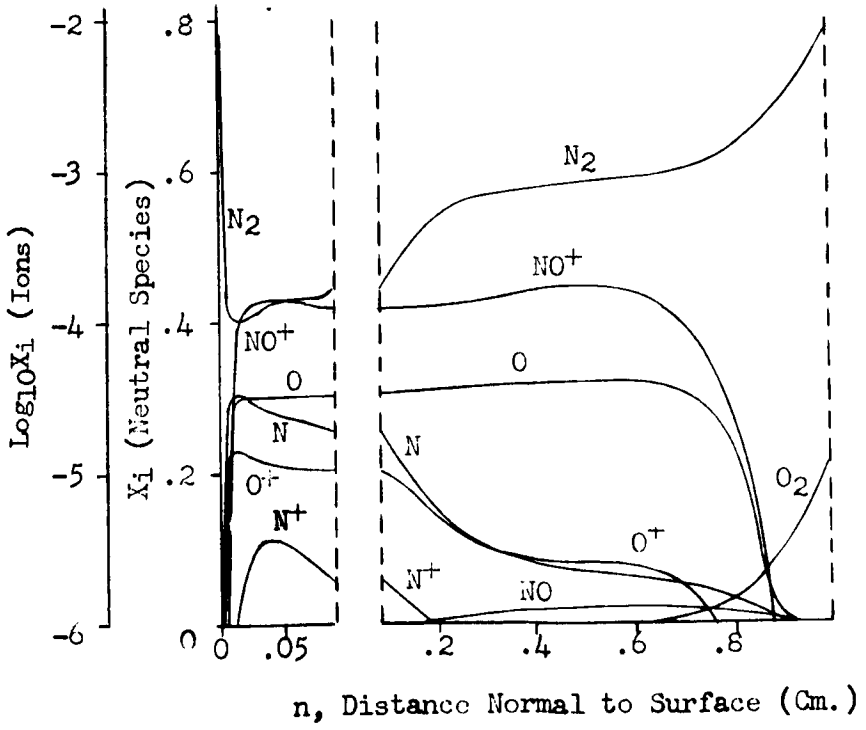

Figure 31b. Flow Field Properties - Case 7, Normal 2

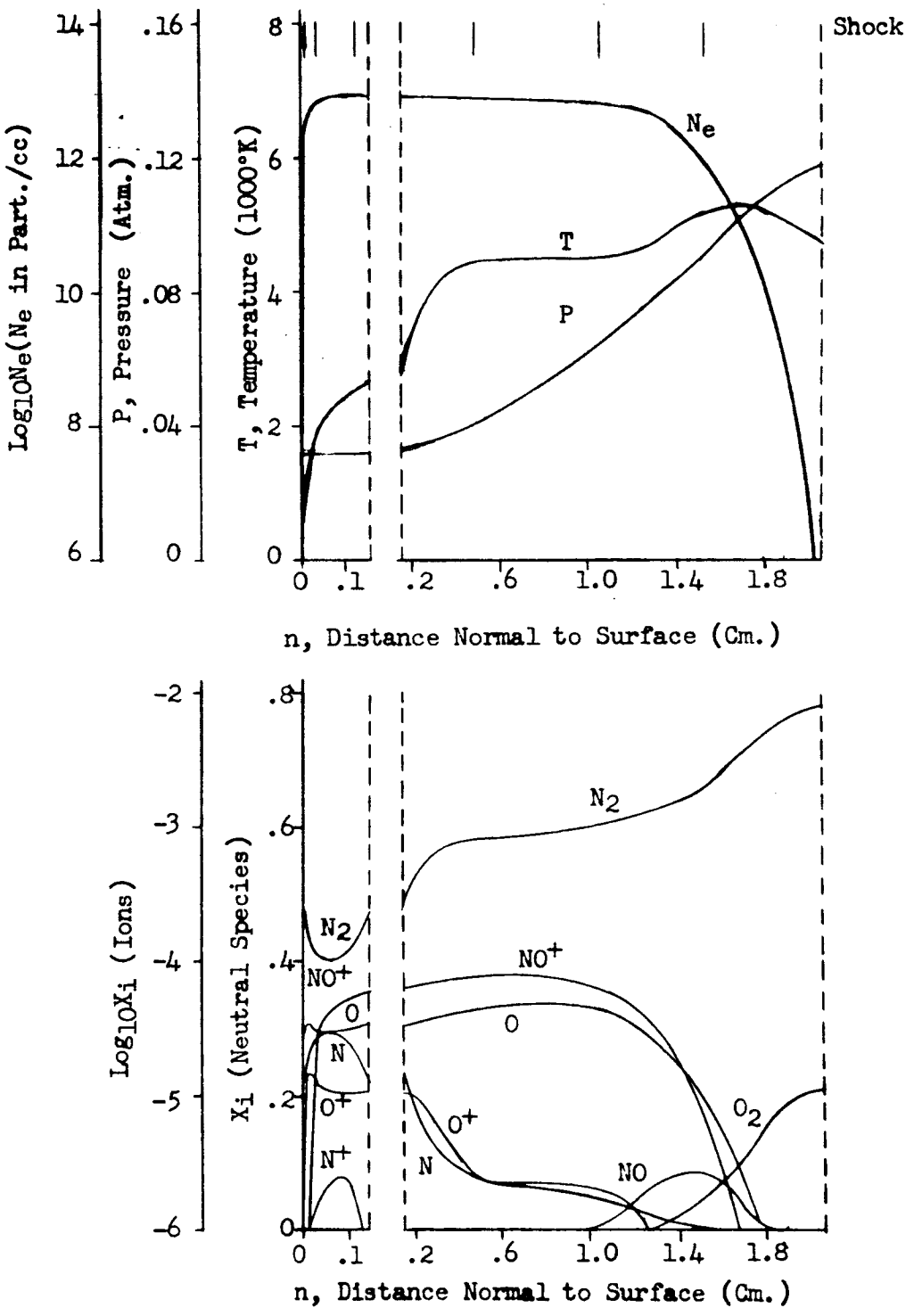

Figure 31c. Flow Field Properties - Case 7, Normal 3

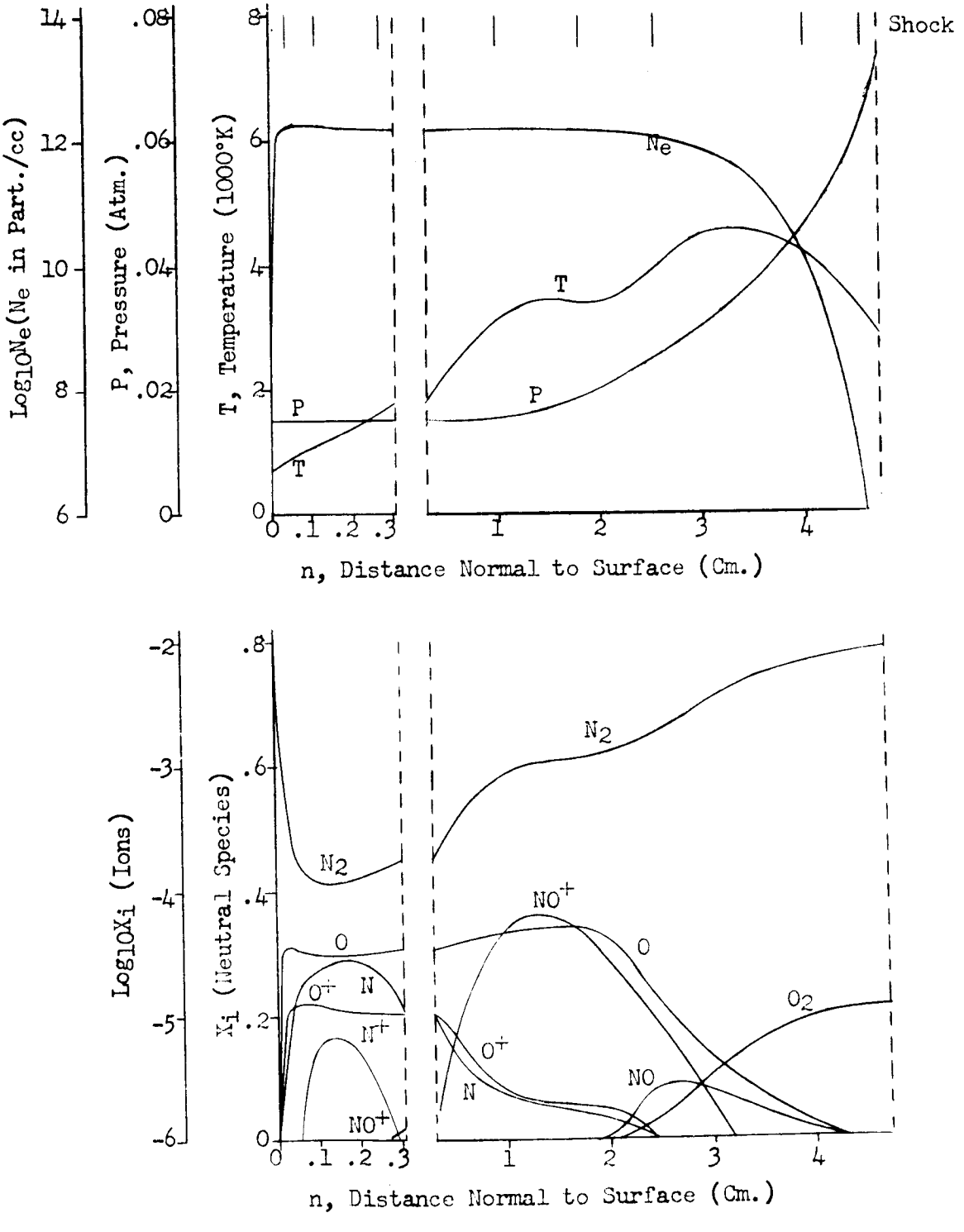

Figure 31d. Flow Field Properties - Case 7, Normal 4

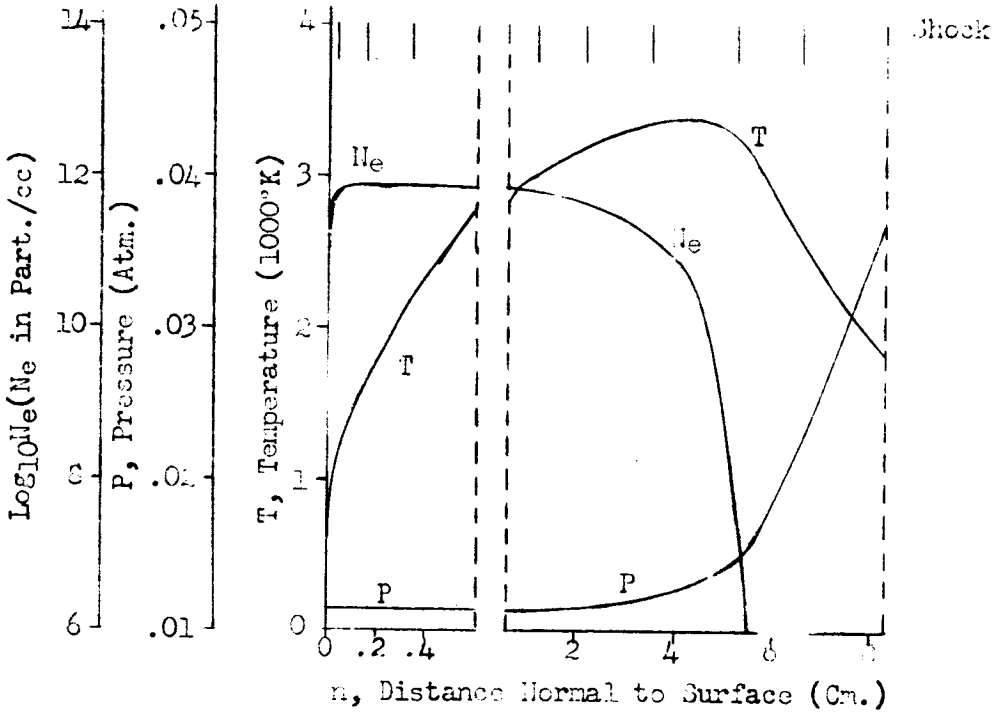

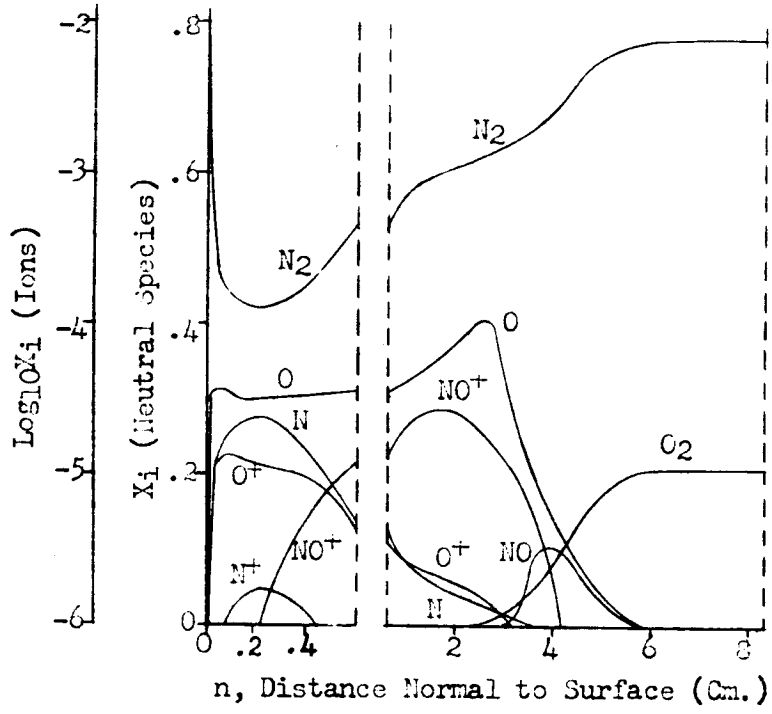

Figure 31e. Flow Field Properties - Case 7, Normal 5

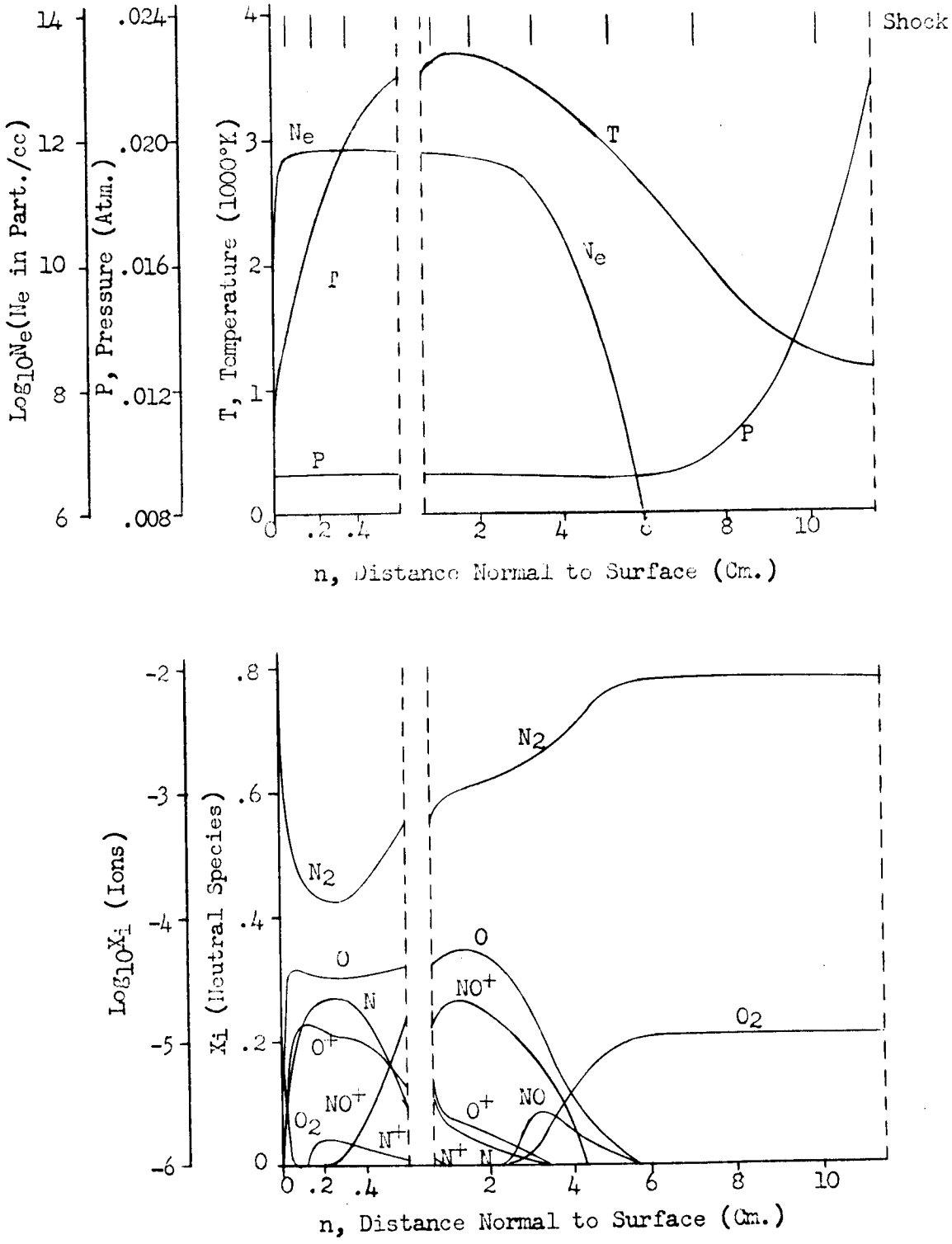

Figure 31f. Flow Field Properties - Case 7, Normal 6

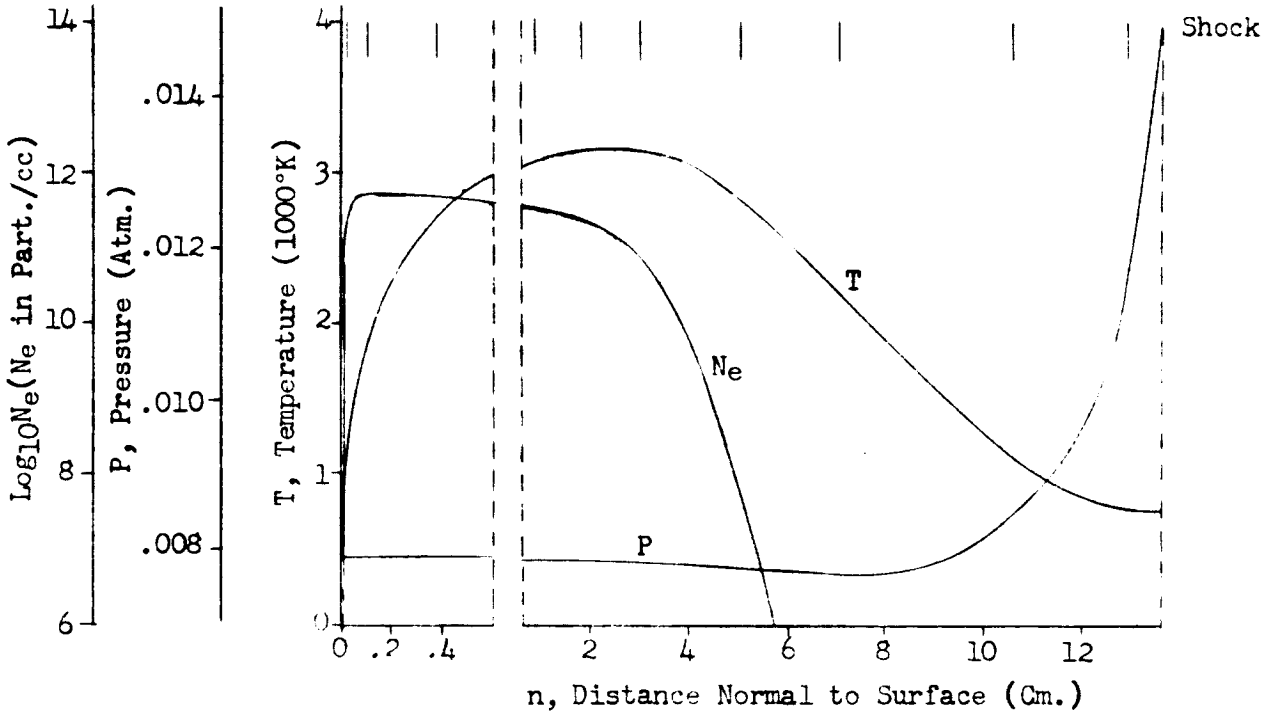

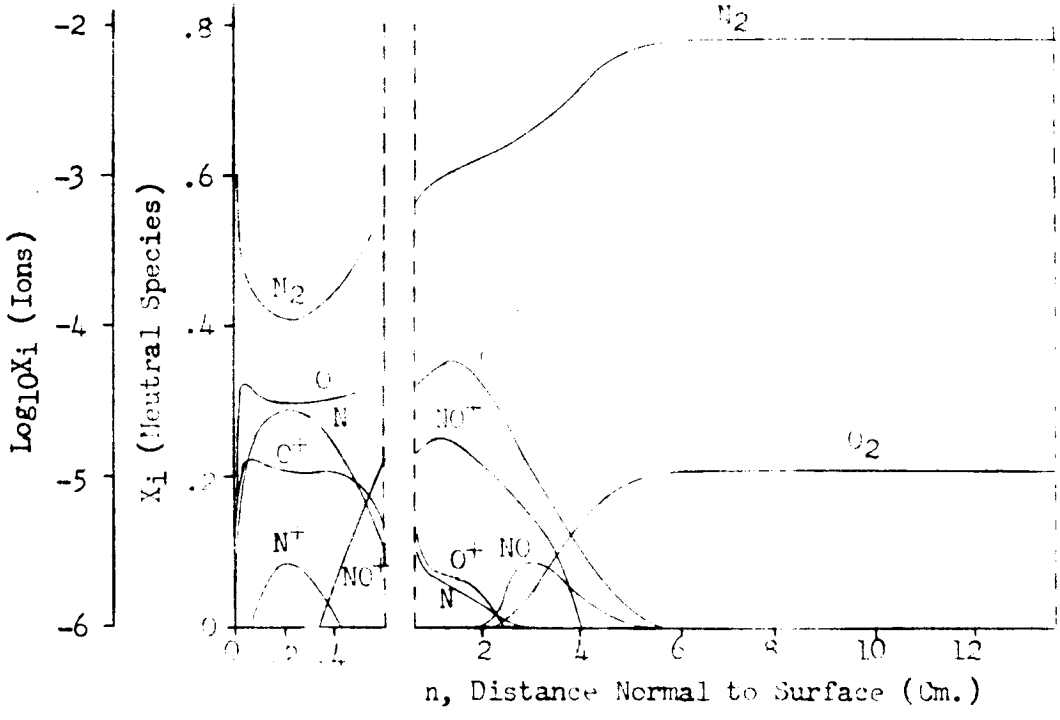

Figure 31. Flow Field Properties - Case 7, Normal

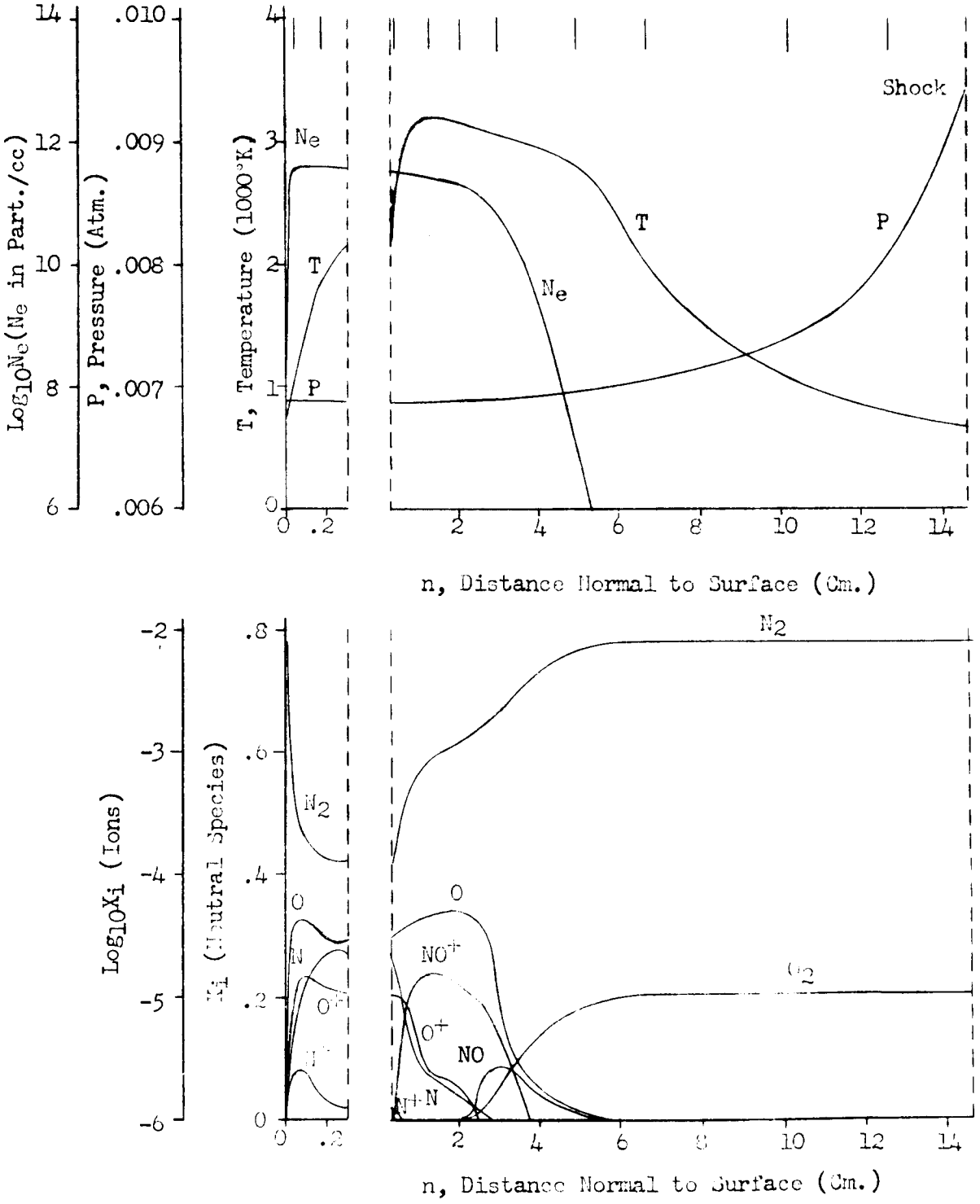

Figure 31h. Flow Field Properties - Case 7, Normal 8

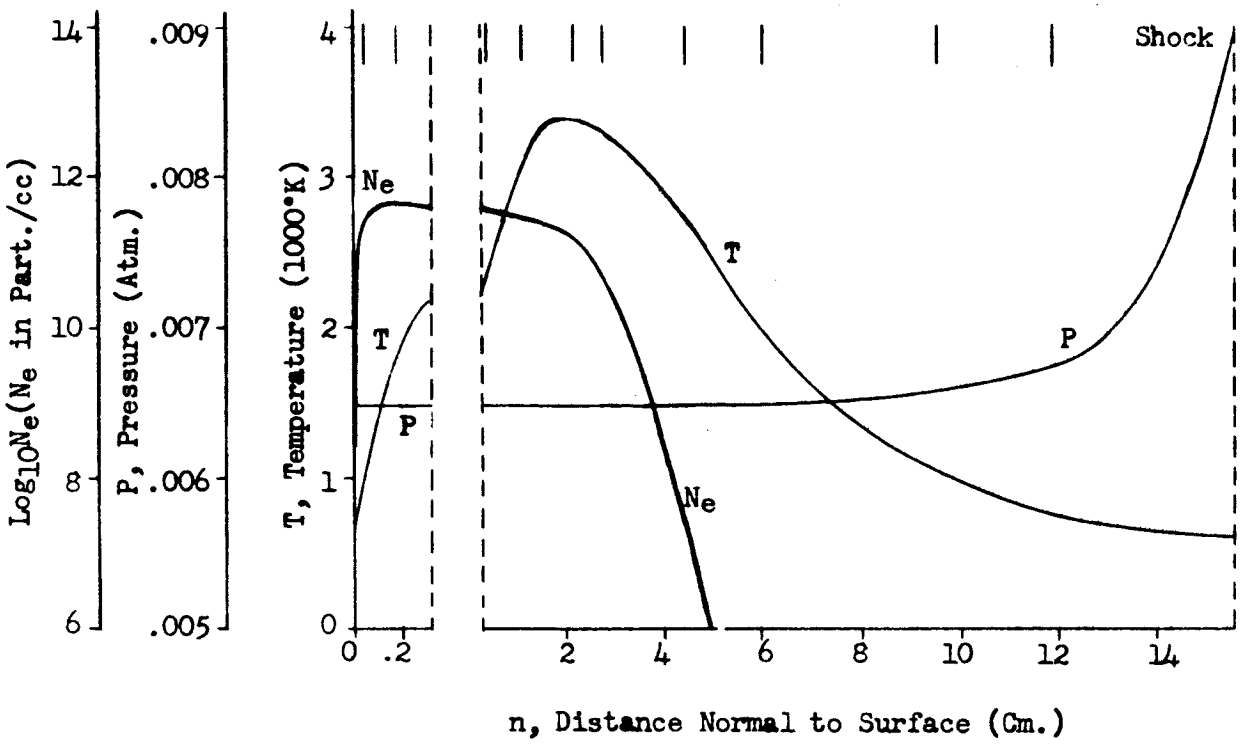

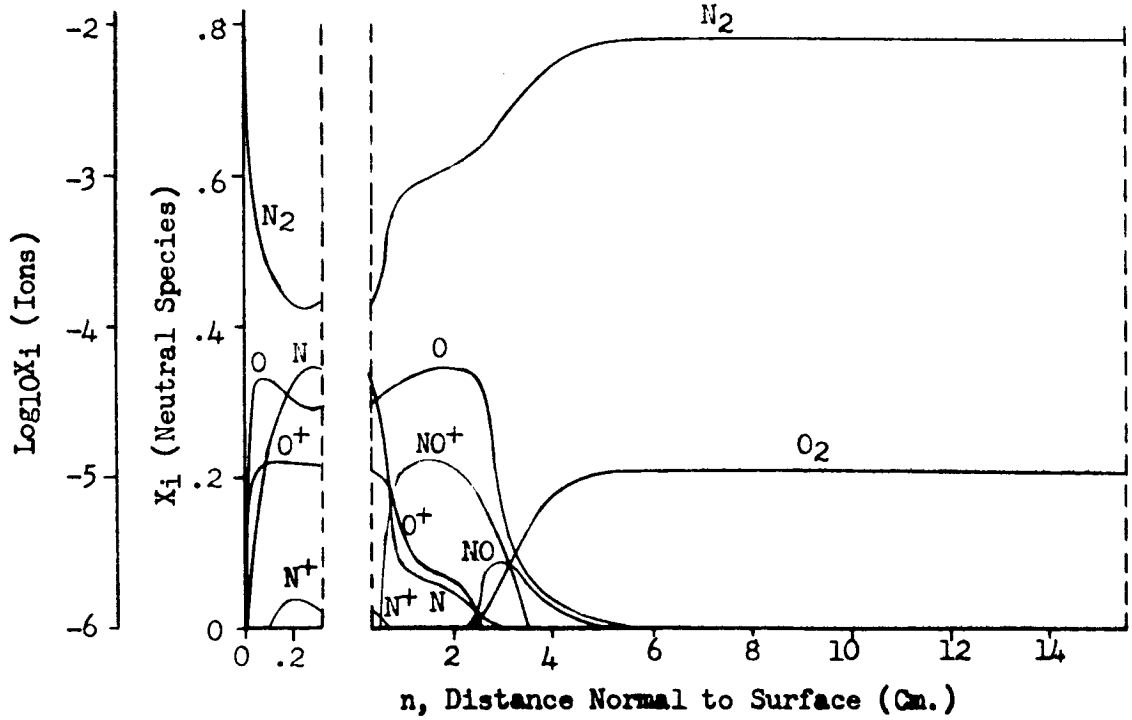

Figure 31i. Flow Field Properties - Case 7, Normal 9

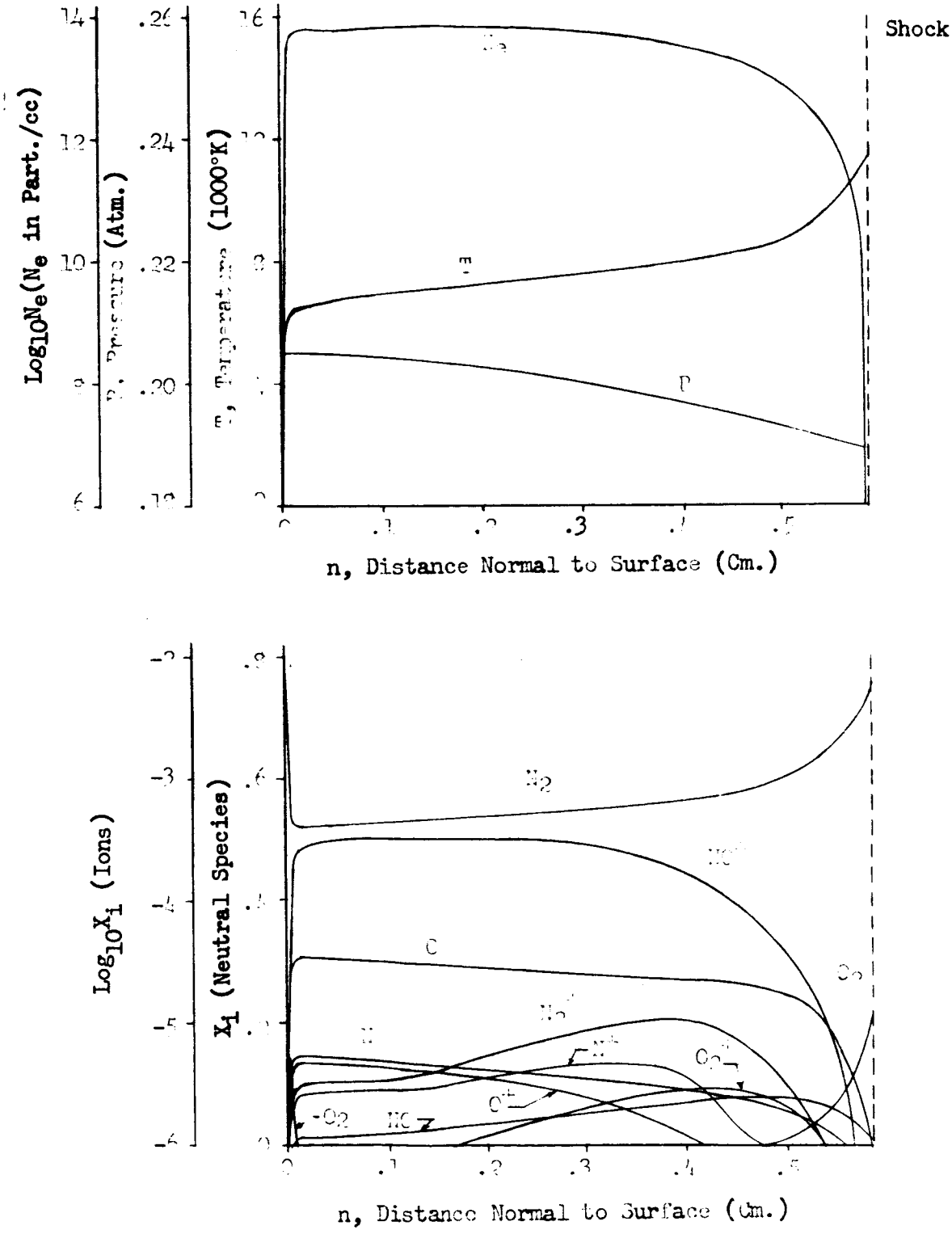

Figure 32a. Flow Field Properties - Case 8, Normal 1

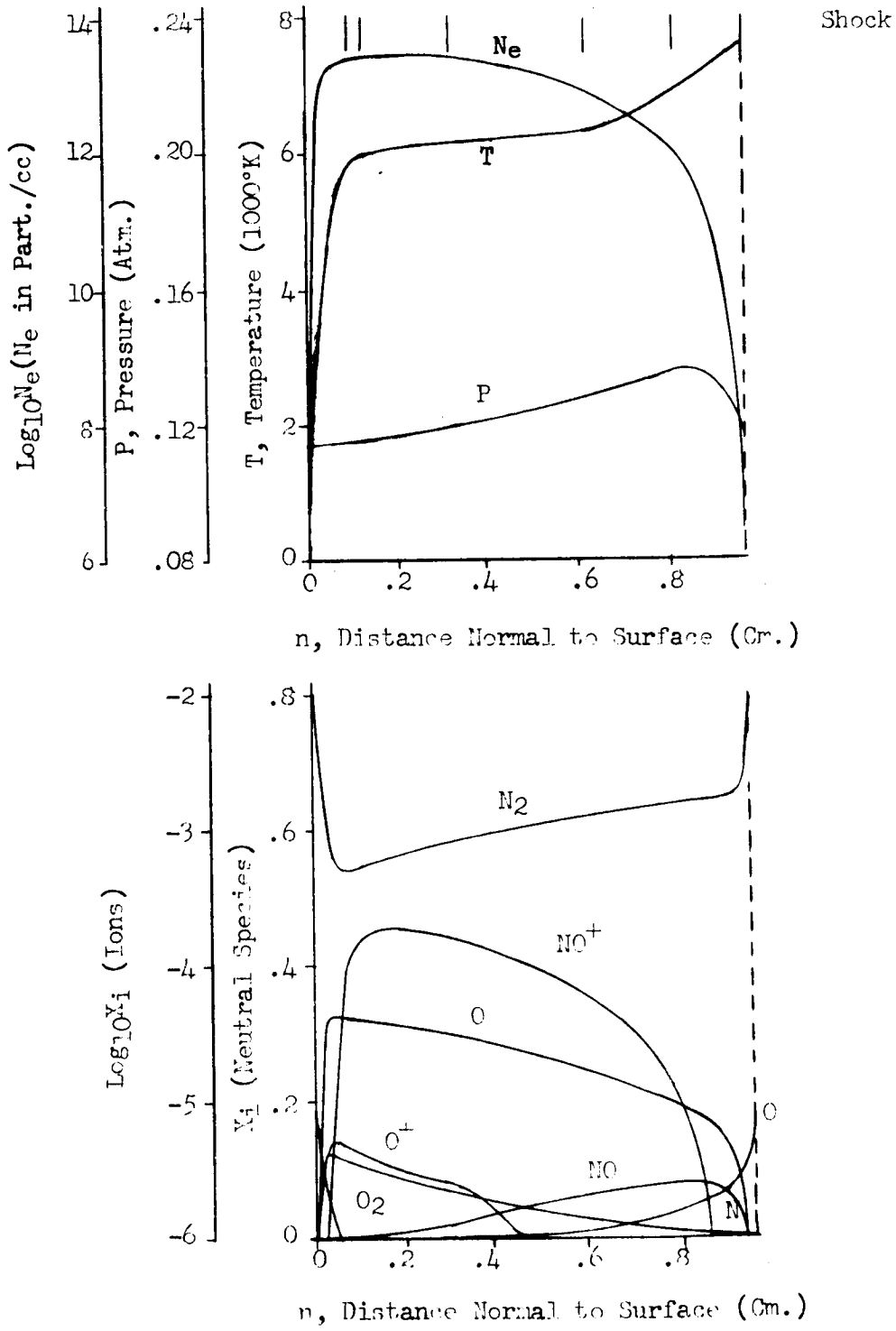

Figure 32b. Flow Field Properties - Case 8, Normal 2

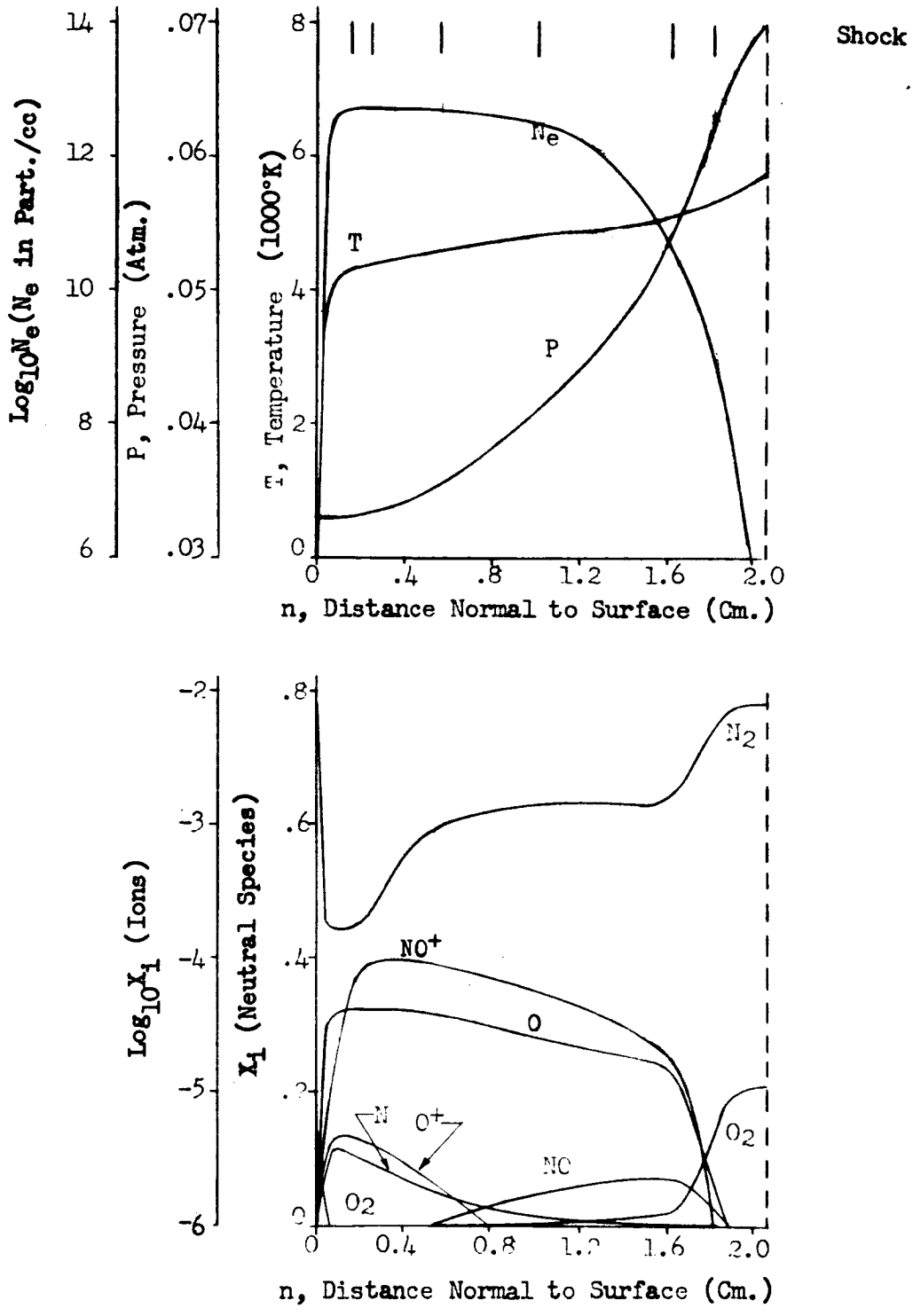

Figure 32c. Flow Field Properties - Case 8, Normal 3

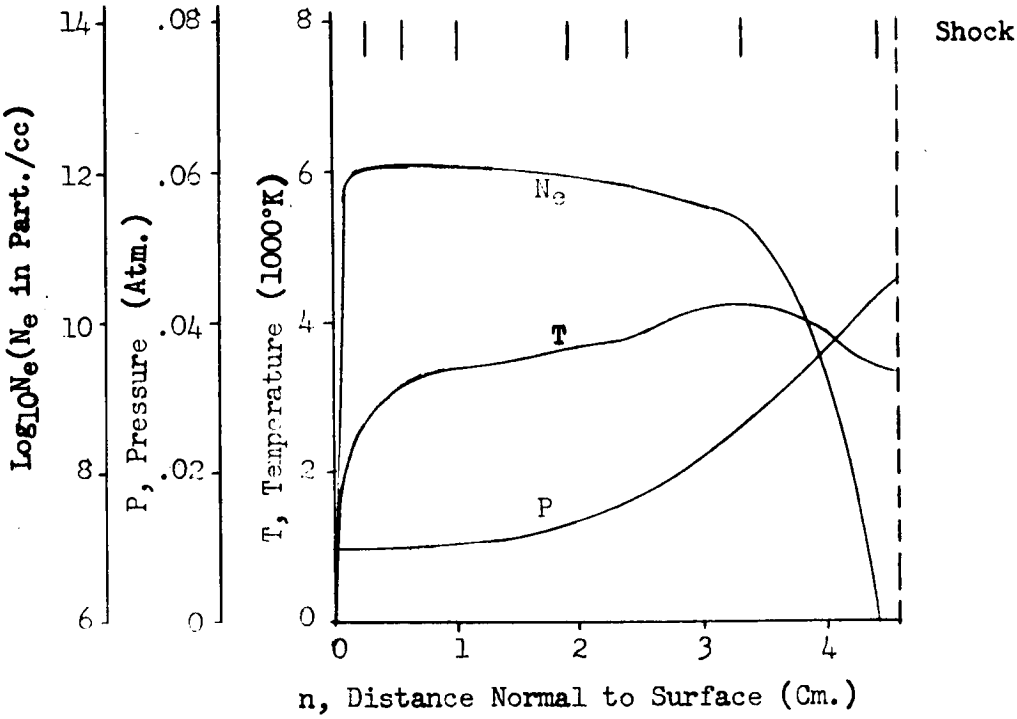

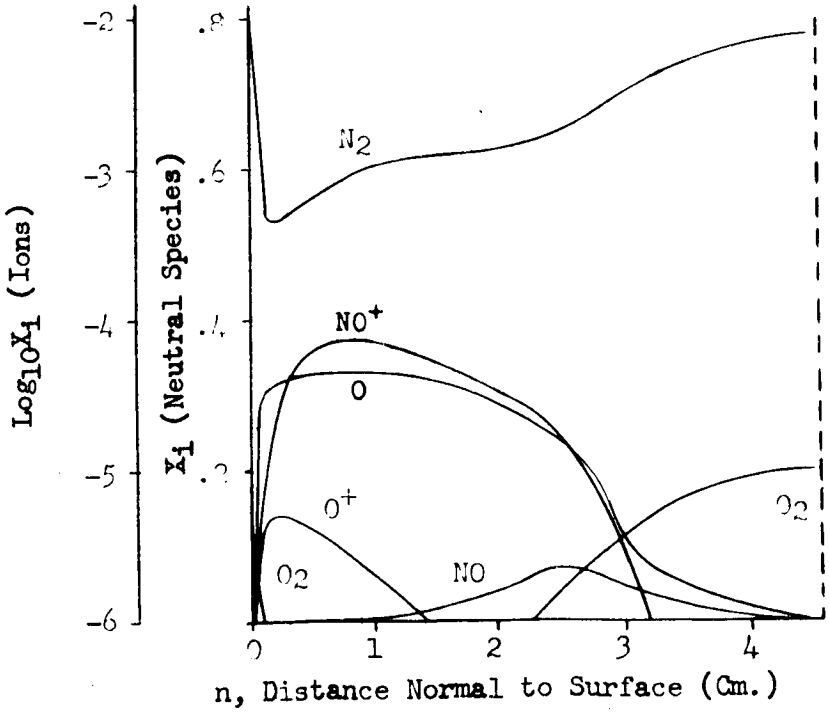

Figure 32d. Flow Field Properties - Case 8, Normal 4

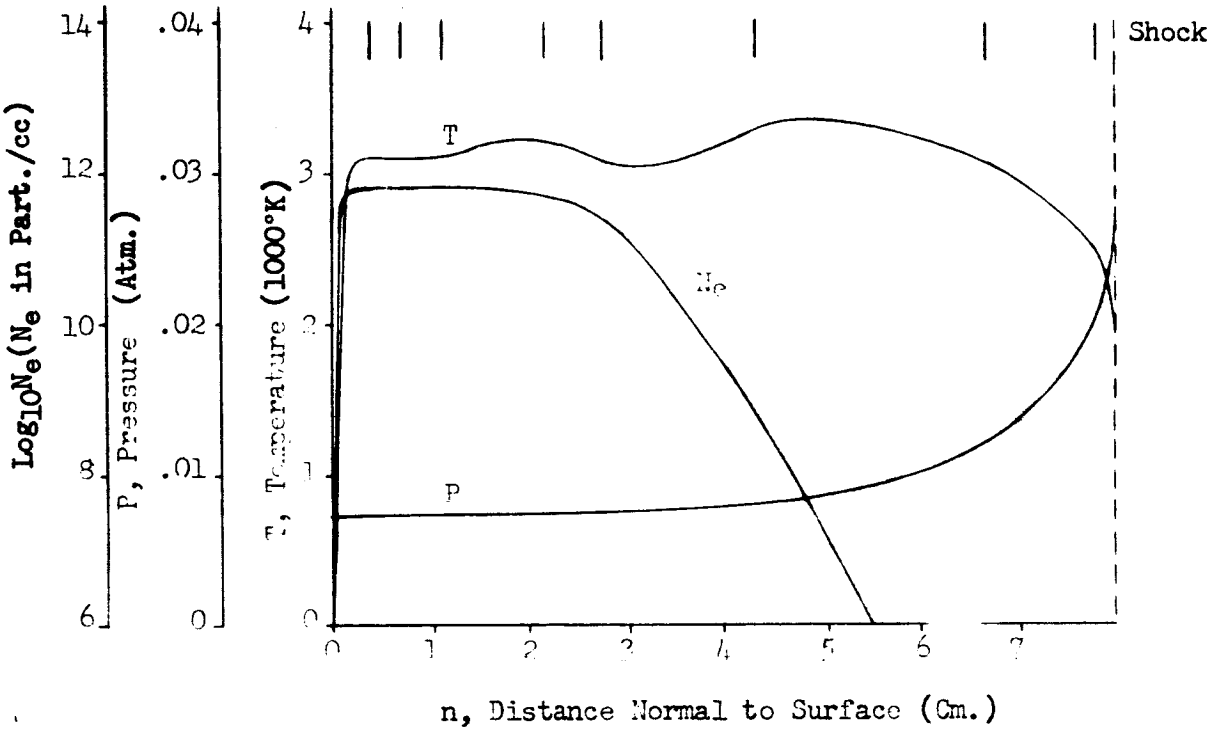

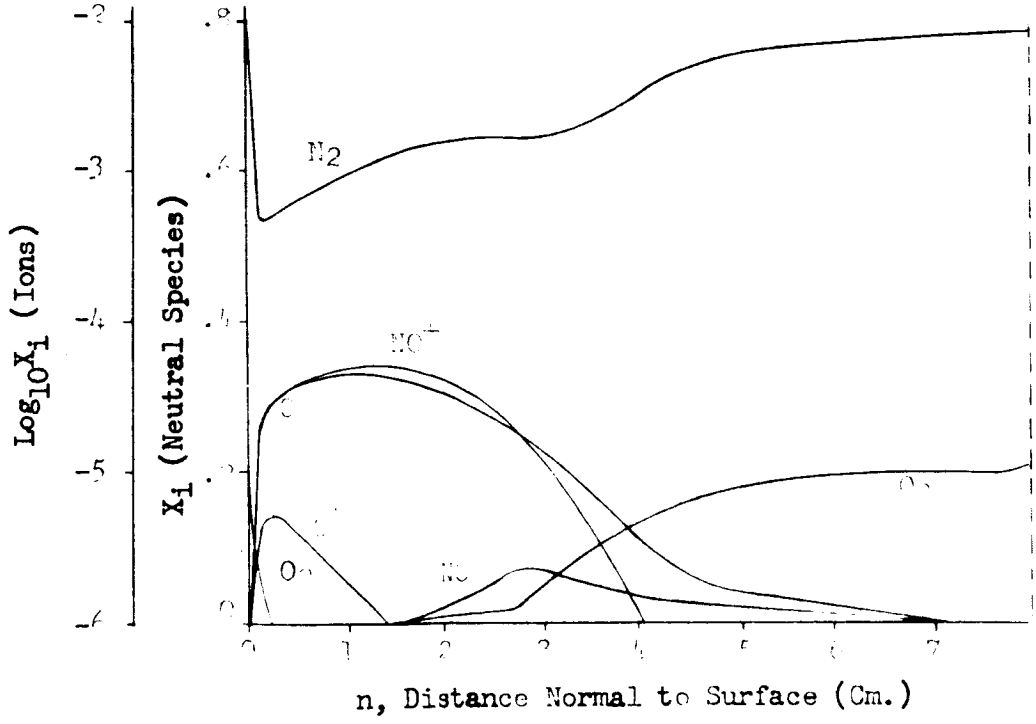

Figure 32e. Flow Field Properties - Case 8, Normal 5

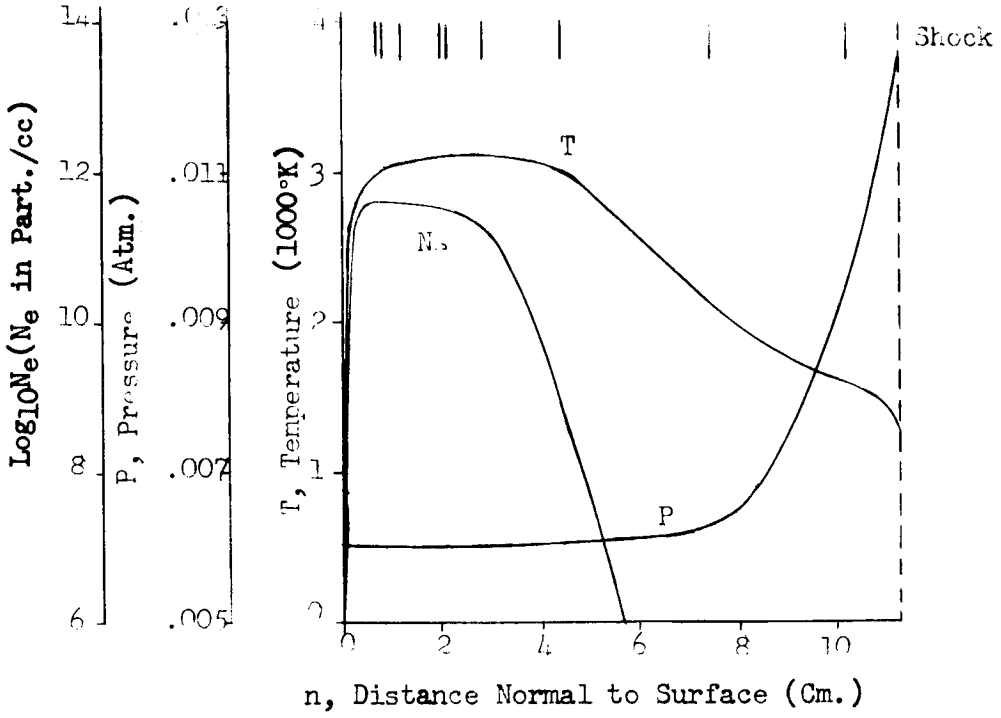

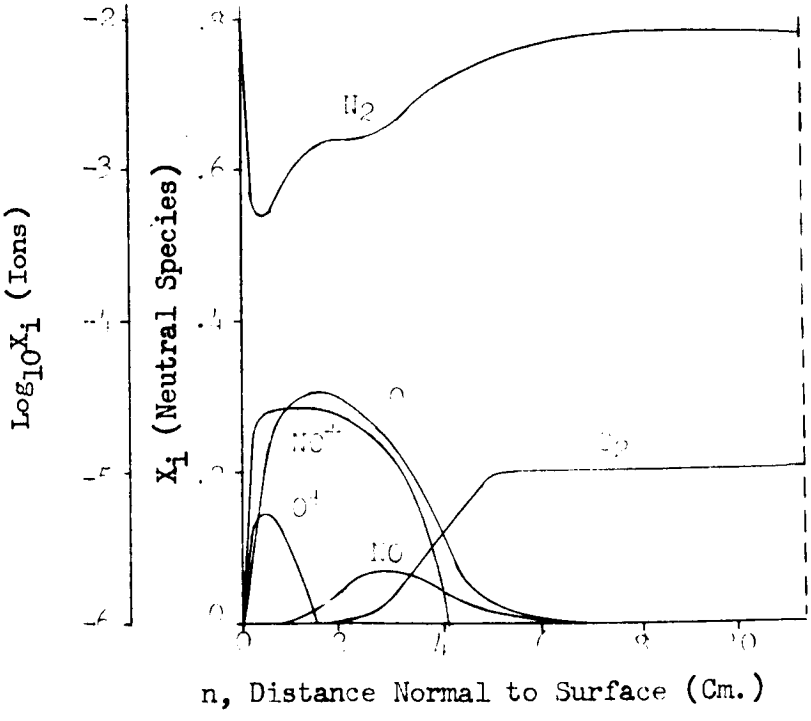

Figure 32f. Flow Field Properties - Case 8, Normal 6

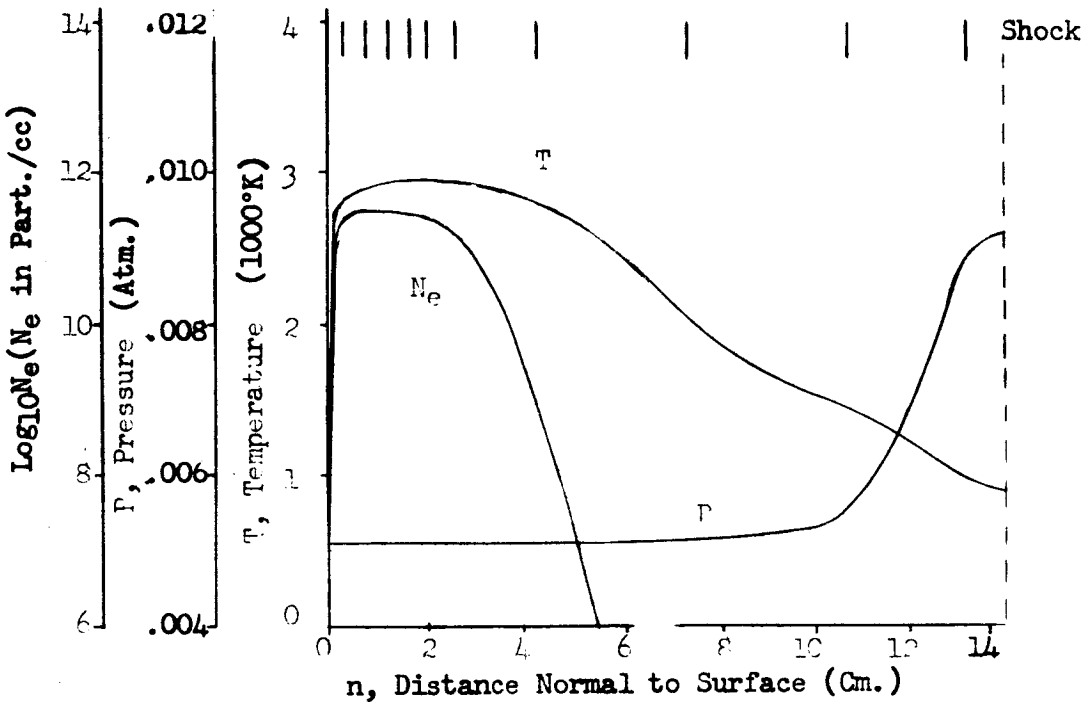

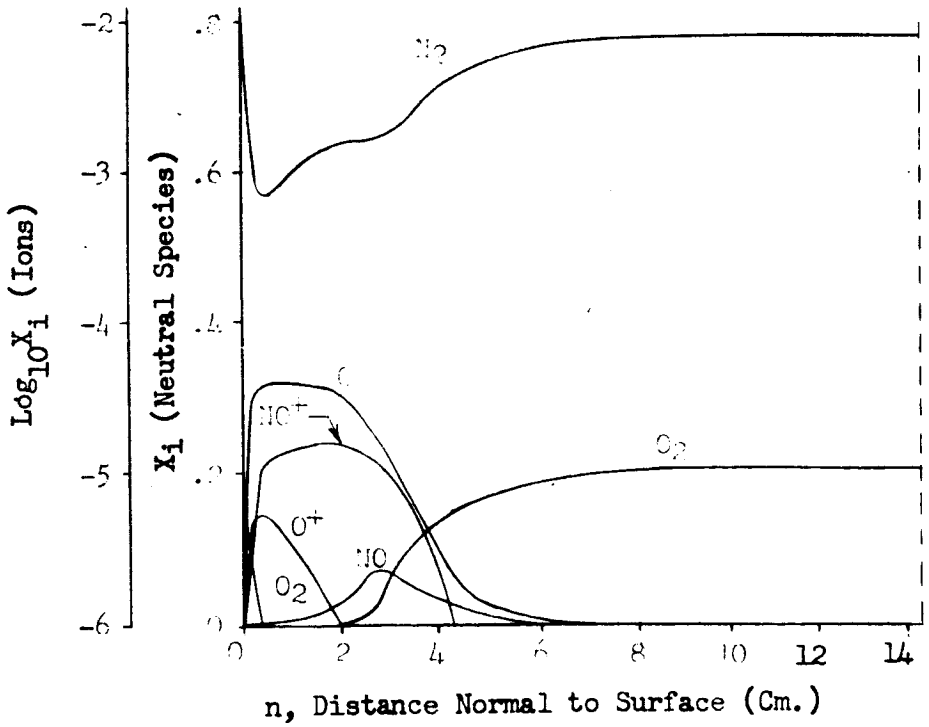

Figure 32g. Flow Field Properties - Case 8, Normal 7

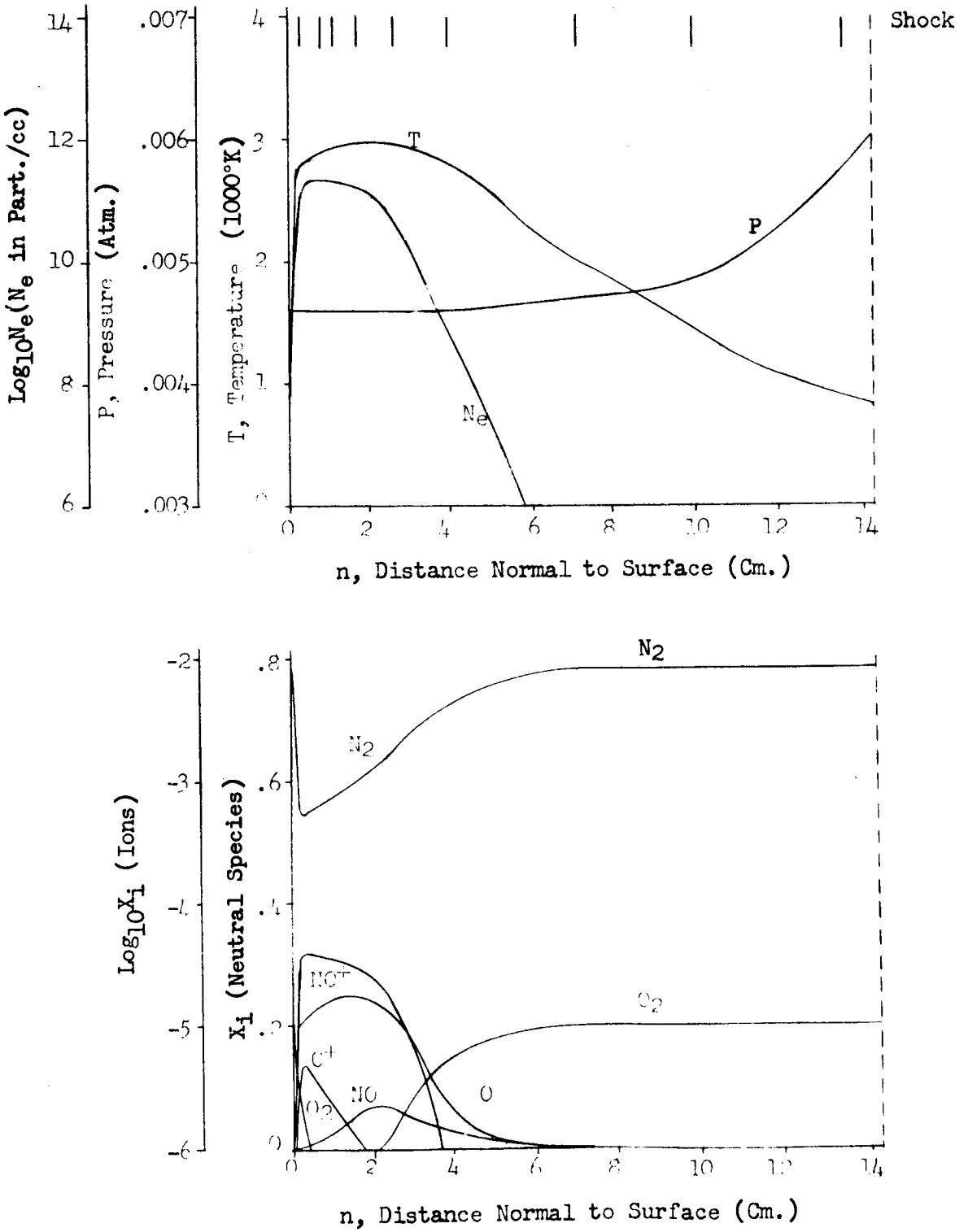

Figure 32h. Flow Field Properties - Case 8, Normal 8

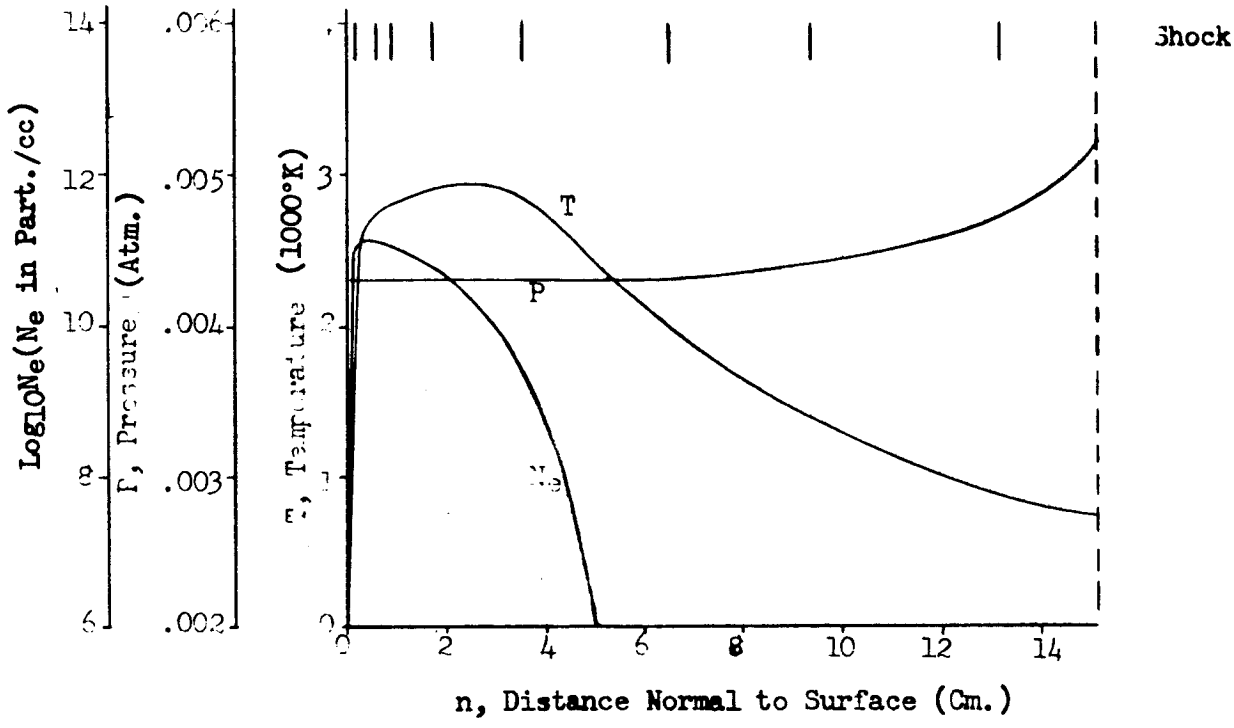

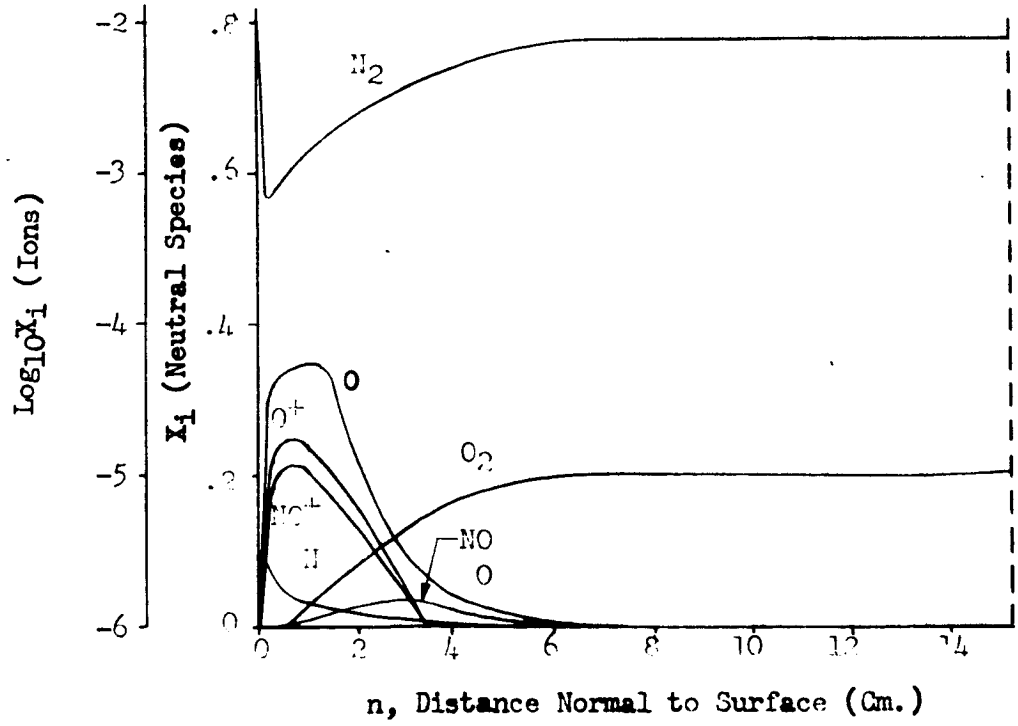

Figure 32i. Flow Field Properties - Case 8, Normal 9

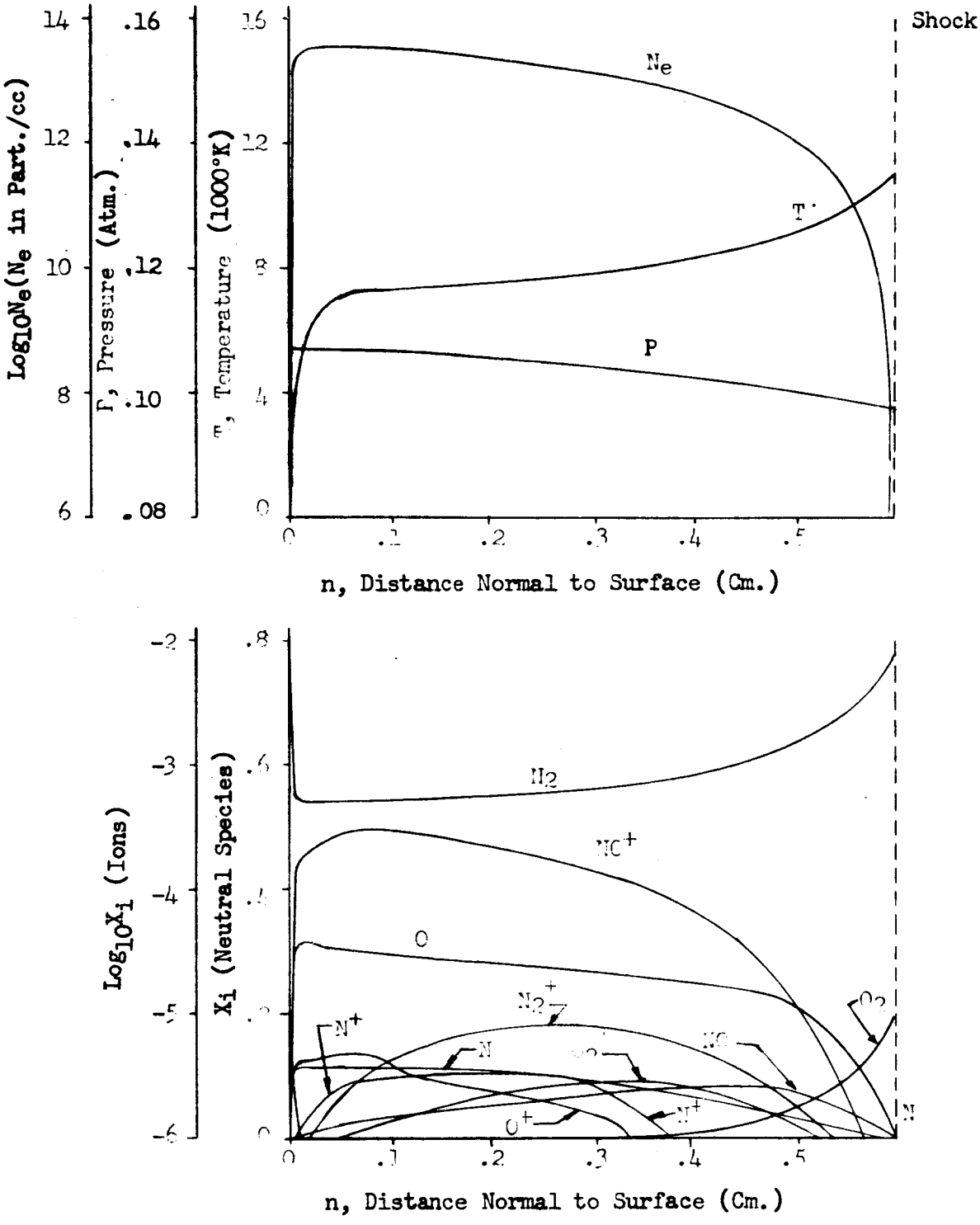

Figure 33a. Flow Field Properties - Case 9, Normal 1

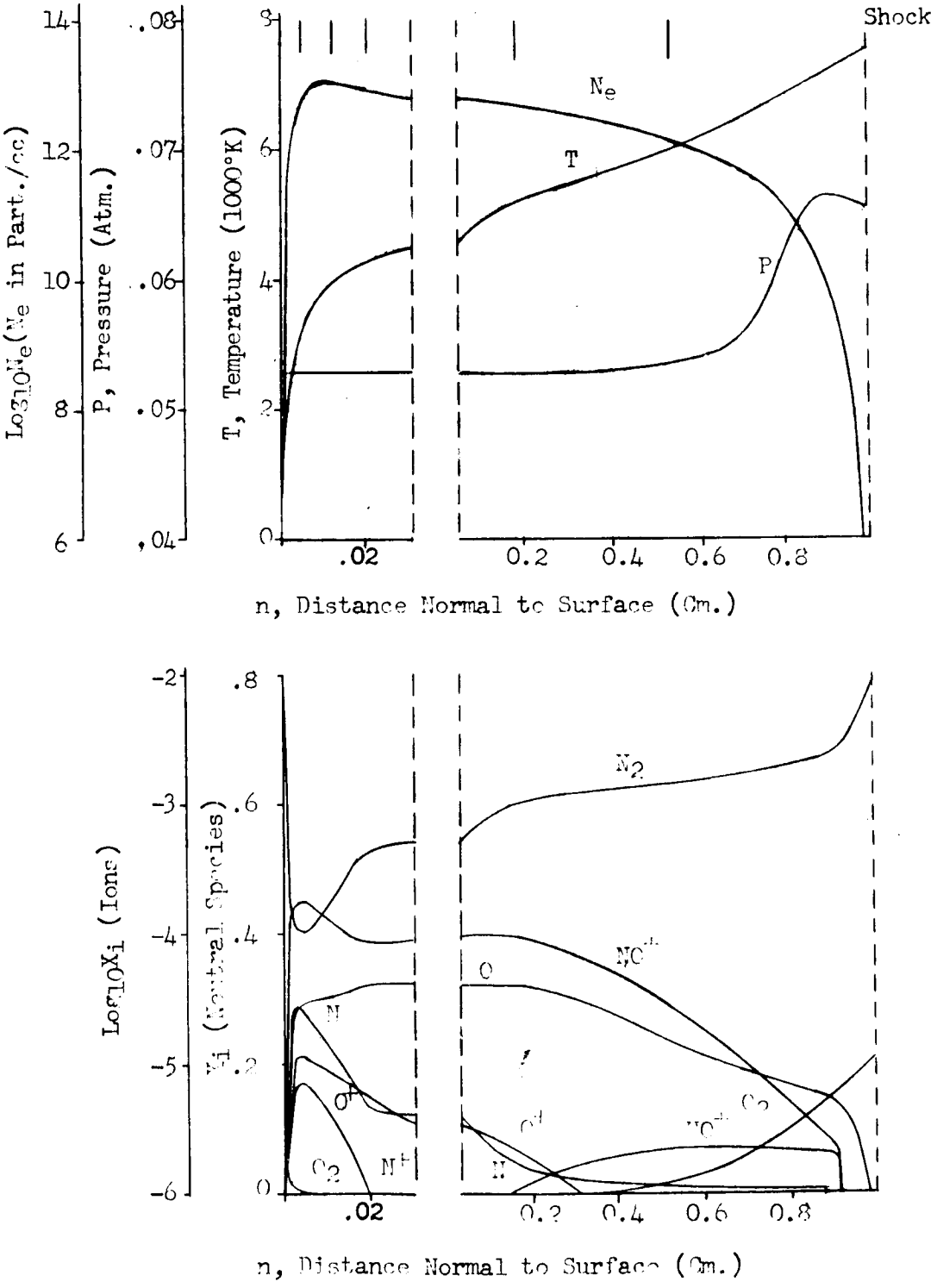

Figure 33b. Flow Field Properties - Case 9, Normal 2

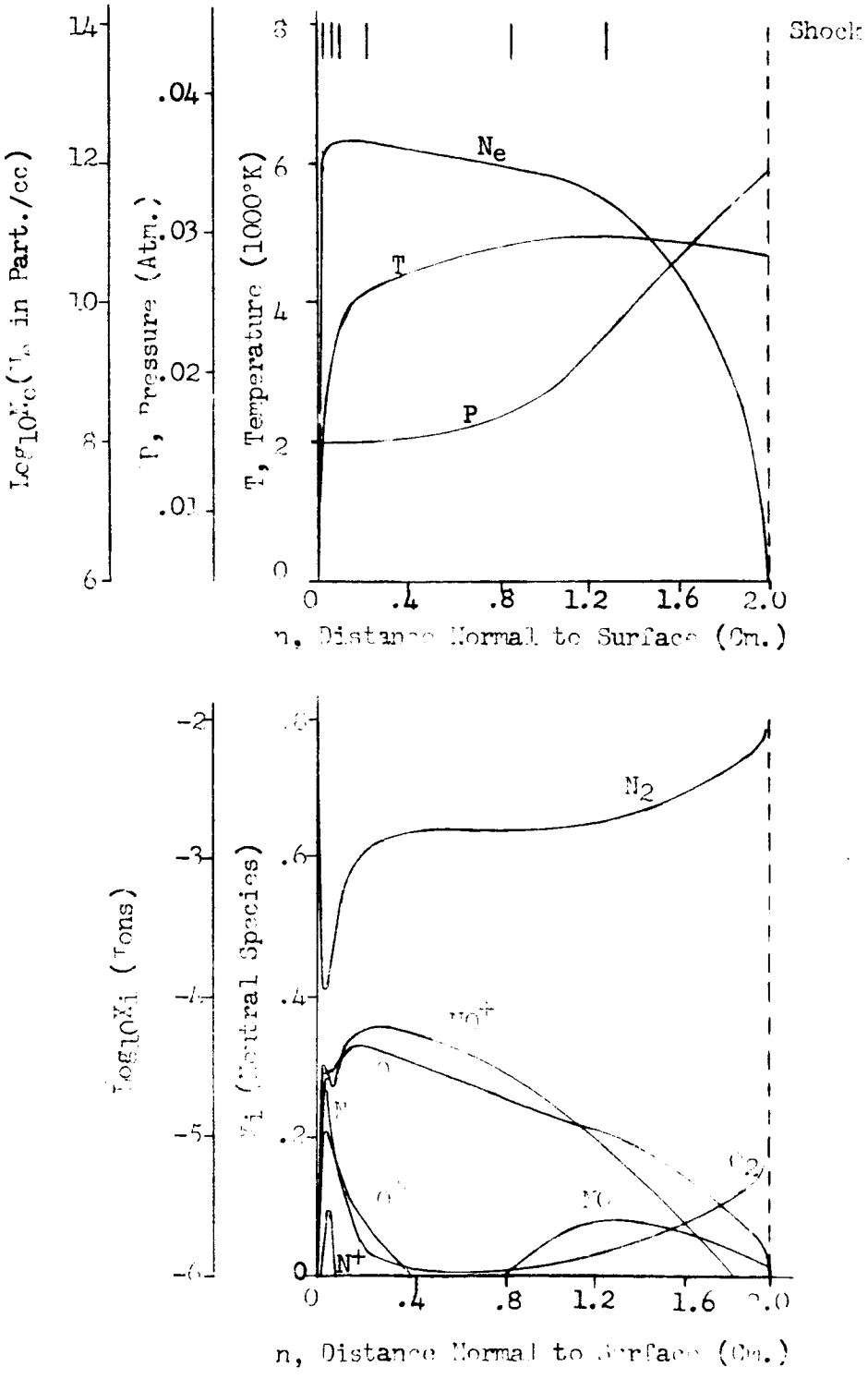

Figure 33c. Flow Field Properties - Case 9, Normal 3

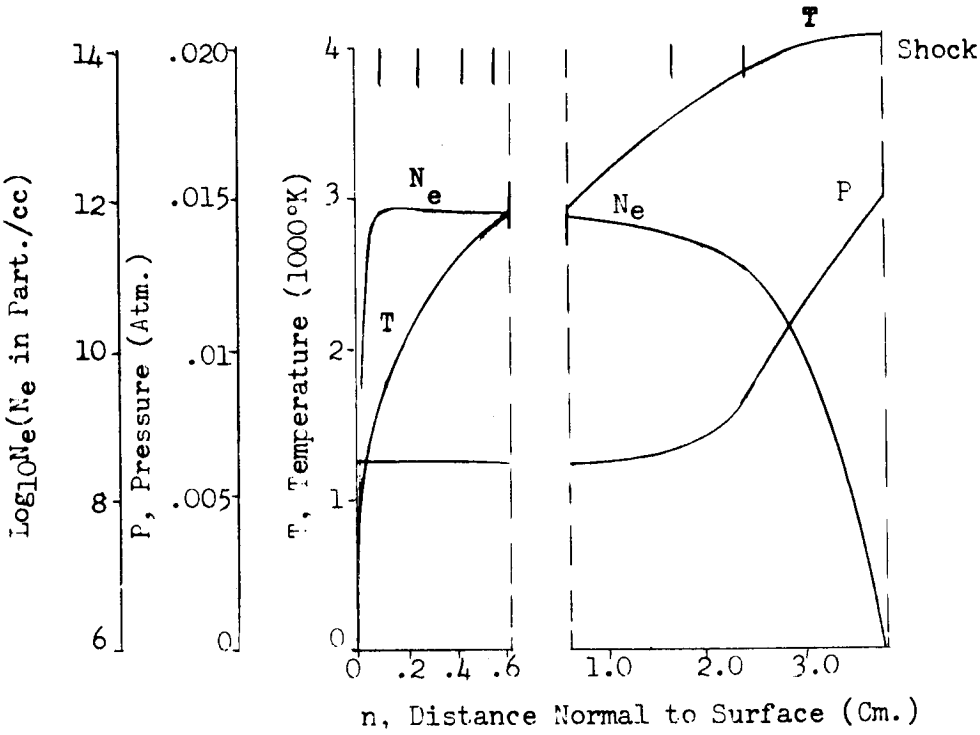

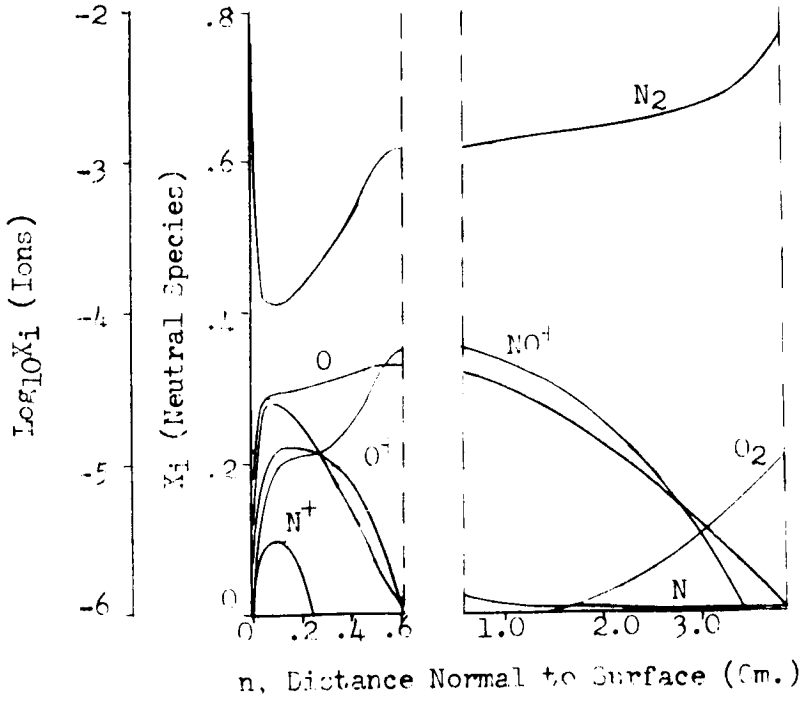

Figure 33d. Flow Field Properties - Case 9, Normal 4

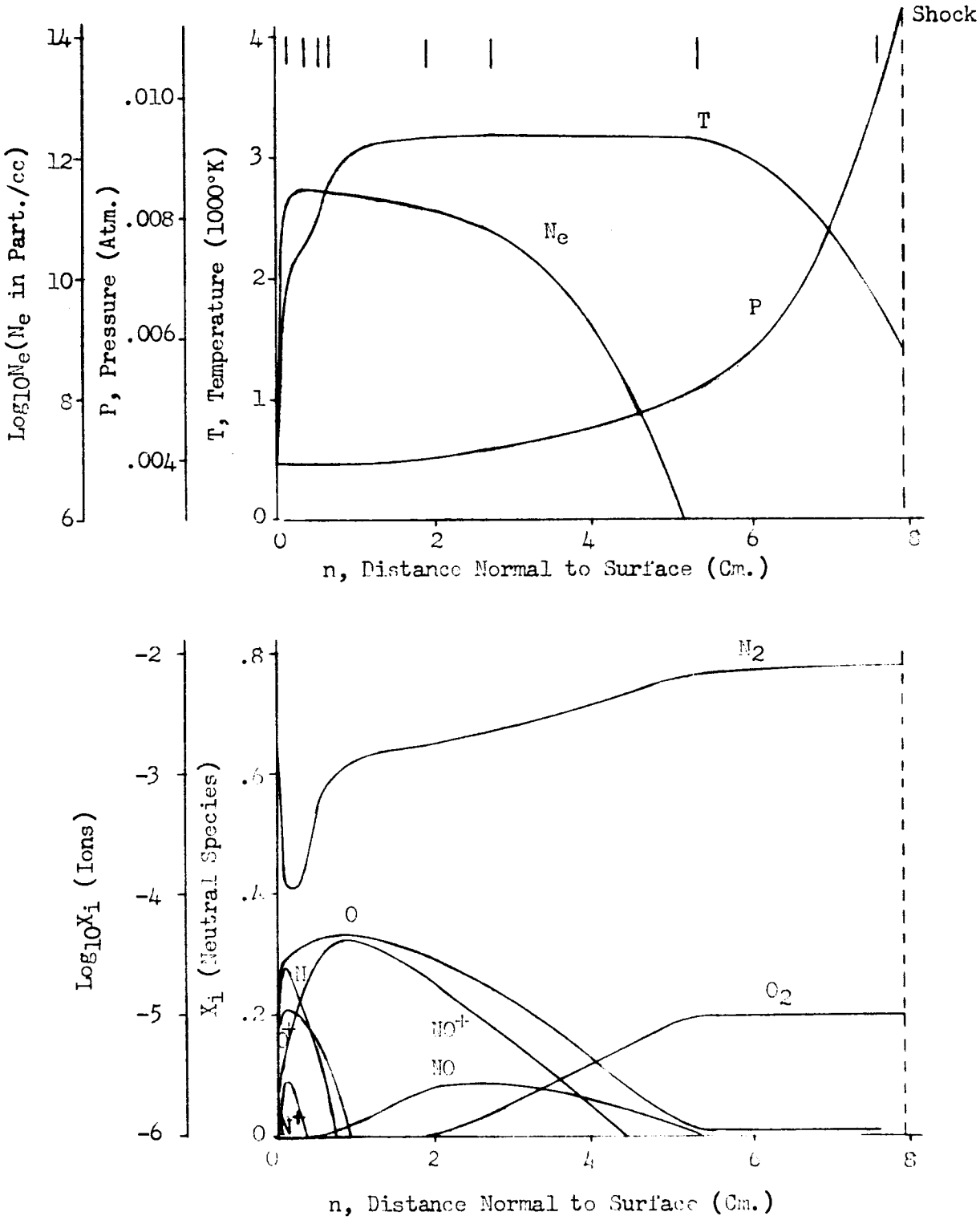

Figure 33e. Flow Field Properties - Case 9, Normal 5

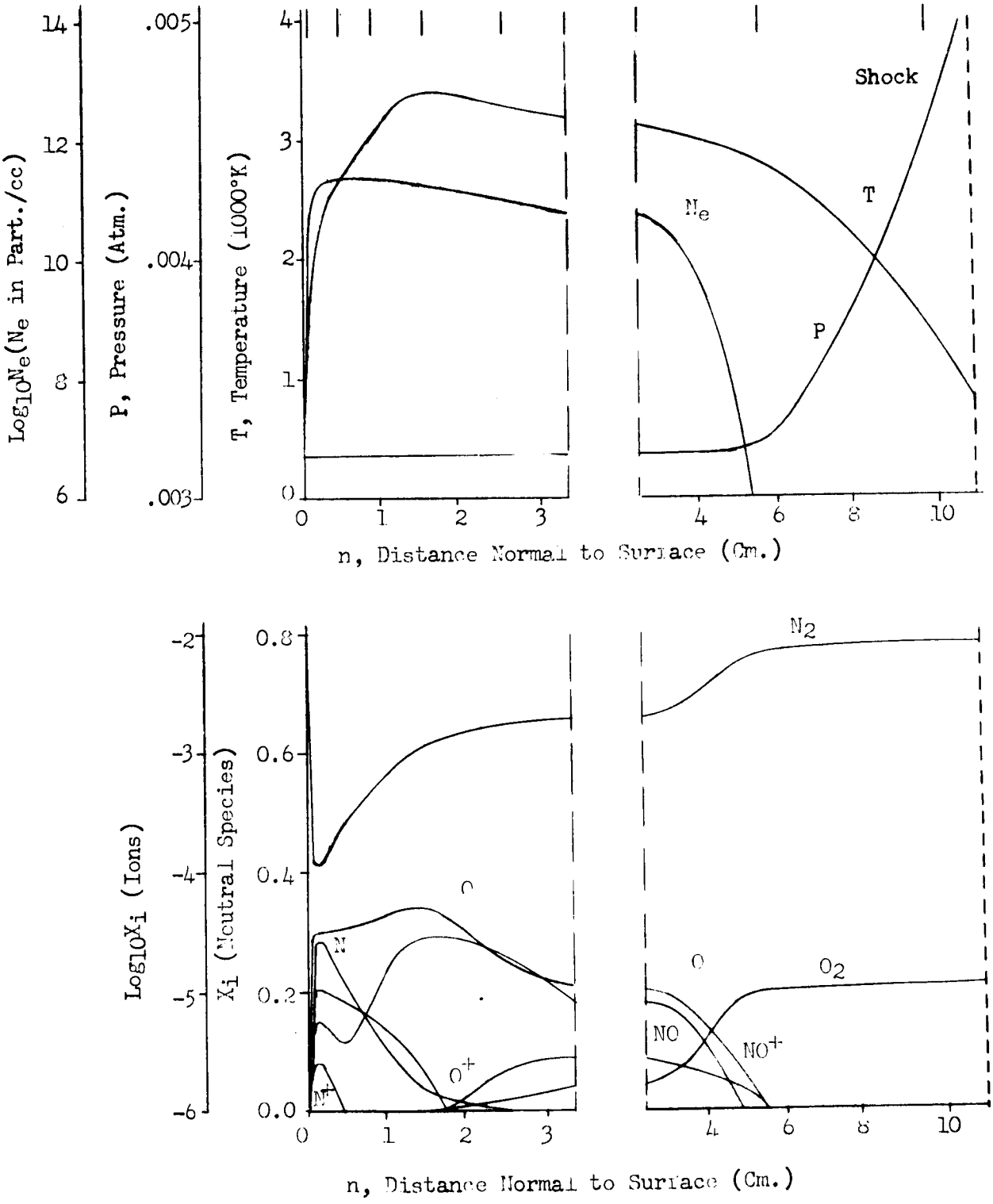

Figure 33f. Flow Field Properties - Case 9, Normal 6

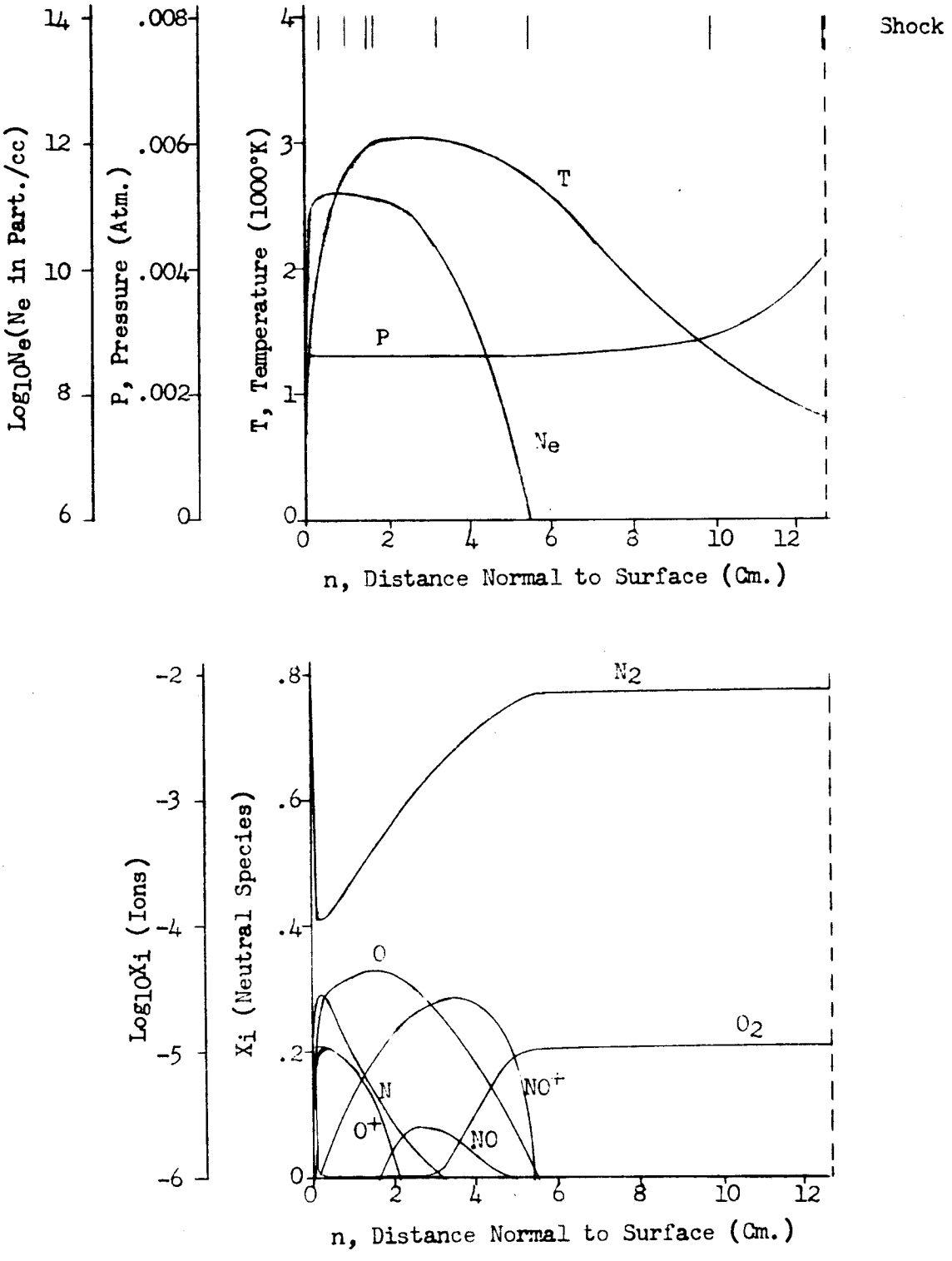

Figure 33g. Flow Field Properties - Case 9, Normal 7

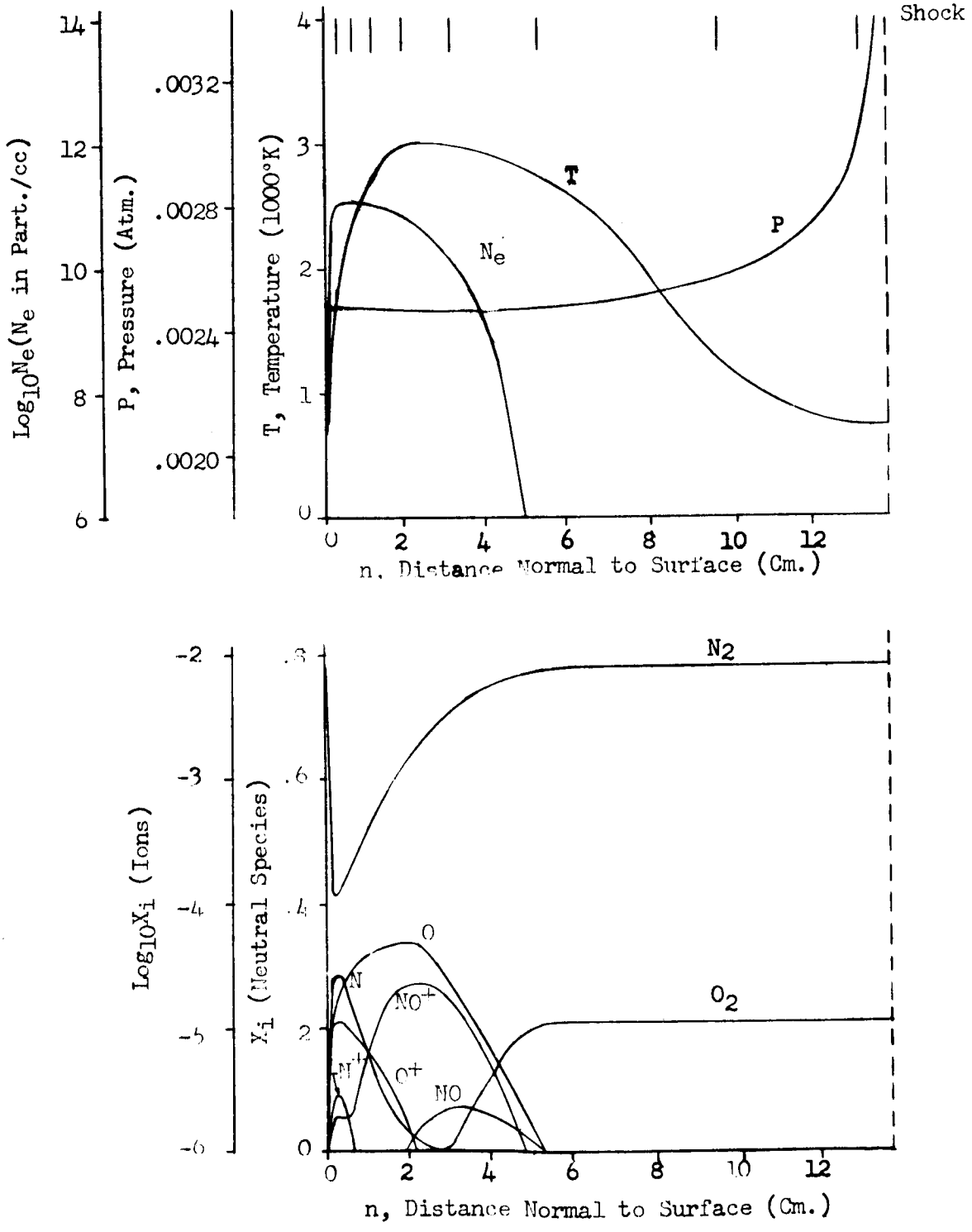

Figure 33h. Flow Field Properties - Case 9, Normal 8

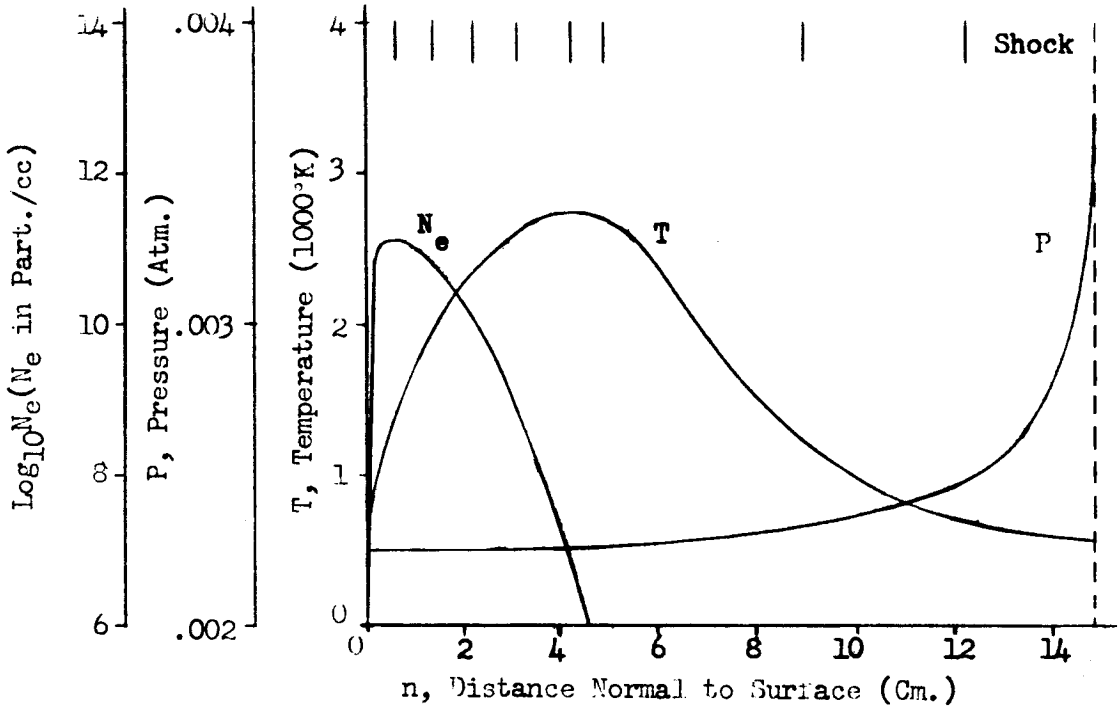

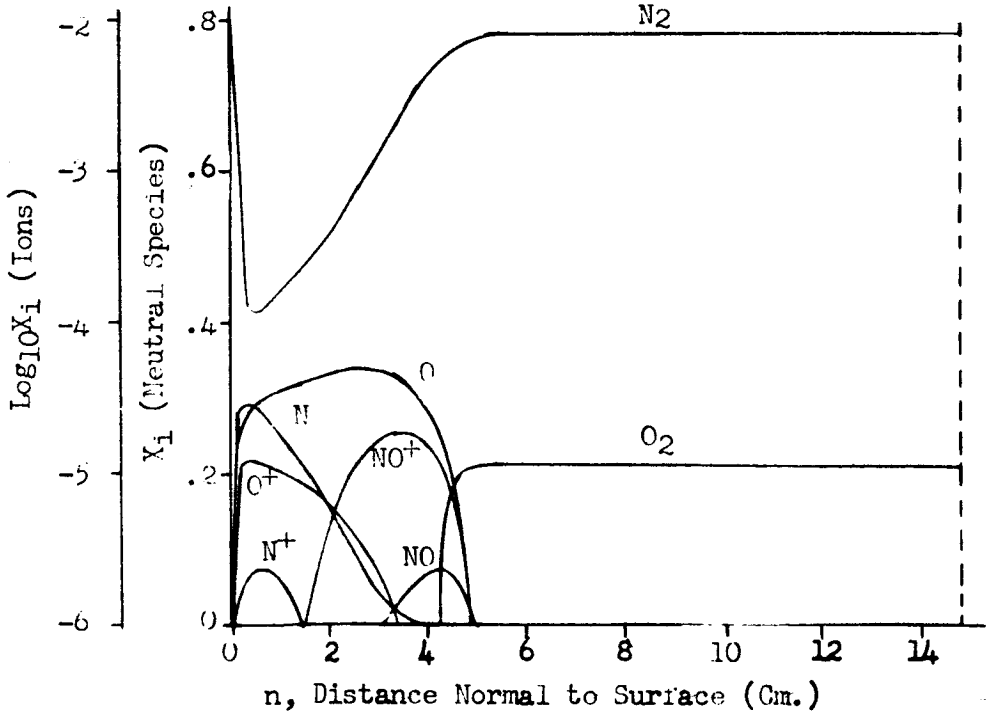

Figure 33i. Flow Field Properties - Case 9, Normal 9

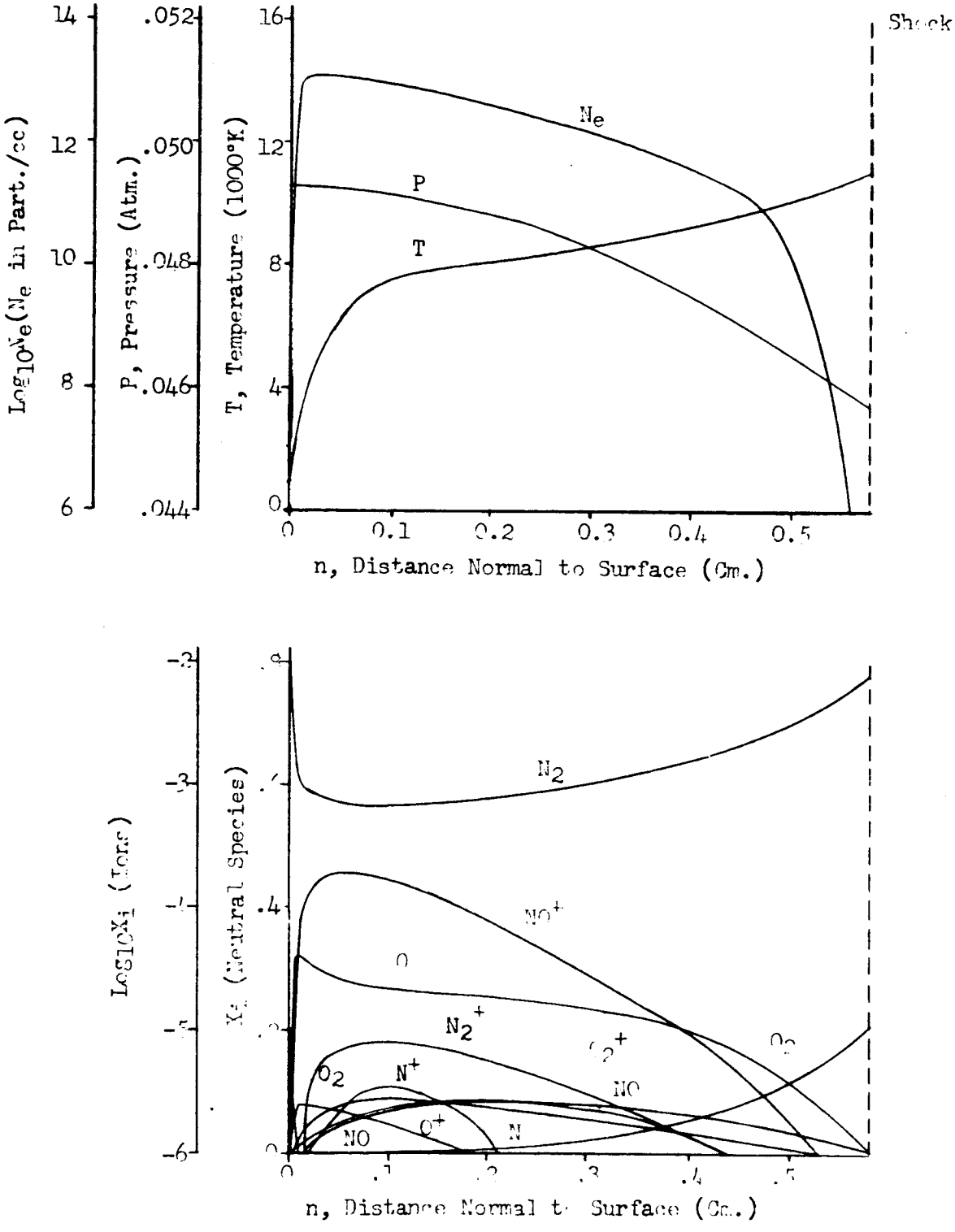

Figure 34a. Flow Field Properties - Case 10, Normal 1

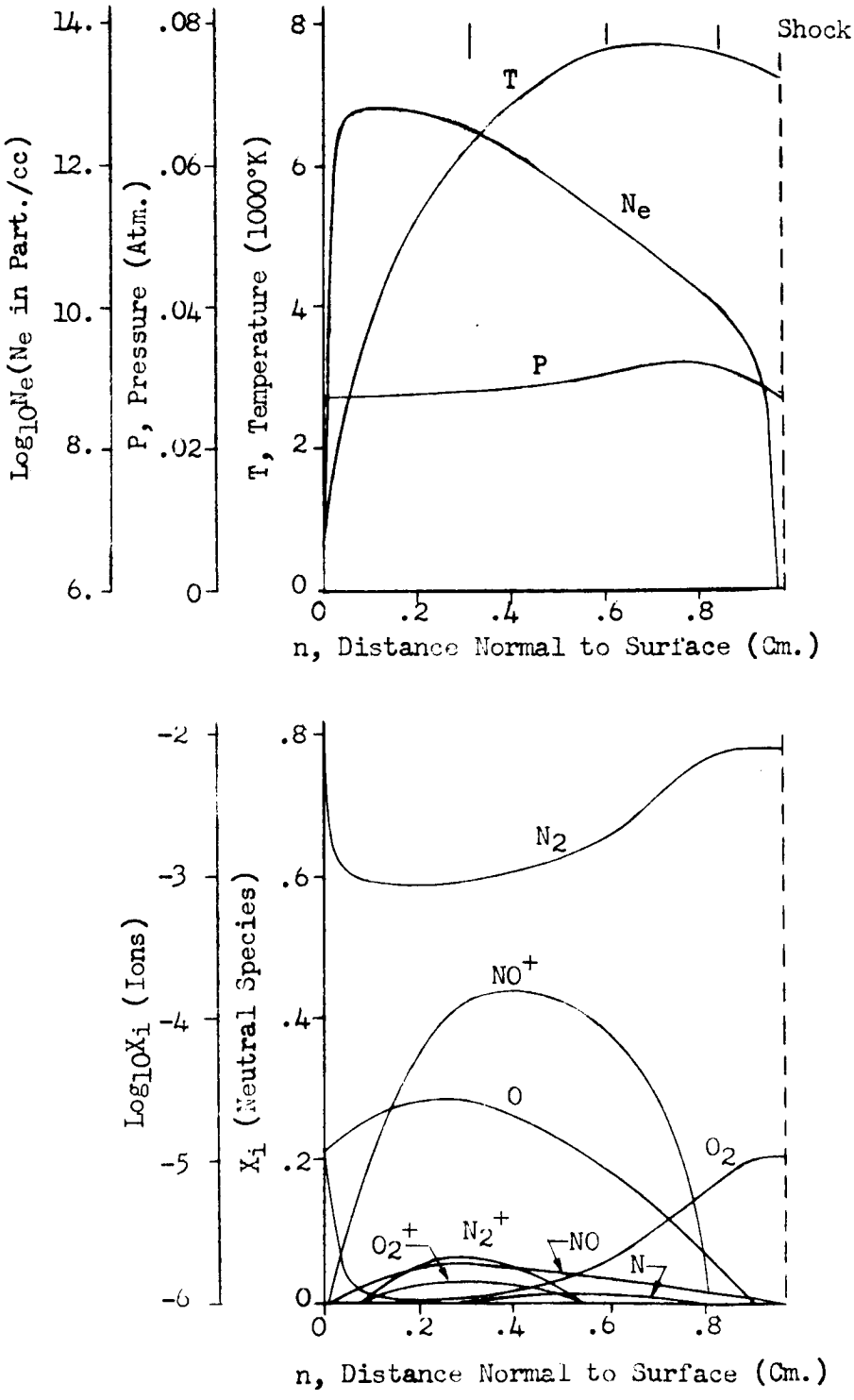

Figure 34b. Flow Field Properties - Case 10, Normal 2

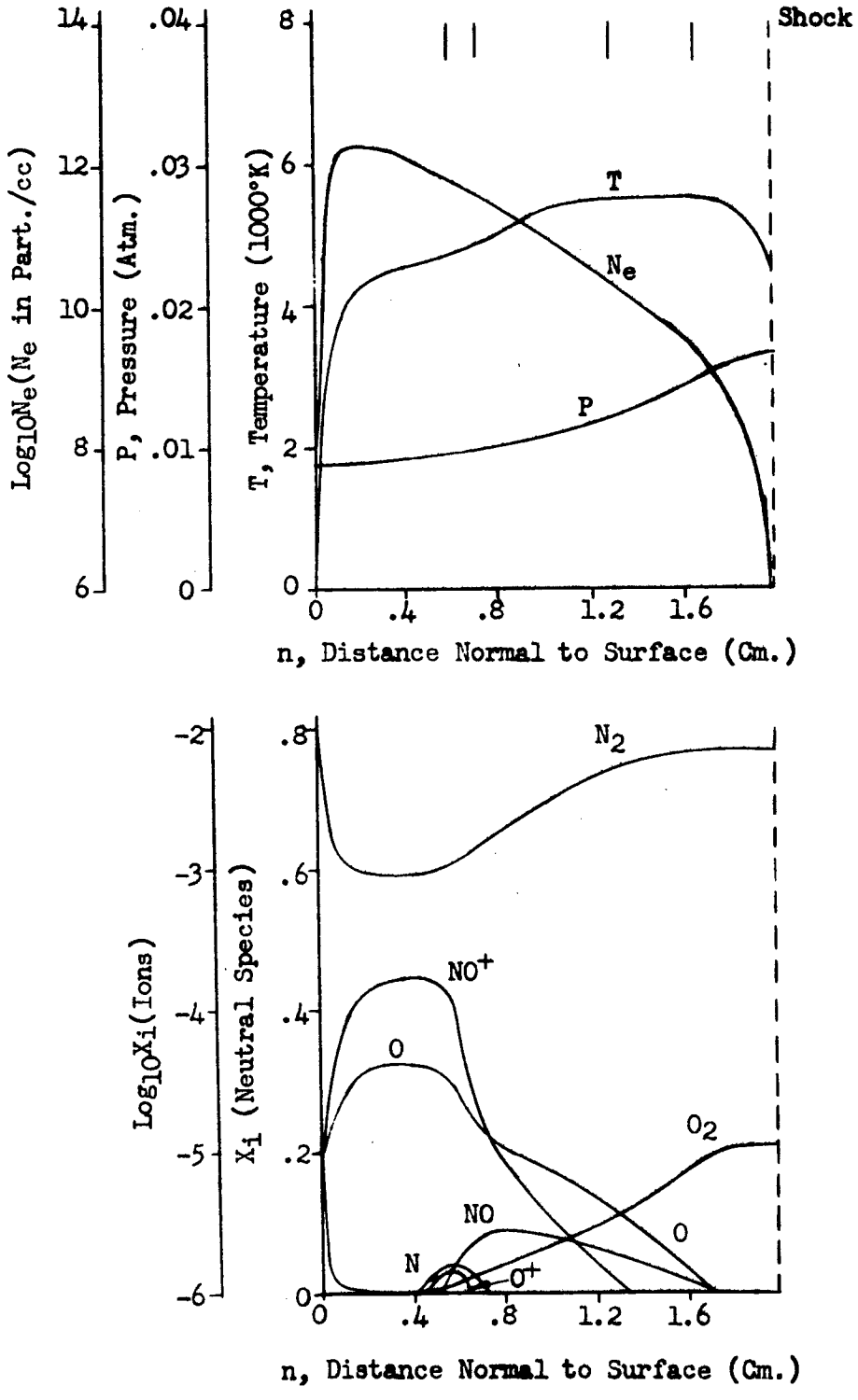

Figure 34c. Flow Field Properties - Case 10, Normal 3

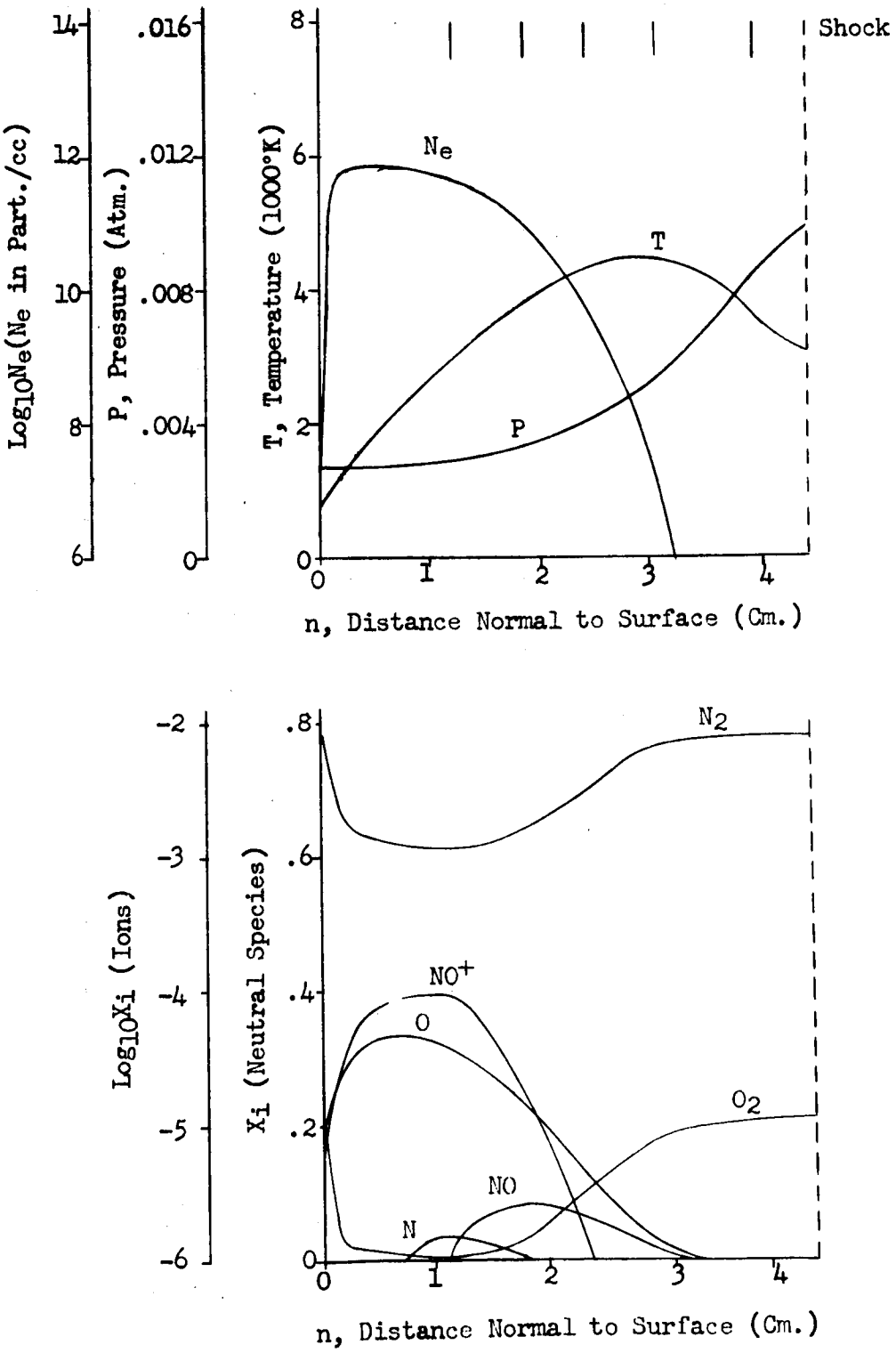

Figure 34d. Flow Field Properties - Case 10, Normal 4

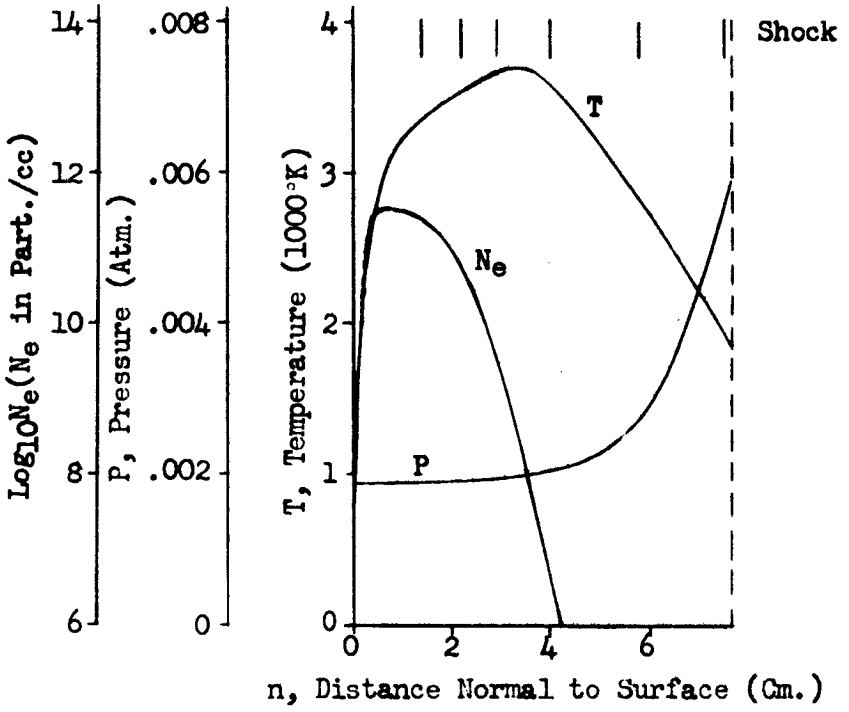

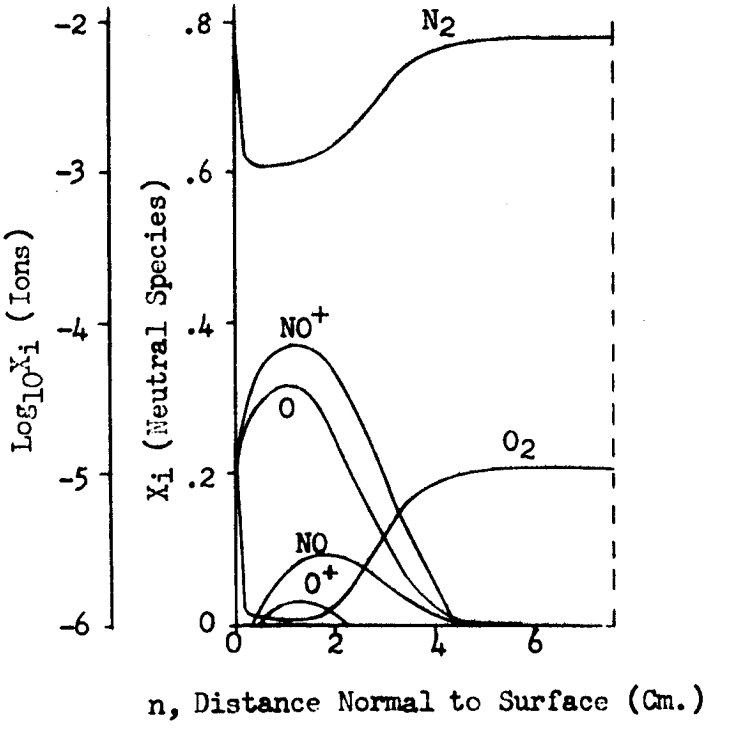

Figure 34e. Flow Field Properties - Case 10, Normal 5

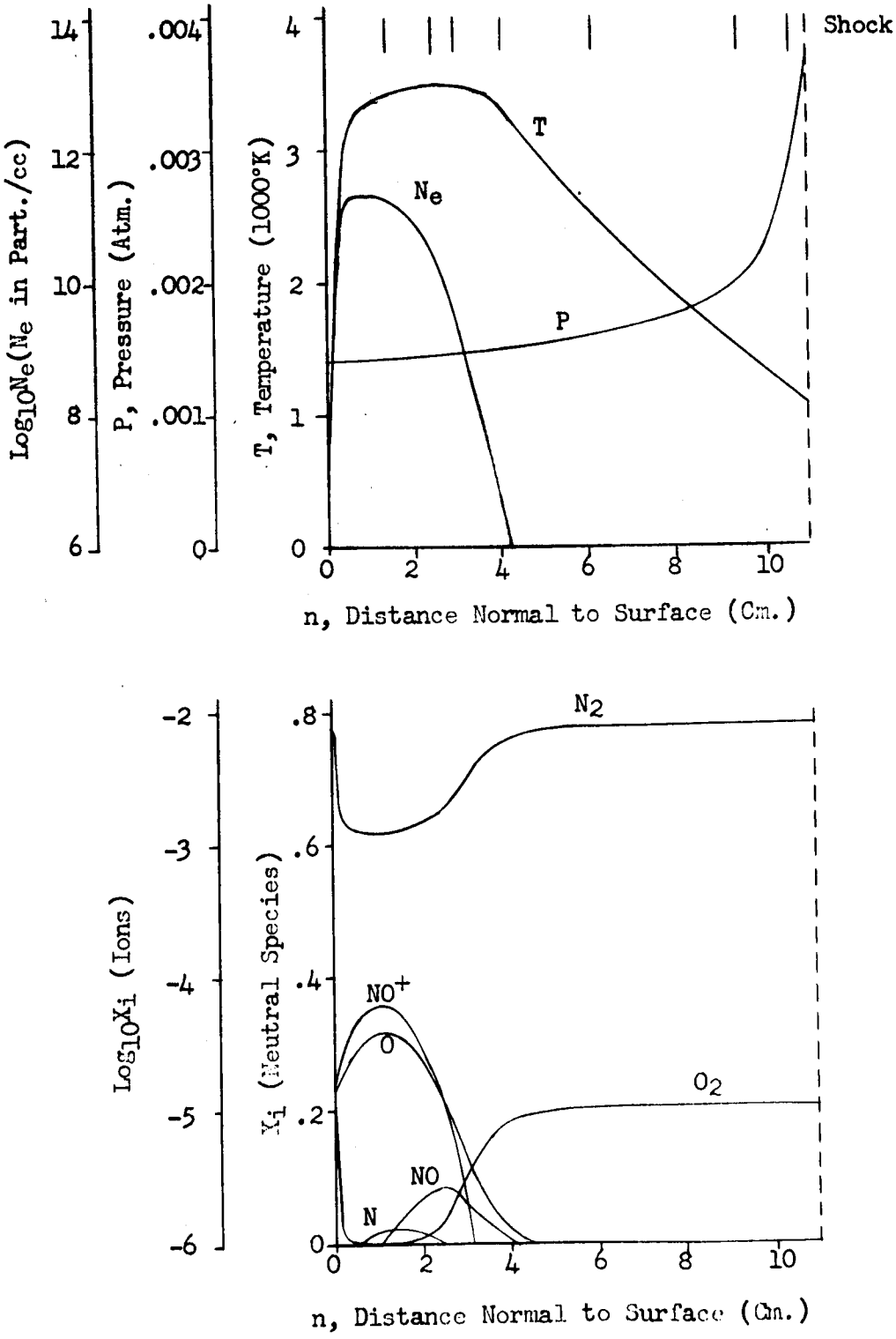

Figure 34f. Flow Field Properties - Case 10, Normal 6

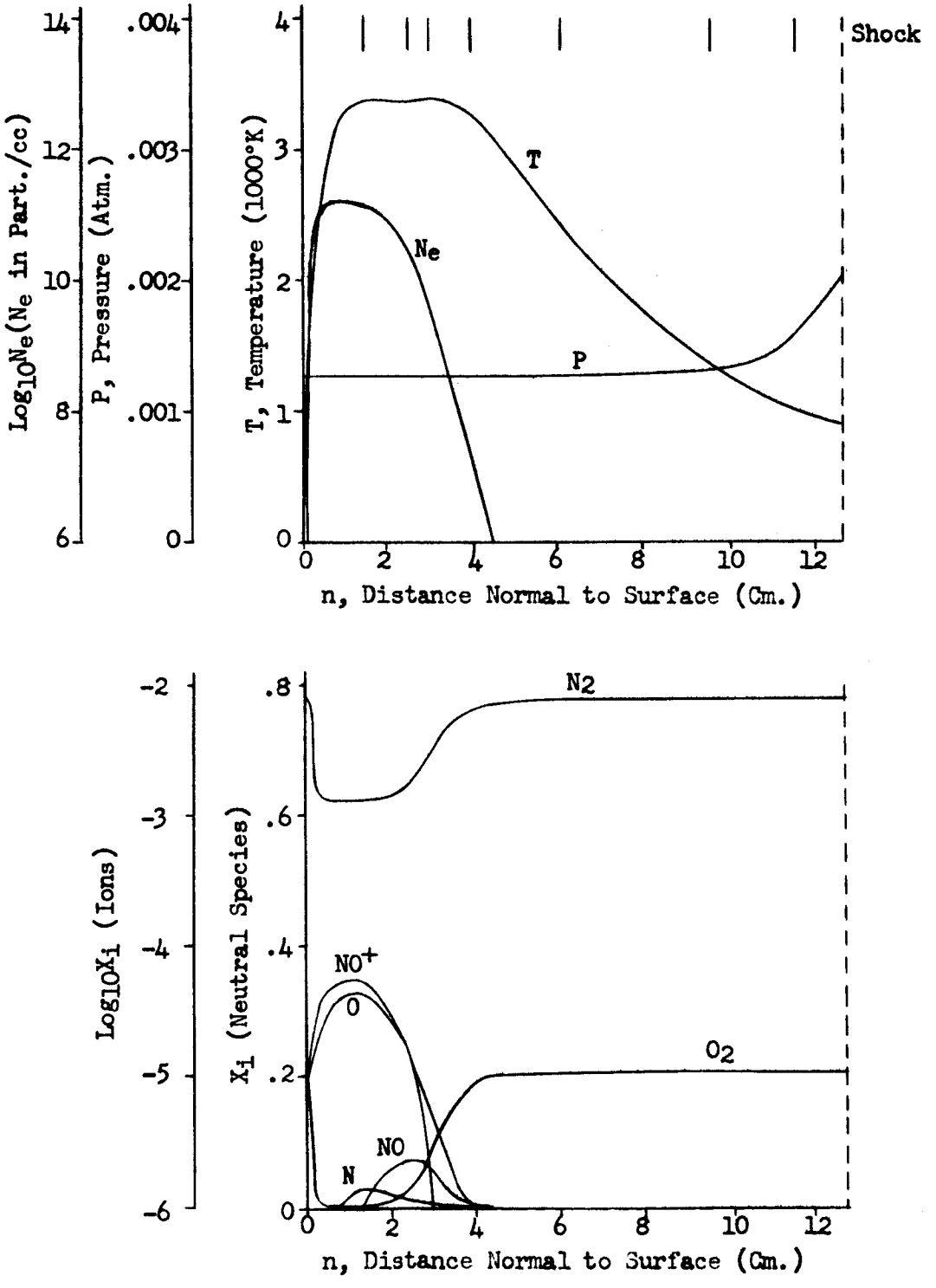

Figure 34g. Flow Field Properties - Case 10, Normal 7

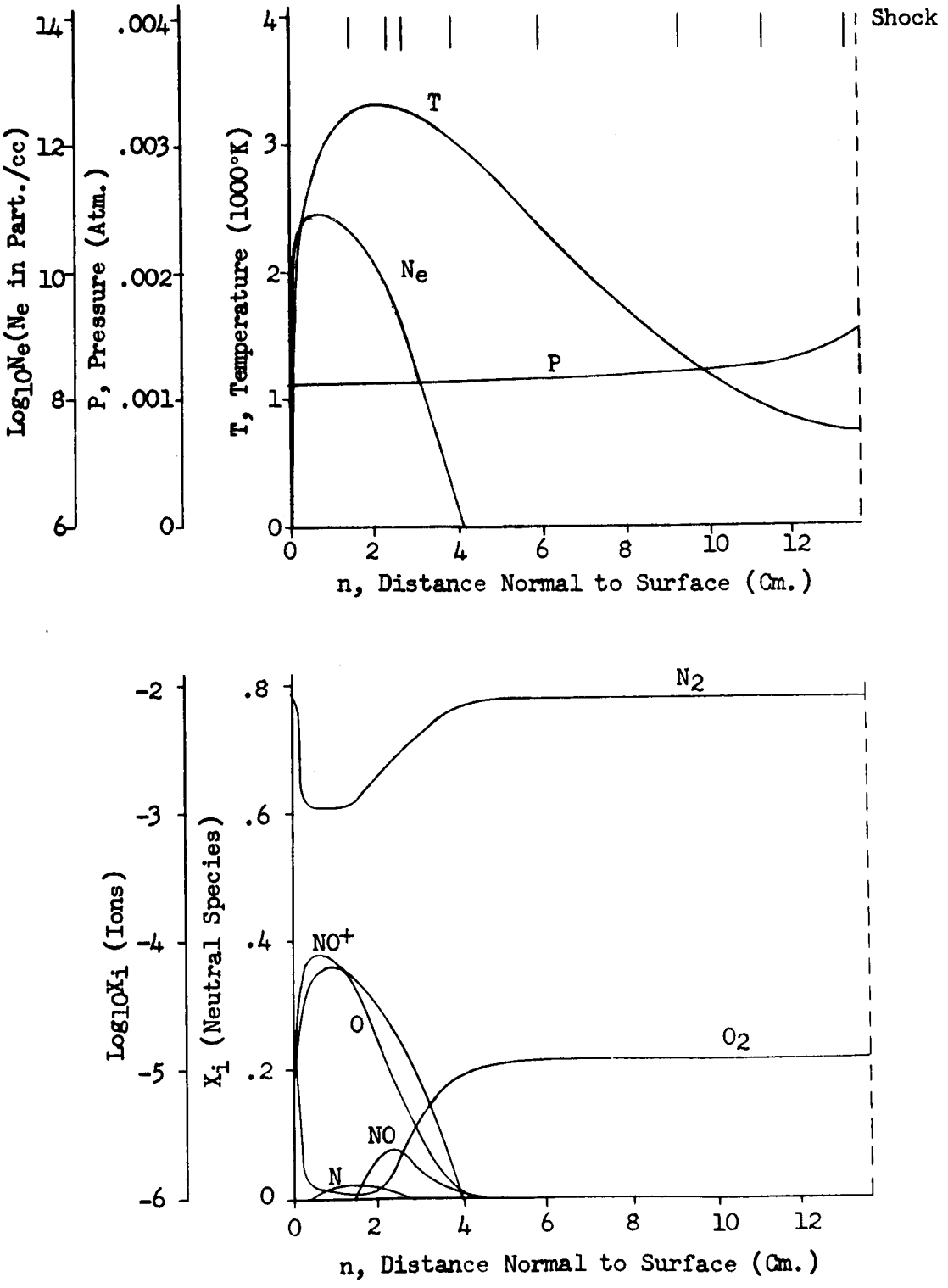

Figure 34h. Flow Field Properties - Case 10, Normal 8

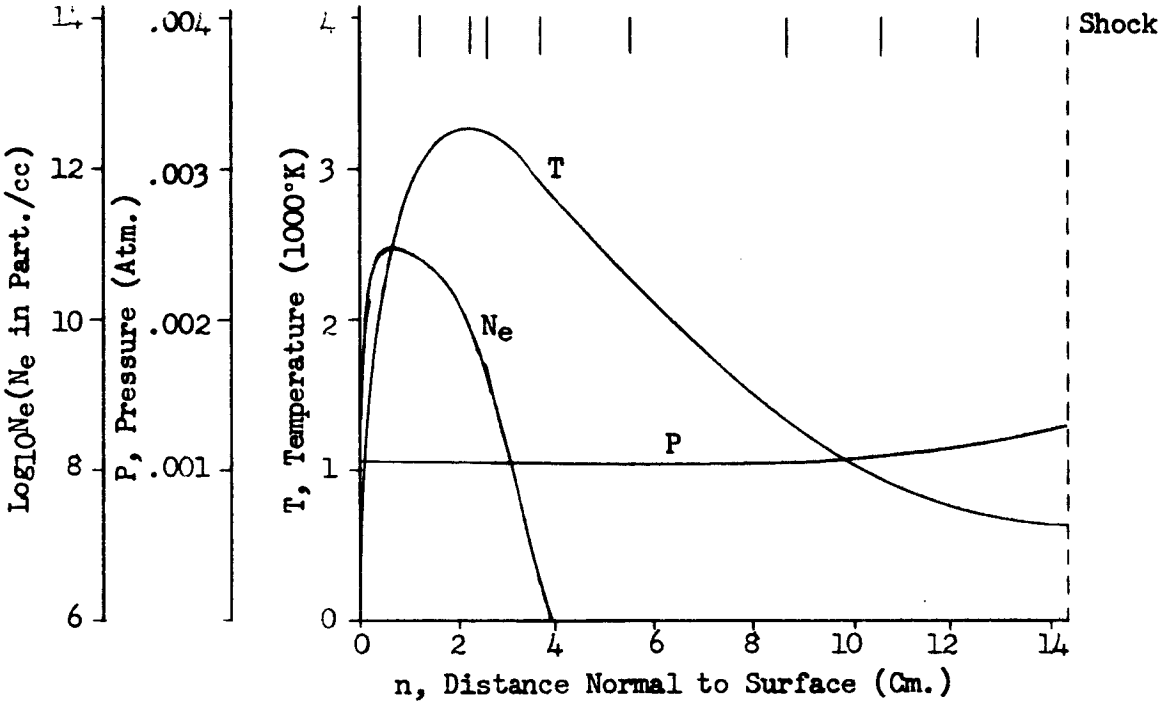

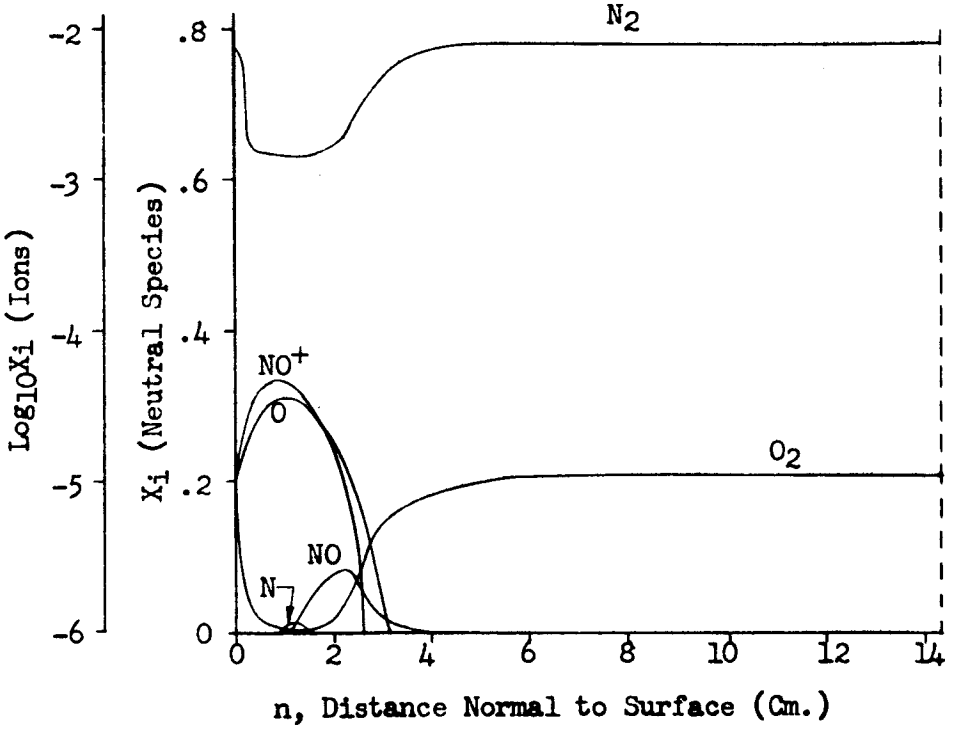

Figure 34i. Flow Field Properties - Case 10, Normal 9

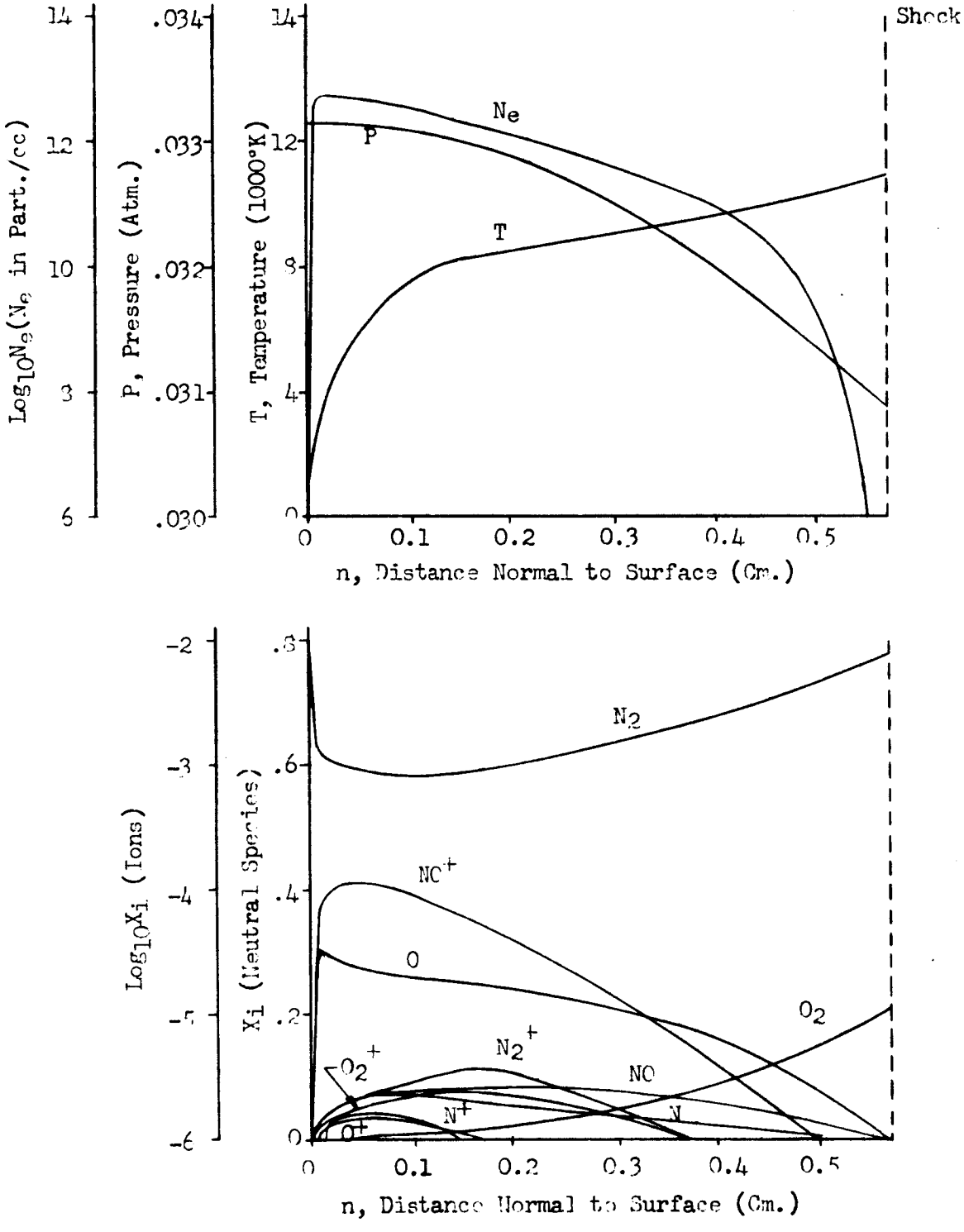

Figure 35a. Flow Field Properties - Case 11, Normal 1

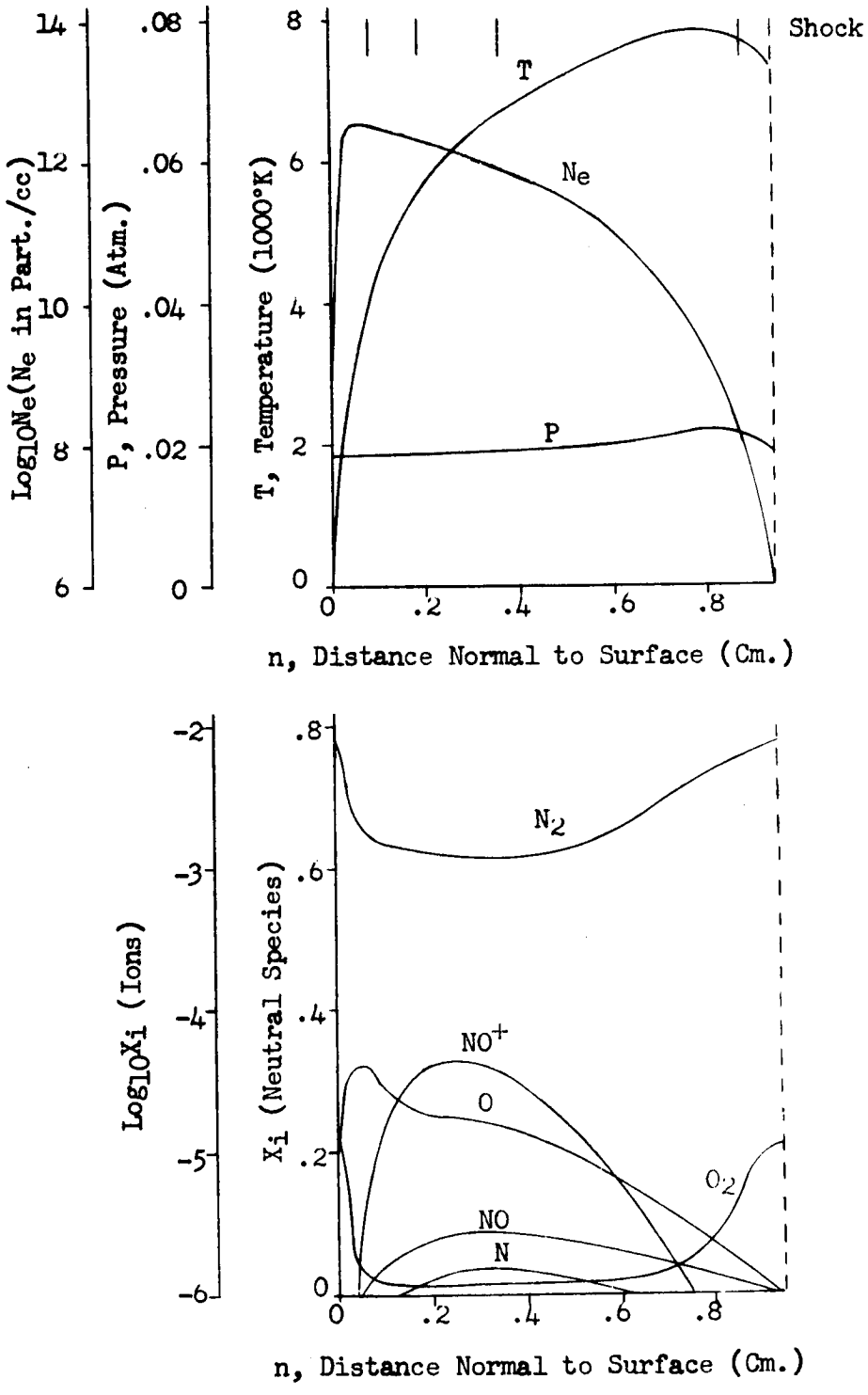

Figure 35b. Flow Field Properties - Case 11, Normal 2

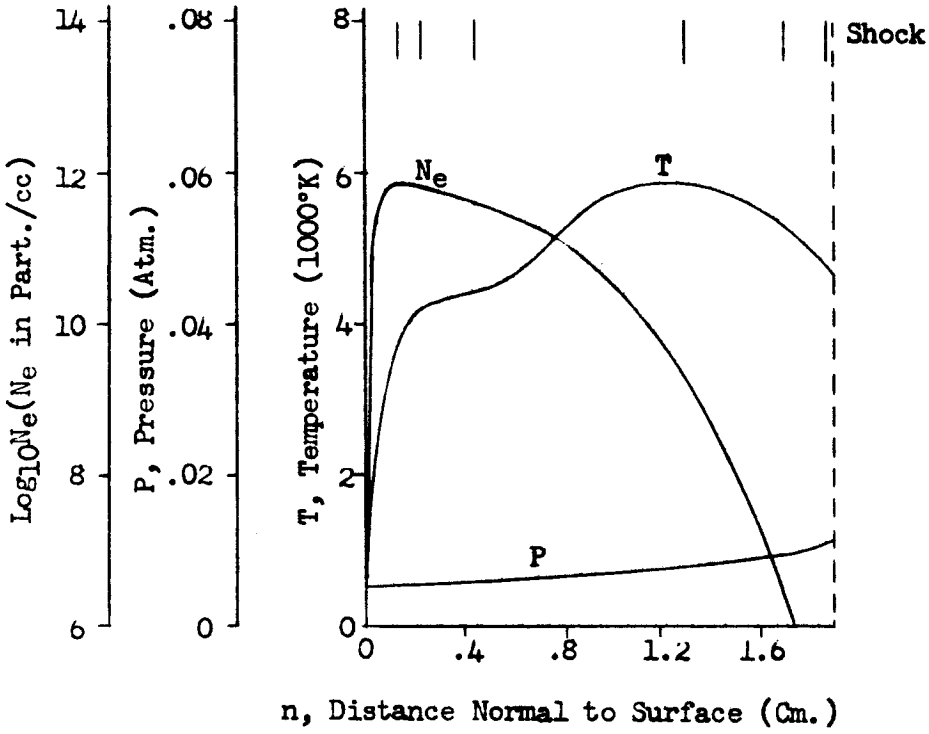

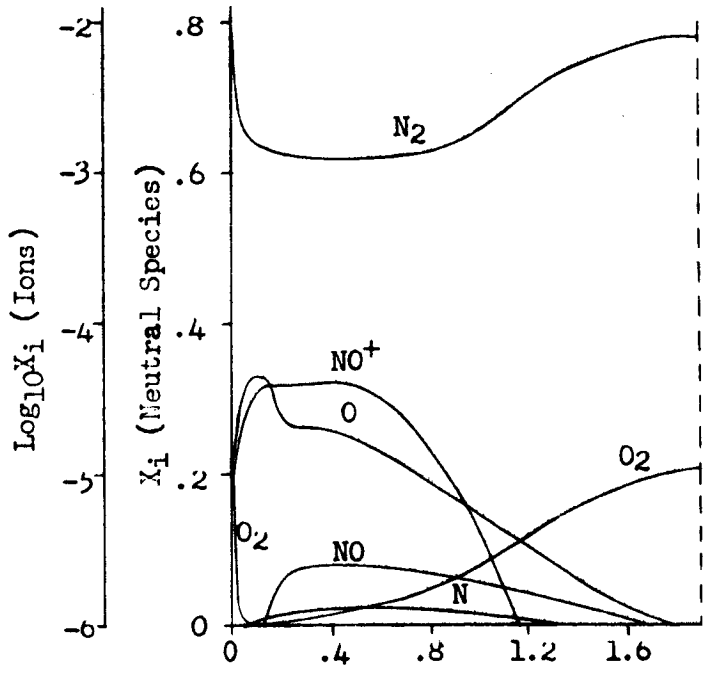

Figure 35c. Flow Field Properties - Case 11, Normal 3

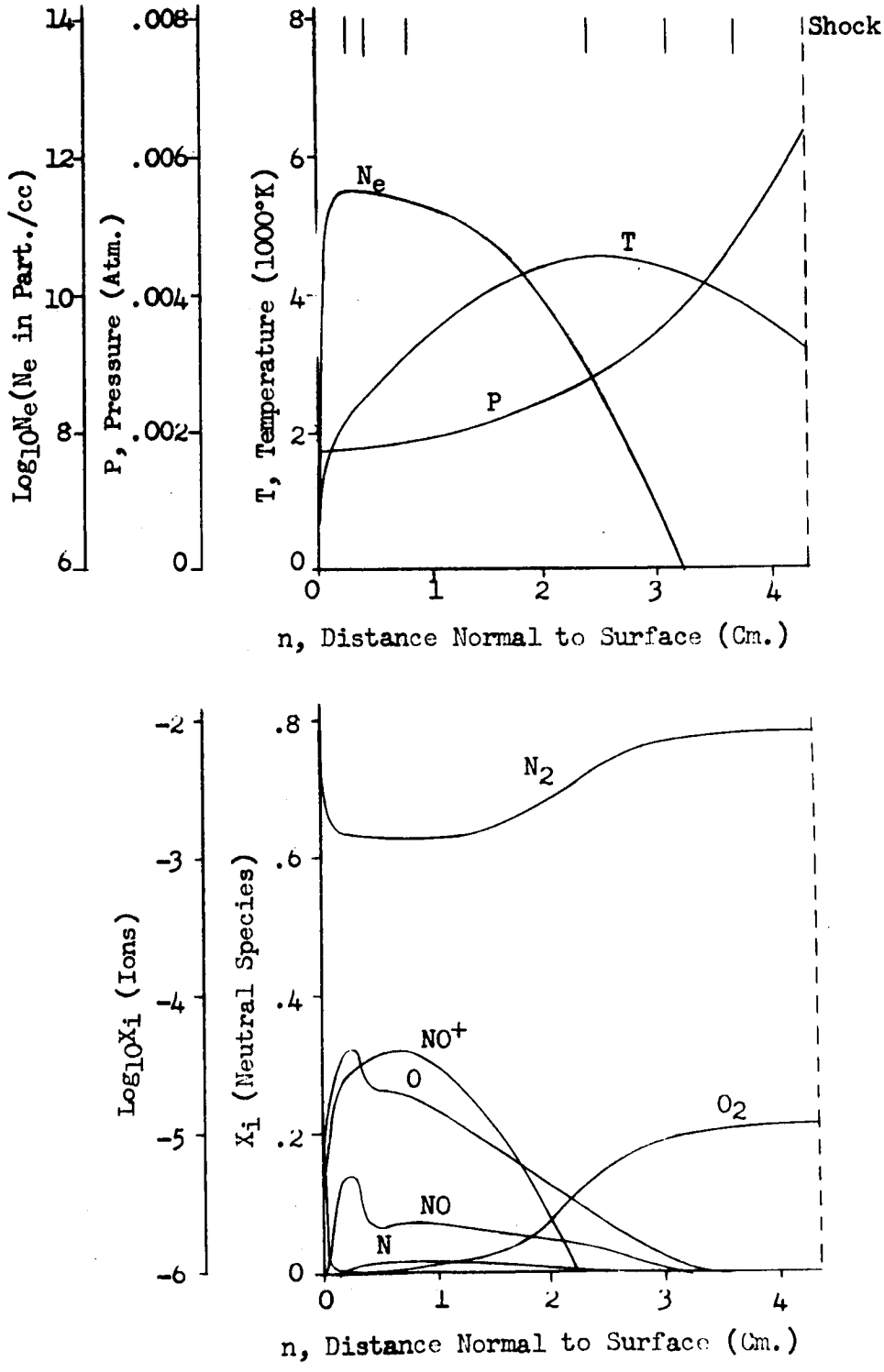

Figure 35d. Flow Field Properties - Case 11, Normal 4

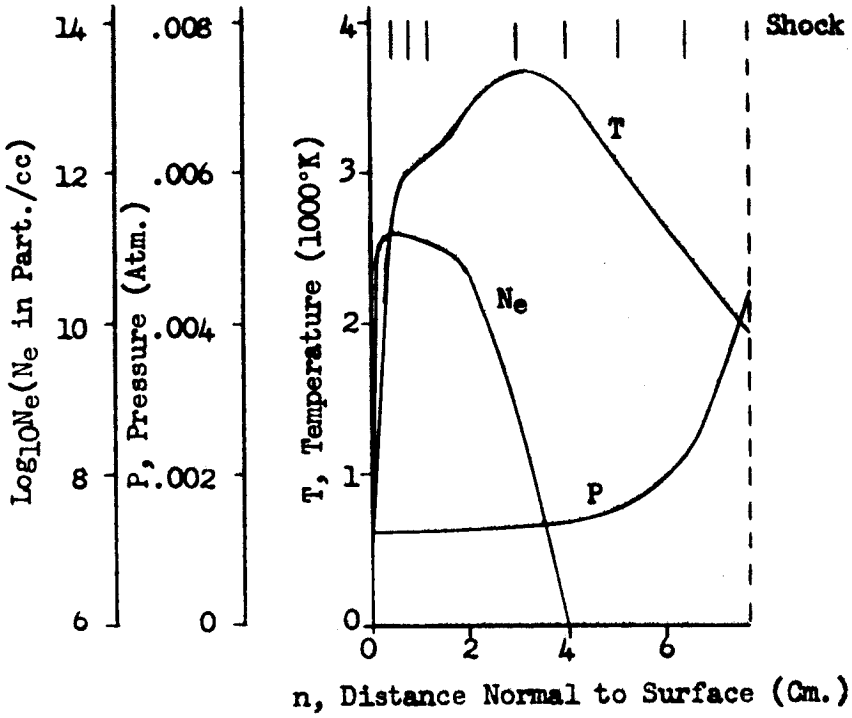

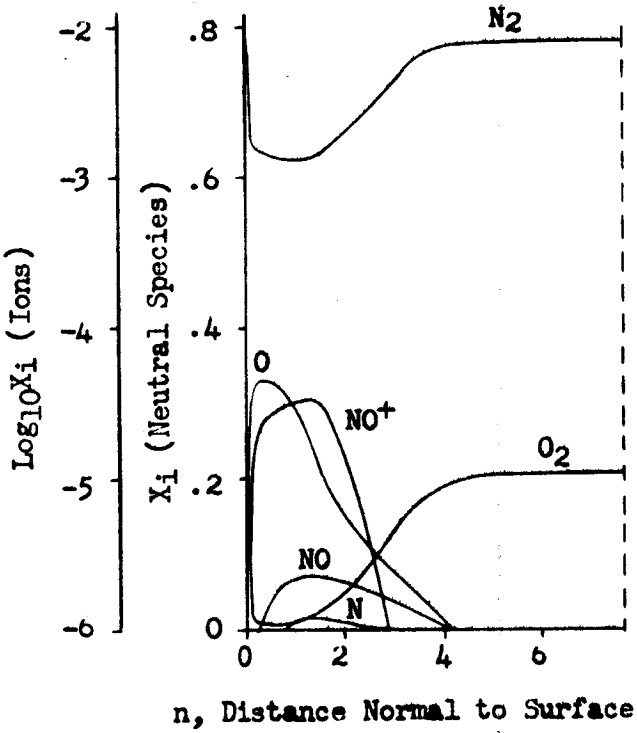

Figure 35e. Flow Field Properties - Case 11, Normal 5

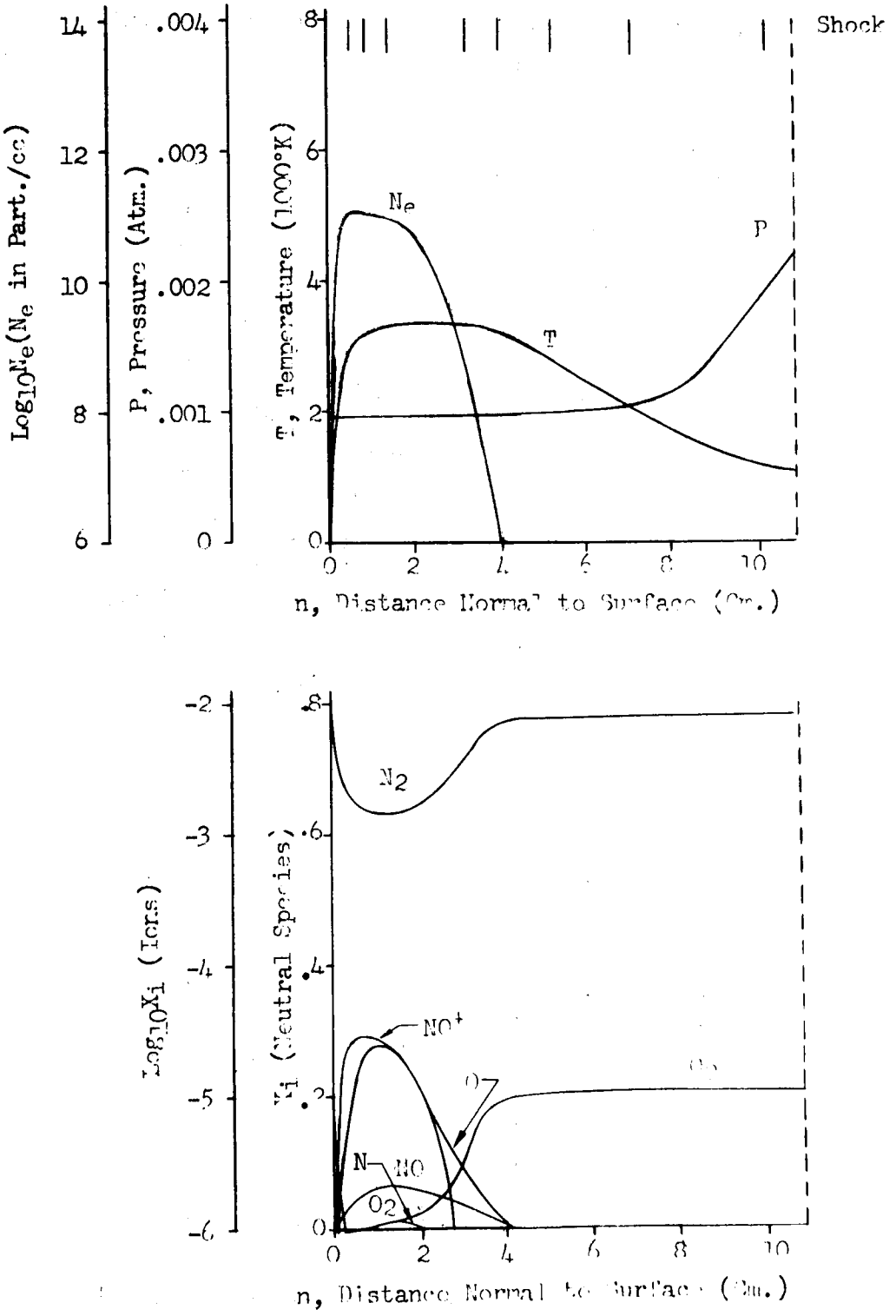

Figure 35f. Flow Field Properties - Case 11, Normal 6

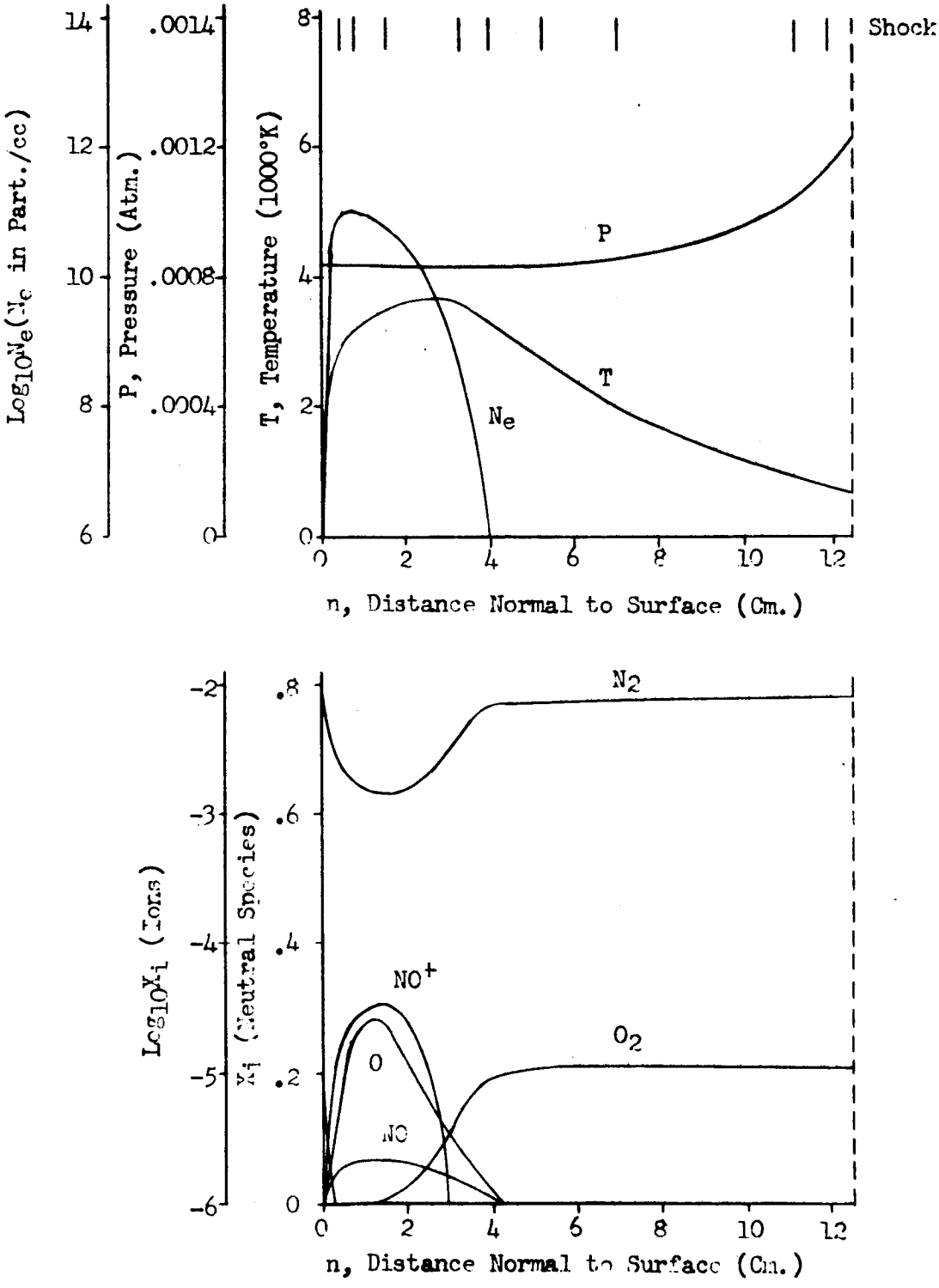

Figure 35g. Flow Field Properties - Case 11, Normal 7

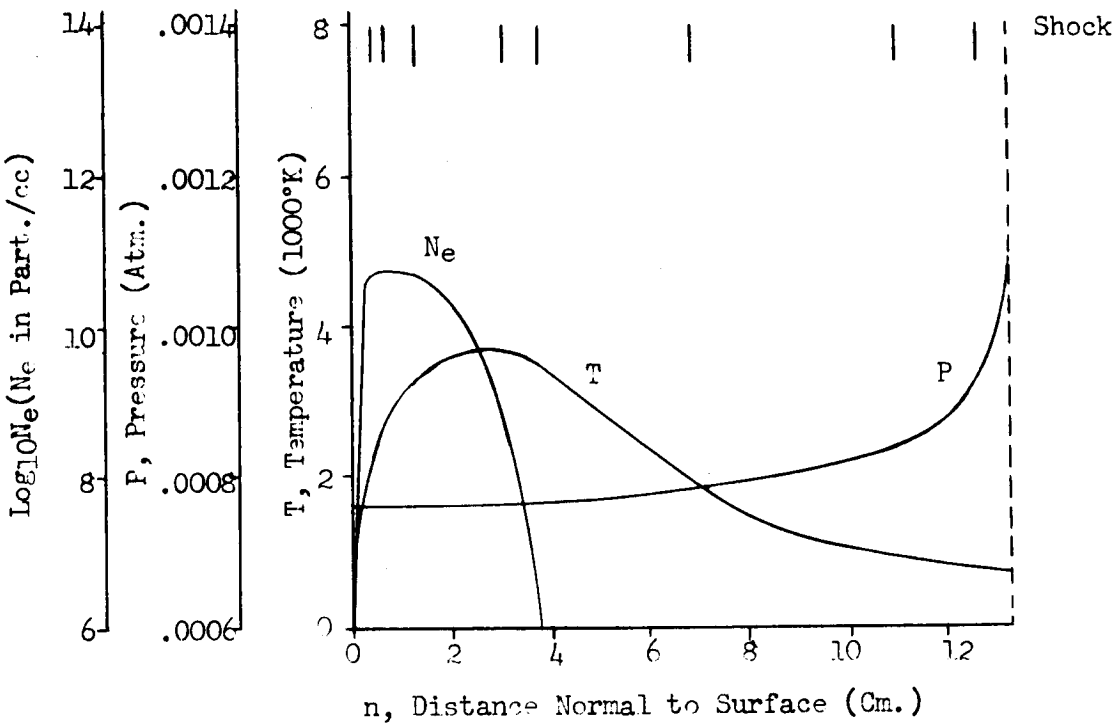

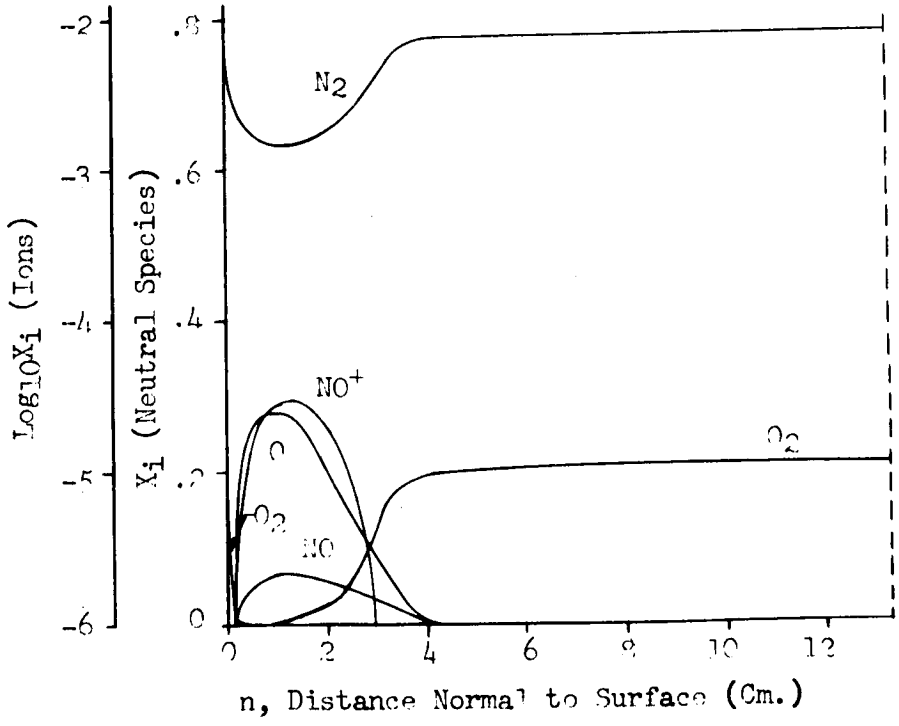

Figure 35h. Flow Field Properties - Case 11, Normal 8

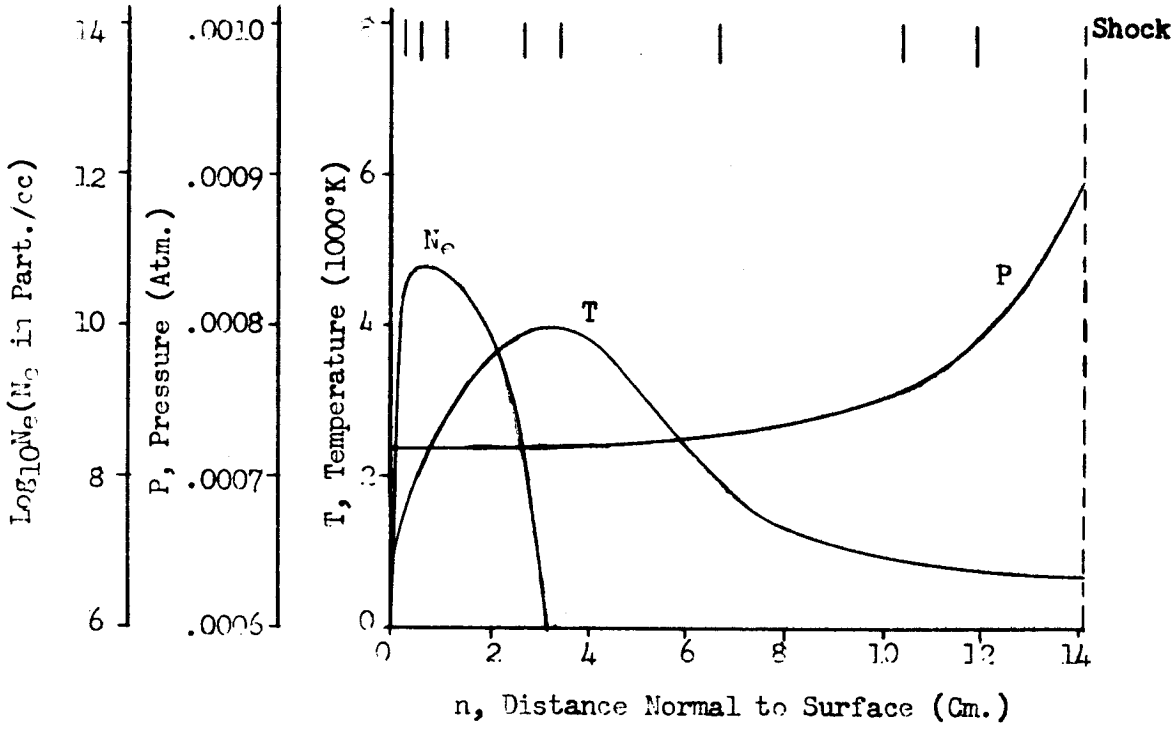

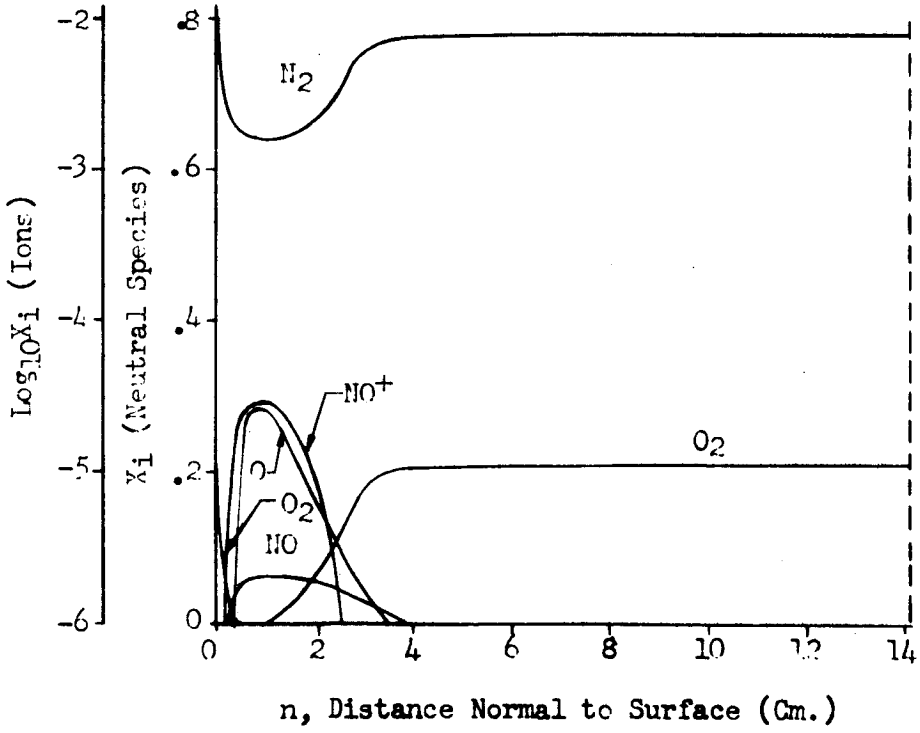

Figure 35i. Flow Field Properties - Case 11, Normal 9

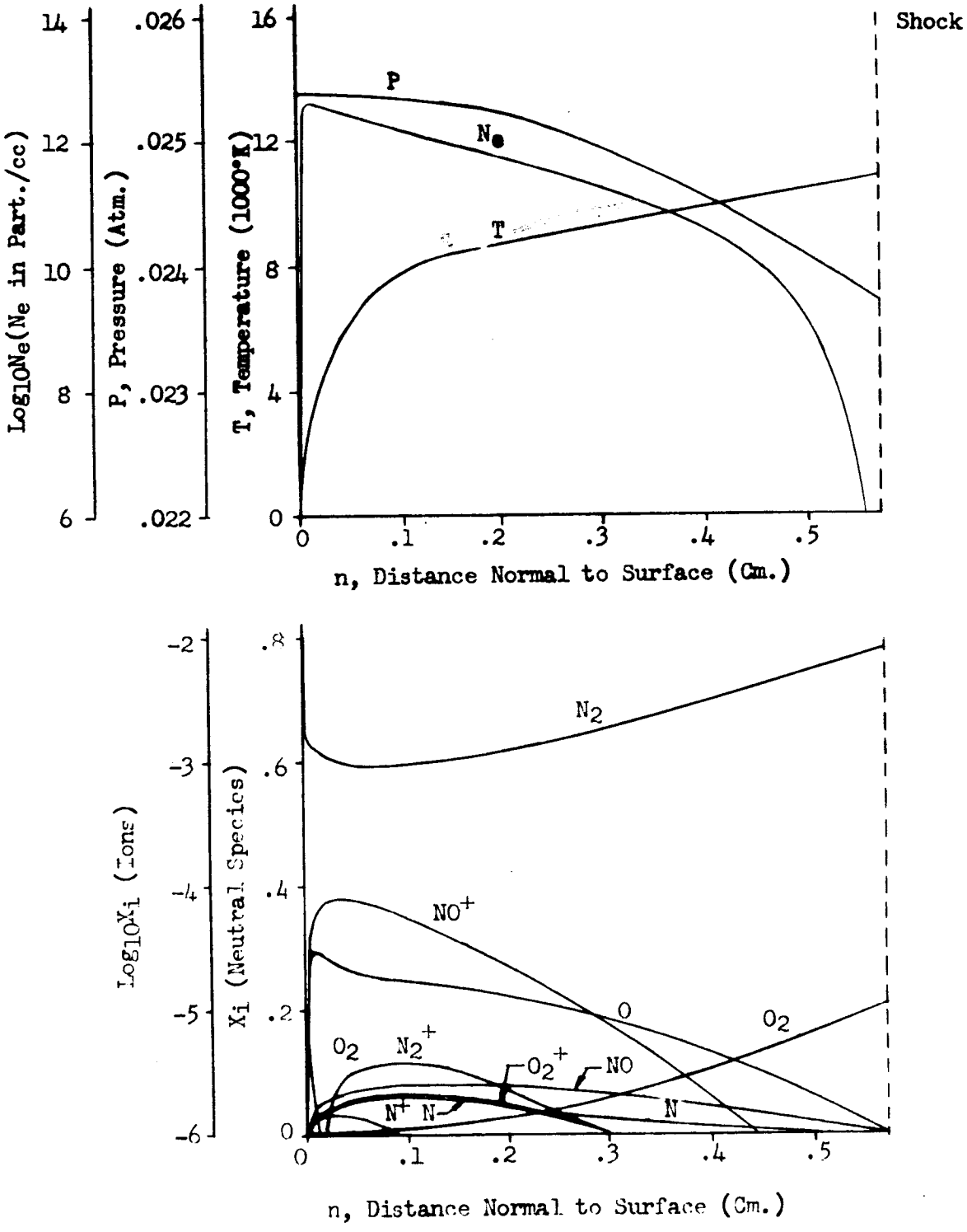

Figure 36a. Flow Field Properties - Case 12, Normal 1

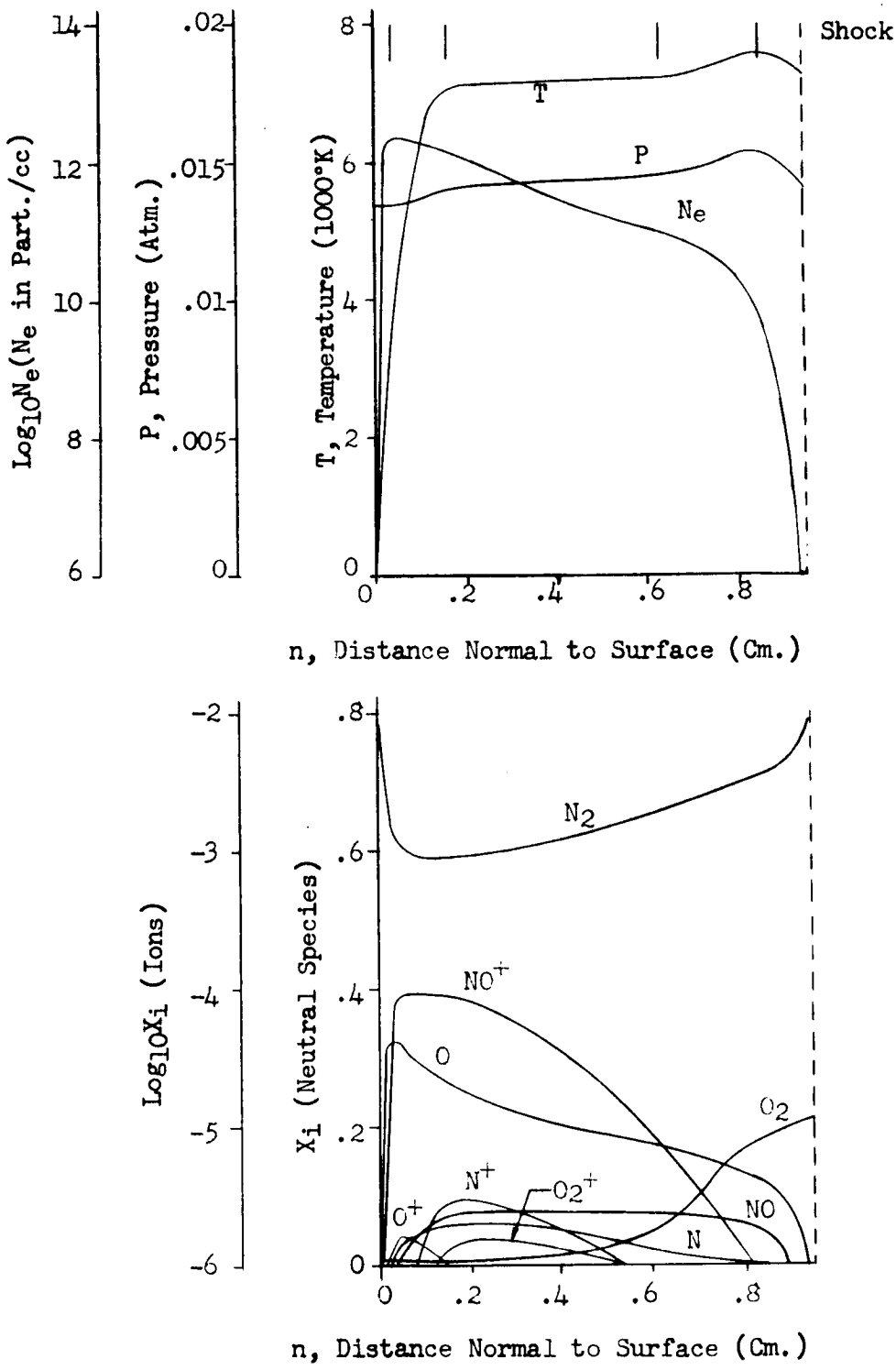

Figure 36b. Flow Field Properties - Case 12, Normal 2

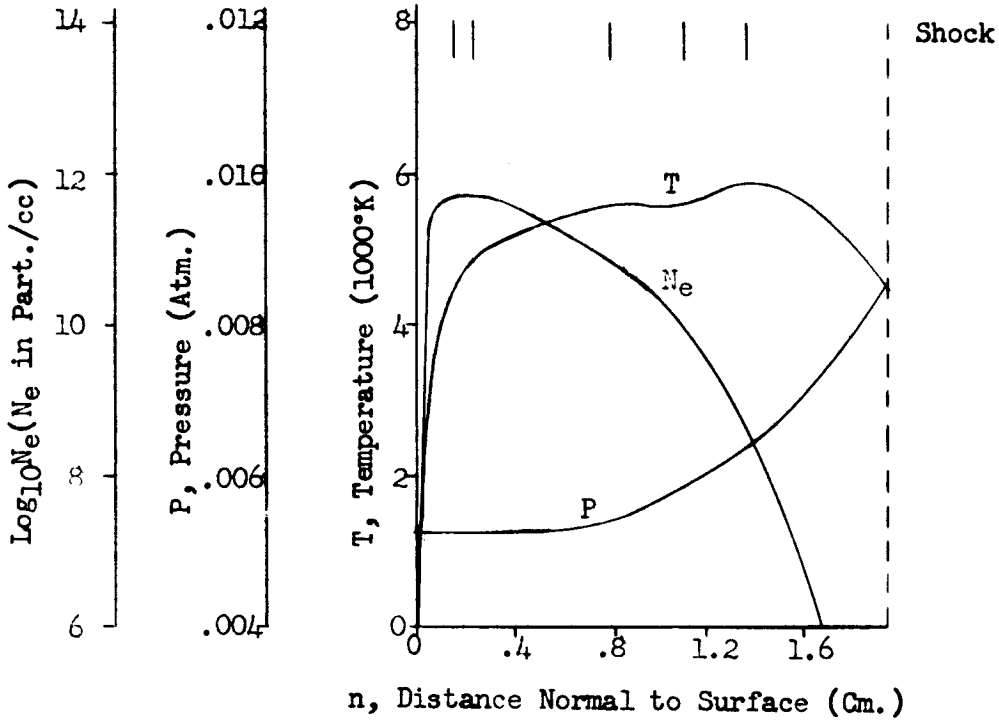

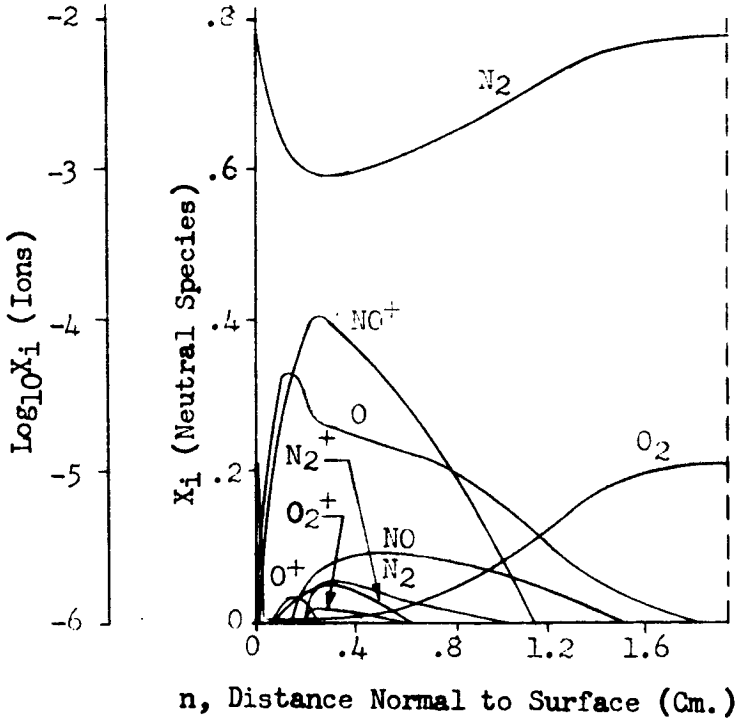

Figure 36c. Flow Field Properties - Case 12, Normal 3

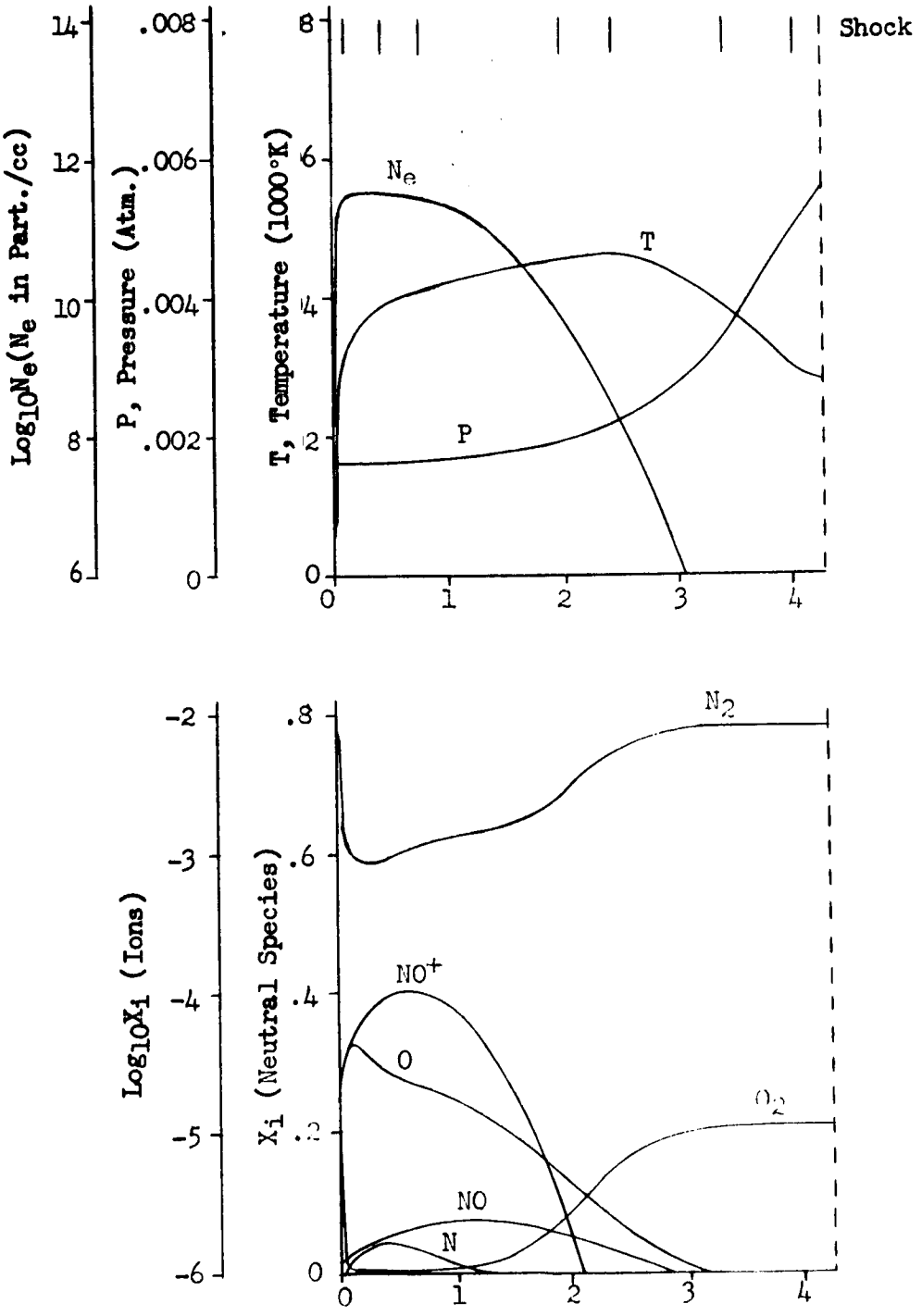

Figure 36d. Flow Field Properties - Case 12, Normal 4

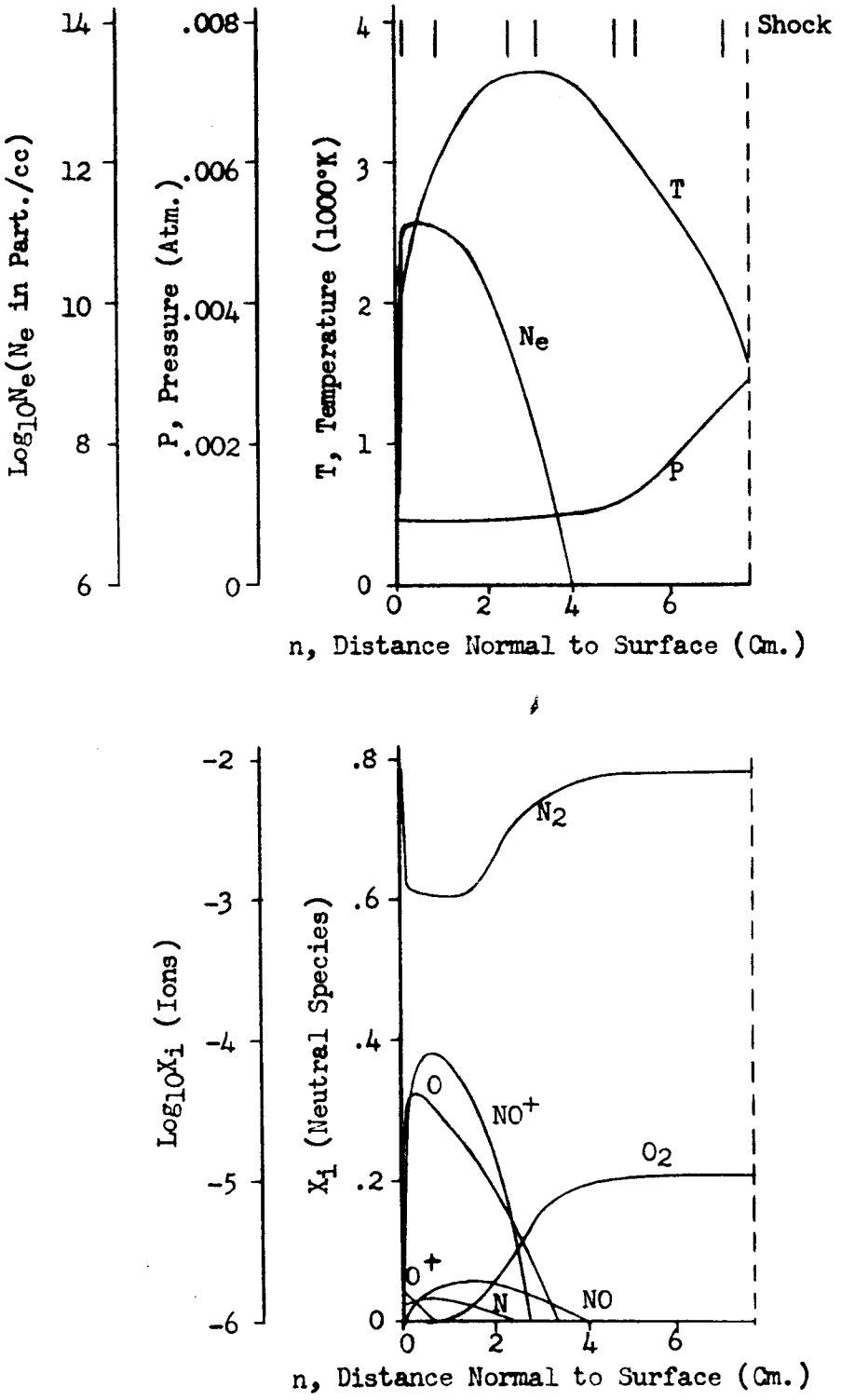

Figure 36e. Flow Field Properties - Case 12, Normal 5

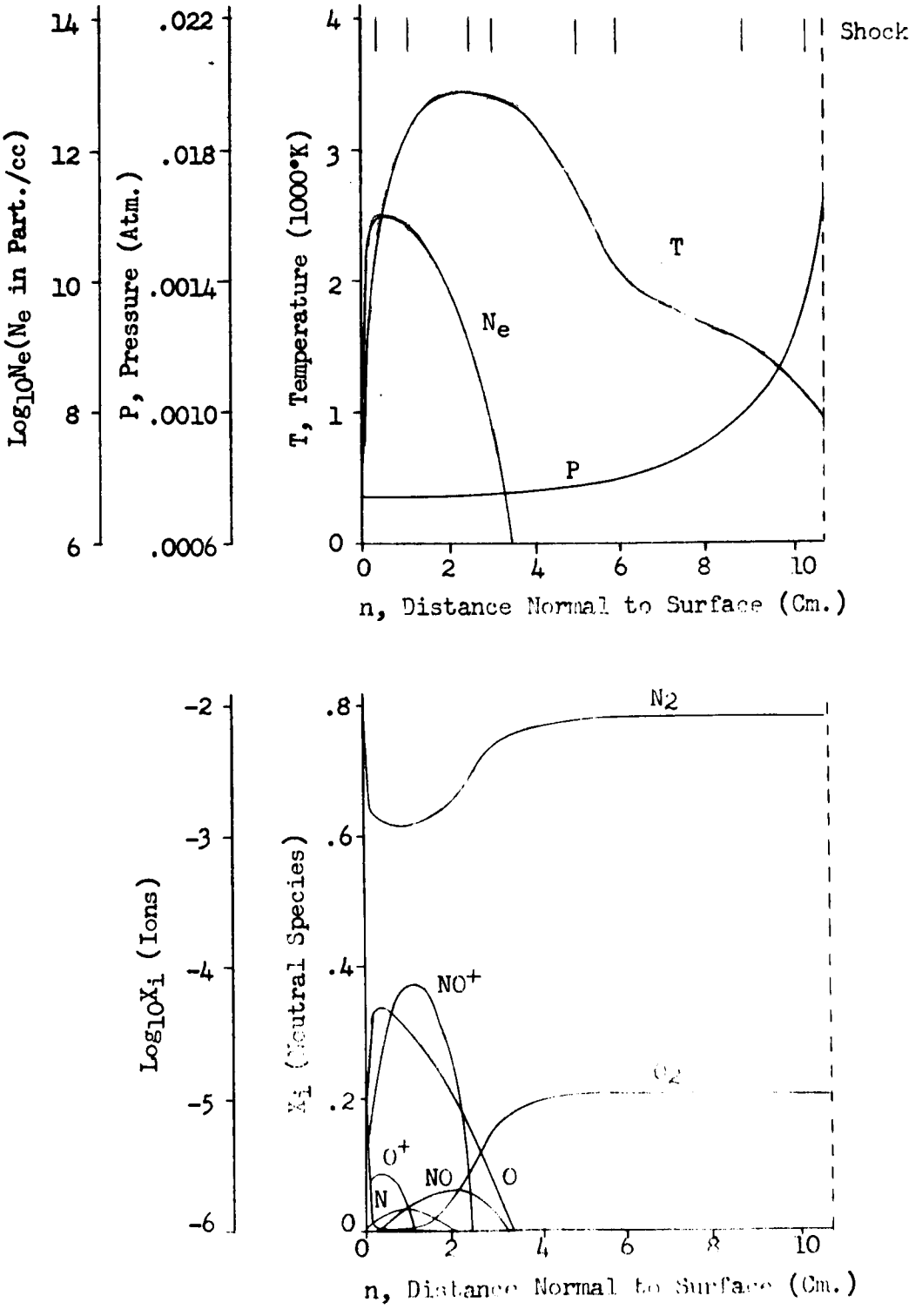

Figure 36f. Flow Field Properties - Case 12, Normal 6

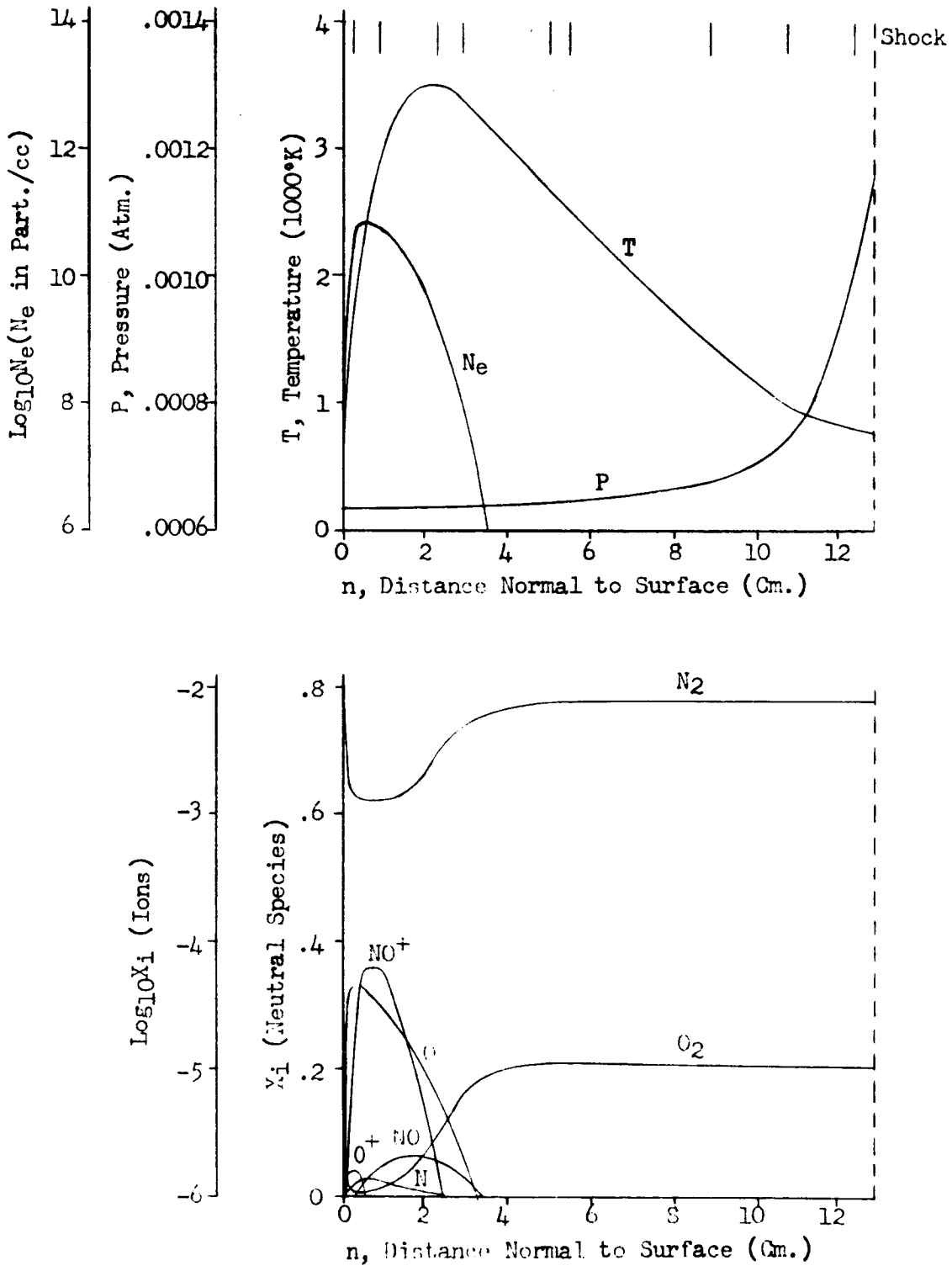

Figure 36g. Flow Field Properties - Case 12, Normal 7

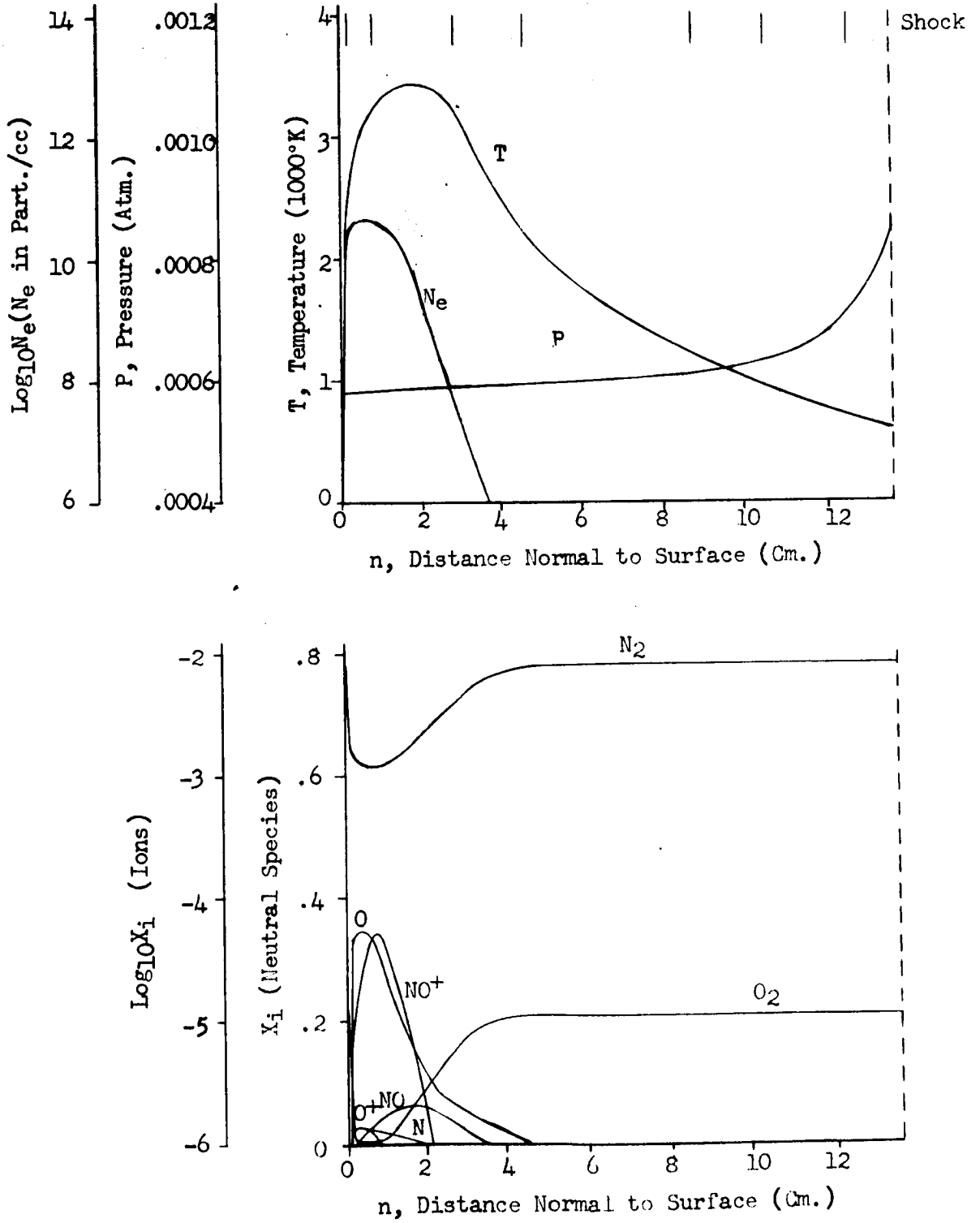

Figure 36h. Flow Field Properties - Case 12, Normal 8

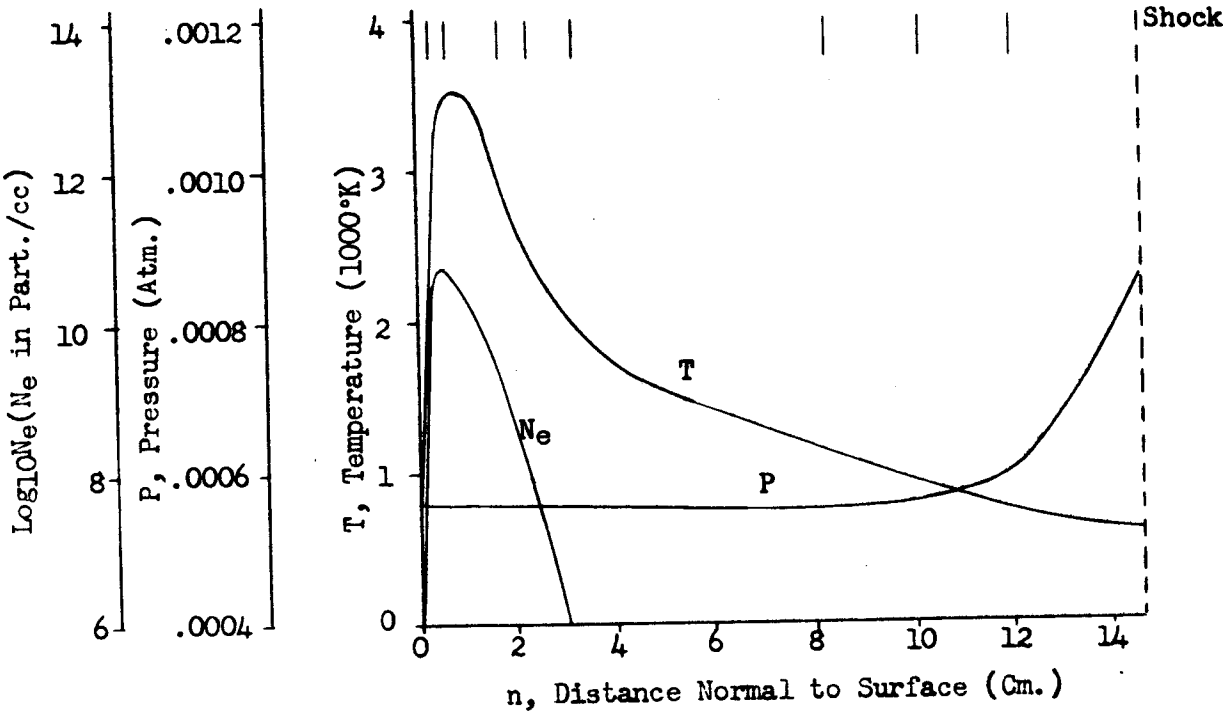

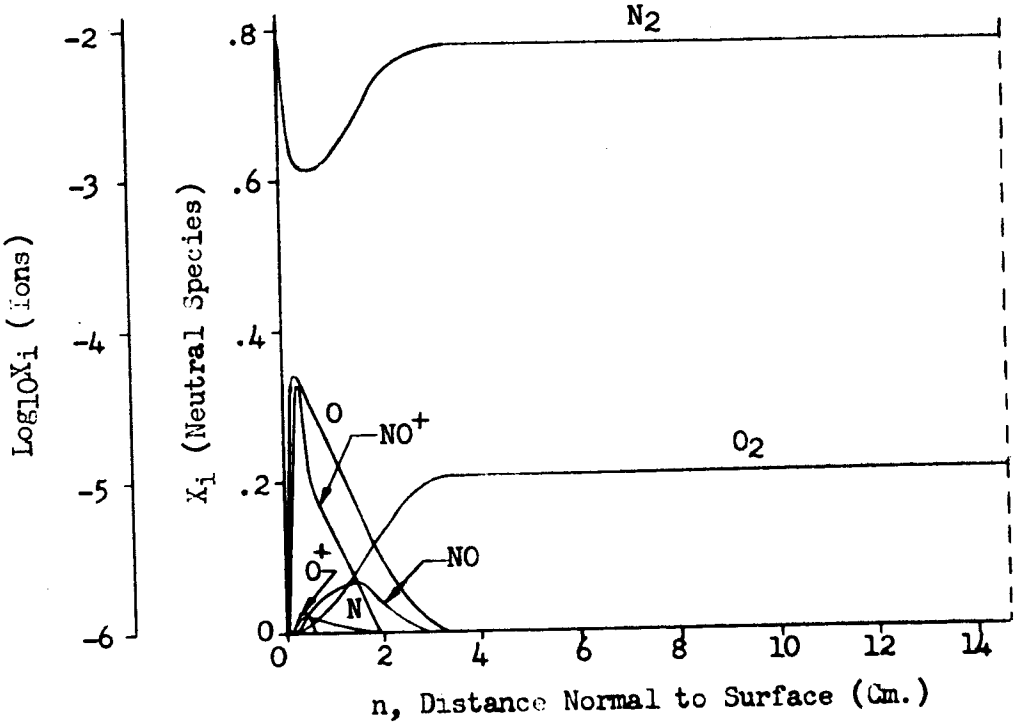

Figure 36i. Flow Field Properties - Case 12, Normal 9

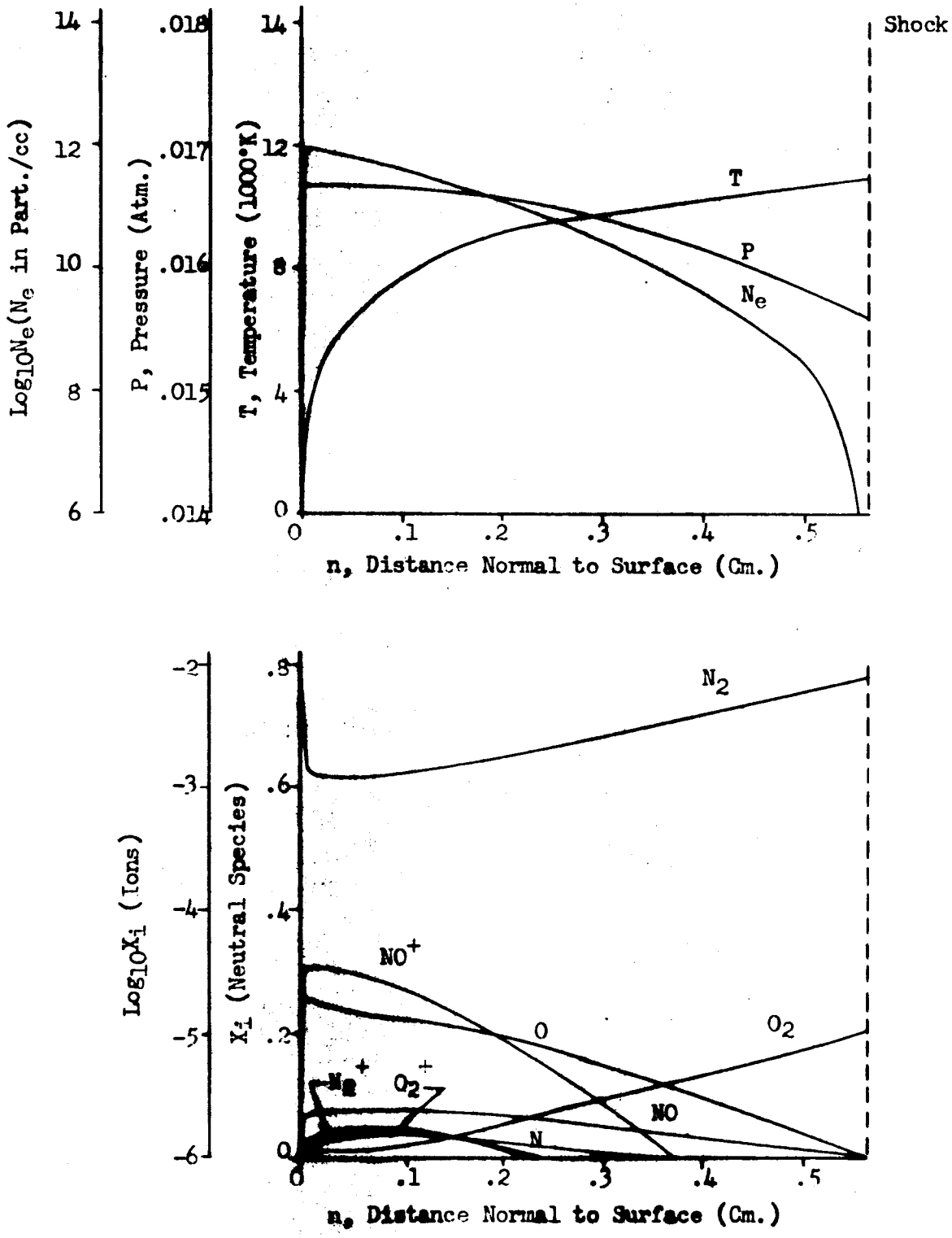

Figure 37a. Flow Field Properties - Case 13, Normal 1

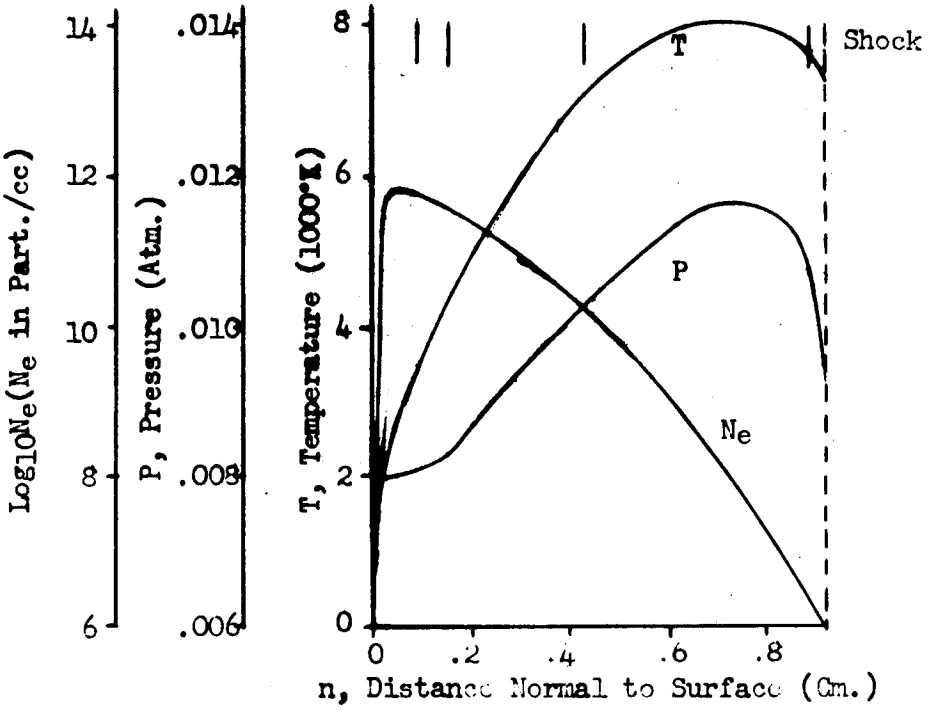

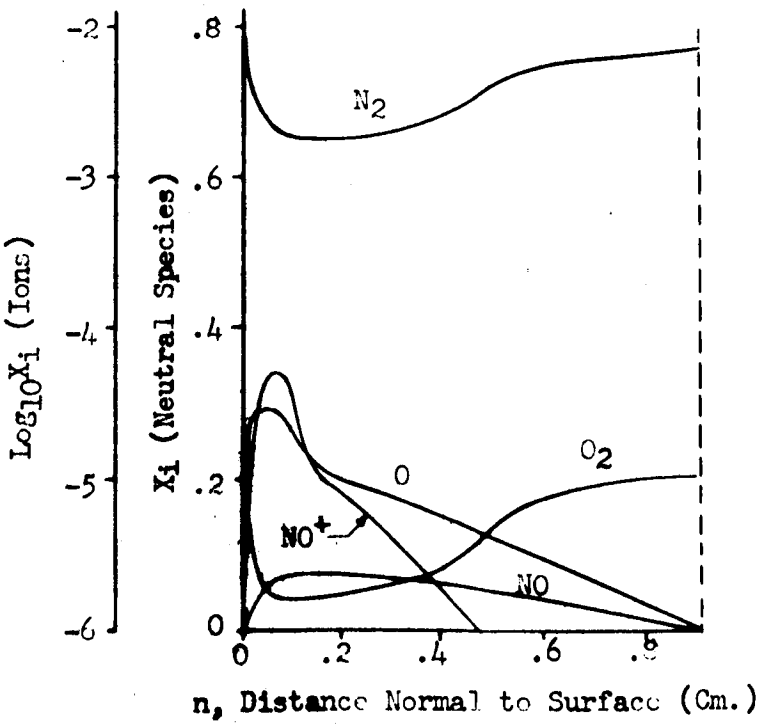

Figure 37b. Flow Field Properties - Case 13, Normal 2

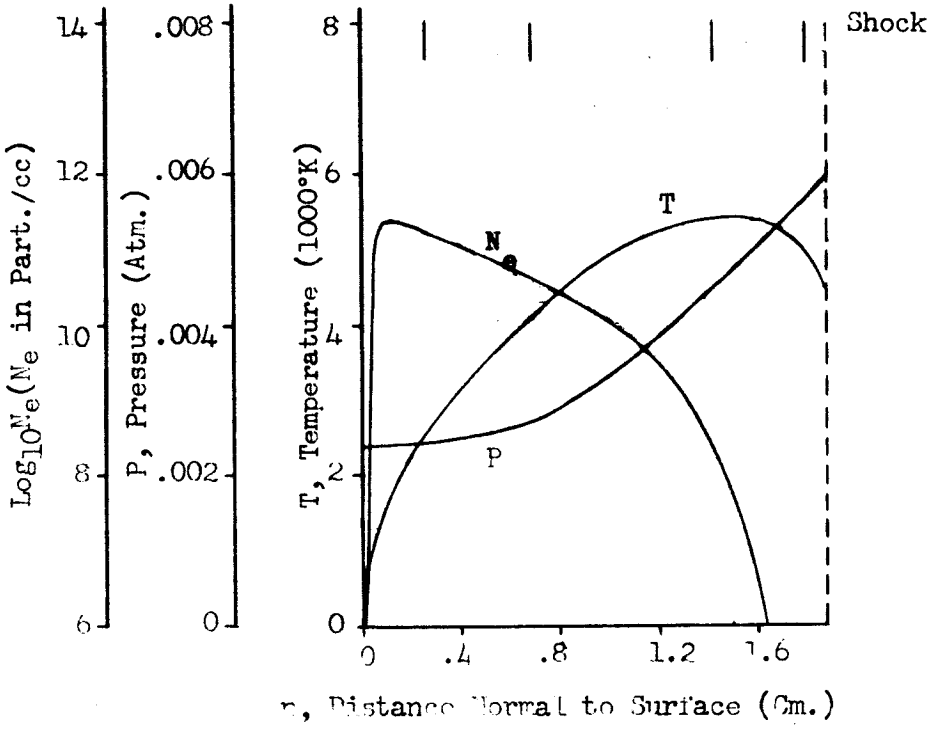

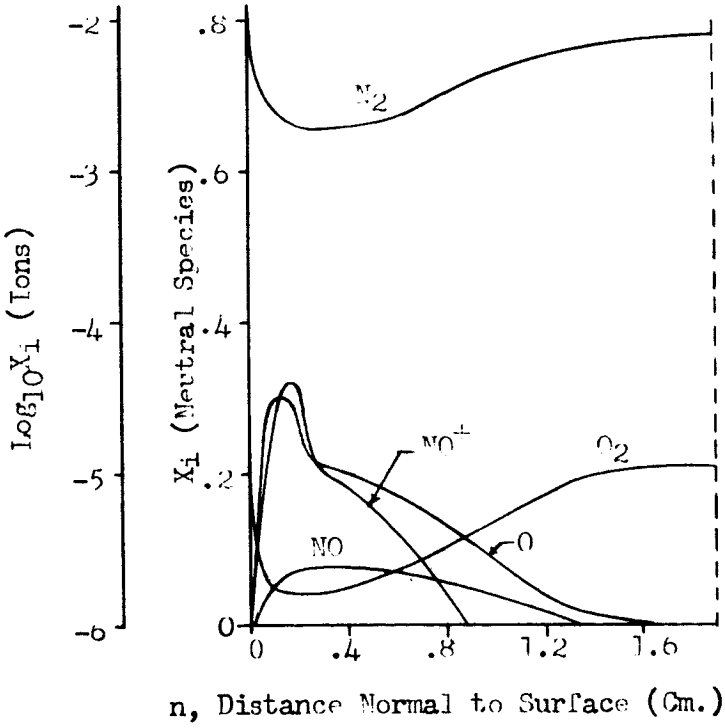

Figure 37c. Flow Field Properties - Case 13, Normal 3

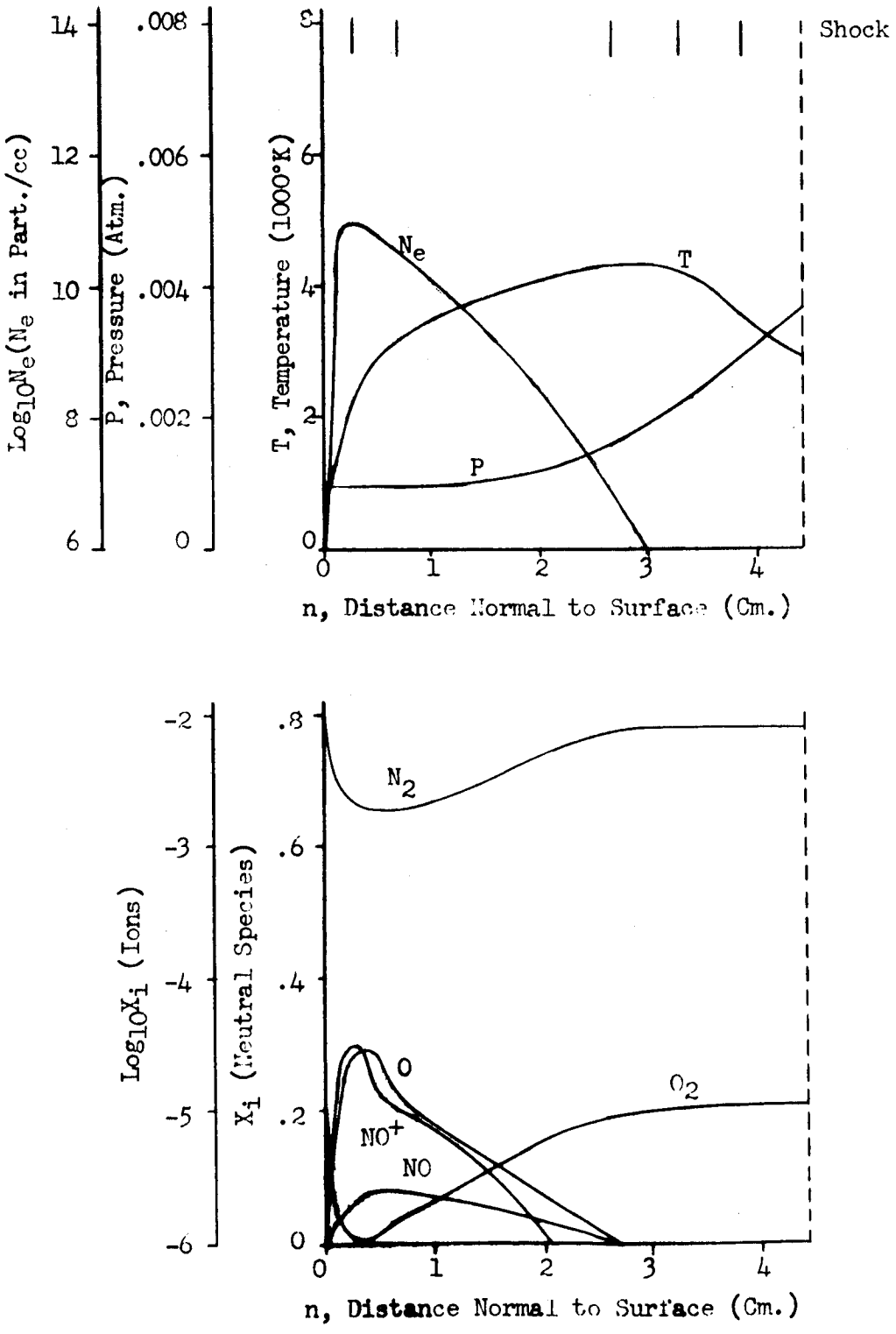

Figure 37d. Flow Field Properties - Case 13, Normal 4

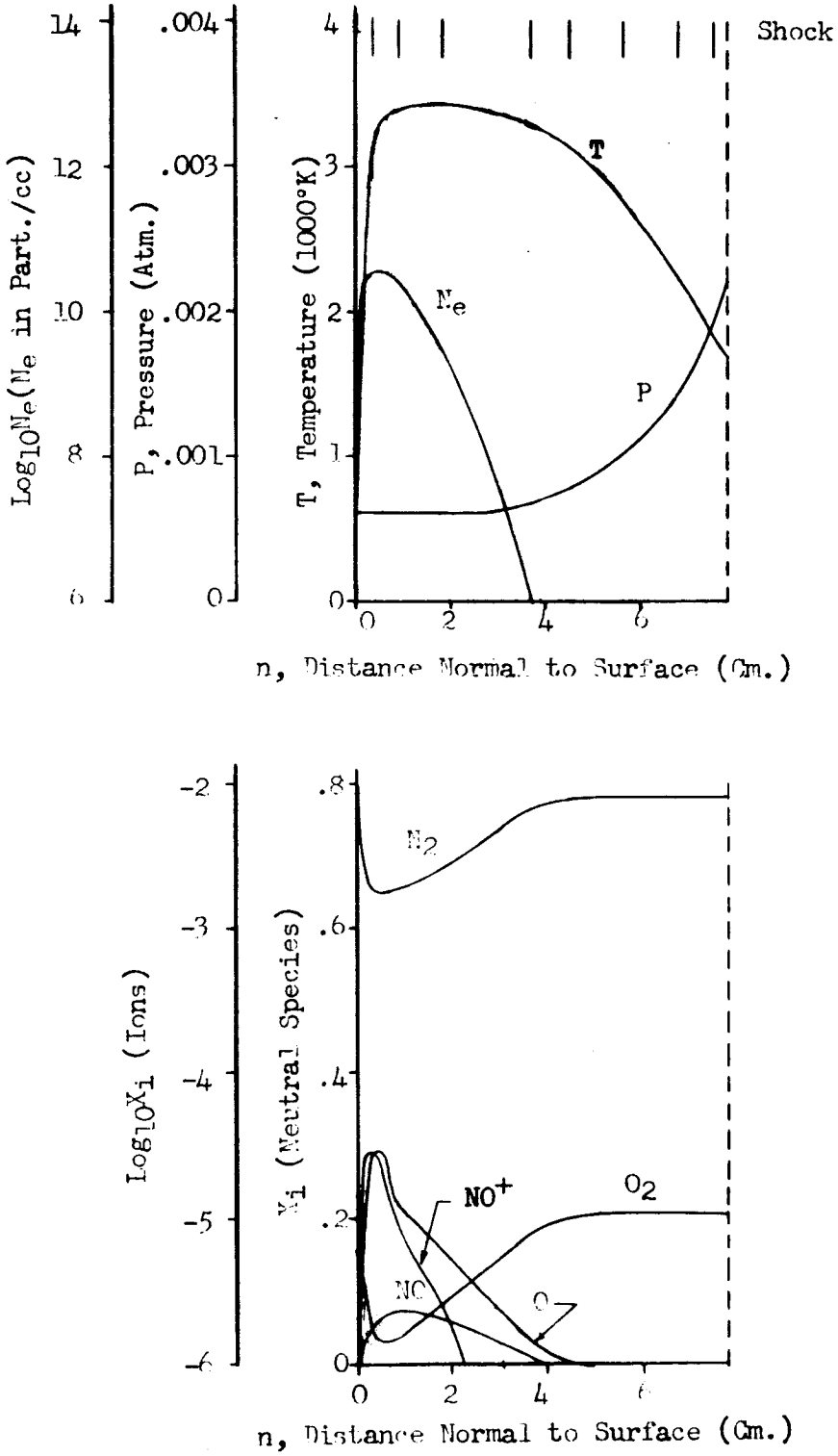

Figure 37e. Flow Field Properties - Case 13, Normal 5

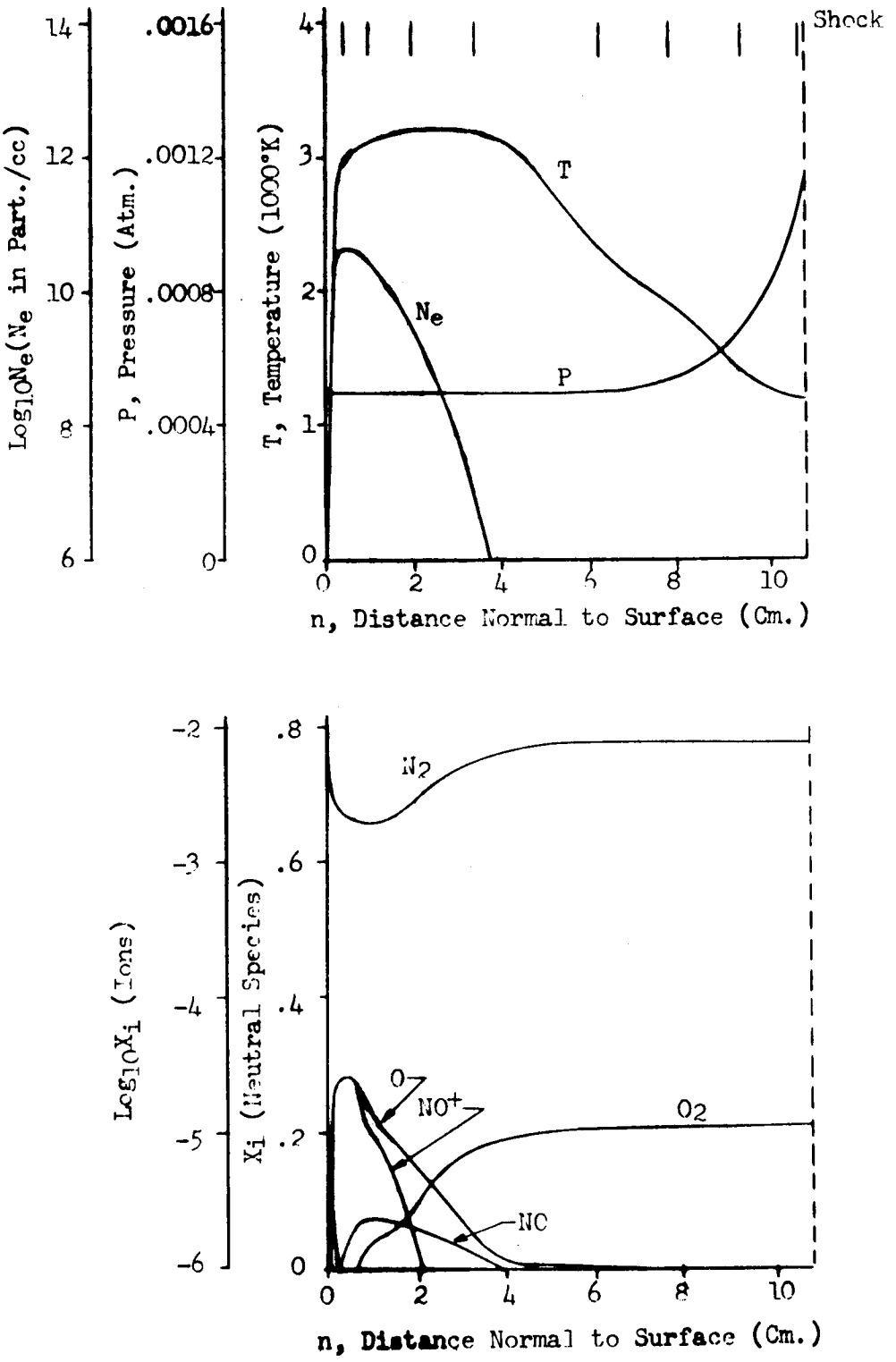

Figure 37f. Flow Field Properties - Case 13, Normal 6

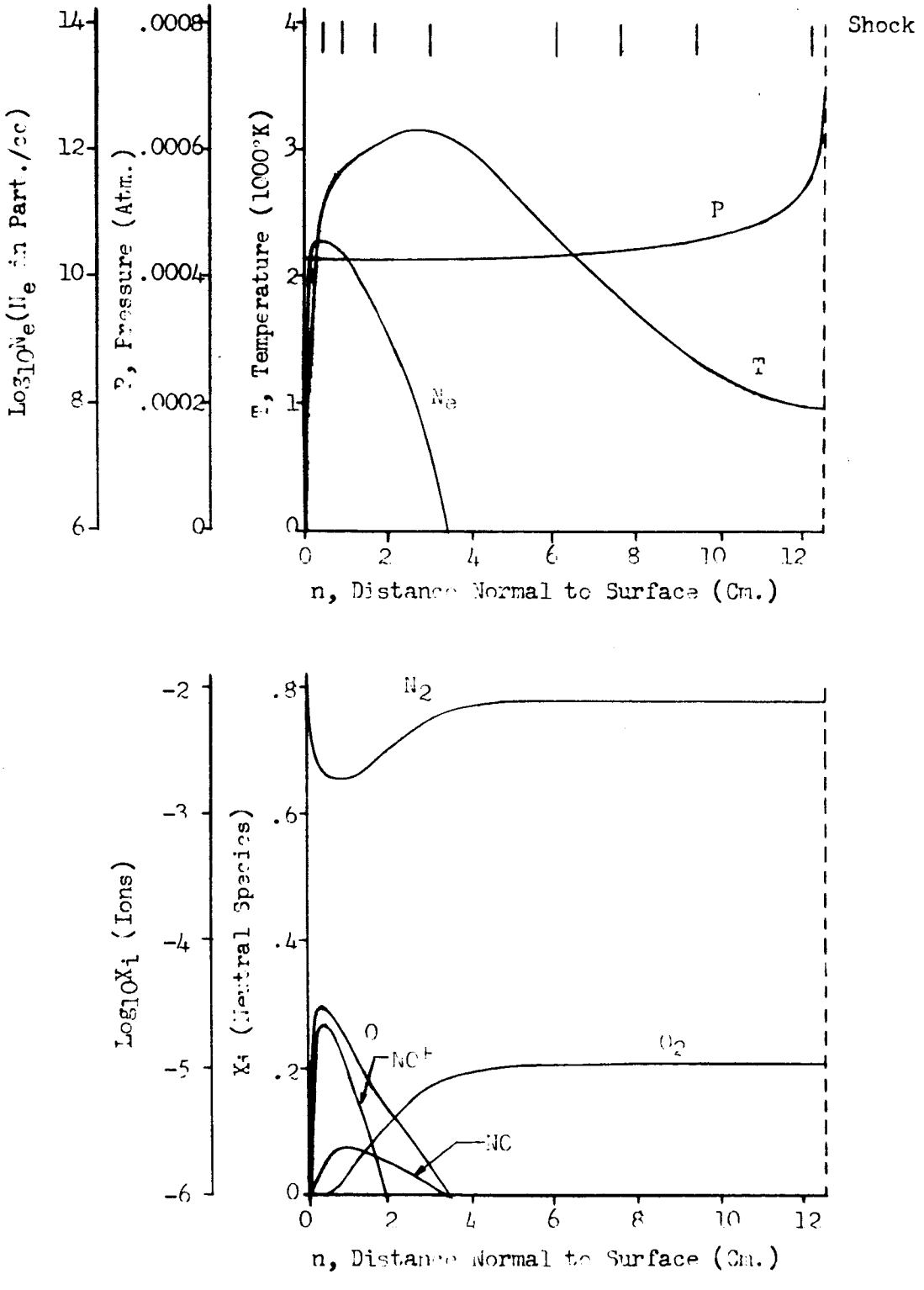

Figure 37g. Flow Field Properties - Case 13, Normal 7

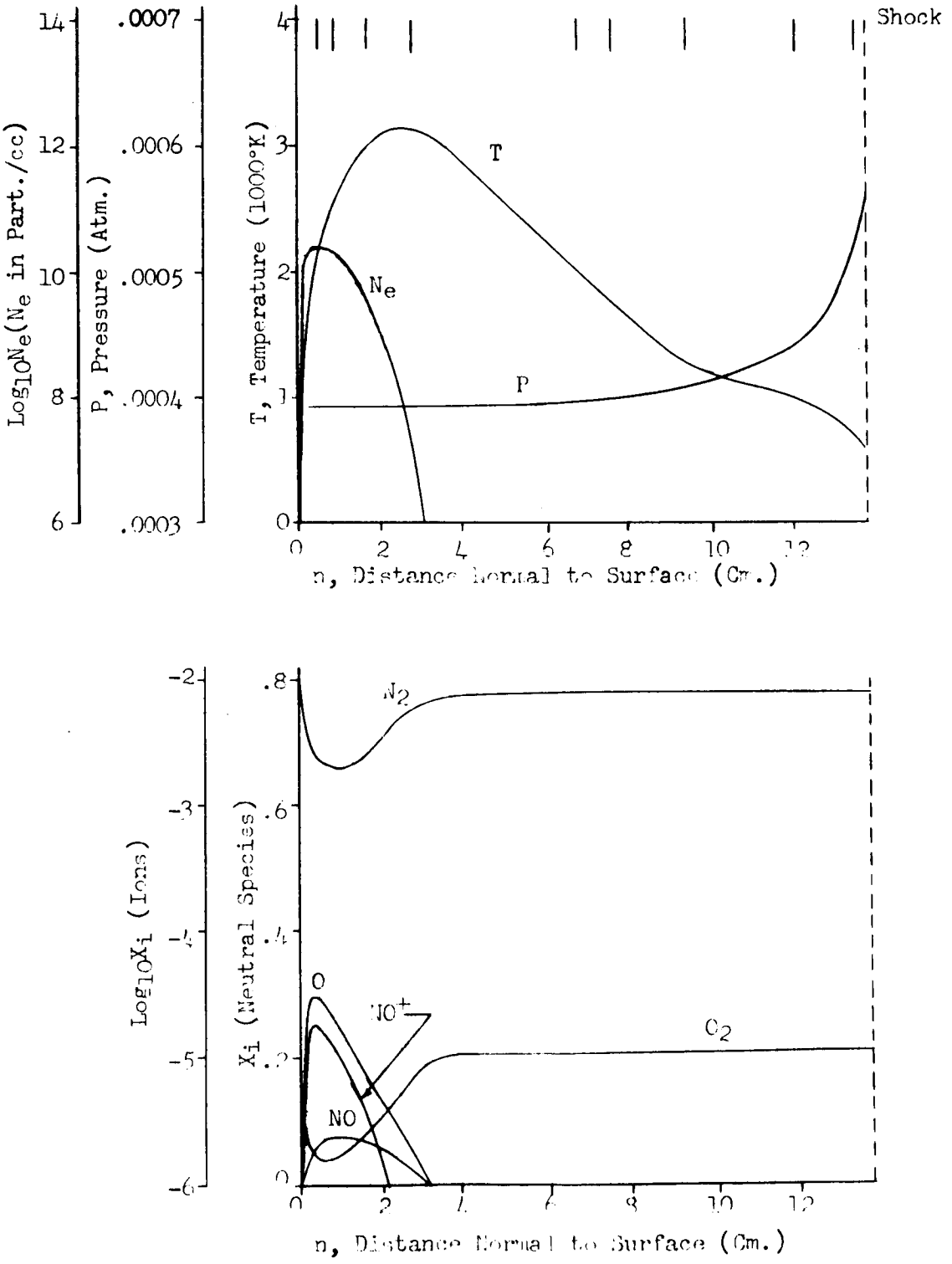

Figure 37h. Flow Field Properties - Case 13, Normal 8

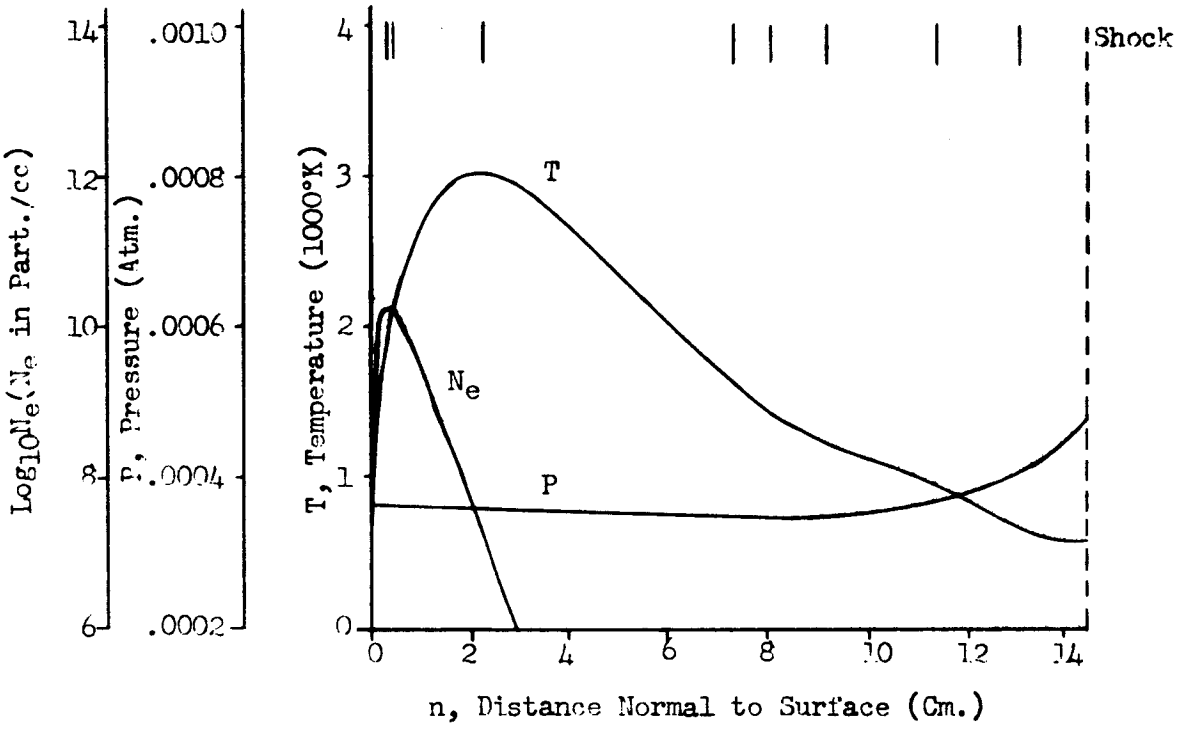

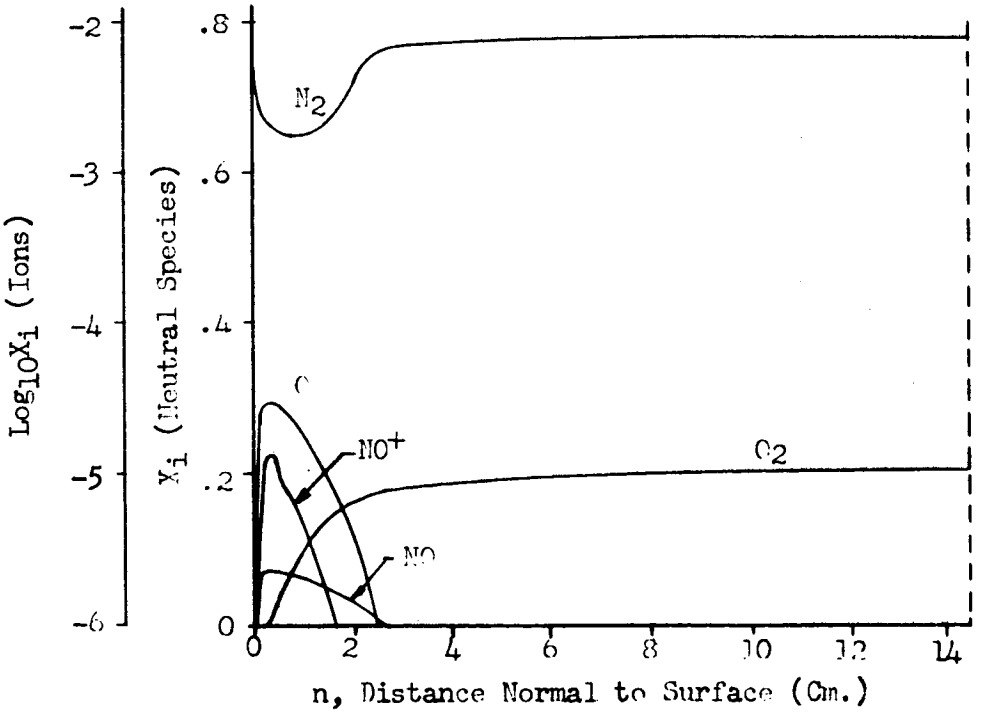

Figure 37i. Flow Field Properties - Case 13, Normal 9

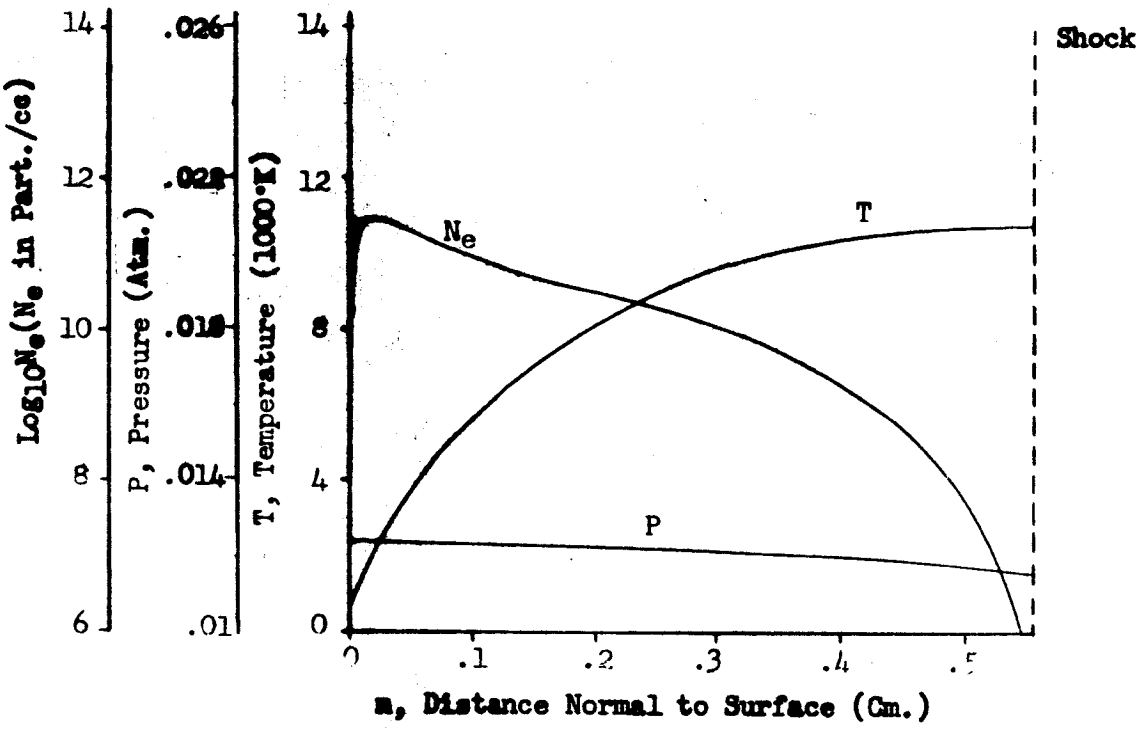

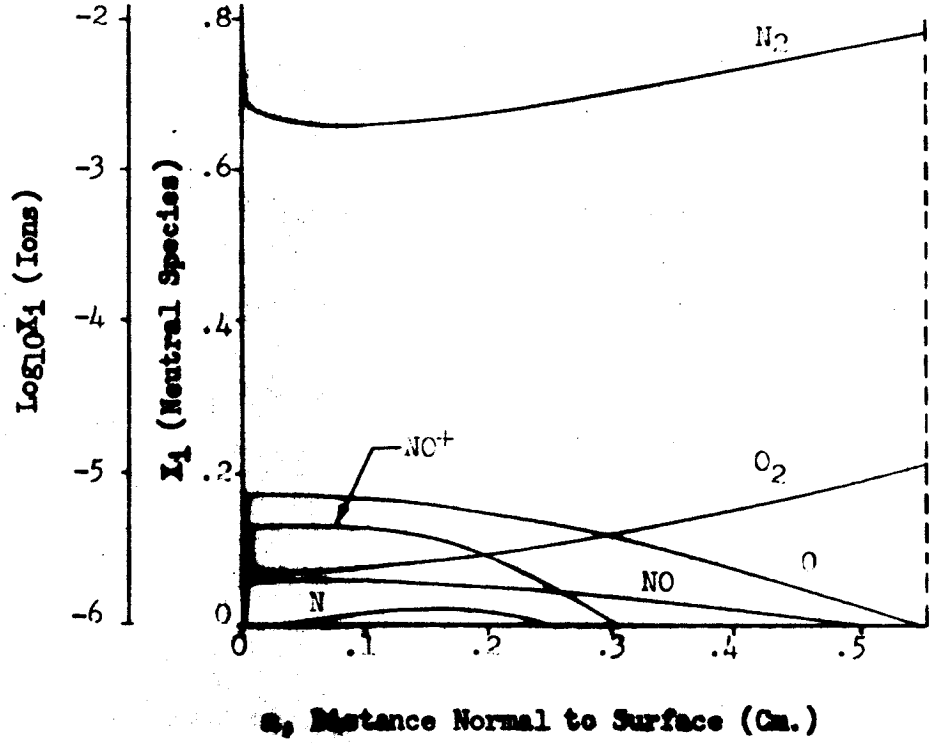

Figure 38a. Flow Field Properties - Case 14, Normal 1

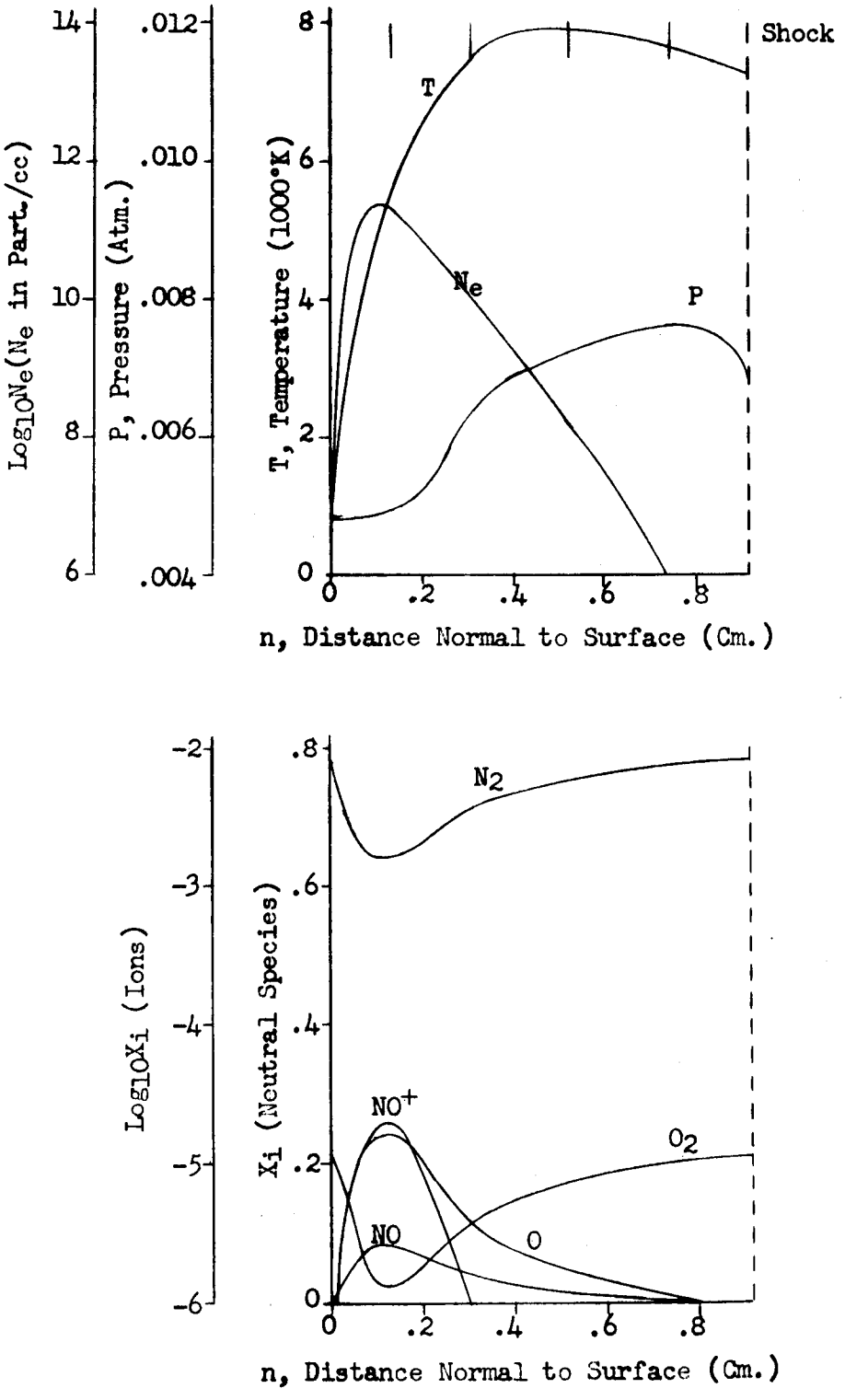

Figure 38b. Flow Field Properties - Case 14, Normal 2

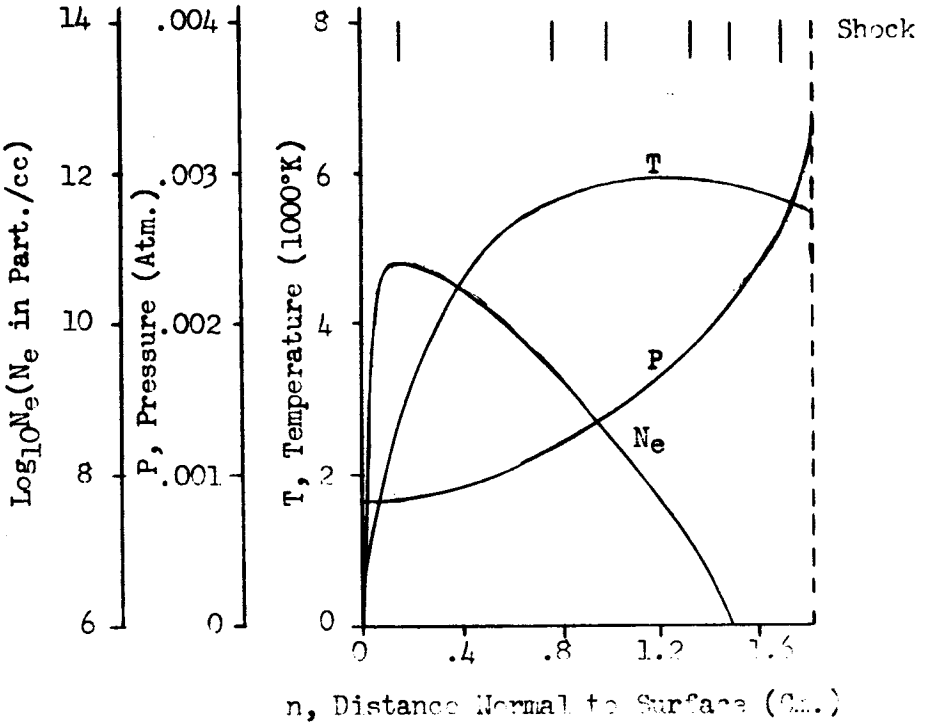

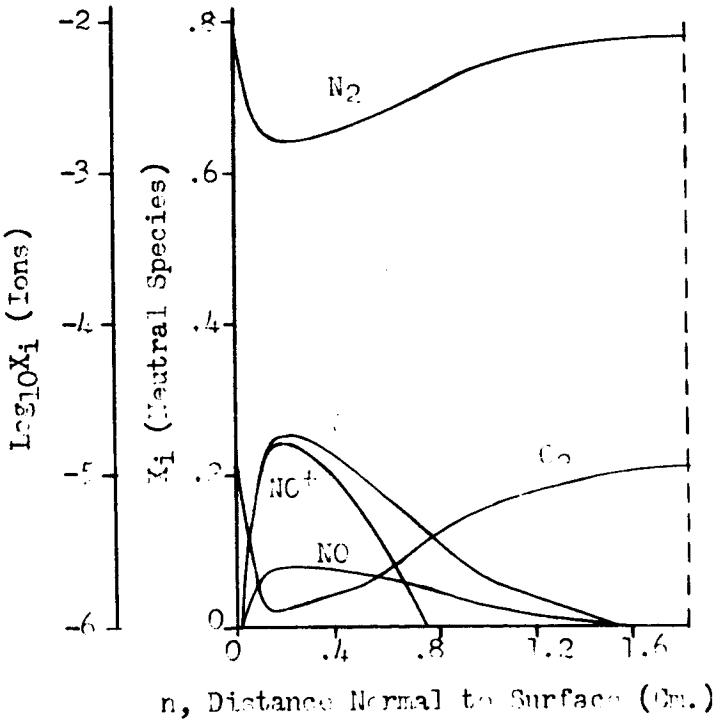

Figure 38c. Flow Field Properties - Case 14, Normal 3

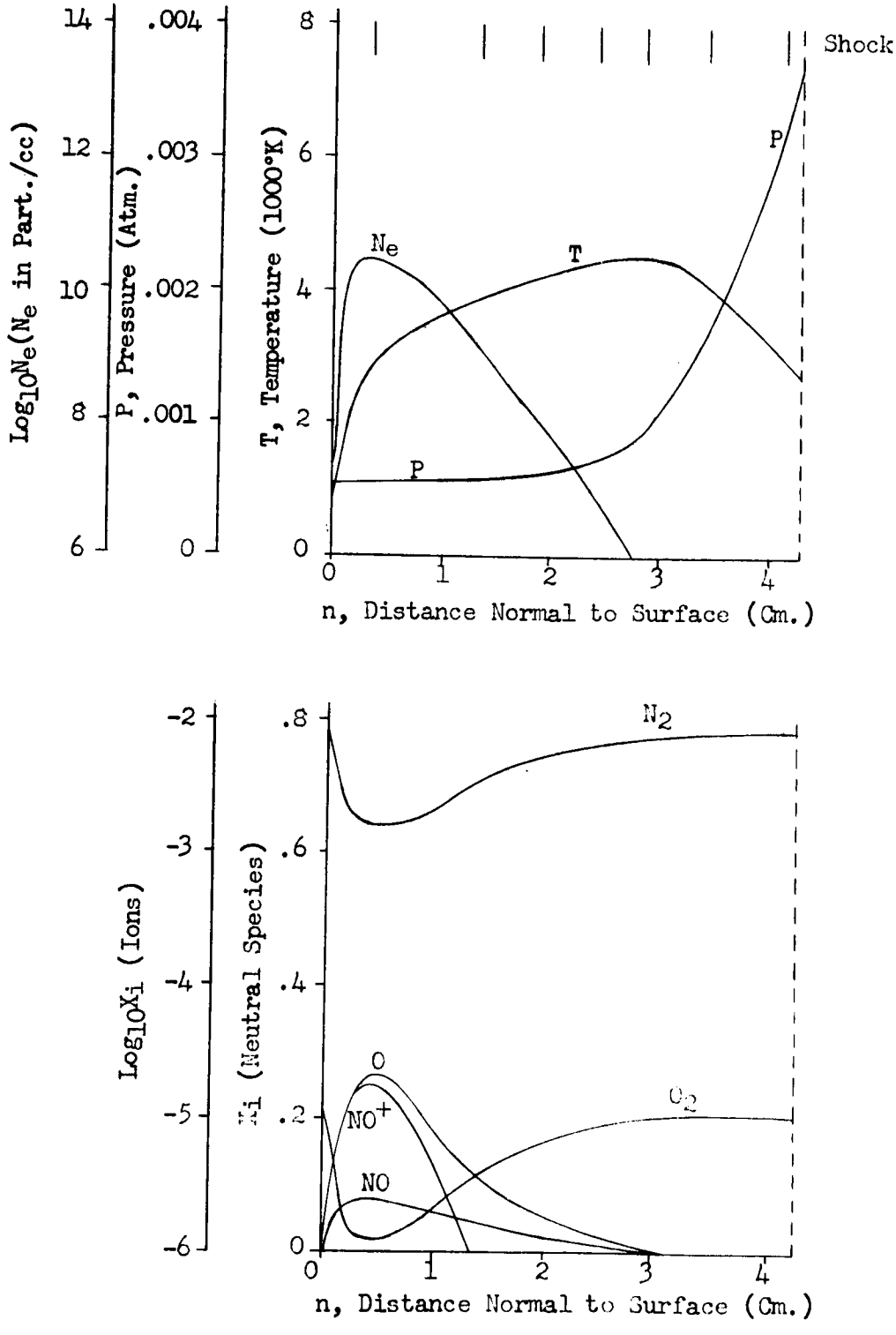

Figure 38d. Flow Field Properties - Case 14, Normal 4

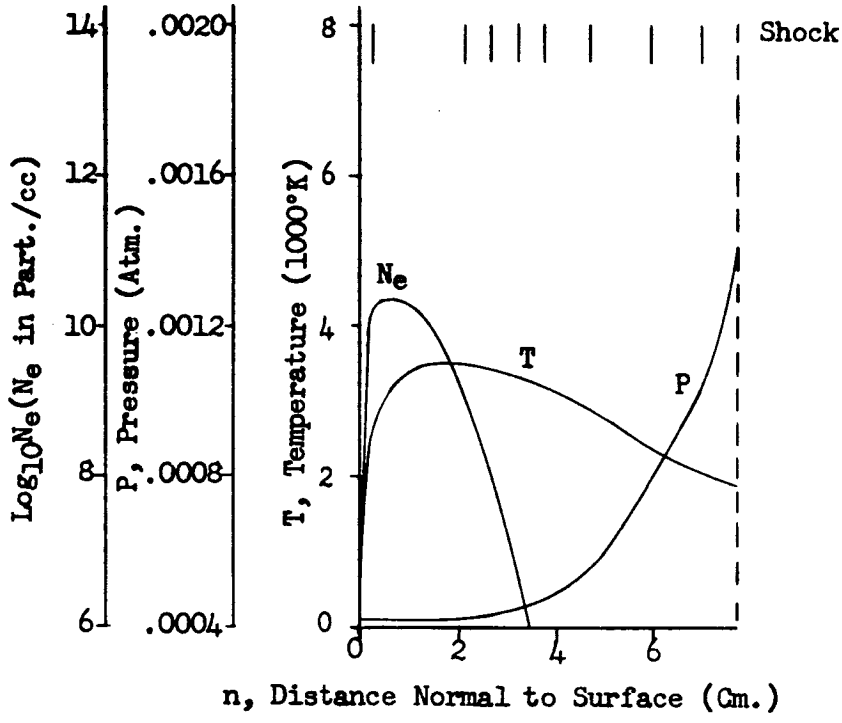

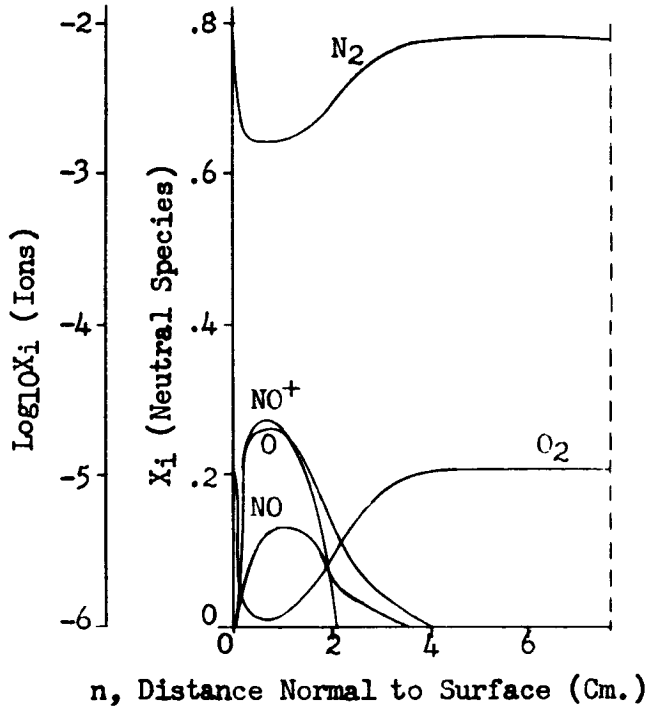

Figure 38e. Flow Field Properties - Case 14, Normal 5

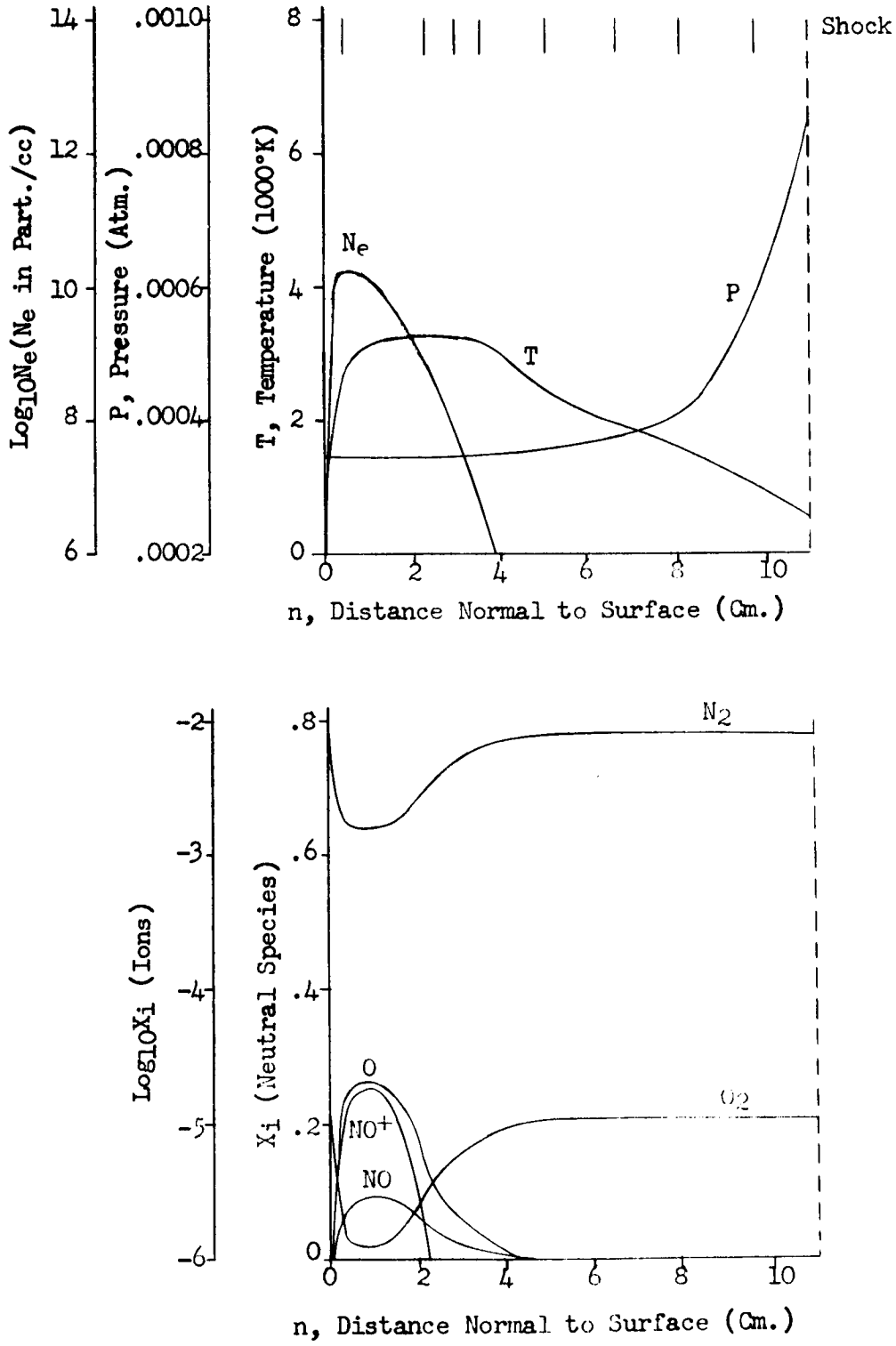

Figure 38f. Flow Field Properties - Case 14, Normal 6

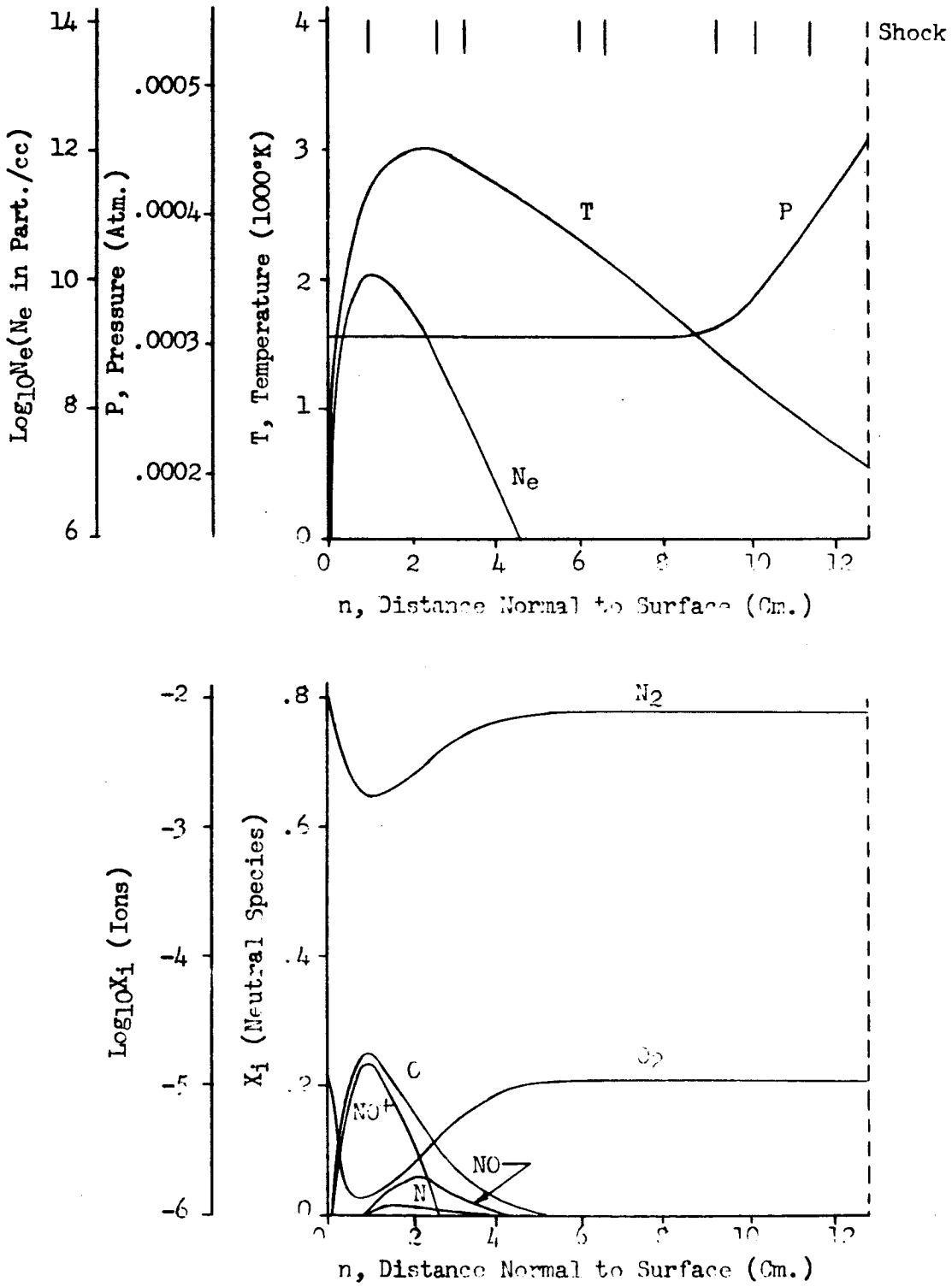

Figure 38g. Flow Field Properties - Case 14, Normal 7

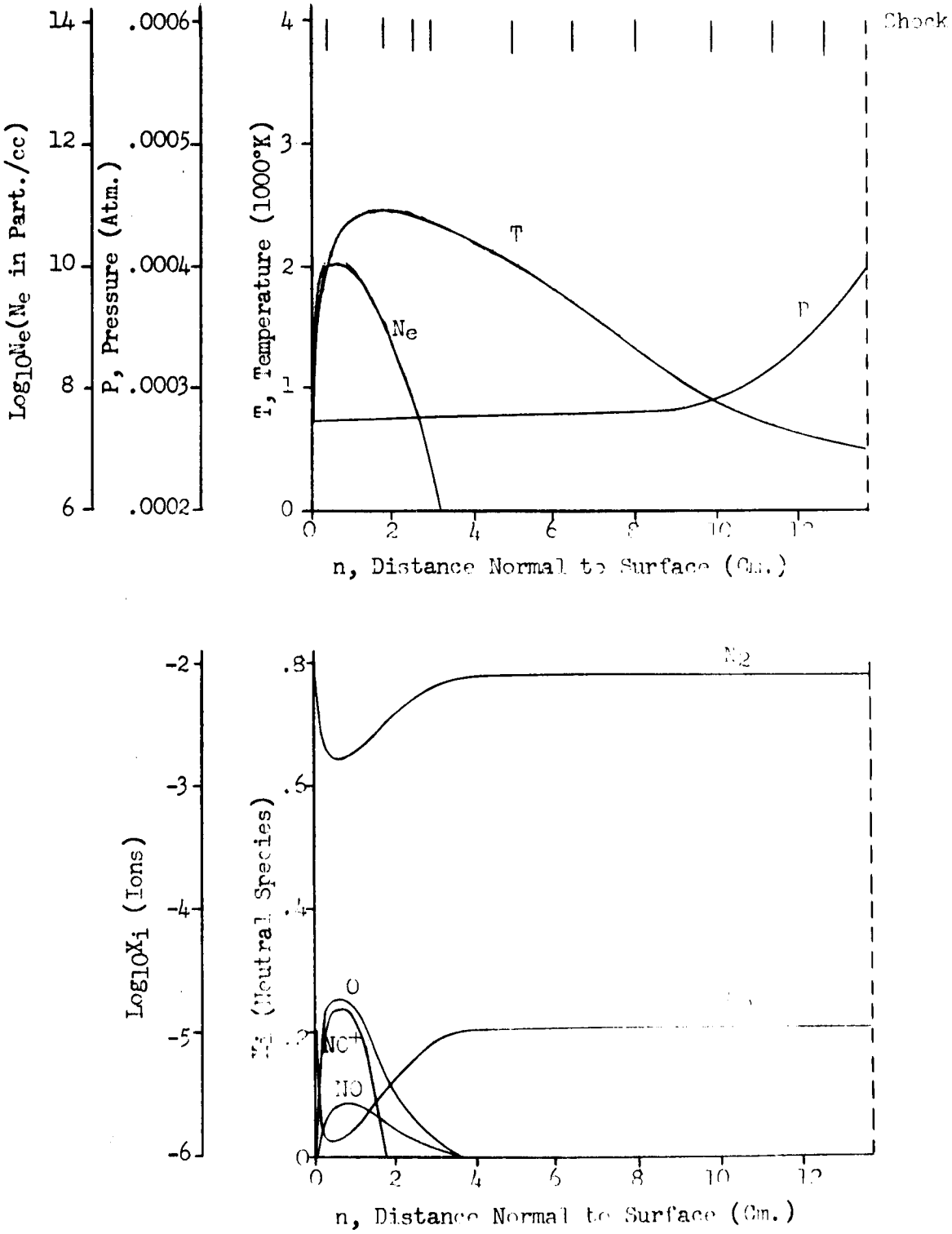

Figure 38h. Flow Field Properties - Case 14, Normal 8

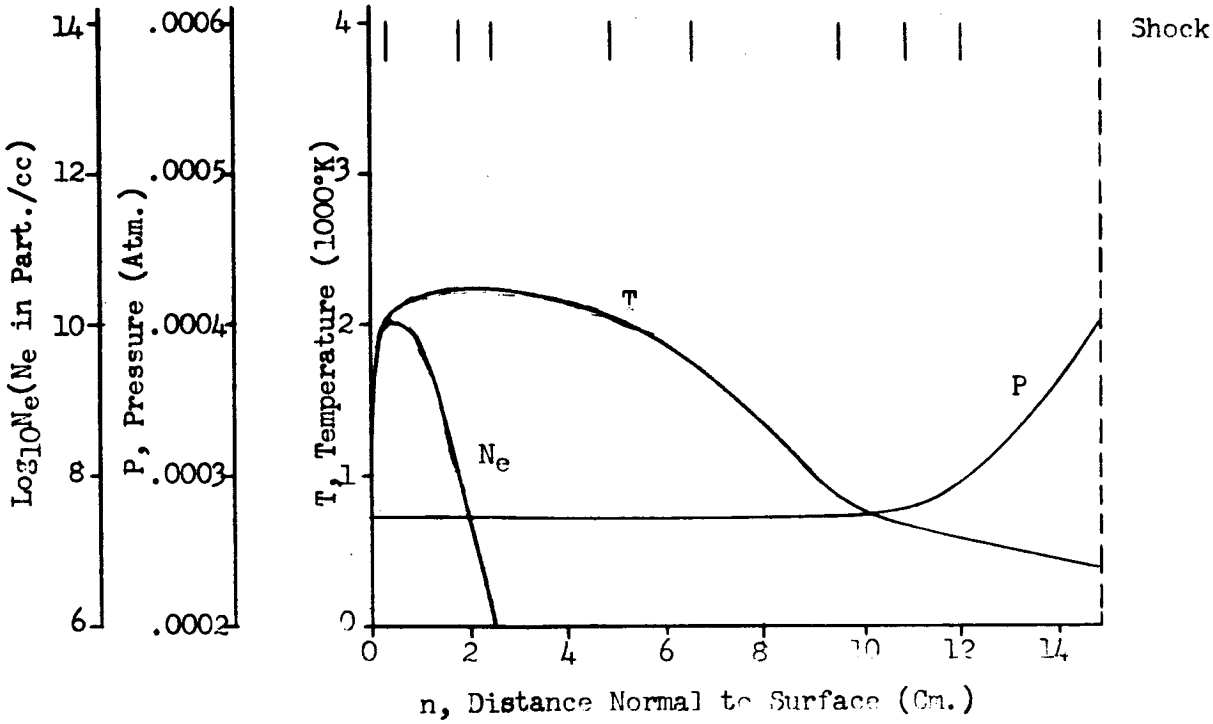

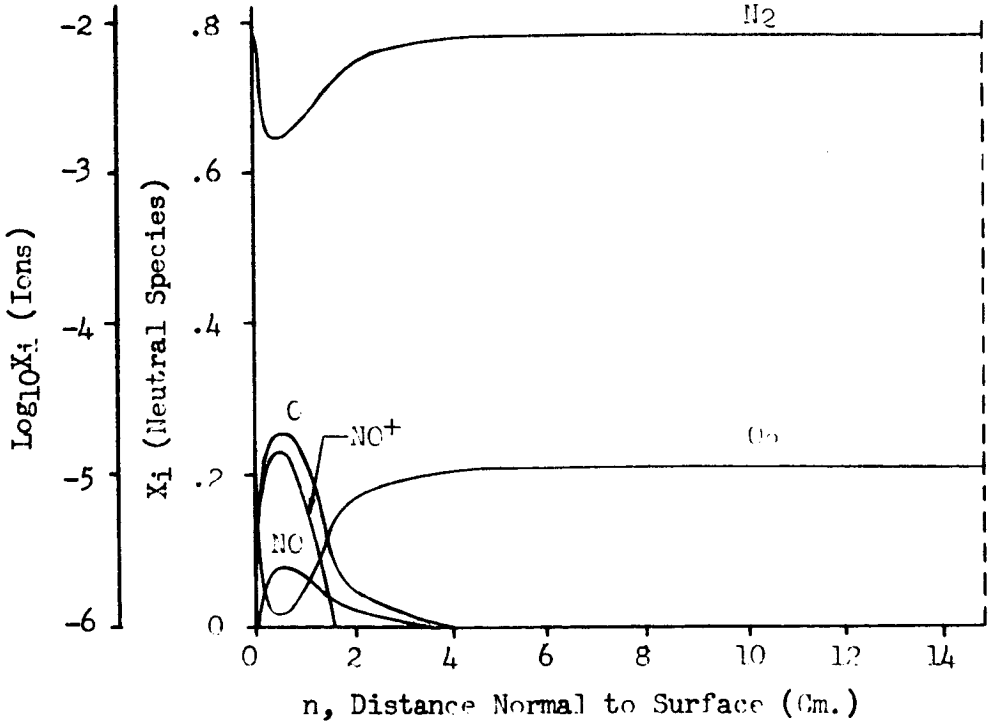

Figure 38i. Flow Field Properties - Case 14, Normal 9

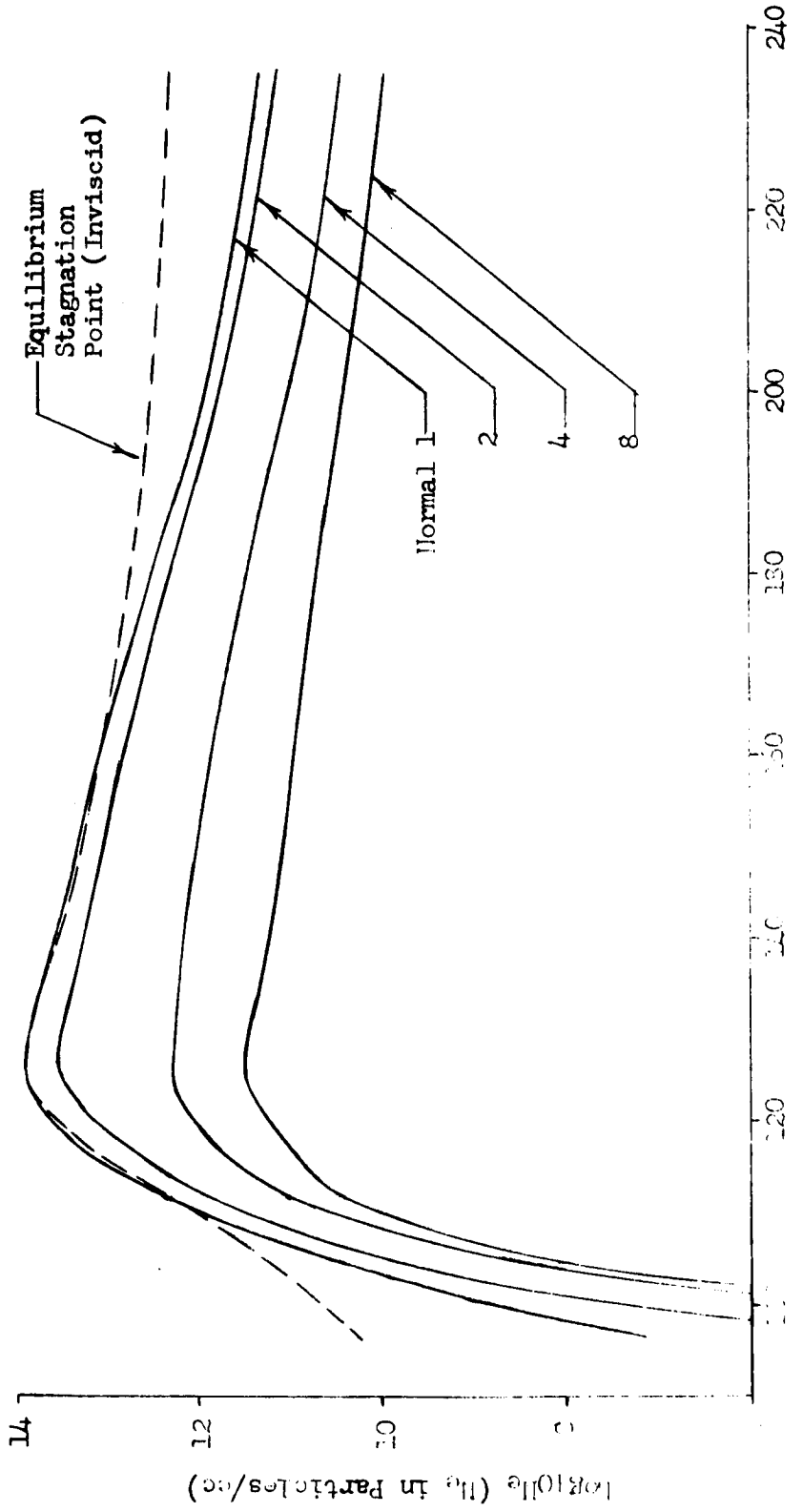

Figure 22. Variation of Peak Electron Density Along RAM B3 Flight Trajectory

CONCLUSIONS AND RECOMMENDATIONS

Complete shock layer flow fields have been computed for a series of fourteen flight conditions, taking into account the effect of finite rate chemical reactions on the distribution of flow field properties using a one-dimensional streamtube approach.

The maximum electron concentration computed during the study was 10^{14} particles per cubic centimeter and occurred in the stagnation region for Case 7, at an altitude of 163,868 ft and a flight velocity of 18,154 ft/sec. This flight condition represented the highest velocity attained along the trajectory. At lower velocities, the maximum electron density decreases sharply. The effect of increasing altitude at a nearly constant velocity is to decrease gradually the maximum electron density. The effect of the boundary layer was to reduce the maximum electron concentration due to non-equilibrium flow conditions.

It is recommended that complete equilibrium flow field data, including chemical composition, be calculated to aid in evaluating the extent of the nonequilibrium effects and to serve as a standard for comparison. In the present study, the departure from chemical equilibrium appeared quite pronounced in some cases; and the assumption of chemical equilibrium could lead to large errors in chemical composition and electron concentration. A program should be undertaken to determine the effects of diffusion on the distribution of chemical species throughout the flow field. In the present analysis, diffusion effects were neglected in the application of a one-dimensional streamtube calculation method.

NOMENCLATURE

Symbol	Definition
a	Speed of sound
A	Streamtube area
C_p	Specific heat at constant pressure
g	Gravitational constant
h	Static enthalpy
H	Total enthalpy
j	Dimensional flow indicator { 0 - two-dimensional; 1 - axisymmetric
J	Mechanical equivalent of heat
K_b	Backward chemical rate constant
K_{EQ}	Chemical equilibrium constant
K_f	Forward chemical rate constant
M	Mach number
n	Intrinsic normal coordinate; chemical specie mole-to-mass ratio; distance outward along body normal
N1	Total number of chemical species
N2	Total number of chemical reactions
p	Pressure
q	Total velocity
r	Radial body coordinate
R	Universal gas constant
R_c	Radius of curvature
R_s	Shock radius

Symbol	Definition
S	Enthalpy function; entropy; streamline intrinsic coordinate; distance along body surface from stagnation point
t	Time
T	Temperature
u	Longitudinal velocity component
U	Transformed longitudinal velocity component
v	Normal velocity component
V	Transformed normal velocity component; volume
w	Chemical specie molecular weight
X	Chemical mole fraction
$\overline{X}$	Axial distance downstream from stagnation point
Z	Compressibility factor, altitude, axial coordinate
α	Forward stoichiometric coefficient
β	Backward stoichiometric coefficient
γ	Specific heat-ratio
γ_e	Effective specific heat ratio
δ	Boundary layer thickness
$\bar{\delta}$	Shock standoff distance
δ^*	Boundary layer displacement thickness
Δn	Streamtube width
θ	Boundary layer momentum thickness; flow angle
μ	Mach angle
ρ	Density

Subscripts

Symbol	Definition
∞	Free-stream conditions
e	Edge of boundary layer
o	Stagnation conditions
i	Subscript denoting species
k	Subscript denoting reactions
max	Maximum value
w	Wall or body conditions
1	Outboard streamline designation
2	Inboard streamline designation

REFERENCES

1. Waiter, S. A. Analytical Study of Laminar Boundary Layer Growth at Hypersonic Velocities. NAA S&ID, SID 64-1929 (November 1964).

2. Waiter, S. A. and R. B. Anderson. Determination of the Transonic Flow Field Around a Blunt Body. NAA S&ID, SID 64-634 (February 1964).

3. Webb, H. G., Jr. Final Report, Flow Field Prediction and Analysis for Project RAM-Phase II. NAA S&ID, SID 64-548 (July 1964).

4. Lomax, H. and M. Inouye. Numerical Analysis of Flow Properties About Blunt Bodies Moving at Supersonic Speeds in an Equilibrium Gas. NASA TR R-204 (July 1964).

5. Hayes, W. D. and R. F. Probstein. Hypersonic Flow Theory. New York: Academic Press (1959).

6. Grabau, M. A Method of Forming Continuous Empirical Equations for the Thermodynamic Properties of Air from Ambient Temperatures to 15,000 K, With Applications. AEDC-TN-59-102 (August 1959).

7. Dresser, H. S. Method of Characteristics Program for Real Gas Equilibrium Flow. NAA S&ID, SID 64-633 (March 1964).

8. Hansen, C. F. Approximations for the Thermodynamic and Transport Properties of High-Temperature Air. NASA TR-50 (1959).

9. Vaglio-Laurin, R. and M. H. Bloom. Chemical Effects in External Hypersonic Flows. ARS Paper 1976-61. Presented at International Hypersonics Conference (August 1961).

10. Eschenroeder, A. Q.; D. W. Boyer; and G. J. Hall. Exact Solutions for Nonequilibrium Expansions of Air With Coupled Chemical Reactions. Cornell Aeronautical Laboratory Report AF-1413-A-1 (May 1961).

11. Gravalos, F. G.; I. H. Edelfelt; and H. W. Emmons. The Supersonic Flow About a Blunt Body of Revolution for Gases in Chemical Equilibrium. Presented at the Congress of International Astronautical Federation (August 1958).

12. Stein, A. M. and R. B. Anderson. Computer Program, Thermodynamic and Thermal Functions of Individual Species Including Elementary Ablation Products, for Hypersonic Flow Air Model. NAA S&ID, SID 64-635 (December 1963).

13. Penner, S. S. Chemistry Problems in Jet Propulsion, Vol. I. New York: Pergamon Press (1957).

14. Stein, A. M. High-Temperature Thermodynamics and Chemical Equilibria for a Hypersonic Flow Air Model. NAA S&ID, SID TNA63-1 (December 1963).

15. Dresser, H. S. and A. M. Stein. One-Dimensional, Reacting Gas Flow Program. NAA S&ID, SID 64-632 (February 1964).

16. Ralston, A. and H. S. Wilf. Mathematical Methods for Digital Computers. New York: John Wiley and Sons (1960).

17. Vincenti, W. G. Calculations of the One-Dimensional Nonequilibrium Flow of Air Through a Hypersonic Nozzle--Interim Report. AEDC-TN-61-65 (May 1961).

18. Emanual, G. and W. G. Vincenti. Method for Calculation of the One-Dimensional Nonequilibrium Flow of a General Gas Mixture Through a Hypersonic Nozzle. AEDC-TDR-62-131 (June 1962).

19. Wray, K.; J. D. Teare; B. Kivel; and P. Hammerling. Relaxation Processes and Reaction Rates Behind Shock Fronts in Air and Component Gases. Avco-Everett Research Laboratory, Research Report 83 (1959).

20. Wray, K. Chemical Kinetics of High-Temperature Air. Avco-Everett Research Laboratory, Report 104 (1961).

21. Feldman, S. Trails of Axi-Symmetric Hypersonic Blunt Bodies Flying Through The Atmosphere. Avco-Everett Research Laboratory, Research Report 82 (1959).